

2013-08-20

Hydrogen in Low Carbon Steel: Diffusion, Effect on Tensile Properties, and an Examination of Hydrogen's Role in the Initiation of Stress Corrosion Cracking in a Failed Pipeline

Eggum, Troy Justin

Eggum, T. J. (2013). Hydrogen in Low Carbon Steel: Diffusion, Effect on Tensile Properties, and an Examination of Hydrogen's Role in the Initiation of Stress Corrosion Cracking in a Failed Pipeline (Doctoral thesis, University of Calgary, Calgary, Canada). Retrieved from <https://prism.ucalgary.ca>. doi:10.11575/PRISM/26402

<http://hdl.handle.net/11023/881>

Downloaded from PRISM Repository, University of Calgary

UNIVERSITY OF CALGARY

Hydrogen in Low Carbon Steel: Diffusion, Effect on Tensile Properties, and an Examination of
Hydrogen's Role in the Initiation of Stress Corrosion Cracking in a Failed Pipeline

by

Troy Justin Eggum

A THESIS

SUBMITTED TO THE FACULTY OF GRADUATE STUDIES
IN PARTIAL FULFILMENT OF THE REQUIREMENTS FOR THE
DEGREE OF DOCTOR OF PHILOSOPHY

DEPARTMENT OF MECHANICAL AND MANUFACTURING ENGINEERING

CALGARY, ALBERTA

AUGUST, 2013

© Troy Justin Eggum 2013

Abstract

This thesis covers three topic areas: hydrogen diffusion in steel, hydrogen effects on steel's mechanical properties, and examination of a pipeline that fractured due to stress corrosion cracking (SCC).

A hydrogen diffusion experiment using low carbon steel, passive hydrogen charging (5% NaCl, 1.1 pH, N₂ deaeration), and mercury eudiometry for hydrogen measurement was used to develop a concentration profile in a specimen. This profile was compared to an analytical solution to Fick's Law of Diffusion. The experimental concentration profile follows Fick's prediction and allows determination of hydrogen's effective diffusion coefficient and surface and bulk concentrations. The effective diffusion coefficient and surface concentration were found to increase with aggressiveness of the charging solution.

Tensile tests were performed on low carbon steel from a mobile solute in solid solution perspective. Different combinations of values of strain rate and hydrogen concentration were used to determine the effect of hydrogen concentration and to find interactions between hydrogen diffusion rate and strain rate. Increasing the strain rate increased the flow stresses (yield, ultimate, and fracture), uniform plastic strain, and strain hardening exponent. Increasing the hydrogen concentration decreased necking strain, elongation at fracture, and increased fracture stress. This led to a natural division of the tensile response of the steel into two areas: prior to the ultimate changes to the strain rate dominate the material's behaviour and post-ultimate where changes in hydrogen concentration dominate the material's behaviour. It was shown that hydrogen had a hardening effect near the yield point and softening effect near the ultimate, indicating that these techniques can detect changes in the competing embrittling and plasticizing processes of solute hydrogen in steel.

Crack morphology was examined on a SCC fractured pipeline both from axial and radial directions to observe relationships between corrosion pits and the crack field. The pitting and cracking processes were observed to be separate events. It is likely that pitting occurred first, generating hydrogen, which then moved into the steel. When sufficient hydrogen was present, the steel became sensitized to the applied hoop stress and oriented crack fields developed which eventually led to a large fracture.

Table of Contents

Abstract	ii
Table of Contents	iv
List of Tables	viii
List of Figures and Illustrations	x
List of Symbols, Abbreviations and Nomenclature	xv
CHAPTER ONE: INTRODUCTION	1
1.1 Short Description of Problem Area	1
1.2 Significance of SCC and Hydrogen in Pipelines	1
1.3 Translating a Complex Situation to the Laboratory.....	2
1.4 Study of Hydrogen Diffusion	3
1.5 Hydrogen's Effects on Material Properties	4
1.6 Failure Analysis of a Pipeline due to SCC	4
CHAPTER TWO: LITERATURE REVIEW AND RELEVANT BACKGROUND	5
2.1 Conceptual Models of SCC	5
2.2 SCC in Field Conditions	7
2.3 SCC Crack Morphology	9
2.4 Anodic Dissolution Crack Model	10
2.5 Describing the Crack: Fracture Mechanics.....	12
2.6 SCC in Materials other than Pipeline Steels; and Related Phenomena	13
2.7 Chemical Reactions of Interest	14
2.7.1 Relevant Reactions	14
2.7.2 Nernst Equation and Pourbaix Diagram.....	16
2.7.3 Some Experiments Relating the Reactions of Interest	17
2.8 Hydrogen in Materials	20
2.8.1 Overview of Hydrogen in Materials.....	20
2.8.2 Review of Crystal Structure	21
2.8.3 Properties of Hydrogen.....	22
2.8.4 How is Hydrogen Present?	23
2.8.5 How does Hydrogen Enter Steel?.....	23
2.8.6 How does Hydrogen Diffuse through Steel?.....	24
2.8.7 Where does Hydrogen Reside in Steel?	27
2.8.8 How is Hydrogen Measured?	29
2.9 The Tensile Test.....	31
2.10 Solid Solution Hardening and Mobile Solutes	34
2.11 Effect of Hydrogen on Mechanical Properties of Metals	35
CHAPTER THREE: OBJECTIVES AND SPECIFIC AIMS	38
3.1 Hydrogen Diffusion Profiles in Pipeline Steel	38
3.2 Tensile Tests with Varying Strain Rate and Hydrogen Concentration.....	39
3.3 Examination of Field-Failed Pipeline from Stress Corrosion Cracking	40

CHAPTER FOUR: EXPERIMENTAL METHODS FOR DETERMINING HYDROGEN DIFFUSION IN A LOW-CARBON STEEL	41
4.1 Main Experiment: Round Bar Test of Uniaxial Hydrogen Concentration Gradient	41
4.1.1 Sample Preparation.....	42
4.1.2 Hydrogen Charging	43
4.1.3 Mobile Hydrogen Measurement.....	43
4.1.4 Standard Procedures and Validation Experiments	44
4.2 Specimen Acquisition	45
4.3 Standard Procedure: Sample Mounting, Polishing, and Etching.....	46
4.4 Standard Eudiometer Procedure	47
4.4.1 General Points	48
4.4.2 Sample Weights.....	48
4.4.3 Apparatus.....	49
4.4.4 Loading Samples into the Eudiometers	49
4.4.5 Taking Experimental Readings	50
4.4.6 Measurements Taken Once Per Experimental Set-up	52
4.4.7 Recordkeeping.....	53
4.4.8 Data Treatment and Data Processing	55
4.4.9 Safety Protocols and Personal Protective Equipment for Mercury Use.....	58
4.5 Standard Procedure: Calibration of the Eudiometer Units	58
4.6 Standard Procedure: Cleaning the Eudiometers	62
4.7 Cleaning the Mercury	63
4.8 Validation: Determination of Appropriate Time to take Final Hydrogen Measurements	63
4.9 Validation: Baseline Hydrogen Concentration Present After Bake-Out	65
4.10 Validation: Vicker’s Hardness of Round Bar	67
4.11 Validation: Electropotential Scans.....	68
4.12 Effect of Charging Solution and Time on Apparent Surface Concentration.....	69
 CHAPTER FIVE: RESULTS OF ROUND BAR HYDROGEN DIFFUSION EXPERIMENTS	 72
5.1 Microstructure.....	72
5.2 Determination of Appropriate Time to take Final Hydrogen Measurements.....	73
5.3 Baseline Hydrogen Concentration Present after Bake-Out	77
5.4 Vicker’s Hardness of Round Bar	79
5.5 Electropotential Scans.....	81
5.6 Scanning Electron Microscope – X-Ray Energy Dispersion Spectroscopy	83
5.7 Main Experiment: Round Bar Test of Uniaxial Hydrogen Concentration Gradient	83
5.8 The Effect of Charging Solution on Apparent Surface Concentration.....	87
 CHAPTER SIX: DISCUSSION OF ROUND BAR HYDROGEN DIFFUSION EXPERIMENTS	 90
6.1 Main Experiment: New Method to Measure Diffusion Coefficient and Estimate Surface Concentration.....	91
6.2 The Effect of Charging Solution on Apparent Surface Concentration	93

6.3 Supplemental Observations	95
CHAPTER SEVEN: EXPERIMENTAL METHODS FOR PERFORMING TENSILE TESTS WITH SAMPLES OF VARYING HYDROGEN CONCENTRATION AND STRAIN RATE.....	
7.1 Main Experiment: Tensile Tests of Low Carbon Steel with Varying Strain Rate and Hydrogen Concentration.....	98
7.2 Specimen Acquisition.....	102
7.3 Calibration of Time in Solution to Hydrogen Concentration	102
7.4 Standard Operating Procedure: The Tensile Test.....	104
7.5 Standard Procedure: Data Collection and Tensile Test Data Processing	108
7.6 Effect of Surface Condition on Tensile Tests.....	113
7.7 Repeatability of Tensile Tests.....	115
7.8 Effects of Momentum on Tests with High Crosshead Speeds.....	115
7.9 Effect of Hydrogen Egress during Tensile Tests	116
CHAPTER EIGHT: EXPERIMENTAL RESULTS OF TENSILE TESTS WITH VARYING STRAIN RATE AND HYDROGEN CONCENTRATION.....	
8.1 Microstructure of Steel Specimen Material	118
8.2 Calibration of Time in Solution to Hydrogen Concentration	120
8.3 Repeatability of Tensile Tests and Basic Material Properties	123
8.4 Effect of Surface Condition on Tensile Tests.....	127
8.5 Effect of Hydrogen Egress during Tensile Tests	130
8.6 Effect of Momentum on Tests with Highest Crosshead Speeds.....	133
8.7 Main Experiment: Tensile Tests of Low Carbon Steel with Varying Strain Rate and Hydrogen Concentration.....	134
8.7.1 Statistical Analysis of Outcome Measures	134
8.7.2 Flow Stresses (Yield Stress and Ultimate Stress).....	139
8.7.3 Fracture Stress	144
8.7.4 Fracture Strain	146
8.7.5 Strain Hardening Exponent	147
8.7.6 Plastic Strains (Uniform Strain and Necking Strain)	149
8.8 Presence of Yield Point Elongation, Upper and Lower Yields, and Serrated Yielding	152
8.9 Failure Surface Imaging.....	154
CHAPTER NINE: DISCUSSION OF TENSILE TESTS WITH VARYING STRAIN RATE AND HYDROGEN CONCENTRATION	
9.1 Microstructure.....	158
9.2 Hydrogen Concentration Profile in the Tensile Test Sample	158
9.3 Validation: Repeatability and Effect of Surface Degradation	161
9.4 Main Experiment: Results Replicating Previous Knowledge.....	162
9.5 Main Experiment: New Observations.....	162
9.6 Main Experiment: Yield Point Elongation, Upper and Lower Yields, Lüder Region.....	176
9.7 Overall Effect of Strain Rate and Hydrogen Concentration on the Tensile Test	176

CHAPTER TEN: FIELD SCC EXAMINATION	181
10.1 Overview.....	181
10.2 Specimen Acquisition and Field History	181
10.3 Microstructure Revealed through Polishing and Nital Etching	182
10.4 Method for Electroless Nickel Plating.....	184
10.5 Methods for Depth-wise Sectioning	184
10.6 Registering Images and Following Features.....	185
10.7 Results and Discussion for SCC Sample Depth-Wise Sectioning.....	187
10.8 Residual Hydrogen in the Pipe Sample	194
10.9 Overall Discussion.....	196
 CHAPTER ELEVEN: CONCLUSIONS AND FUTURE WORK	 200
11.1 Hydrogen Diffusion in Low Carbon Steel.....	200
11.2 Hydrogen Effect on Material Properties of Low Carbon Steel.	201
11.3 Examination of SCC Field-Failed Pipe.	204
11.4 Concluding Remarks.....	206
References.....	207

List of Tables

Table 2-1 Interstitial hole sizes for BCC and FCC Structures from King 1971	22
Table 2-2 Relative sizes of interstitial elements from King 1971	22
Table 2-3 Hydrogen trap types and relative strengths	28
Table 4-1 Composition of Passive Hydrogen Charging Solution.....	43
Table 4-2 Composition of Nital Etchant Prepared for this Study.....	47
Table 4-3 Raw Data Collected Prior to Placing Samples in the Eudiometers	54
Table 4-4 Raw Data Collected During Hydrogen Discharge	54
Table 4-5 Raw Data Collected Once Per Experimental Set-up	54
Table 4-6 Raw Data for Calibration of the Eudiometer Unit.....	61
Table 5-1 Time Required to Reach 90, 95, and 99% of Steady State Hydrogen Volume.....	74
Table 5-2 Hydrogen Concentrations Measured After Bake-Out at 110 Celcius for 72 Hours.....	78
Table 5-3 Results of Vicker's Hardness Tests for Round Bar	80
Table 5-4 Statistical p-Values Comparing the Different Sampling Locations	80
Table 5-5 Results for all Round Bar Hydrogen Diffusion Experiments.....	86
Table 6-1 Effects of Solution Composition and Time on Apparent Surface Concentration	94
Table 7-1 Sample Identifiers for Each Combination of Testing Parameters	101
Table 7-2 Specifications for Tinius Olsen H25K Universal Testing Machine	106
Table 7-3 Experimental Settings for the Tensile Testing Machine	107
Table 7-4 Sample Raw Data Table Collected Prior to Tensile Testing.....	109
Table 7-5 Spreadsheet Format for Processing Tensile Test Data	109
Table 8-1 Hydrogen Charging Time and Associated Hydrogen Concentrations	121
Table 8-2 Means and Standard Deviations for the Repeatability Tests of all Outputs.....	124
Table 8-3 Means and Standard Deviations for the Surface Condition Tests of all Outputs.....	128

Table 8-4 Statistical p-Values for all Main Effects, Interactions, and Effect Size for all Outcome Measurements from the Tensile Test	136
Table 8-5 Pearson Correlation Category Definitions for Main Experiment.....	137
Table 8-6 Correlation Coefficients between Strain Rate and Various Outcome Measures.....	137
Table 8-7 Correlation Coefficients between Hydrogen Concentration and Various Outcome Measures	138
Table 8-8 Table/Contour Plot Indicating the Presence of Yield Point Elongation.....	152
Table 8-9 Table/Contour Plot Indicating Presence of Upper and Lower Yield Points	153
Table 8-10 Table/Contour Plot Indicating the Presence of 'Serrated' Yielding	154
Table 10-1 Composition of Electroless Nickel Plating Solution	184
Table 10-2 Residual Hydrogen Concentrations in the Pipe Sample.....	195
Table 10-3 Characteristics of the Two Main Features of this Field-Failed SCC Specimen.....	197

List of Figures and Illustrations

Figure 2-1 Overlapping Domains Model of SCC	6
Figure 2-2 The Bathtub Model of SCC from Parkins 1987	7
Figure 2-3 Field Pipeline Sample with SCC Colony Oriented Up/Down on Right Hand Side (1X)	8
Figure 2-4 Schematic of the Chemistry and Electrochemistry in Cracks from Turnbull 2001	11
Figure 2-5 Outline of the Anodic Dissolution Cell from Tironbond 2004	12
Figure 2-6 Pourbaix Diagram for Iron in Water from Jones 1996 pg 59	17
Figure 2-7 a) Linear Voltammogram of Sulfur Covered Iron Surfaces in Borate Buffer (pH=8.4) and b) same as (a) but at Higher S from Seshadri et al, 1997	20
Figure 2-8 Typical Barbell-Shaped Tensile Test Specimen	31
Figure 2-9 Illustrative Stress-Strain Curve, adapted from Callister, 6 th ed., 2003, pg. 126.....	32
Figure 2-10 Illustrative Stress-Strain Curve showing Complex Yielding Behaviour, from ASTM E8 09	33
Figure 4-1 Hydrogen Ingress into Coated Round Bar	42
Figure 4-2 Predicted Outcome of Hydrogen Concentration after Round Bar Sectioning	42
Figure 4-3 Mounted Metallurgical Sample of SCC Affected Pipeline, 32 mm Diameter.....	46
Figure 4-4 Eudiometer Detail Showing Globe Valve and Graduations	52
Figure 4-5 Schematic of Eudiometer Apparatus adapted from Senadheera, 2009.....	56
Figure 4-6 Eudiometer and Specimen Carrier from Senadheera, 2009	57
Figure 4-7 Sampling Locations for Vickers Hardness Tests	68
Figure 4-8 Experimental Set-up for Electropotential Scans	69
Figure 5-1 Photomicrographs of Experimental Steel in Radial (A, C) and Transverse (B, D) Directions	73
Figure 5-2 Hydrogen Release with Time in Eudiometer for Round Bar Disc Specimen.....	75
Figure 5-3 Hydrogen Collection and Mercury Temperature Profile for Unit 2	76

Figure 5-4 Hydrogen Collection and Mercury Temperature Profile for Unit 4	76
Figure 5-5 Hydrogen Evolution with Time for the Small Tensile Samples	77
Figure 5-6 Hydrogen Concentrations after 72 h Bake-Out.....	78
Figure 5-7 Sampling Locations on Round Bar for Vicker's Hardness Tests	79
Figure 5-8 Results of Vicker's Hardness Testing at Different Sampling Locations	81
Figure 5-9 Potentiodynamic Scan of Experimental Material in Deaerated Acid Solution.....	82
Figure 5-10 Linear Polarization Region of Potentiodynamic Scan within ± 30 mV of E_{corr}	83
Figure 5-11 Example of Best Fit Procedure for Fick's Law to Experimental Data	84
Figure 5-12 Effects of Small Variation in Diffusion Coefficient to Best Fit Procedure	85
Figure 5-13 Comparison Plot of all Experimental Data	85
Figure 5-14 Testing the Effect of Hydrogen Trapped on the Charging Surface	87
Figure 5-15 Hydrogen Diffusion Concentration Profile from Hydrogen Sulfide (H_2S) Deaerated Solution.....	88
Figure 5-16 Hydrogen Diffusion Concentration Profile using Non-Deaerated Solution	89
Figure 5-17 Hydrogen Diffusion Concentration Profile for Long-Term Charging (9 Days) in Standard Nitrogen Deaerated Solution	89
Figure 7-1 Tensile Specimen Machined from 9.5 mm (3/8 inch) Round Bar	99
Figure 7-2 Glass Eudiometer Holder for Small Tensile Specimen.....	104
Figure 7-3 Typical Plot of Tensile Data and Effect of Data Transformations.....	112
Figure 7-4 Typical Plot of True Stress and True Plastic Strain for Tensile Test Results	113
Figure 8-1 Microstructure of the Low Carbon Steel used for Tensile Tests shown in Radial (or Longitudinal) (A, C) and Transverse (B, D) Sections.....	120
Figure 8-2 Calibration Curve for Hydrogen Concentration vs. Time in Solution	122
Figure 8-3 Hydrogen Concentration versus Charging Time Calibration from Escobar, 2009 ...	123
Figure 8-4 Repeatability of Yield and Ultimate Stress Measurement at 0 ppm Hydrogen	125
Figure 8-5 Repeatability of Fracture Strain Measurement at 0 ppm Hydrogen	125

Figure 8-6 Repeatability of Strain Hardening Exponent Measurement at 0 ppm Hydrogen.....	126
Figure 8-7 Repeatability of Plastic Strain Measurements at 0 ppm Hydrogen.....	126
Figure 8-8 Photograph of Tensile Samples showing Extent of Surface Corrosion	127
Figure 8-9 Effect of Surface Corrosion on Yield and Ultimate Strengths.....	129
Figure 8-10 Effect of Surface Corrosion on Fracture Strain and Strain Hardening Exponent ...	129
Figure 8-11 Effect of Surface Corrosion on Plastic Strains (Uniform, Necking, and Total)	130
Figure 8-12 Stress-Strain Curve showing Unload Cycle (20 minutes rest for this sample).....	131
Figure 8-13 Flow Stresses and Elongation versus Rest (Hydrogen Egress) Time	132
Figure 8-14 Plot of Normalized Ultimate and Fracture Stresses versus Rest Time	132
Figure 8-15 Displacement versus Time Plot to Check for Momentum Effects during Tensile Tests at High Crosshead Speeds	133
Figure 8-16 Strain Rate vs. Yield Strength for all Hydrogen Concentration Conditions	139
Figure 8-17 Strain Rate vs. Ultimate Strength for all Hydrogen Concentration Conditions	140
Figure 8-18 Exploded Plot of Hydrogen Concentration vs. Yield Strength (curves generated for each strain rate are artificially separated for clarity).....	141
Figure 8-19 Exploded Plot of Hydrogen Concentration vs. Ultimate Strength (curves generated for each strain rate are artificially separated for clarity)	141
Figure 8-20 Exploded Plot of Strain Rate vs. Yield Strength (curves generated for each hydrogen concentration are artificially separated for clarity).....	143
Figure 8-21 Exploded Plot of Strain Rate vs. Ultimate Strength (curves generated for each hydrogen concentration are artificially separated for clarity).....	144
Figure 8-22 Fracture Stress versus Strain Rate for all Hydrogen Concentrations	145
Figure 8-23 Fracture Stress versus Hydrogen Concentration for all Strain Rates	145
Figure 8-24 Strain Rate vs. Fracture Strain for all Hydrogen Concentration Conditions.....	146
Figure 8-25 Hydrogen Concentration vs. Fracture Strain for all Strain Rate Conditions.....	147
Figure 8-26 Strain Rate vs. Strain Hardening Exponent for all Hydrogen Concentrations.....	148
Figure 8-27 Hydrogen Concentration vs. Strain Hardening Exponent for all Strain Rates.....	148

Figure 8-28 Strain Rate vs. Uniform Plastic Strain for all Hydrogen Concentrations	149
Figure 8-29 Hydrogen Concentration vs. Uniform Plastic Strain for all Strain Rates	150
Figure 8-30 Strain Rate vs. Necking Strain for all Hydrogen Concentrations	151
Figure 8-31 Hydrogen Concentration vs. Necking Strain for all Strain Rates	151
Figure 8-32 Failure Surfaces for Samples Showing the Most (A) and Least (B) Ductility.....	155
Figure 8-33 Photo-Table of Failure Surfaces for Each Testing Condition.....	156
Figure 9-1 Plot of Hydrogen Normalized to Surface Concentration within Tensile Specimen .	159
Figure 9-2 Tensile Specimen Configuration.....	160
Figure 9-3 Radial Hydrogen Concentration in a Round Bar Sample from Sainter, 2011	161
Figure 9-4 Calibration Data showing Groups Applied for Discussion and Analysis	165
Figure 9-5 Exploded Plot of Strain Rate versus Yield Strength Showing Analysis Groups	165
Figure 9-6 Yield Strength vs. Strain Rate with Data Pooled into Ranges to Reduce Scatter	166
Figure 9-7 Yield Strength vs. Strain Rate Showing Envelope for Pooled Data	167
Figure 9-8 Curves showing form of Yield Strength vs. Strain Rate Pooled Data	168
Figure 9-9 Ultimate Strength vs. Strain Rate, Pooled into Ranges to Reduce Scatter	169
Figure 9-10 Curves showing form of Ultimate Strength vs. Strain Rate Pooled Data	170
Figure 9-11 Plotting Fracture Points (σ_f , ϵ_f) for different Hydrogen Concentrations with an Overlaid Typical Stress-Strain Curve	171
Figure 9-12 Pooled Necking Strain vs. Strain Rate	172
Figure 9-13 Contributions of Uniform and Necking Strains to the Total Plastic Strain, sorted by Hydrogen Concentration	173
Figure 9-14 Contributions of Uniform and Necking Strains to the Total Plastic Strain, sorted by Strain Rate.....	174
Figure 9-15 Plot of Pooled Flow Stresses vs. Hydrogen Concentration to Visualize Solution Strengthening Effects.....	176
Figure 9-16 Overall Effects of Increasing Strain Rate ($\dot{\epsilon}$) and Hydrogen concentration ($[H]$) on the Tensile Response of a Low Carbon Steel	178

Figure 10-1 Pipe Specimen Showing Radial Curvature and Surface Cracks	182
Figure 10-2 Schematic of Pipe Section showing Axial and Radial Directions used to View Specimen Microstructure and SCC Features	183
Figure 10-3 Ferritic/Pearlitic Microstructure of Pipe Sample	183
Figure 10-4 Flowchart for Generating Successive Images	185
Figure 10-5 Experimental Setup for Calibrating Lens Movement to the Adjustment Gauge	186
Figure 10-6 Map of Surface Pit and Crack Features.....	187
Figure 10-7 Axially Sectioned SCC Specimen Showing Cracking and Anodic Dissolution.....	188
Figure 10-8 Etched Sample Showing Grain Size and Crack Size	189
Figure 10-9 SCC Colony Radial Section Showing Crack Alignment after Removal of 120 Micrometers of Material	190
Figure 10-10 Multiple Cracks Associated with One Pit and Thickness of Corrosion Products.	191
Figure 10-11 Crack Interference and Coalescence	192
Figure 10-12 Nickel Plated (for edge retention, the nickel appears unetched) and Nital Etched Sample showing Small Secondary Cracks and Thickness of Corrosion Products	192
Figure 10-13 Image showing Rapid Localized Corrosion (Pit Generation).....	193
Figure 10-14 Sample Configuration for Externally and Internally Weighted Samples Cut from a Pipe Sample	194
Figure 10-15 Phases of the Progression of SCC.....	198

List of Symbols, Abbreviations and Nomenclature

Symbol	Definition
∇	Gradient Operator
ACS	American Chemical Society
ASTM	American Society for Testing and Materials
b	Burger's Vector
BCC	Body Centred Cubic
C	Concentration (ppm mass)
C_b	Bulk Hydrogen Concentration (ppm)
CEPA	Canadian Energy Pipeline Association
CNC	Computer Numerically Controlled
C_s	Surface Hydrogen Concentration (ppm)
D	Diffusion Coefficient (m^2/s)
D_{app}	Apparent Diffusion Coefficient (m^2/s)
DNV	Det Norske Veritas
E	Young's Modulus (GPa)
$\dot{\epsilon}$	Strain Rate
e, ϵ	Strain
F	Faraday's Constant (C/mol)
FCC	Face Centred Cubic
G	Shear Modulus (GPa)
G_{ASTM}	ASTM Grain Size Number
$[H]$	Hydrogen Concentration (ppm)
$[H]_{\infty}$	Asymptotic Hydrogen Concentration (ppm)
H_{ads}	Adsorbed Hydrogen
HAZMAT	Hazardous Materials
i	Current Density ($\mu A/cm^2$)
i_{corr}	Corrosion Current Density ($\mu A/cm^2$)
i_{SS}	Steady State Current Density ($\mu A/cm^2$)
IUPAC	International Union of Pure and Applied Chemistry
J	Diffusive Flux (mol/m^2s)
J_{SS}	Steady State Diffusive Flux (mol/m^2s)
K_I	Mode I Fracture Toughness (MPa \sqrt{m})
K_{IC}	Limiting Fracture Toughness (MPa \sqrt{m})
K_{ISCC}	Limiting SCC Fracture Toughness (MPa \sqrt{m})
L	Specimen Thickness (m)
LYS	Lower Yield Strength (MPa)
MERCONVAP	Mercury Vapour Control Solution
n	Strain Hardening Exponent
NS4	SCC Test Solution

P_{atm}	Atmospheric Pressure (mmHg)
pH	Acidity Measure
PPE	Personal Protective Equipment
ppm	Parts per Million Mass
PTFE	Polytetrafluoroethylene
Q	Concentration of Hydrogen (ppm mass)
R	Gas Constant (J/molK)
R^2	Best Fit Parameter
R_A	Radius of Solvent Atom (pm)
SCC	Stress Corrosion Cracking
SCE	Saturated Calomel Electrode
SIMS	Secondary Ion Mass Spectroscopy
SMYS	Specified Minimum Yield Strength (MPa)
STP	Standard Temperature and Pressure
t_b	Hydrogen Breakthrough Time (s)
UYS	Upper Yield Strength (MPa)
V	Volume of Hydrogen (ml)
V_{STP}	Volume at Standard Temperature and Pressure (ml)
W	Weight (g)
YPE	Yield Point Elongation
β	Tafel Slope (mV/decade)
β_a	Anodic Tafel Slope (mV/decade)
β_c	Cathodic Tafel Slope (mV/decade)
ϵ_f	Fracture Strain
ϵ_n	Necking Strain
ϵ_u	Ultimate Strain
σ	Stress (Strength) (MPa)
σ_f	Fracture Strength (MPa)
σ_u	Ultimate Strength (MPa)
σ_y	Yield Strength (MPa)
φ	Concentration Gradient (mol/m ³)
ϵ	Lattice Dilation Parameter

Chapter One: **Introduction**

This thesis covers research performed in three general topics: Hydrogen diffusion and concentration profile in low carbon steel, hydrogen's effects on the mechanical properties of similar low carbon steel as revealed by a modified tensile test, and an examination of a pipeline that failed in service due to the effects of stress corrosion cracking (SCC).

1.1 Short Description of Problem Area

An in-service steel pipeline is expected to safely carry product for a long service life.

Historically pipelines were generally designed for a 20-40 year lifespan but, as of 2002, 60% of North American Pipelines were over 40 years old [Koch et al, 2002]. One problem encountered in the field is SCC, where a combination of a corrosive environment, tensile stress, and a susceptible pipeline material leads to premature, often catastrophic, failure.

1.2 Significance of SCC and Hydrogen in Pipelines

The National Association of Corrosion Engineers (NACE) report on the cost of corrosion [Koch, 2002] estimated the annual cost of corrosion in the United States to be 276 billion dollars, of which 7 billion is for gas/liquid transmission pipelines alone. The cost to the oil and gas exploration and production industry was estimated to be 1.4 billion dollars annually. For pipelines, the majority is spent on problems related to internal corrosion, but a significant amount is spent on external corrosion problems, one of which is SCC. In Alberta in 2005 there was 377,000 km of energy pipelines [EUB, 2005]. Of all releases to 2005 58% were due to internal corrosion and 12% to external corrosion. A pipeline engineer's design philosophy is to first design a pipeline that will not fail in service, and then to follow the "leak before break" criteria, meaning that a small leak is favourable to total rupture and possible explosion. SCC failures

occur contrary to “leak before break” in that a large flaw opens potentially releasing large amounts of product. There is currently no reliable way to monitor an entire pipeline system for the localized conditions that lead to SCC failures, even though considerable effort has been put toward that goal. The Canadian Energy Pipeline Association (CEPA) has published recommended practices to avoid SCC when operating pipelines [CEPA, 2007].

Hydrogen is thought to be a necessary contributor to the problem of SCC in pipelines. Whether it comes from hydrogen gas product streams, hydrogen sulfide product contaminates, groundwater, cathodic protection, welding, acid pickling, electroplating, forming, casting, or some other source, it is ubiquitous in the oil and gas industry. Hydrogen affects a material’s performance by altering its ability to withstand the stresses it is expected to see in service, lowering its resistance to fracture and creating or exacerbating cracks and other material defects. It is one of the few industrially significant gases that can enter and diffuse through metals, in part due to its small size. The internal end of a crack in a steel component is a place where hydrogen can have a large impact. By preferentially collecting at locations of high internal stress, hydrogen can weaken the material’s ability to resist crack growth, leading to premature failure.

1.3 Translating a Complex Situation to the Laboratory

There has been a large amount of academic and industrial research devoted to the study of SCC and hydrogen ingress in a wide variety of materials. Of the many types of materials and environmental conditions studied, there is no one underlying mechanism tying SCC and other environmentally assisted cracking phenomena together. It almost seems that every case of a material and environment producing SCC is unique. Another major problem with study of this area is the tremendously complex environmental conditions where it occurs. In the Canadian

situation, pipelines affected by SCC are usually found buried in wet soil, with damaged coating shielding the pipe from beneficial cathodic protection. Other problems include: the steel may have been made or installed incorrectly, may have an unknown stress and strain history, and yet may have been in the ground for 30 years without incident.

While this complexity is no reason to abandon the study of this area, to reproduce the soil and water chemistry, imposed potentials and current, natural potentials and current, steel composition and microstructure, and other variables is impossible. So as with other models and experiments that have come before, we will try to determine the most important parameters and processes and find general principles to allow us to understand and minimize the negative impacts.

1.4 Study of Hydrogen Diffusion

The two most intense areas of hydrogen diffusion research have involved diffusion modeling studies and experimental programs making use of electrochemical techniques to find diffusion property data from hydrogen entering or leaving a material. Hydrogen diffusion models are developed from Fick's laws, and rely on material properties, such as the diffusion coefficient, derived from experimentation. But, in order to derive these properties, experimentalists have relied on overly-simplified diffusion models. The simplified models have not been fully validated and may not properly describe the measured quantities. Hydrogen charging, residence time, effects of entry/exit surface conditions, presence of hydrogen traps with various activation energies, microstructure, and simplified models bring the values obtained and reported into question. A natural question arises: What if we aren't measuring what we think we are measuring?

As a result of the SCC/hydrogen problem's significant economic impact, a number of attempts have been made to bring hydrogen detectors into the field. This would avoid the necessary simplification of real-world conditions and allow operators to make repair and safety decisions on a case by case basis in the actual working environment.

1.5 Hydrogen's Effects on Material Properties

Hydrogen's effect on material performance has been studied for a long time, yet currently there is no definitive model. There are methods and standards in place to assess a material for fitness for hydrogen service, yet aside from a demonstrated ability to differentiate between materials, the reasons for those conditions showing differences are not clear. This research looks at hydrogen as a mobile solute in solid solution, and varies strain rate and hydrogen concentration to examine the deformation properties of a type of low carbon steel. If hydrogen can be shown to behave like other mobile solute systems, the large and well-studied area of dynamic strain aging can shed new light on the interaction between hydrogen and dislocations. Dynamic strain aging has been a valuable tool in studying dislocation behaviour experimentally.

1.6 Failure Analysis of a Pipeline due to SCC

In this section a case study and failure analysis were performed on an actual pipeline that failed due SCC. SCC colony formation was examined, especially with regard to corrosion conditions and possible hydrogen effects in an effort to determine the SCC initiation and progression mechanisms.

Chapter Two: **Literature Review and Relevant Background**

The study of hydrogen in metal and stress corrosion cracking (SCC) involves contributions from many different areas. Environmentally assisted cracking involves aspects of fracture mechanics, electrochemistry, and materials science. Considering hydrogen's effect on steel is not possible without significant background in how hydrogen enters, resides, and moves through a material, how it is detected and measured, and how it can affect a material's physical properties and deformation mechanisms. Background is also presented on the tensile test method of examining a material's mechanical response to loading as well as the known effects of hydrogen on the mechanical response on carbon steel.

2.1 Conceptual Models of SCC

There are two main conceptual models of SCC that help to understand the overall phenomenon, the overlapping domains model and the so-called 'bathtub' model. The overlapping domains model (Figure 2-1) illustrates the interdependence of a corrosive environment, tensile stress, and a susceptible material in creating favourable conditions for SCC. If you place pipeline steel into a corrosive environment you will encounter general corrosion where there is a relatively uniform corrosion of the metal surface in contact with the environment, and local corrosion where non-uniform conditions lead to more aggressive corrosion attack at a specific location (corrosion pit). This is the overlap shown on the diagram between the domains of 'material' and 'corrosion.' If you apply a stress field to pipeline steel that contains cracks or other defects the interaction is described by fracture mechanics. Fracture mechanics is the relationship between crack size and shape, applied stress, and the likelihood that the crack will grow or the component will fail entirely. The relationship between stress and corrosion can be illustrated by hydrogen, which is

often a product of electrochemical reactions, entering and diffusing into the steel where it can reside in the atomic matrix, distorting the normal crystal structure and creating stress internally. The combined interaction between a material, corrosion, and stress is the realm of SCC, where localized corrosive attack creates: deeper cracks which have less resistance to fracture, and hydrogen which further stresses the material near the crack, leading to further reduction of the resistance to fracture.

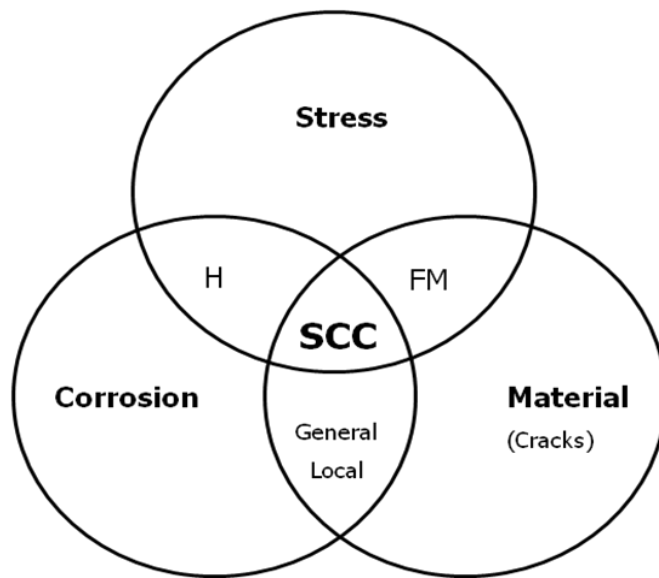


Figure 2-1 Overlapping Domains Model of SCC

The ‘bathtub’ model illustrates the time-progression of SCC (Figure 2-2). Parkins [1987] described four stages of the SCC process, including a waiting period as stage 1, crack initiation as stage 2, crack growth as stage 3, and finally crack coalescence and final fracture as stage 4. Currently, stage 1 is thought of more as a nucleation phase, where the conditions for SCC are present and microscopic changes are occurring to set the stage for crack initiation and growth. The labels stage 1, stage 2, etc. could be replaced with nucleation, initiation and growth, growth

and coalescence, and failure. This process can take 10-20 years. The time required for the latter stages gets shorter with final coalescence and fracture happening very quickly.

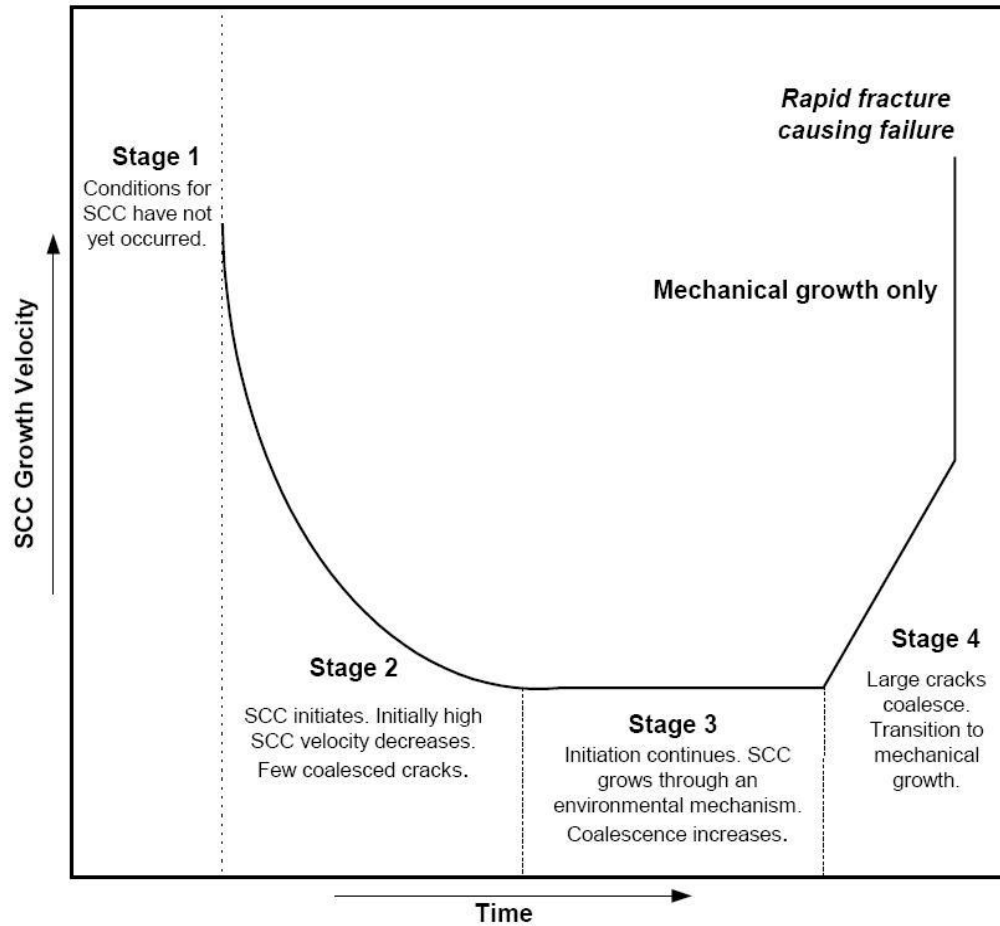


Figure 2-2 The Bathtub Model of SCC from Parkins 1987

2.2 SCC in Field Conditions

There are two distinct types of SCC seen in North American pipelines: High pH SCC seen predominantly in the United States, and near-neutral pH SCC, which was first identified in Canada in the 1980s and is the focus of this study. There are a few features of SCC that are considered typical: Colonies of cracks with cracks oriented along the axis of the pipe (Figure 2-3), located under disbonded pipeline coating, buried in soil in anaerobic conditions with local

pH between 6 and 7, with significant corrosion on the inside surfaces of cracks. SCC cracks appear in colonies, with a specific local region containing hundreds to thousands of cracks. The density of cracks in an area allows them, once they have grown large enough, to interact with each other. Eventually enough of these cracks will coalesce to weaken the steel such that fracture can occur. Unlike high pH SCC, near-neutral pH SCC shows aggressive anodic dissolution along the crack walls. For SCC, or any electrochemical reaction to occur in the field or in the lab, there are four required elements of the system: **Anode**, **Cathode**, **Electrolyte**, and an **Electronic Path**.



Figure 2-3 Field Pipeline Sample with SCC Colony Oriented Up/Down on Right Hand Side

(1X)

Disbonded coating is critical to the formation of SCC. A specific type of coating used in the past was polyethylene tape. This tape was applied, often in the field, to protect the pipe from the underground environment. This tape suffered from a number of shortcomings. If it was not

applied properly, water could get between the wraps and reach the pipe surface. It could be damaged by the backfill process during burial. Slumping or moving soil could cause wrinkles. Plasticizers could leach out over time, leaving the tape brittle. The result of these shortcomings is that water can reach the pipe surface. A further complication is that polyethylene tape is dielectric, meaning that it can shield the pipe from cathodic protection. This shielding, along with the presence of electrolyte, allows the creation of a corrosion cell with different chemistry than the surrounding environment.

2.3 SCC Crack Morphology

SCC cracks tend to nucleate and grow in colonies (see Figure 2-3) [Parkins & Singh, 1990].

Once the cracks have grown large enough they interact with each other, eventually coalescing into much larger cracks. At some point a coalesced crack will have sufficient size that the stress intensity factor will have sufficient magnitude to cause a through-thickness fracture in the pipe.

The fracture surface will show signs of brittle failure mechanisms. How these colonies nucleate and develop is still a matter of conjecture. The latter stages of the SCC process, where the cracks are relatively large, are well understood. Parkins has developed a model for crack interaction and coalescence, and the final fracture can be described by fracture mechanics methods. What is less well known is the process of nucleation and initiation of cracks. Study of this area in an academic sense is difficult as much of the research done in the area is proprietary and can represent trade secrets.

As mentioned in Section 2.2 there are some things known to correlate with near-neutral SCC in pipelines: Damaged polyethylene tape coating, possibly shielding the pipe from cathodic protection, deoxygenated electrolyte of near-neutral pH, cyclic loading conditions and elevated temperatures downstream of compressor stations [CEPA, 2007]. A standard test solution called

NS4 has been developed to mimic the electrolyte conditions commonly seen in Canadian SCC conditions. The corrosion pits that lead to a crack colony could originate from a number of sources: Inclusions, dislocations reaching the surface, inconsistent scale, damage, or other thermodynamically favoured sites. Microcracks have been seen emerging from pits [Parkins & Singh, 1990], which may have something to do with an increased local hydrogen concentration, but the mechanical causes for this are not known. SCC in new pipeline materials has been greatly decreased with the use of new fusion bonded epoxy and multilayered coatings. They offer a much more stable coating over the long term.

2.4 Anodic Dissolution Crack Model

A more complex and representative model than those presented in the conceptual models (Section 2.1) is the anodic dissolution model of SCC. The anodic dissolution model [Itagaki et al, 2000, Itagaki, 2002, Mao, 2001, Parkins, 1987, Sieradzki & Newman, 1987] is often summarized in the following way. The surfaces inside a crack, including the tip, are covered by an oxide film. During loading, the brittle oxide film is mechanically disrupted exposing bare metal, which actively undergoes anodic dissolution to re-passivate the surface. This new oxide film can be disrupted during proceeding loading cycles, and repeating the whole process as the crack progresses into the material. The presence of hydrogen, a product of corrosion reactions (Section 2.7.1), aggravates this process in a number of ways. A portion of the hydrogen produced will enter the material increasing the lattice strain. Hydrogen also migrates to, and preferentially collects at locations of high strain, such as the plastic zone near the crack tip [Cheng, 2007a&b, Mao & Li, 1998, Toribio, 1993, Turnbull et al, 1996]. This decreases the fracture resistance of the crack tip leading to enhanced progression of the crack into the material.

Turnbull [Turnbull, 2001] has summarized the modeling of chemistry and electrochemistry in cracks. A schematic of the processes that are thought to occur in a crack's environment is given in Figure 2-4. Anodic dissolution within the crack produces metal ions (M^{n+}) and hydrogen ions (H^+). These hydrogen ions can either combine to form hydrogen gas or be adsorbed and then absorbed into the metal, weakening the crack tip by a number of mechanisms. The concentration of metal cations within the crack draws in anions from the bulk solution to balance the local solution charge.

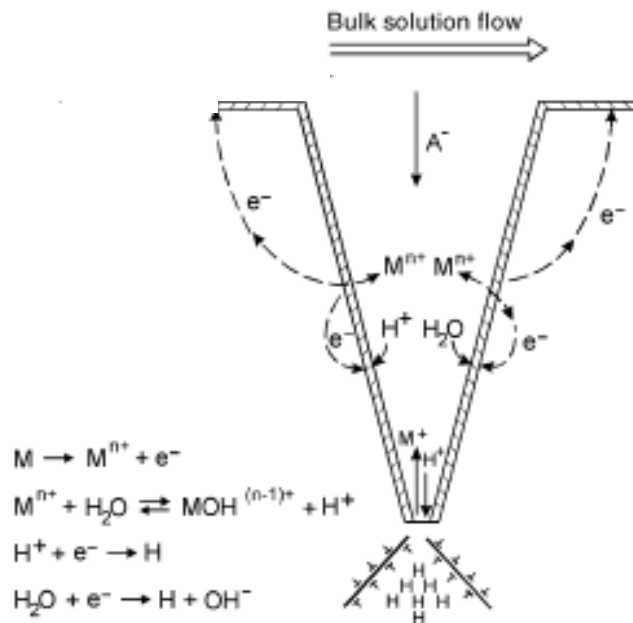


Figure 2-4 Schematic of the Chemistry and Electrochemistry in Cracks from Turnbull

2001

Tironbond [2004] also presents a crack model (Figure 2-5) which illustrates the concept that a local galvanic couple is established within a crack because of the enhanced anodic dissolution at the crack tip and the cathodic reactions along the much greater surface area of the crack walls. This anodic dissolution is enhanced by local plastic deformation and rupture of the brittle passivating film.

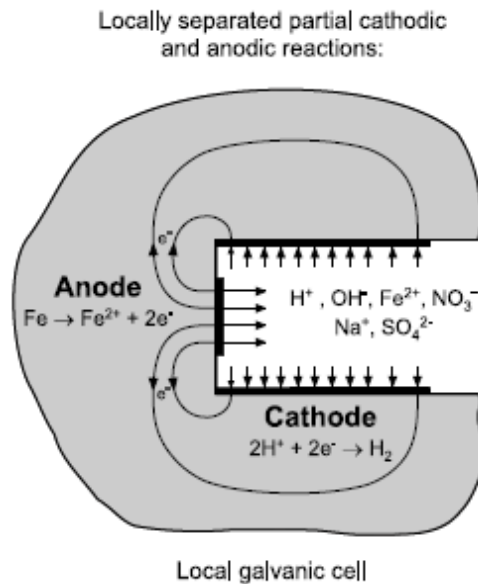


Figure 2-5 Outline of the Anodic Dissolution Cell from Tironbond 2004

2.5 Describing the Crack: Fracture Mechanics

Fracture mechanics theory allows us to predict whether a material will fail if it has a crack of a given size and the stress conditions are known [Kysar, 2003]. The base fracture mechanics relation is:

$$K_I = \sigma \sqrt{\pi a} f\left(\frac{a}{W}\right)$$

Where K_I is the stress intensity factor of the crack (MPa \sqrt{m}), σ is the applied stress, a is the length of the crack, and then an empirical function based on geometry, namely the length of the

crack and W , the total depth of the component. We can then compare K_I to that material's critical value, K_{IC} , which is called the fracture toughness. When $K_I > K_{IC}$, then the crack will grow. K_{IC} is a material property that can be modified by environmental conditions. Under conditions of SCC, the modified fracture toughness, K_{ISCC} , can be a fraction of its normal value. The values of K_{IC} and K_{ISCC} are used extensively by engineers when making materials selection decisions. The standard method for obtaining K values is ASTM E399. Their value should not be overstated, however, because this empirical equation is not robust enough to be applied outside of the tight geometrical constraints of testing specimens. There are also factors involved in SCC in pipelines that limit applicability of K values: The effect of strain rate on the size of the plastic zone ahead of the crack tip, the effect of hydrogen concentration gradients on the ability of the plastic zone to deform, and the process of anodic dissolution at the crack tip. When considering the 'bathtub' model of crack growth rate versus time (Figure 2-2), there are two competing processes contributing to crack growth, the anodic dissolution process, and mechanical growth. During the nucleation phase, all growth is due to dissolution and during the final running fracture phase, all growth is probably due to mechanical factors.

2.6 SCC in Materials other than Pipeline Steels; and Related Phenomena

There are many more materials that are affected by SCC, though each material has its own needs in terms of environment and loading [Suess, 2007]. A short selection of these include: austenitic stainless steel in chloride solution [Magnin et al, 1996], Alloy 600 (nickel-based) in primary water in nuclear power generation [Foct et al, 2000], aluminum alloys in seawater [Bayoumi, 1993] and chloride solution [Shaw, 1986], magnesium in air, sulfate solutions, and chromate solutions [Winzer et al, 2005]. SCC, or at least a form of environment assisted cracking, even

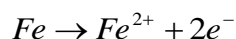
occurs on silicate glass [Gy, 2003]. There are also other industries that have SCC concerns: in mining, SCC has been identified on rock bolts [Gamboa & Atrens, 2003], in the nuclear power industry [Bruemmer & Was, 1994, Magnin et al, 2000, Rios et al, 1995, Scott, 1994], and in high strength suspension wires due to nitrates [Zhou et al, 2000]. Ferritic stainless steels and other iron alloys have been shown to be susceptible to SCC in a variety of environments, including chlorides, sulfates [Nishimura, 1992], and high temperature with dissolved oxygen [Zhou et al, 1998]. Hydrogen sulfide stress cracking is a concern for well casings made from steel [Astaf'ev et al, 1999].

Other phenomena show similarities to the SCC/hydrogen effect in pipeline steels. In hydrogen induced cracking a critical concentration of hydrogen develops in the material leading to cracking or blistering. Hydrogen embrittlement effects sometimes do not involve cracked components. In liquid metal embrittlement [Fernandes & Jones, 1997, Ina & Koizumi, 2004] a liquid metal attacks the grain boundaries leading to decreased fracture toughness and failure. In corrosion fatigue [Ray & Thomas, 1994] cyclic loading is necessary. Another interesting phenomenon is strain aging [Drahiem & Schlipf, 1996, Hong & Lee, 2005, Srinivas et al, 1991, Wang et al, 2000], where diffusible solutes, like nitrogen, travel through the material with similar velocities as dislocations leading to material strengthening.

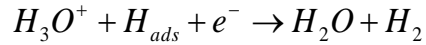
2.7 Chemical Reactions of Interest

2.7.1 Relevant Reactions

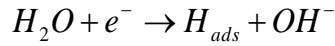
Iron oxidation is the anodic reaction [Bockris & Reddy, 2000, pg 1671].



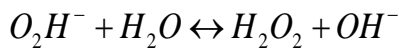
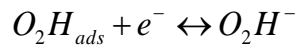
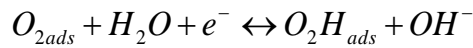
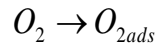
The Hydrogen Evolution Reaction is the cathodic reaction in acid solutions



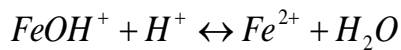
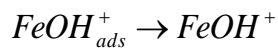
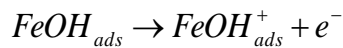
Where H_{ads} is hydrogen adsorbed on the surface. In alkaline solutions:



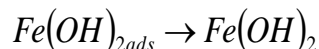
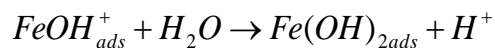
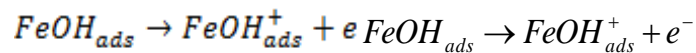
The Oxygen Reduction Reaction can also act as a cathodic reaction.

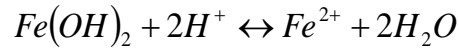


The overall iron dissolution reaction at the surface is of particular concern, so a few likely reactions are listed below. For the general reaction in acidic solution:

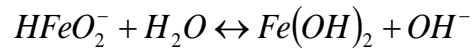
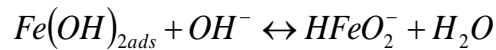
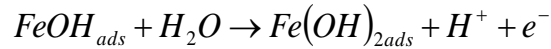
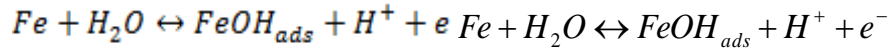


In neutral solution:





In alkaline solution:

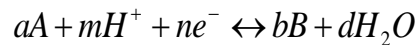


2.7.2 Nernst Equation and Pourbaix Diagram

The Nernst equation allows calculation of the potential of an electrochemical half-reaction when conditions are other than unit activities [Jones, 1996 pg 45]. A useful form of the Nernst equation is given below.

$$e = e^0 + \frac{0.059}{n} \log \left(\frac{A^a}{B^b} \right) - \left(\frac{m}{n} \right) 0.059 pH$$

For the generalized electrochemical reaction:



Where e is the cell potential, e^0 is the standard cell potential, A and B represent the reactant and products with a and b their stoichiometry, m is the stoichiometric number of participating H^+ , and n is the number of electrons transferred [Jones, 1996 pg 45]. The overall corrosion reactions above (Section 2.7.1) can be seen to be pH dependant, which allows us to create the Pourbaix diagram (Figure 2-6) linking the stable iron state in water to the pH and potential by use of the Nernst equation [Jones, 1996 pg 59]. These diagrams show the most stable state of iron, but nothing about the kinetics of the reactions.

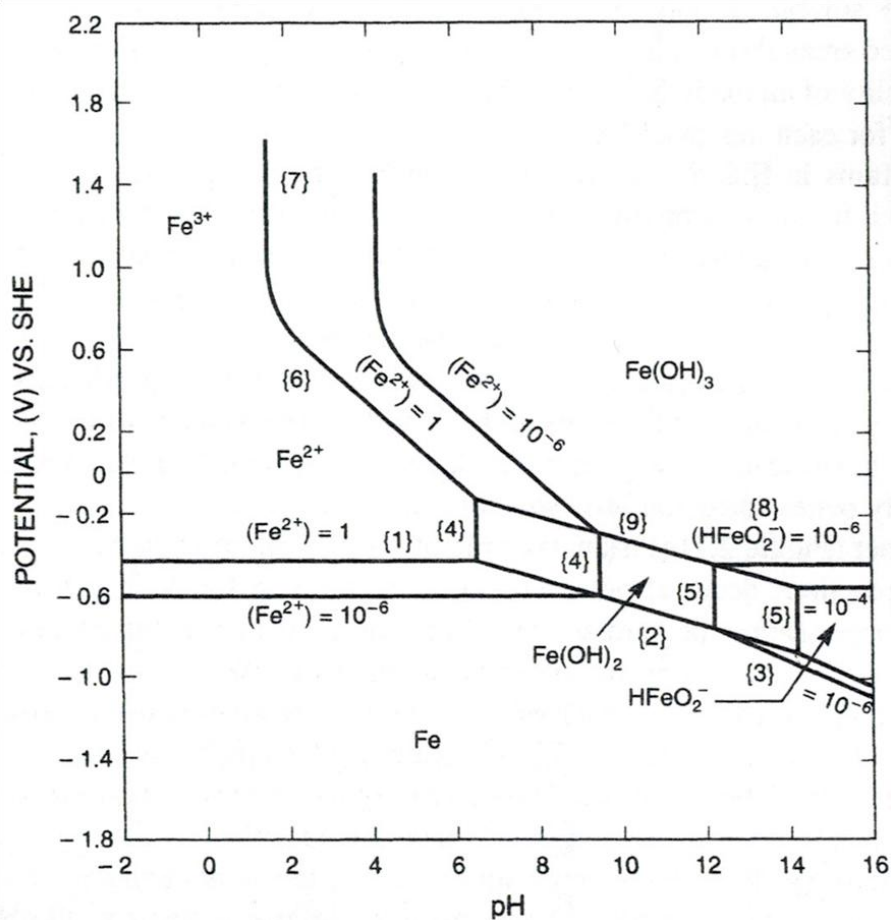


Figure 2-6 Pourbaix Diagram for Iron in Water from Jones 1996 pg 59

2.7.3 Some Experiments Relating the Reactions of Interest

Anodic Dissolution and Strain. An important aspect of the anodic dissolution behaviour of iron is the effect of high stress and strain conditions and yielding, especially since the conditions at the crack tip are thought to produce extreme local yielding. Despic et al [1968] applied both elastic and yielding strain on an iron wire electrode in 0.1 N H₂SO₄ solution. The anodic current density changed very little in the elastic loading regime, but increased rapidly in the yield loading regime. Once the strain loading produced permanent deformation, the rate of dissolution of iron increased drastically. This is of great importance when looking at the chemistry inside

the crack, as differences in localized electrochemical behaviour lead to great differences in chemical and electrical potential, species equilibria, and migration and diffusion behaviour.

Artificial Crack and the Hydrogen Evolution Reaction. To examine the contribution of the potential drop inside a stress corrosion crack to hydrogen charging at the tip, Li & Ferreira [1996] constructed an artificial crack of 0.1 mm thickness and measured the current density and H^+ potential drop within the crack. At the free corrosion potential and anodic potentials, the current density and hydrogen potential drop increased with time to asymptotic levels, indicating a potential exists to draw hydrogen into the crack and increase anodic diffusion. A major limitation of this experimental model is the dimensions of the artificial crack. Even a 0.1 mm thickness crack is orders of magnitude greater than a real crack, and the thickness to length ratio allows for much greater material transport than would be observed in practice.

Physical Effects of Varying Potential. To more closely study the effects of anodic dissolution and hydrogen embrittlement on cracked specimen, Wang et al [1998] applied anodic and cathodic potentials to the specimen and looked at the effect on crack propagation rates, elongation under load, and stress/strain curves. Anodic polarization increased the resistance to cracking (presumably by increasing the size of the plastic zone at the crack tip) and increased the elongation under load (again a general increase in plasticity). Hydrogen absorption decreased the material's resistance to crack propagation, decreased the elongation under load, and increased the yield stress. These findings support the contention that anodic dissolution and hydrogen absorption are competing processes that act to increase or decrease the ductility of a material, respectively. While this study does attempt to bring together the electrochemical concepts of anodic dissolution and hydrogen absorption within a crack, there is no account taken of the

actual conditions within the crack, which have been shown to be different from the conditions in the bulk solution.

Measuring Potential at the Crack Tip. Turnbull et al [2004] developed a technique to bring a reference electrode very close to the crack tip to get a measure of crack tip potential. A hole was drilled in a pre-cracked compact tensile specimen such that a small saturated calomel reference electrode (SCE) can be placed on the crack plane near the crack tip. Crack tip polarization was seen to be limited to -0.61 V (SCE), even though greater potentials were present for the whole sample in bulk solution. Bulk solution chloride or sulphate concentration and bulk pH had little effect on crack tip potential compared to pure water. Increasing the load on the crack initially increased the potential but slow load cycling had little effect. This technique seems very promising to have a major impact on validation and analysis of crack electrochemistry models as it is a good attempt to establish some measurable parameters within a real crack.

Effect of Adsorbed Sulfur on Anodic Dissolution and Passivation. In real world stress corrosion cracking situations there are many more species that can be reproduced in the NS4 solution. “Pure” solutions and clean electrode surfaces definitely do not represent the conditions in service. Sulfur is one element that actively adsorbs on the iron surface and has an effect on dissolution and passivation behaviour. Seshadri et al [1997] examined the effect of increasing adsorbed sulfur coverage (percent of saturation) on the anodic dissolution behaviour of pure iron. Increasing sulfur saturation increased anodic dissolution rates though passivation is present for all sulfur levels at some point, as seen in Figure 2-7. Another conclusion of this work is that at saturations less than 64% the dissolution of Fe is enhanced but at saturations above 64% there is an increase in the oxidation of Fe(II) to Fe(III). This paper points to sulfur adsorption increasing

anodic dissolution and passivation, but in using an alkaline borate buffer electrolyte, still can not necessarily be generalized to in-service conditions.

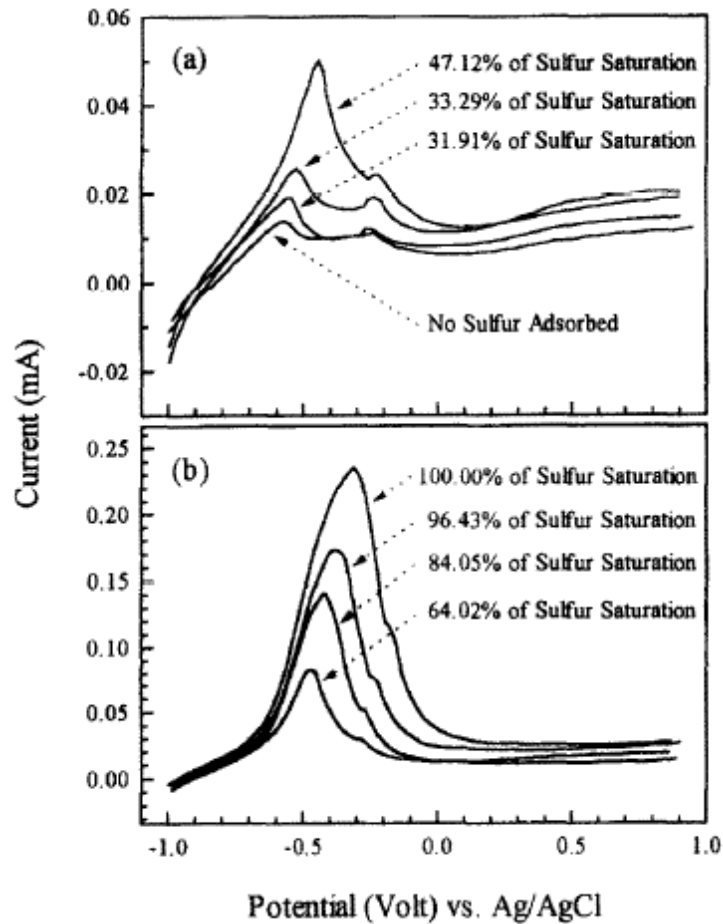


Figure 2-7 a) Linear Voltammogram of Sulfur Covered Iron Surfaces in Borate Buffer (pH=8.4) and b) same as (a) but at Higher S from Seshadri et al, 1997

2.8 Hydrogen in Materials

2.8.1 Overview of Hydrogen in Materials

Hydrogen is able to enter pipeline steel and diffuse within it. The following sections will present the theory, experimental practice, and history related to the understanding of hydrogen ingress, internal transport, and egress. The major problem with hydrogen in a susceptible material is the

lowering of its ability to resist fracture (fracture toughness). It is thought to be attracted to areas of the metal where the stresses and strains are the highest [Mao, 2001, Turnbull et al, 1996], particularly the crack tip which is exactly the place where sensitivity to fracture is most critical. While application of standard and tabulated material properties is often not sufficient in this area, due to the wide range of SCC material and environment conditions, a special value of the fracture toughness for SCC (K_{ISCC}) offers engineers some insight into selecting proper materials for service. Of benefit to a materials engineer is knowledge of susceptible microstructures and the behavior of hydrogen in possible materials. One of the major problems of this field remains the reliable measurement of hydrogen, so that existing and new models and experimental techniques can be verified. There are many recognized standard procedures for testing hydrogen effects on different materials, including constant load, rising step load, slow strain rate, inclined wedge, bend tests, disk pressure test, cantilever beam, and the notched round bar tension test [Burwell et al, 2004].

2.8.2 Review of Crystal Structure

Most pipeline steels are mid to low carbon steel, having a ferritic and pearlitic structure. The ferrite phase in these steels has a body-centred-cubic (BCC) structure. In contrast, most stainless steels are austenitic and have a face-centred-cubic (FCC) structure. Carbon and hydrogen are both interstitial solutes in steel, occupying interstitial holes in the crystal lattice [King, 1971]. There are two types of interstitial holes, octahedral and tetrahedral, and the classification depends on the number of iron atoms surrounding it [Saunders, 2005]. Table 2-1 is a summary of the sizes of solute atoms that can fit into each type of interstitial hole without distorting the crystal lattice; FCC values are included for reference and R_A is the radius of the solvent atom, in

our case iron. From this and the relative sizes of the atoms shown in Table 2-2 it is readily apparent that even hydrogen cannot simply fit into the lattice without some distortion, and that the relative solubility of hydrogen in ferrite is much lower than in austenite [Baranowski et al, 1971, King, 1971, Sanchez et al, 2008]. These analyses rely on the hard-shell model of solid solution interaction, which is useful but not sufficient for a very thorough understanding [Fukai, 1984].

Table 2-1 Interstitial hole sizes for BCC and FCC Structures from King 1971

<i>Type of Hole</i>	<i>Crystal Structure</i>	
	BCC	FCC
Octahedral	$0.155R_A$	$0.414R_A$
Tetrahedral	$0.211R_A$	$0.225R_A$
R_A is the radius of the solvent		

Table 2-2 Relative sizes of interstitial elements from King 1971

<i>Interstitial Element</i>	<i>Relative Size</i>
Carbon	$(0.620)R_{\text{IRON}}$
Hydrogen	$(0.371)R_{\text{IRON}}$
Nitrogen	$(0.572)R_{\text{IRON}}$

2.8.3 Properties of Hydrogen

Hydrogen is the lightest element on the periodic table, with an atomic mass of only 1.008 g/mol [Winter, 1993]. It has the simplest structure of any element, with one proton and one electron. It is naturally found as a diatomic gas but is also present in many organic and inorganic compounds. The most common ion it forms is the H^+ ion but can also exist as H^- . In aqueous

solutions the H^+ ion is unlikely to exist and is commonly thought to hydrate to form H_3O^+ .

Hydrogen is often incorrectly thought of as the smallest element with a reported atomic radii of 53pm ($53 \times 10^{-12}m$). In fact helium, neon, fluorine, and oxygen all have smaller atomic radii. For comparison, iron's atomic radius is only three times larger at 156 pm and carbon's is 67 pm.

2.8.4 How is Hydrogen Present?

Hydrogen is ubiquitous in the oil and gas industry and can come from hydrogen gas product streams, hydrogen sulfide product contaminates, groundwater, cathodic protection, welding, acid pickling, electroplating, forming, casting, or other sources. Electrochemical reactions, which occur at both free corrosion potentials and imposed cathodic protection conditions, can produce hydrogen, either as an intermediate or final product [Bockris & Reddy, 2000, pg 1671].

Hydrogen present from solidification is more-or-less uniformly distributed throughout the steel. Hydrogen that comes from electrochemical processes, including acid pickling and plating, or from hydrogen pressure, can form a concentration gradient from the surface.

2.8.5 How does Hydrogen Enter Steel?

Hydrogen adsorbed onto the steel surface is an essential part of many of the reactions of interest shown in Section 2.7.1. Once on the surface, the hydrogen can do a number of things: participate in a reaction with other species, form diatomic hydrogen and evolve from the surface, or become absorbed into the steel [Zachroczymsi, 1985]. The driving force responsible for hydrogen entering steel may be as simple as a concentration gradient between the surface and interior [Jones, 1996]. The mechanism of hydrogen's first jump into the lattice or a grain boundary is unclear. There also exist poisons which enhance hydrogen entry. Perhaps the best of these is H_2S , where not only does it readily dissociate into H^+ and S^{2-} in water, but sulfur

readily adsorbs onto the surface and retards the recombination of hydrogen [Jones, 1996 pg 368, Kelber & Seshadri, 2001]. The more time hydrogen spends on the surface, the more likely it is to enter the metal.

There are many factors that can influence hydrogen entry into the material. Anything that affects the surface concentration of hydrogen, residence time, surface potential, and unknown entry mechanism will affect the concentration gradient. The most common laboratory method to introduce hydrogen into a material, electrochemical charging, presents some opportunities and challenges, as discussed later. The most apparent problem is that, due to the factors listed above, charging current is not the only factor influencing hydrogen ingress. It is also a function of surface condition, film formation, and number of occupied surface sites. A study by Yan & Weng [2006] reports that only 0.01-0.1% of charging current actually represents hydrogen entering the material.

2.8.6 How does Hydrogen Diffuse through Steel?

The laws of diffusion were first developed by Fick in the 1850s and further developed for gaseous diffusion in solution by Richardson in the early 1900s [Richardson, 1904]. They describe the process of a species moving from an area of high concentration to an area of low concentration. Fick's first law describes the change in concentration over time.

$$J = -D\nabla\phi$$

Where J is the diffusive flux in mol/m²s, D is the diffusivity coefficient for that solute and solvent combination in m²/s, ∇ is the gradient operator, and ϕ is the concentration gradient in mol/m³. For many material problems, it is not the flux that is as important as the concentration at

any given time. Fick's second law gives a relation that describes the change in the concentration gradient with time.

$$\frac{\partial \varphi}{\partial t} = D \nabla^2 \varphi$$

If this is simplified to one dimension, which requires a uniform substrate composition and diffusion coefficient, Fick's second law becomes:

$$\frac{\partial C}{\partial t} = D \frac{\partial^2 C}{\partial x^2}$$

These relations have been used to examine the flux of dissolved hydrogen through metal [Foster et al, 1965, Kanayama et al, 2009, Sainter et al, 2011, Wang et al, 2005]. If the boundary conditions are known, namely the entry surface (through knowledge of the electrochemical charging technique) and the exit surface (through maintaining potentials such that all hydrogen is oxidized upon egress) certain properties of hydrogen's behavior can be obtained. If hydrogen is the only species present at the exit side, then the current required is directly related to the amount of hydrogen passing through the material. The following relation is then used to calculate the hydrogen flux [Park et al, 2008, Yan & Weng, 2006]:

$$J_{ss} = \frac{i_{ss}}{nF}$$

Where J is the hydrogen flux, i is the steady-state current density, n is the number of electrons transferred, and F is Faraday's constant. The permeability can then be defined by using the specimen thickness, L :

$$J_{ss} L = \frac{i_{ss} L}{nF}$$

This formula for permeability relies on the assumption of a linear concentration gradient in the sample, an assumption that has been challenged [Hutchings et al, 1993]. The apparent diffusivity of hydrogen through the sample can also be determined using the breakthrough method, which is the time required between ramp-up of ingress and first detection upon egress, t_b :

$$D_{app} = \frac{L^2}{2\pi^2 t_b}$$

The apparent diffusivity will be discussed later as it is a major part of this work. One final formula, which relates probably the most important parameter for materials engineers, is the apparent concentration of hydrogen in the material:

$$C_{app} = \frac{J_{ss} L}{D_{app}}$$

The two major problems with this method are the assumption of linear concentration gradients and a uniform material composition. The apparent (sometimes called effective) diffusion coefficient has been shown to vary by more than an order of magnitude depending on how aggressive the charging conditions are [Griffiths & Turnbull, 1995]. While this technique is robust and relatively easy to perform, care should be taken when applying the results, especially with changing environmental conditions or in materials with significant heterogeneities.

Another significant property of the diffusion coefficient was reported by Chew [1971]. The hydrogen diffusion coefficient in iron and low-alloy steels is temperature dependant, following the relation:

$$D' = D_0 e^{-\left(\frac{E}{RT}\right)}$$

Where D_0 is a constant for the material, E is the activation energy, R is the gas constant, and T is the absolute temperature. Using an adaptation of the above techniques, Piggott & Siarkowski [1972] was able to also determine the diffusion properties of an oxide film on steel. The oxide was of the Fe_2O_3 type, with varying thicknesses. The protective ability of an intact oxide film was shown with diffusion coefficients ten orders of magnitude less than the steel substrate, varying with thickness. These relations are well-summarized by Olden et al [2008].

2.8.7 Where does Hydrogen Reside in Steel?

As seen previously, hydrogen is able to exist in (Section 2.8.2) and move throughout (Section 2.8.6) the crystal lattice. However, there are many other locations and microstructural inhomogeneities that are theorized to be able to accommodate, or trap, diffusing hydrogen (see Table 2-3) [Baranowski et al, 1971, Chew, 1971, Grabke & Riecke, 2000, Park et al, 2008, Turnbull et al, 1994, 1997, 1989]. An important concept related to these traps is their relative abilities to hold on to the trapped hydrogen. Traps can be considered reversible or irreversible depending on the relative activation energies required for hydrogen to escape. For example, hydrogen may be easily able to be swept up and out of a dislocation by a lower energy dislocation moving by, or by a modest increase in temperature. Diatomic hydrogen molecules, formed inside micro-voids or cracks in the material, may be held very strongly and only able to escape when the metal is melted.

Table 2-3 Hydrogen trap types and relative strengths

<i>Location</i>	<i>Trap Energy/ Type</i>
Interstitial Holes	Weak
Lattice Vacancies	Weak
Dislocations	Reversible
Voids	Irreversible
Inclusions	Reversible
Grain Boundaries	Reversible
Phase Transitions	Reversible

As the temperature goes up (above approximately 200°C), and the energy required to escape reversible traps is met, lattice diffusion is the rate determining process in hydrogen transport [Chew, 1971]. Below that temperature the effect of reversible and irreversible traps become more apparent. One method to evaluate the effect of trapping is to examine the breakthrough time and apparent diffusion coefficient (see Section 2.8.6) achieved on successive transients using a Devanathan experimental set-up (see Section 2.8.8). In a sample with initially low hydrogen concentration, the first pass will yield a value of diffusion coefficient that is a result of lattice diffusion as well as the ‘filling up’ of the reversible and irreversible traps. If the experiment is repeated on the same sample, another breakthrough time and apparent diffusion coefficient is seen. This second trial produces a higher diffusion coefficient, due to a decreased effect of reversible traps, as they are already partially filled and do not delay the passage of hydrogen as much. In this way some researchers have been able to quantify the relative strengths of some microstructural features and their effect on the diffusion coefficients [Bulger et al, 2006, Griffiths & Turnbull, 1995, Jones, 1996 pg 337, Olden et al, 2008, Park et al, 2008, Turnbull & Hutchings, 1994].

2.8.8 How is Hydrogen Measured?

The Devanathan and Stachurski apparatus is the most common method for determining diffusion properties and the amount of hydrogen in a material, using the method described in Section 2.8.6. The cell consists of two electrochemical cells joined by a metal membrane, which is the material of interest. The charging side applies a cathodic potential to encourage the hydrogen evolution reaction on the surface. As hydrogen is produced, some is absorbed into the material to diffuse to the other side of the membrane. On the other side an oxidizing potential is maintained so that all hydrogen evolving will be oxidized and the oxidation current recorded [Davis & Butler, 1958]. A popular modification to the Devanathan and Stachurski method is the Barnacle cell, where only the hydrogen oxidizing cell is used. This can be attached to any material under consideration, with the charging side able to be any combination of environment and potential desired. This allows common or proposed industrial materials to be placed in real conditions and the hydrogen in the material quantified. It has also been proposed as a field method to monitor internal corrosion processes, as hydrogen measured on egress is an indirect measure of corrosion intensity inside the pipe or vessel [Shaw et al, 1998].

Another popular method is the mercury eudiometry technique. Hydrogen has very low solubility in liquid mercury [Jiang & Li, 2011]. Hydrogen diffusing out of a sample that is placed inside a eudiometer tube with liquid mercury is captured as described in the welding standard ANSI/AWS A4.3. The volume of hydrogen collected is a direct measure of the mobile hydrogen in the sample. The temperature of the mercury can be raised so that certain types of reversibly held hydrogen can be measured as well [Senadheera & Shaw, 2009]. The Vacuum foil method was researched extensively at the University of Calgary [Shaw et al, 1998, Shaw & Matie, 1998]. In this technique, a vacuum was created under a metal foil. Decay in the vacuum was attributed

to hydrogen egress from the metal and recombination to H₂ and was indicative of corrosion activity on the opposite side of the sample. This technique could be applied to a large number of material and environmental conditions.

There are several other techniques that have met with varying degrees of success and acceptance.

The hydrogen evolving from a well-defined surface can be collected in an air stream and analyzed by a remote hydrogen detector to a reported sensitivity of $<10^{-3}$ bar [Dean & Fray, 2000]. A possible advantage of this method is that the unit could be taken into the field.

Another method makes use of thermal outgassing, where a previously charged material is placed in air or a vacuum and then allowed to outgas [Iacoviello et al, 1998]. The material's change in weight, measured by the deflection of a sensitive spring, is then measured. An advantage of this method is that the temperature could be raised much higher than most other methods. The hydrogen microprint technique [Ichitani & Kanno, 2003] uses silver adsorbed on the exit surface. As hydrogen reaches the exit surface, it reduces the silver, whose colour change can be quantified. The sensitivity of this technique is reported to be 40-75% of a hydrogen permeation method.

A questionable technique involves dissolving a known amount of substrate (presumably a uniform layer) and collecting the hydrogen released in that operation [Beloglazov, 2003].

Successive operations of this type will then reveal the concentration in the material at a given depth. A laser ablation method was proposed to examine hydrogen in welds that used a number of different detectors from opto-electronic (a tungsten oxide detector), spectroscopy, gas chromatography, and mass spectroscopy [Smith et al, 2001 a & b]. Another technique uses a more traditional electrochemical set-up but instead of the diffusion relations makes use of Sievert's law, which relates the partial pressure of hydrogen gas to the concentration in metal.

The concentration in metal is then related to the cathodic charging current by the hydrogen retention ratio. The technique seemingly uses two indirect methods [Yan & Weng, 2006]. Secondary ion mass spectroscopy [Birnbaum et al, 1982] has also been used.

2.9 The Tensile Test

The tensile test is a common and powerful tool in materials engineering to determine some of the mechanical properties of a material. The most commonly applied standardized tensile test procedure is the American Society for Testing and Materials International, ASTM E8, last revised in 2011. To perform the test a specimen of the material (prepared to a specified configuration, see Figure 2-8 for one example), is fixed in a frame that is capable of applying a tensile load to the specimen. A controlled load (or controlled deformation) is applied to the specimen to see how the material responds. Pairs of values of load and deformation are recorded to be used later to visualize the material's response to loading. Load and deformation values are highly dependent on sample size so the more generally applicable values of stress and strain are used. Engineering stress is just the value of the load divided by the specimen's original cross sectional area and engineering strain is the value of the deformation divided by the specimen's original length. The engineering stress and strain are then plotted as seen in Figure 2-9.

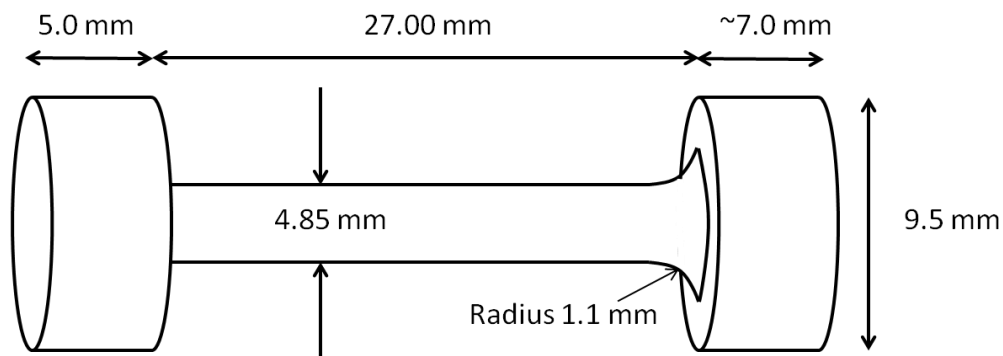


Figure 2-8 Typical Barbell-Shaped Tensile Test Specimen

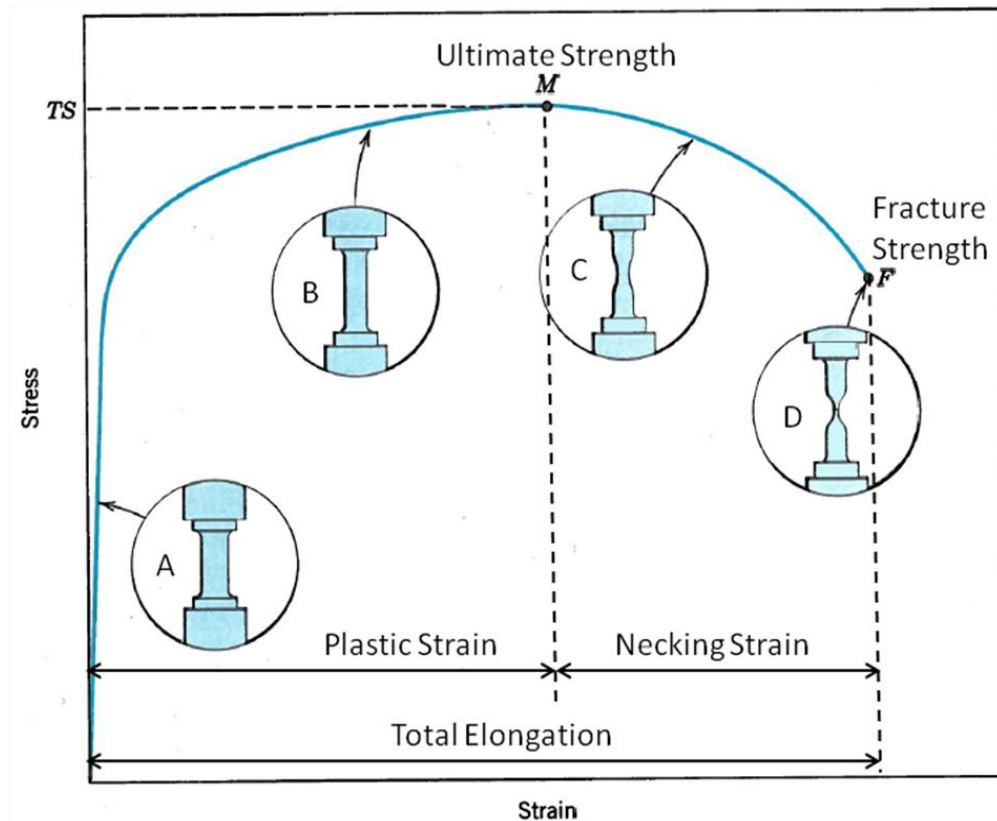
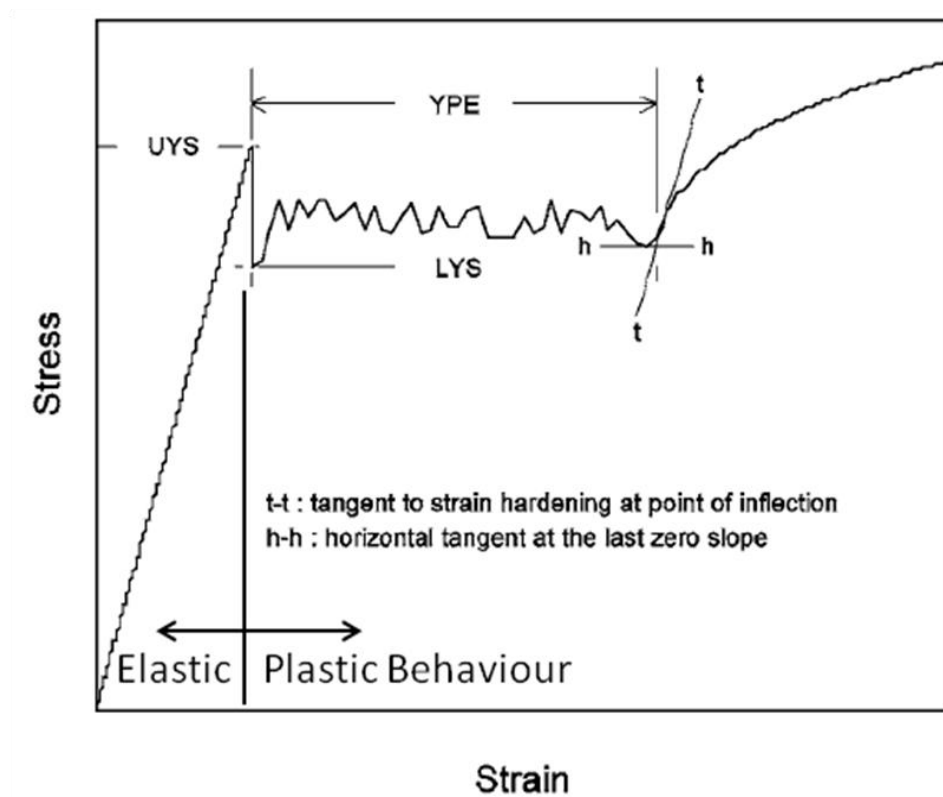


Figure 2-9 Illustrative Stress-Strain Curve, adapted from Callister, 6th ed., 2003, pg. 126

The engineering stress-strain curve shows many features that are characteristic of what is going on in the material at a given time. At low levels of stress and strain (illustrated by inset A above) the material is in the **elastic** region, which is characterized by a linear response with constant slope. The slope is defined to be the Young's modulus and if the material were then unloaded it would follow that line back to zero. Once the material reaches a certain stress, called the yield stress (discussed in detail below, and shown in Figure 2-10), it experiences some permanent deformation (**plastic** strain). From here to the highest experienced engineering stress the material is said to be in the work hardening region, and is illustrated by inset B. It is also called the uniform strain region because the sample experiences uniform stretching along its length. After the maximum engineering stress (called the Ultimate Tensile Strength or Ultimate

Strength) is reached an instability forms in the specimen and it begins to ‘neck’ down, as seen in inset C. Further deformation is concentrated in this necking volume until the sample finally ruptures, illustrated by inset D. Some important mechanical properties that can be seen on Figure 2-9 are Ultimate Strength, Fracture Strength, Elongation at Fracture, Plastic Strain, and Necking Strain.

Some materials, particularly low carbon steels, can have complex yielding behaviour. Figure 2-10 illustrates several features of that complex behaviour including upper and lower yield strengths (UYS and LYS in the figure), yield point elongation (Lüders Region), and the beginning of the work hardening region.



**Figure 2-10 Illustrative Stress-Strain Curve showing Complex Yielding Behaviour, from
ASTM E8 09**

Dislocations are atomic-scale crystal lattice defects that, given the right conditions of local stress, are able to translate and are responsible for the overall deformation seen in the sample [Callister, 2003 pg 73 & 164, Hart, 1967, Hertzberg, 1996 Chapter 2]. From zero stress up to the yield point, no dislocations have moved. The observed response is due to static intermolecular forces of repulsion and attraction. Once the yield point is reached there is enough energy in the system to cause dislocations to move and there is permanent deformation. Yield point elongation (YPE) occurs when there are many dislocation features of similar activation energy that must release before significant work hardening can begin. In the work hardening region new dislocations are generated within the material. Dislocations interfere with the movement of each other, and generally the more dislocations there are, the more interference, which leads to higher stresses. Eventually a tensile instability will form and the specimen will start to neck down. All further deformation will be concentrated within this region. The material deforms in all directions (complex triaxial conditions), new macroscopic voids are generated within the material, and eventually it will fail.

2.10 Solid Solution Hardening and Mobile Solutes

Pure metals are almost always weaker and more ductile than alloys of the same base metal [Callister, 2003, pg 177]. Substitutional and interstitial solutes introduce lattice distortions, increasing strength. Solute distortion strain fields and dislocation strain fields can interact to raise or lower the overall strain field. Solutes that are able to diffuse to or away from a dislocation will do so in an effort to reduce the overall strain, thereby increasing the resistance to slip [Balik & Lukac, 1989 a & b]. A general solid solution strengthening relationship for carbon is $\Delta\sigma \sim c^{1/2}$, indicating that the change in flow stress from standard condition grows with the square root of the concentration [Hertzberg, 1996, pg 132].

Dynamic strain aging occurs when a favourable combination of dislocation velocity (strain rate dependant) and solute diffusivity (temperature dependant) produce elevated yield stress and decreased elongation [Almeida et al, 1998]. If the solute diffusion rate is high enough, a so-called “Cottrell atmosphere” of solutes can form around a dislocation when it has arrested at an obstacle and then follow it during deformation [Head et al, 1970, McCormick, 1972, Zhao et al, 2000]. This raises the activation energy required to move a dislocation thereby increasing the resistance to plastic flow.

2.11 Effect of Hydrogen on Mechanical Properties of Metals

The effects of hydrogen and especially hydrogen embrittlement have been extensively studied for a long time [Cotteril, 1961, Pfeil, 1926, Thompson & Bernstein, 1978]. The two most industrially important effects of hydrogen are the decreased elongation at fracture and hydrogen’s role in decreased fracture toughness and crack propagation. In addition to the general decrease in elongation seen universally [Brown & Baldwin, 1953, Duprez et al, 2009, Duval & Robinson, 2009, Garber et al, 1976, Hardie et al, 2006, Oriani & Josephic, 1980, Siddiqui & Abdullah, 2005, Sudarshan et al, 1978, Zheng & Hardie, 1991] increasing hydrogen concentration has also been shown to change the mode of failure from ductile to cleavage or intergranular fracture [Lepinoux & Magnin, 1993, Melitis & Hochman, 1986, Melitis & Huang, 1991, Wang et al, 2007]. The presence of hydrogen generally softens the steels slightly but has been shown to harden occasionally, though the conditions for this to happen are poorly explained and differ greatly between materials and test conditions.

Despite the long history of research interest in the effects of hydrogen, there is still no consensus between mechanical models of hydrogen’s effects and the results of experiment [Gerberich, 2009, Krom et al, 1999, Sofronis & Robertson, 2006]. The varied and sometimes complex

response of a single material to different conditions, and variability of responses from similar materials indicate a number of contributing phenomena. The behaviour of a particular material could be dominated by one phenomenon under a particular set of conditions and dominated by different phenomena under different conditions. In a comprehensive review Hirth [1980] noted several potential mechanisms for hydrogen's hardening or softening effects on iron and steel:

- Hydrogen presence in the dislocation core makes dislocation interactions more difficult (Hardening effect).
- Hydrogen trapped in vacancies, stabilizing them and retarding recovery processes (Hardening effect).
- Dislocation core drag effects of hydrogen trapped at dislocations (Hardening effect).
- Hydrogen augmenting carbon's pinning effect on dislocations (Hardening effect).
- Hydrogen charging damage, creating voids and microfissures (Softening effect).
- The extent of damage could lead to softening or hardening.

Both hardening and softening are seen. In theory, diffusing hydrogen tends to harden by making mixed slip more difficult, while hydrogen trapped in voids tends to soften through enhanced mobility of screw dislocations. Oriani & Josephic [1980] also mentions the effect of hydrogen impeding cross-slip of screw dislocations.

During a tensile test the previously mentioned mechanisms largely control initial deformation, while final necking failure occurs by cracking or decohesion of second phase particles, growth of voids, and void coalescence, which could be affected by hydrogen in a different manner. In a later review Sofronis & Robertson [2006] showed that these models are still largely unproven and remain as conjecture. There still remains a lack of integration between mechanics theory and experimental observation. He divided hydrogen's effects into three broad categories:

- Hydride Formation
- Hydrogen Enhanced Local Plasticity (HELP)
- Hydrogen Induced Decohesion (HID)

Hydride formation is not applicable for this study as the iron-carbon system is not a hydride-forming system [Cotterill, 1961]. Hydrogen Enhanced Local Plasticity theory [Brinbaum & Sofronis, 1994] arose from observations of locally increased plasticity on fracture surfaces formed in the presence of hydrogen and is supported by evidence. However, the connection between local areas of increased ductility and an overall loss of ductility in the sample remains unresolved. Hydrogen Induced Decohesion theory, which is not yet backed by observation, proposes a hydrogen-caused decrease in the energy required to create a newly-cleaved surface, resulting in a loss in ductility [Sofronis & Robertson, 2006]. The authors pointed to some significant challenges remaining in the study of hydrogen embrittlement: How can enhanced dislocation mobility lead to decreased bulk ductility? What is the synergistic effect of hydrogen and other solutes, particularly carbon?

There is a great gap between theories and observed physical behaviours, despite extensive research in the hydrogen area. Modeling of hydrogen diffusion and effect on material properties is of great interest to academics and industry, and much literature has been produced either modeling without testing, or testing without validating theory.

Chapter Three: Objectives and Specific Aims

3.1 Hydrogen Diffusion Profiles in Pipeline Steel

The most common methods for determining the characteristics of hydrogen in a metal involve electrochemical studies. The properties most desired involve the solubility and permeability of hydrogen in that material. These methods will commonly determine diffusion rates, solubility and binding energy of hydrogen traps, the amount of hydrogen in a material under a given set of environmental conditions, and the rates of corrosion reactions on metal membranes. Application of the analysis techniques for these methods relies on an underlying assumption of the diffusion of hydrogen, in that it follows a pattern matching that predicted by Fick's Laws, which were developed for gaseous diffusion and later refined for diffusion in solids. This profile has not been experimentally observed and verified, even though it is a core assumption that all these techniques rely on.

Electrochemical systems are always very complex. The electrolyte/metal interface and surface reactions determine how much hydrogen is available to enter a material. Hydrogen's method of entry into a material is poorly understood. If a method can be established to determine the concentration profile in a material, then an estimate can be made of the concentration of hydrogen at the surface of the metal. A reliable method to measure the concentration of hydrogen very near the surface will open new possibilities for studying the reactions on the electrolyte/metal interface and the nature of hydrogen entry into metals.

Specific Aim 1: Develop procedures and techniques to improve understanding of hydrogen diffusion into and through steel, and to provide a direct measurement tool to validate indirect electrochemical measurement techniques.

Specific Aim 2: Develop procedures and techniques to determine the concentration of hydrogen near the surface in contact with electrolyte.

3.2 Tensile Tests with Varying Strain Rate and Hydrogen Concentration

Hydrogen has well-known effects on material behaviour, and hydrogen's effects have been studied for many decades. Hydrogen embrittlement, hydrogen induced cracking, and stress corrosion cracking are a few of the most industrially important, dangerous, and costly phenomena. Hydrogen is able to move through a material and significant research has been done to examine hydrogen's negative effects on, and affinity for, highly strained regions like the tip of a crack. Hydrogen is known to lower the stress required for a crack to propagate and to promote brittle failure. Dynamic strain aging is a phenomenon involving mobile solutes and a deforming material and has been used to examine not only the effects of mobile solute carbon and nitrogen, but to examine the mechanisms of deformation and learn about dislocation movement. Though hydrogen is considered able to move during straining and deformation, linking an experimental approach to the significant body of dynamic strain aging research has not been done. Normally strain aging research varies temperature to change the diffusion rate of the mobile solute through a range where it can interfere with dislocation movement. In this work the strain rate (representing the dislocation velocity) was varied to determine the interactions with diffusing hydrogen (mobile solute) at a fixed temperature.

Specific Aim 3: Develop procedures and techniques to characterize dissolved hydrogen's effects on the mechanical response of low carbon steel through a range of strain rates.

Specific Aim 4: Isolate the conditions of deformation that lead to the greatest effect of hydrogen, both for a mechanistic understanding and to develop potential materials screening techniques.

3.3 Examination of Field-Failed Pipeline from Stress Corrosion Cracking

A sample of pipeline that failed in service due to the effects of stress corrosion cracking was provided for research purposes by an international risk management company. Stress corrosion cracking requires a susceptible material, corrosion, and stress. The typical progression for stress corrosion cracking is incubation, nucleation of a crack field, growth of the crack colony, and final coalescence of the crack field into a running failure. The final process is well understood but the initial causes and stages of crack colony formation are poorly understood. This specimen has a well established crack colony with both corrosion pits and cracks. The sample was examined post-hoc with an emphasis on the relationships between the observed pits and the mature crack colony. The specimen was also examined using a depth wise sectioning technique to view subsurface features of the crack colony.

Specific Aim 5: Improve the stress corrosion cracking model through new understandings of crack morphology and stress corrosion crack colony growth.

Chapter Four: **Experimental Methods for Determining Hydrogen Diffusion in a Low-Carbon Steel**

This chapter examines the series of experiments conducted to test, for the first time, whether the assumptions and outcomes of Fick's Laws of Diffusion can be supported by experiments using passive hydrogen charging, mercury eudiometry to collect and measure hydrogen, and a novel sectioning technique. These techniques were used to determine an experimental hydrogen concentration profile in a round bar which was compared to the profile predicted by the uniaxial solution to Fick's Law. The analytical solution requires four parameters to generate the gradient profile: Surface Concentration, Bulk Concentration, Diffusion Coefficient, and Time.

Generally, an attempt is made to keep bulk concentration and time constant, so that surface concentration and diffusion coefficient can be determined. However, in the final experiment presented in this chapter both surface concentration and time are also manipulated. The order of topics in this chapter follows the general form: Main Experiment, Standard Procedures, Validation Experiments, and finally a supplemental experiment.

4.1 Main Experiment: Round Bar Test of Uniaxial Hydrogen Concentration Gradient

This experiment provides a spatial map of hydrogen concentration gained from a direct method of hydrogen measurement. A round bar of approximately 38 mm (1.5 inches) diameter by 100 mm (four inches) length was lacquer-coated on all surfaces with the exception of one end. This method of coating was meant to prevent appreciable hydrogen ingress from all surfaces except the uncoated end by separating the bare metal from the corrosive solution (Figure 4-1). This promotes one dimensional travel of absorbed hydrogen away from the charging surface according to the Fick's Law model presented in Section 2.8.6. The specimen was immersed in a deaerated acidic solution (specified in Table 4-1) and allowed to undergo passive corrosion.

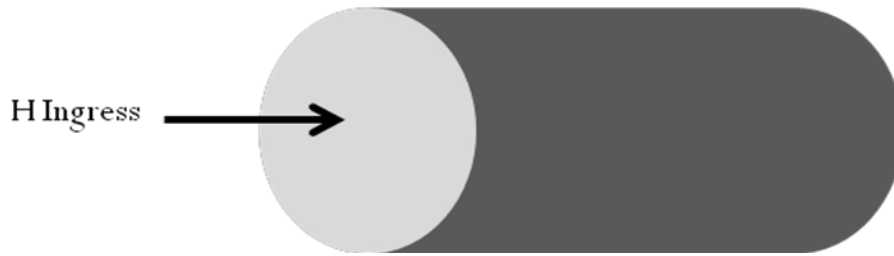


Figure 4-1 Hydrogen Ingress into Coated Round Bar

After a suitable charging time (48 hours), the sample was cut into sections appropriate for the eudiometer apparatus and specimen carrier and tested for mobile hydrogen concentration. Figure 4-2 shows a schematic of the sectioned bar and a predicted outcome of the hydrogen concentration and position. Six of these experiments were attempted leading to four valid tests.

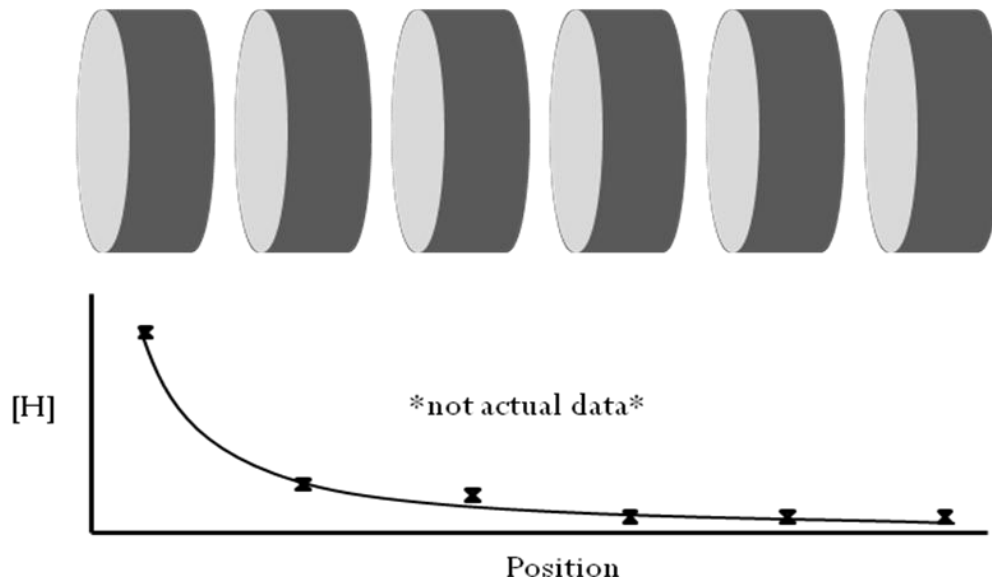


Figure 4-2 Predicted Outcome of Hydrogen Concentration after Round Bar Sectioning

4.1.1 Sample Preparation

The round bar was cut to approximately 100 mm (4 inches) length. The section of round bar was then sand-blasted (silicon oxide) to remove any mill scale and produce a white metal surface.

Then the end of the bar to be left uncoated was progressively ground from 240, to 320, and finally 400 grit. The sample was then placed in an oven at 110°C for 72 hours to bake out any residual mobile hydrogen. After baking, the specimen was allowed to cool for several hours and a coating of red lacquer applied. The first coat was allowed to dry overnight and a second coat applied. The uncoated end was ground again to a 400 grit surface prior to hydrogen charging.

4.1.2 Hydrogen Charging

To charge a sample with hydrogen, a passive corrosion technique was used. The coated round bar was immersed in a deaerated acidic solution (5% NaCl, 1.1 pH, stable throughout experiment, see Table 4-1 for solution details). Some of the hydrogen participating in the corrosion reactions entered the steel (described in Section 2.8.5) and became mobile dissolved hydrogen. After 48 hours in the acidic solution the specimen was removed, washed in distilled water and prepared for mobile hydrogen measurement.

Table 4-1 Composition of Passive Hydrogen Charging Solution

<i>Hydrogen Charging Solution</i>	<i>(1 L)</i>	
Sodium Chloride	5%	26.0 g
Hydrochloric Acid (35%)	0.1 Normal	10.0 mL
Distilled Water	Remainder	1.00 L
Nitrogen gas	Bubbling	

4.1.3 Mobile Hydrogen Measurement

The washed sample was taken to the horizontal band saw and cut into sections using cutting fluid to keep the specimen cool. Because the concentration increases greatly nearer the hydrogen entry side of the specimen, sections near there were sliced thinner, in the range of 6 to 10 mm

(1/4 to 3/8 of an inch). After the first two slices, the remaining specimen is cut into slices from 10 to 13 mm thick (3/8 to 1/2 of an inch) (see Figure 4-2 above). In this way, four to seven discs could be recovered from each charged sample for eudiometry. Because hydrogen concentration was calculated using the specimen weight (i.e. directly tied to volume), the sample sizes did not need to be identical.

After the specimen is cut into sections, each section was washed in acetone and scrubbed with a wire brush to remove the red lacquer. The sections were allowed to dry and were measured for length and weight, which were used to calculate concentration and to plot against position. For detail on how this data was recorded see Table 4-3. Once the sections are cleaned and measured they were placed into the mercury eudiometers to measure the mobile hydrogen concentration. The procedure for using the mercury eudiometers is found in Section 4.4 below. It generally took one hour to perform all necessary operations from initial removal from the charging solution to placing each sample in a eudiometer and turning on the heating mantles. Hydrogen egress during this time is considered in Section 5.2. The outcome measures from this operation are hydrogen concentration, and a location of the centre of the section that has that concentration, to be plotted together in the manner shown in Figure 4-2 above.

4.1.4 Standard Procedures and Validation Experiments

The remainder of this chapter describes the standard operating procedures used to carry out this research and the series of experiments used to validate the technique. These operating procedures and validation experiments are presented in the order below.

- Section 4.2 – Specimen Acquisition
- Section 4.3 – Sample Mounting, Polishing, and Etching
- Section 4.4 – Standard Eudiometer Procedure
- Section 4.5 – Calibration of the Eudiometer Units
- Section 4.6 – Cleaning the Eudiometers
- Section 4.7 – Cleaning the Mercury
- Section 4.8 – Determination of the Appropriate Time to take Final Hydrogen Measurements.
- Section 4.9 – Baseline Hydrogen Concentration Present in Baked-Out Samples.
- Section 4.10 – Vicker’s Hardness of Round Bar
- Section 4.11 – Electropotential Scans
- Section 4.12 – Effect of Charging Solution and Time on Apparent Surface Concentration

In addition to validating the experimental process the properties of the sample material were investigated through an experiment looking at Vicker’s hardness (Section 4.10). The corrosion behavior of the metal in the experimental acidic solution was examined by an electropotential scan (Section 4.11). Finally, the effect of the charging solution and charging time on the apparent hydrogen surface concentration was examined (Section 4.12).

4.2 Specimen Acquisition

The material used for this part of the research was a low-carbon steel, purchased from engineering stores. The steel has a carbon percentage of approximately 0.13% and was hypoeutectic, consisting of ferrite and pearlite (see results Section 5.1). The microstructure was

confirmed in the axial as well as transverse directions. All testing was done on a single batch of steel to avoid any variability in results due to material batch differences.

4.3 Standard Procedure: Sample Mounting, Polishing, and Etching

To view sample microstructure, samples were mounted in Bakelite according to the standard procedure listed below. See Figure 4-3 for an example of a mounted sample.

1. Sample is cut to an appropriate size for mounting, typically less than $\frac{1}{2}$ cm³.
2. The sample is placed in the mounting press.
3. An annular ring is added to the press, to assist in grinding a flat surface.
4. Powdered thermo-set plastic is added.
5. Following the machine instructions heat and pressure are applied to set the plastic.



Figure 4-3 Mounted Metallurgical Sample of SCC Affected Pipeline, 32 mm Diameter

Samples were progressively wet-ground from 240 grit through 320, 400 and finally 600. Then the samples were polished using standard polishing solutions and cloth polishing wheels with progressively finer polishing compounds of 15 μ m, 9 μ m, 6 μ m, 3 μ m, 1 μ m, and finally 0.05

µm. At 0.05 µm the samples appeared completely smooth, even at maximum optical magnification.

After mounting and polishing, some samples were etched to reveal the grain boundaries and underlying microstructure. Samples used for Vickers Microhardness testing remained unetched. 2% Nital (see Table 4-2) was used for an etchant and the samples were immersed for approximately 10 seconds, then washed with distilled water and dried immediately. The Nital solutions were prepared in-house and had the composition listed below.

Table 4-2 Composition of Nital Etchant Prepared for this Study

<i>2% Nital Formula</i>	
Ethanol, Anhydrous, Denatured	98%
Ethyl Alcohol	84-88%
Methyl Alcohol	4-5%
Isopropyl Alcohol	8-10%
Methyl Isobutyl Keytone	1%
Nitric Acid, 70% A.C.S.	2%
Nitric Acid	70%
Water	30%

4.4 Standard Eudiometer Procedure

This procedure starts at the point where samples are removed from whatever experimental condition they were in. The following procedure applies to both the round bar experimental specimen (discs) and the tensile test configured experimental specimen (barbells) from Section 7.1.

4.4.1 General Points

Speed was important when carrying out the tasks required in preparing samples to be measured in the eudiometers. As soon as a specimen is removed from a hydrogen charging condition it begins to discharge hydrogen back to the environment. The discharge rate increases with temperature so it is important to avoid raising the specimen's temperature. To minimize these losses each step is designed to minimize time and specimen heating. In addition to this, the timing and sequence of all steps is prescribed and recorded to ensure all samples are treated the same. As mentioned previously, due to the number of steps involved in the round bar diffusion work it generally took an hour between initial removal of the specimen from the charging solution to placement in the eudiometers and turning on the heating mantles. Tensile test configured samples could be removed from the charging condition and be placed in the eudiometers within about 10 minutes.

4.4.2 Sample Weights

This experimental procedure produces an amount of hydrogen collected, so each sample must be weighed accurately before being placed in a eudiometer, otherwise it will not be possible to calculate a concentration. A possible alternative to this is to measure the dimensions of a sample and calculate a volume, which can be converted to mass using the density of the material. Need for this alternative technique might arise if a sample was not weighed before being placed in the mercury, as it could not be weighed after (due to contamination issues). A method was tested and found to be accurate within 1-2% but never needed to be used.

4.4.3 Apparatus

The eudiometers used are based on the welding standard (ANSI/AWS 4.3) configuration with some modifications as per Senadheera & Shaw [2009]. A schematic of the apparatus can be seen in Figure 4-5.

4.4.4 Loading Samples into the Eudiometers

All eudiometer operations were carried out within the fume hood to minimize contaminating the laboratory environment with dangerous mercury vapours.

1. Make sure the specimen is dry.
2. Open the eudiometer stopcock and allow the mercury to drain into the kettle.
3. Remove the clamps holding the condensation cover on the kettle.
4. Lift the eudiometer and cover together carefully, to avoid dislodging any mercury condensed on the cover. An alternative to this is to gently tap the cover a few times before lifting to allow mercury droplets to fall back into the kettle.
5. Remove the sample holder from the bell end of the eudiometer and replace the eudiometer and cover.
6. Discard any previous specimen from the holder and place the specimen into the sample holder. Pick up the holder and specimen in one hand.
7. With the other hand, lift the eudiometer and condensation cover until it is clear of the mercury in the kettle and insert the holder/specimen into the eudiometer.
8. Carefully lower the eudiometer/cover and holder/specimen into the mercury until the condensation cover is back in place.
9. Replace the clamps holding the condensation cover to the kettle.
10. Attach the vacuum pump to the tube on the eudiometer.

11. Ensure the eudiometer stopcock is open, and then use the vacuum pump to draw mercury up into the graduated eudiometer tube, filling it completely. Once it is full, close the stopcock and disconnect the vacuum pump.
12. Gently tap the eudiometer tube against the kettle bottom to dislodge any air bubbles that may be adhered to the sample or walls of the eudiometer. Continue gentle tapping to allow any bubbles to collect and rise to the top of the eudiometer. This process should take only a minute or two at most.
13. Reconnect the vacuum pump and draw a slight vacuum. Slightly open the stopcock and use the vacuum pump to again fill the eudiometer tube. Once it is full, close the stopcock and disconnect the vacuum pump. At this point the eudiometer should be full, all air bubbles should be gone from the system, and the apparatus is ready to start collecting hydrogen.
14. Turn on the heating mantle.
15. Clean the catch tray and fume hood of clutter and any loose mercury.

4.4.5 Taking Experimental Readings

Final readings were taken after 72 hours in the eudiometer. Raw experimental data was recorded in the format shown in Table 4-4. 72 hours was found to be a suitable time that represented the total amount of mobile hydrogen recoverable from the specimen (validation and reasons for this time can be found in Section 4.8). Intermediate readings of the volume of hydrogen collected were taken, generally once per day throughout the 72 hour period. There were several reasons for this: to monitor the proper functioning of the equipment, to continuously reinforce the validity of the 72 reading period, and to empty any eudiometers that were in danger of overflowing with hydrogen (thus making accurate readings impossible).

The general procedure for taking intermediate and final readings is as follows:

1. Using the lab's manometer, measure and record the atmospheric pressure, in mmHg.
2. Using the temperature probe and portable thermometer, measure the mercury temperature in each of the active eudiometers. Because the mercury is unstirred the temperature will be stratified [Senadheera & Shaw, 2009]. Therefore it is important to take the temperature at the same depth, specifically the bottom of the kettle.
3. Holding the eudiometer's stem, gently raise and lower the eudiometer, tapping it against the bottom of the kettle. This will release any hydrogen bubbles that are adhered to the sample or eudiometer. Care must be taken to avoid breaking the fragile glass tube. Continue tapping to encourage the hydrogen to move up the eudiometer tube until it has all collected near the stopcock. This movement will agitate and stir the mercury in the kettle, so move on to the next eudiometer and allow the system to settle and the exposed eudiometer tube to cool before taking the reading.
4. Once all the hydrogen has been collected near the stopcocks for all the active eudiometers, return to the first one and take a reading. Each eudiometer tube has graduation marks printed on it, so simply read the scale at the uppermost level of the meniscus (see Figure 4-4). The centimeter and millimeter values are marked and can be read accurately, and the digit between millimeter graduations can be estimated.
5. If the amount of hydrogen collected is so small that it has not reached the first graduation, then an estimate of the amount of hydrogen filling the headspace must be made (see Figure 4-4). The volume of each eudiometer's headspace is known, so estimate the hydrogen's volume to the nearest 10%.
6. Record these measurements along with the eudiometer's temperature, date and time, as well as the atmospheric pressure at the time of the reading.

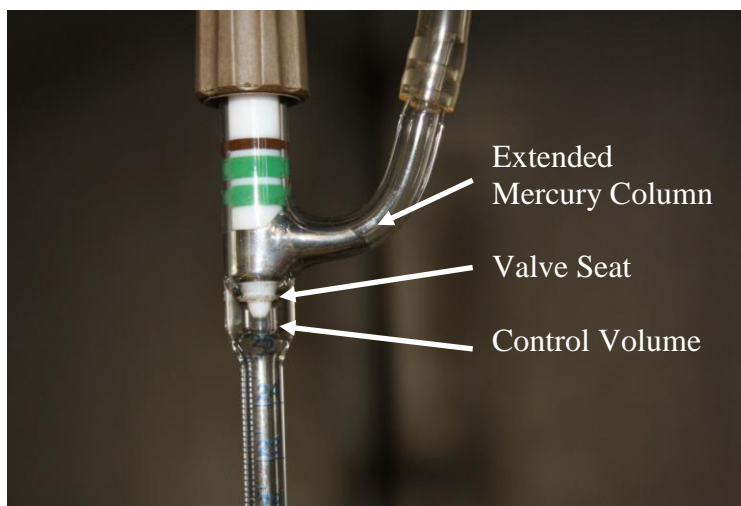


Figure 4-4 Eudiometer Detail Showing Globe Valve and Graduations

4.4.6 Measurements Taken Once Per Experimental Set-up

Once per individual experiment, a series of mercury bath level readings were taken and recorded in the form indicated in Table 4-5. These levels were necessary to calculate the amount of hydrogen from the volume and pressure readings, using the formulas detailed in Section 4.4.8. Refer to Figure 4-5 and the indicated distances $\langle r \rangle$, $\langle p \rangle$, and $\langle q \rangle$ to see what these values represent.

- Depth from top of PFTE lid to mercury surface.
- Depth from top of PFTE lid to bottom of kettle.

A conductivity apparatus was used to find these levels. Two steel rods with position markers were passed into the kettle through two access ports on the lid. One rod was pushed all the way to the bottom of the kettle, and the position marker set at the top of the lid. The rods were both connected to a digital multimeter set to conductivity mode, such that readout displays either an open circuit or a closed circuit. Since there is no electrical connection between the two rods, the

multimeter will read an open circuit. The second rod was then pushed through its access port slowly until the multimeter starts to read a closed circuit and its position marker set at the top of the lid. There is now an electrical connection present between the two rods, with the first immersed in the electrically conductive mercury, and the second now just touching the mercury surface.

With a ruler, measure the distance between the position marker and the bottom of the steel rod. One rod will be set to the distance from the lid to the bottom of the kettle and the other measures the distance from the top of the lid to the mercury surface.

4.4.7 Recordkeeping

The important measured quantities are:

- The specimen weight, in grams to the nearest hundredth of a gram.
- Hydrogen volume collected, as read by the graduated scale on the eudiometers. The value recorded is in centimeters and will be converted to millilitres through knowledge of the calibration of eudiometer scale readings and headspace measurement.
- Atmospheric pressure taken at the same time as the readings. This pressure is required to convert the volume of hydrogen collected at current pressure to a volume at standard temperature and pressure.
- Temperature of the mercury bath in degrees Celsius.
- Distance from the lid to the bottom of the kettle, in centimeters.
- Distance from the lid to the mercury surface, in centimeters.

The sample charts below show how this data was recorded for each experiment and some sample data.

Table 4-3 Raw Data Collected Prior to Placing Samples in the Eudiometers

Sample ID	I	II	III	IV	V	VI	VII
Weight (g)	53.80	55.37	62.38	66.74	65.67	71.47	65.73
*Thickness (mm)	6.22	6.34	7.20	7.72	7.52	8.04	7.66
Eudiometer Unit	A	B	C	One	Two	Three	Four

*Thickness measurements were only required for the round bar experiments.

Table 4-4 Raw Data Collected During Hydrogen Discharge

Eudiometer Unit	A	B	C	One	Two	Three	Four
Eudiometer Reading	23.6	25.0	19.5	22.8	25.0	40% Head- space	24.9
Temperature (°C)	113.0	111.5	108.3	111.2	113.6	109.4	113.0
Atmospheric Pressure (mmHg)	663.1	Time	Date				

Table 4-5 Raw Data Collected Once Per Experimental Set-up

Eudiometer Unit	A	B	C	One	Two	Three	Four
Depth – Lid to Hg Surface (cm)	10.05	8.10	8.90	8.20	8.15	7.50	8.95
Depth – Lid to Bottom of Kettle (cm)	19.60	19.90	20.00	19.60	19.50	19.85	19.65

4.4.8 Data Treatment and Data Processing

The use of a mercury eudiometer for mobile hydrogen measurements is specified in the welding society standard ANSI/AWS A4.3. A schematic of the eudiometer apparatus is shown in Figure 4-5. Some modifications were made to the standard test regime, as recommended by Senadheera [Senadheera & Shaw, 2009] namely the globe valve with extended mercury column and specimen carrier (Figure 4-6 a) and b)). Hydrogen has very low solubility in mercury, making it a very good eudiometer fluid. Definitive numbers for mercury do not exist, but hydrogen solubility in molten metals is a characteristic strongly related to its valence and thus group in the periodic table. Mercury is a Group 12 (IUPAC) metal, along with zinc and cadmium, and is predicted to have solubility in the range of $10^{-5}\%$ [Jiang & Li, 2011]. Any hydrogen gas released from the sample will bubble up the eudiometer tube and collect in the headspace below the valve and into the tube. The volume of hydrogen collected can be used to calculate the concentration in the sample through the following method. First the volume (ml) must be corrected to standard temperature and pressure (STP).

$$V_{STP} = \frac{273}{(273+T)} \times \frac{(P-H)V}{760}$$

Where T is the temperature ($^{\circ}\text{C}$), P is the atmospheric pressure (mmHg), H is the mercury head in the eudiometer (mm), and V is the measured volume of hydrogen (ml). The concentration Q can then be calculated in parts per million (ppm mass) by using the previously calculated V_{STP} (ml) and the sample weight W (g).

$$Q = 1.11 \times \frac{V_{STP}}{W} \times 100$$

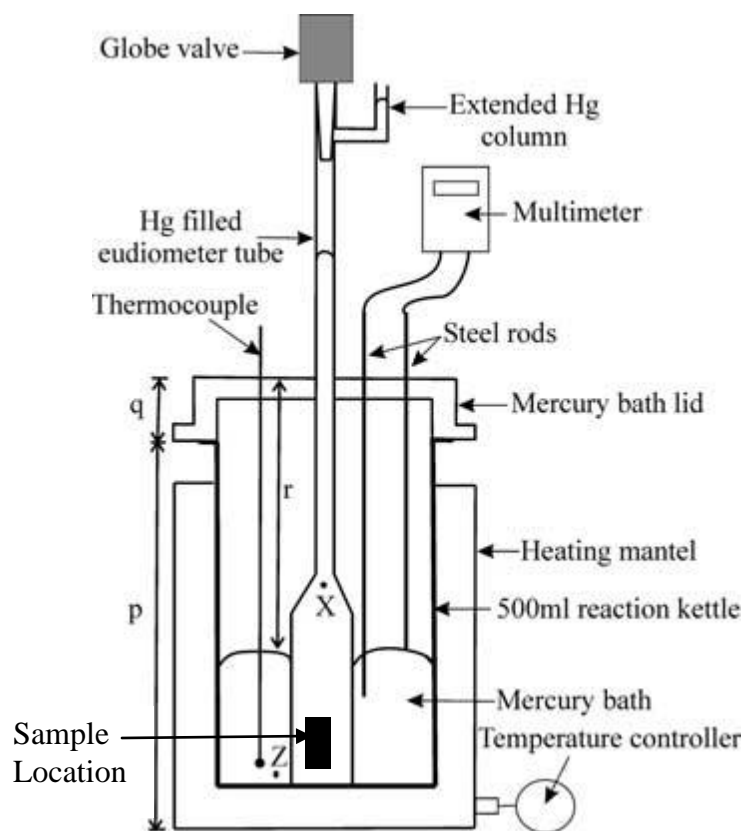


Figure 4-5 Schematic of Eudiometer Apparatus adapted from Senadheera & Shaw, 2009

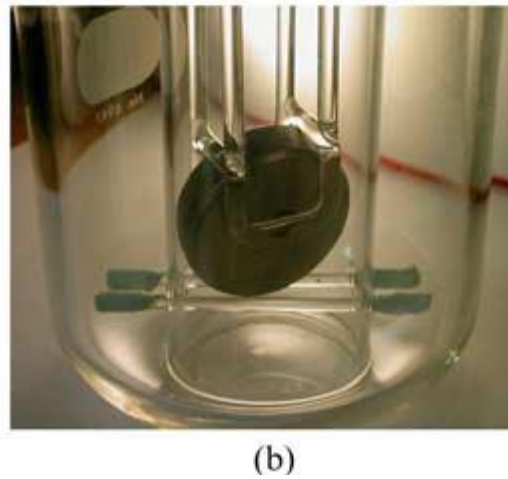
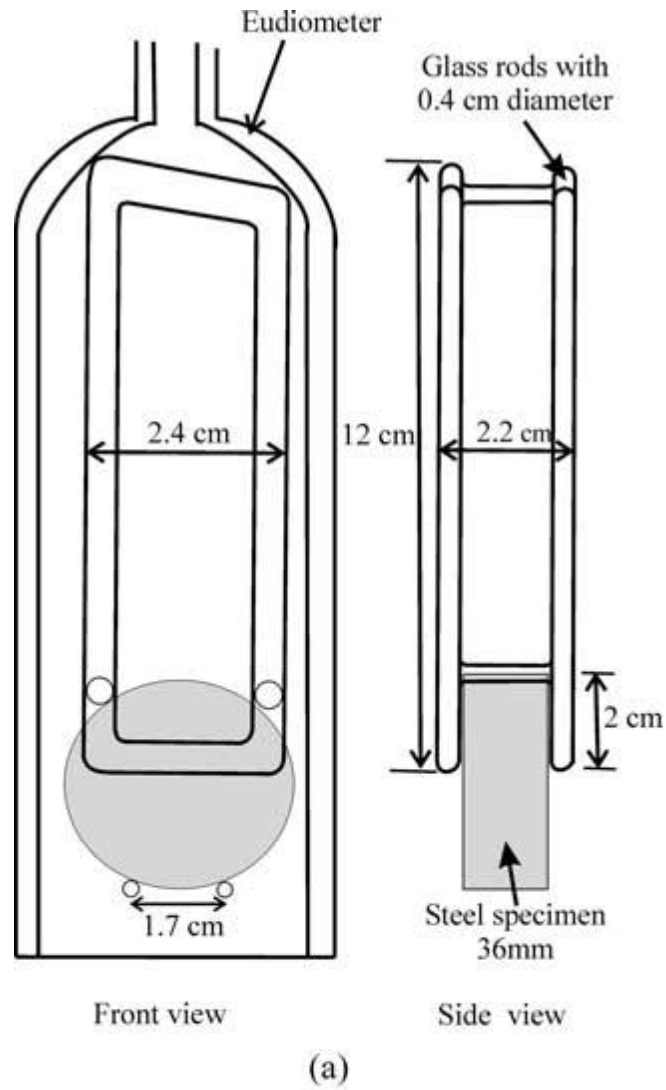


Figure 4-6 Eudiometer and Specimen Carrier from Senadheera, 2009

4.4.9 Safety Protocols and Personal Protective Equipment for Mercury Use

The following personal protective equipment (PPE) was worn at all times when dealing with the mercury eudiometers and related equipment: lab coat, glasses or face shield, respirator with cartridges for mercury chloride vapours, and disposable nitrile gloves. All work with the eudiometer apparatus or any equipment which had contacted mercury was performed inside the fume hood. Every sample or piece of equipment that came into contact with the mercury was stored in the fume hood until disposed of in accordance with University HAZMAT procedures. Spilled mercury or any mercury outside of the eudiometers or waste containers was first collected by using a dedicated brush and dustpan and disposed of in a waste container. Then to ensure no mercury chloride or vapours remained, a MERCONVAP solution was used to clean all surfaces. On several occasions outside consultants on environmental contamination were brought in to ensure the mercury exposure protocols in the lab were effectively reducing mercury exposure. The atmospheric concentrations were always within accepted environmental limits and any surface contamination issues were limited to within the dedicated mercury fume hood and storage cabinets and were dealt with immediately.

4.5 Standard Procedure: Calibration of the Eudiometer Units

Purpose. The goal of this experiment was to define the control volume and volume per graduation values for each eudiometer.

Introduction. The eudiometers must be able to collect the hydrogen released from the experimental specimen, then accurately measure the amount collected. Each eudiometer was custom-made or has been custom-repaired, so no 'as-received' calibration values exist and calibrations were done manually. The eudiometers are essentially upside-down pipettes with a

larger bell-shaped section to hold the specimen. Hydrogen liberated from the sample bubbles up through the mercury and collects at the top of the eudiometer, near the stopcock (as shown in Figure 4-5 and Figure 4-6). A graduated scale (in centimeters, to the tenth) has been fixed on the eudiometer stem. In practice, a measurement could be taken on the graduated scale exactly to the tenth of a centimeter, and estimated to the hundredth. There needed to be two other pieces of information to be able to convert that measurement on the scale to a volume measurement: the volume described by one graduation on the eudiometer stem and the headspace (or control volume) that is above the maximum graduation.

The graduated eudiometer stem is a glass tube with a non-varying cross-sectional area. Calibration of this section could be accomplished numerically by using the tube inner diameter and calculating the volume of a cylinder of length one centimeter, or empirically by placing a known volume of liquid into the eudiometer stem and recording the before-and-after eudiometer readings. The eudiometer stem is connected to a stopcock section with an irregular internal volume. This section is called the headspace or control volume, and is defined as the volume from the stopcock valve to the first graduation. It is not possible to calculate this volume analytically so it must be determined empirically, using a known quantity of liquid and measurement off the graduated scale.

Outcomes. What was to be determined for each eudiometer: The volume contained in one graduation of the eudiometer and the control volume of the eudiometer, from the stopcock valve to the first graduation.

Material. The working fluid placed into the eudiometer is acetone coloured blue with a small amount of food colouring for easier viewing. Acetone was used because it clings very little to the glass stem, ensuring the reading taken is not low due to fluid adhering to the walls of the

eudiometer, and because it readily evaporated after the calibration is completed, leaving no residue.

Method. The calibration was most conveniently carried out with periodic maintenance and cleaning of the eudiometers (Section 4.6). Once the eudiometer was clean and dry, it was mounted upside down (with the stopcock down) on a pipette holder, making sure the eudiometer was held as close to plum as convenient. Approximately 20 ml of acetone was added to a 50 ml beaker with add a drop or two of blue food colouring. Using a 1 ml pipette, 1.0 ml of acetone was placed into the eudiometer. After all the acetone collected at the bottom of the eudiometer, the amount added was noted and then observed to see if the acetone has come up to the level of the first graduation. If it had reached the first graduation, a note was made of the eudiometer reading. If not then another 1.0 ml of acetone was added. This procedure was continued until there were at least three measurements where there were graduation readings before and after adding acetone.

When this was finished the eudiometer was rinsed with acetone a few times to get rid of any trace of the food colouring. Then the eudiometer was emptied of acetone and allowed to dry completely before reassembly.

Measures/Observations/Analysis. At the beginning of the calibration procedure the eudiometer was completely empty. As acetone was added the control volume was filled first and eventually reached the level where the eudiometer stem is graduated. Starting with the final measurements, work backwards to calculate the volume per graduation. Take the volumes before and after adding the last 1.00 ml of acetone and subtract them. This was the number of graduations per 1 ml. Take the inverse of that number to get a value for volume per graduation (in ml per graduation). Do this again for the reading before and after the second last 1.00 ml of acetone,

and for all additions of acetone that have before and after readings. Compare all the volume per graduation values calculated making sure none are significantly different. If the values are consistent calculate the average to use as the volume per graduation for that eudiometer. If the values are inconsistent, perform the calibration again to see if there was a measurement error or if there is an inconsistency in the eudiometer.

The first graduation is labelled as '25'. Take note of the volume of acetone needed to get past the first readable graduation. Using the volume per graduation calculated above, and the number of graduations between the first reading and '25' (or fraction thereof), calculate the volume between the first reading and '25.' Subtract this volume from that needed to get to the first graduation to get the control volume for that eudiometer.

Record the control volume and volume per graduation and repeat the whole operation for each eudiometer. See sample data in Table 4-6 and sample calculations below.

Table 4-6 Raw Data for Calibration of the Eudiometer Unit

<i>Acetone Added</i>	<i>Eudiometer Reading</i>
1.0 ml	23.2
1.0 ml	19.7
1.0 ml	16.1
1.0 ml	12.6

$$\frac{1.0\text{ml}}{16.1-12.6} = 0.285 \frac{\text{ml}}{\text{graduation}}$$

$$1.00\text{ml} - (25.0 - 23.2) \times \frac{0.285\text{ml}}{\text{graduation}} = 0.487\text{ml Control Volume}$$

4.6 Standard Procedure: Cleaning the Eudiometers

The eudiometers should be periodically cleaned for a number of reasons:

- To ensure proper function.
- To perform inspections to determine the state of the equipment.
- To make repairs as necessary
- To validate the calibration values for control volume and volume per graduation

Mercury is a very hazardous substance and full PPE (defined and listed in Section 4.4.9) should be worn and safety considerations should be taken when performing cleaning operations. All equipment, cleaning supplies, gloves, and waste should remain in the fume hood until safely disposed of in accordance with HAZMAT procedures.

The only parts of the apparatus that need to be cleaned are the eudiometer itself, the valve, and less frequently, the kettle. The eudiometer apparatus should be taken apart with special care not to dislodge mercury that has condensed on inner surfaces. Gently tapping parts with condensed mercury present, such as the glass eudiometers, PTFE lid and port covers, before removing them will often cause the mercury to fall back into the reservoir in the kettle. Open the stopcock and let the mercury flow back into the kettle. Once it is drained, place it on a smaller containment tray. Keep a reservoir of dilute nitric acid for cleaning purposes. Pipette a few millilitres of nitric acid into the eudiometer with the stopcock closed and swirl it around to clean the glass surfaces then drain the acid back into the reservoir. Remove the stopcock and, using the nitric acid, pipe-cleaners, and cotton-tipped cleaning sticks proceed to clean the eudiometer. After cleaning, allow all components to dry completely before reassembly. Often this was a good time to calibrate the eudiometers, according to the procedure in Section 4.5.

4.7 Cleaning the Mercury

Occasionally the mercury became contaminated with trace metals dissolved from the steel, products of mercury's corrosion reaction with air, or other reactions with other atmospheric constituents. Because mercury is so dense, most contaminants will collect on the surface or adhere to the containment vessel. Mercury can be distilled and brought back to a high level of purity, but there are very few facilities remaining to perform this operation. A less effective, but simpler method involves decanting the mercury from one vessel to another in such a way to leave behind all the contaminants that float on the surface or adhere to the vessel. To do this, a 50 ml syringe was lowered into the mercury and filled, taking care not to draw up any of the surface mercury or contaminants. The syringe was then emptied into a clean container. This was repeated many times until very little mercury was left in the original container. Then the vessel was cleaned with dilute nitric acid and the clean mercury returned.

4.8 Validation: Determination of Appropriate Time to take Final Hydrogen Measurements

Purpose. The goal of this experiment was to establish a standardized time for collection of hydrogen in the eudiometers before a final reading is taken.

Introduction. Hydrogen begins to egress from a sample as soon as it is taken out of the charging conditions. The amount of hydrogen collected has been seen to asymptotically increase with time in the eudiometers. Given an unlimited amount of time, an absolute measure of the mobile hydrogen in the sample can be obtained. Practically, an experimental measure must be made in a reasonable amount of time. An acceptable balance can be struck with an asymptotically increasing system by choosing a time at which the rate of change is small enough

to ignore any further increase. This measurement time will then be considered standard and will be applied to all further measurements.

Outcomes. What was to be determined: the appropriate amount of time to collect hydrogen from a sample and hence the time required in the eudiometers before the final reading can be taken.

Material. The experimental material (low carbon steel round bar) was cut into a cylinder approximately 100 mm (4 inches) long. The cylindrical specimen had one end polished to 400 grit and the remaining surface covered with three coats of red lacquer. The mercury eudiometers were used according to the welding standard, with several modifications as specified above in Section 4.4.8.

Method. The sample was placed in an oven at 110°C for 72 hours to bake out any mobile hydrogen already present in the steel. After the baking out procedure the samples were charged for 72 hours in the standard charging apparatus and solution (5% NaCl, 1.1 pH, deaerated with nitrogen). After the charging period, the sample was cut into four discs in accordance with the standard procedure for round bar experiments, cleaned with acetone, weighed, and placed in separate eudiometers. Once the eudiometers were set up and the heating mantles turned on, measurements of hydrogen collected were taken at 0, 1.5, 4, 8, 11, 22.5, 49, 72, and 95.5 hours. In addition to recording the hydrogen collection amounts with time, the temperatures were varied on the four eudiometers to gain insight into the effect of mercury temperature on hydrogen collection. Units 1 and 3 were brought directly up to operating temperature of 110°C over four hours. Unit 4 was left at 20°C until after the 4 hours measurement was taken and then brought up to 110°C over the next 4 hours. Unit 2 was initially brought up to approximately 90°C until after the 11 hours measurement then slowly brought up to 110°C over the next 11 hours.

The above procedure was applied to the disc-shaped specimen, which was common to all procedures in this chapter. The general procedure was also used to verify the time required to measure the hydrogen in the tensile test specimen used in the following chapters. The difference in that procedure is that only three tensile specimen were used and they were all brought to 110°C directly, and were charged with hydrogen using the appropriate protocol for tensile specimens given in Section 7.1 (of the tensile methods chapter). The times to take these measurements varied from 18 to 114 hours.

Measures/Observations/Analysis. Since the actual concentrations were not important for this experiment, eudiometer readings were compared without conversion to sample concentrations. It is misleading to think of concentrations when looking at the evolution of hydrogen over time. The eudiometer readings were plotted against the time passed since turning the heating mantles on. The standardized time to take final hydrogen readings was based on the time required to ensure all testing conditions reach a volume that is 99% of the long-term asymptotic value. This study was useful to visualize how fast the majority of hydrogen evolves from the sample, and lend support the choice of a time well outside the initial discharge.

4.9 Validation: Baseline Hydrogen Concentration Present After Bake-Out

Purpose. The goal of this experiment was to establish the minimum baseline hydrogen concentration that was found using the general experimental procedure. This baseline was important when using the solution to Fick's Law generalized to uniaxial diffusion.

Introduction. Hydrogen can reside in different types of locations (called traps) in steel such as in dislocations, voids, internal cracks, in the crystal lattice in interstitial holes, or inclusions [Iyer, 1990]. These traps have different escape energies for hydrogen to exit. If more energy is

required to leave a trap than is available, the hydrogen is considered fixed. If the activation energy of the trap is low enough that hydrogen is only temporarily held there before moving on, the hydrogen is considered mobile. The bake-out procedure is designed to remove all or as much as possible of the mobile hydrogen in the sample prior to beginning charging.

One of the parameters necessary to solve for concentration based on our solution to Fick's Laws is the initial or bulk hydrogen concentration. The bake-out procedure is not 100% effective in removing all the hydrogen prior to testing. There could be many reasons for this, including the dramatically different metal-solution interfaces (metallic solution versus aqueous). The after-bake-out concentrations were important because:

- It was important to know the minimum level to expect when performing experiments.
- It was useful in application of our solution to Fick's Law.
- It was able to confirm volumes in our samples that hydrogen has not yet diffused into.
- It was a check on our experimental procedure.

Outcomes. What was to be determined: The baseline concentration of hydrogen, as determined by mercury eudiometry, which could be read from a disc sample after the bake-out procedure.

This may or may not coincide with the bulk (C_s or C_b) hydrogen concentration as seen from other materials or experimental techniques.

Material. The experimental material (low carbon ferritic/pearlitic steel) was sectioned on a horizontal band saw to provide three discs approximately 38 mm (1.5 inches) in diameter and 13 mm (0.5 inches) thick. The mercury eudiometers were used according to the welding standard, with several modifications mentioned previously.

Method. The samples were placed in an oven at 110°C for 72 hours to bake out any mobile hydrogen already present in the steel. Each sample was weighed and dimensions measured.

After the baking-out procedure each sample was placed into a separate individual eudiometer. Each eudiometer was brought up to 110°C and the amount of hydrogen collected in the trap recorded. The final hydrogen amount was recorded after 72 hours in the eudiometer.

Measures/Observations/Analysis. Using mercury eudiometry with the associated weight, atmospheric pressure, and temperature, the concentration of hydrogen in each specimen was calculated. The concentration from each sample was compared to calculate a mean and standard deviation.

4.10 Validation: Vicker's Hardness of Round Bar

Purpose. The goal of this experiment was to determine if there was any anisotropy in the round bar samples used for the hydrogen concentration profile experiment.

Introduction. Depending on how the sample was made, there may have been some changes in the material depending on location. Often thick samples cool faster around the edges and more slowly in the middle, leading to some segregation of alloying elements and impurities, and changes in microstructure. Differences in microstructure can often be detected as differences in hardness and hardness testing is often used in quality control in steel case-hardening. Vickers Hardness, which is related to the strength of a material, was used as an indicator of changes in microstructure. For the purposes of the round bar diffusion experiments a uniform material microstructure was desirable.

Outcomes. What was to be determined: is there a difference in Vickers Hardness in our sample material between the edge, centre, and the midpoint between them?

Material. The source material used is a round bar of 38 mm (1.5 inch) diameter low carbon ferritic/pearlitic steel. This is the same material used in all other round bar hydrogen diffusion experiments.

Method. A radial section was cut from the parent material such that the sample contained unaltered material from the edge and centre of the original bar (see Figure 4-7). This section was mounted in Bakelite and polished to $0.05\ \mu\text{m}$ as per the mounting and polishing procedure in Section 4.3. The Vickers Hardness test is fully described in the standard ASTM E-384. The standard Vickers pyramidal diamond indenter was used along with a 200 gram load applied for 10 seconds. Three representative locations were used to represent the edge, mid-point, and centre of the sample, respectively. Six or seven repetitions at each location were done, making sure to locate each successive test at least three indentation diameters away from all previous tests to avoid any interference from work-hardened material.

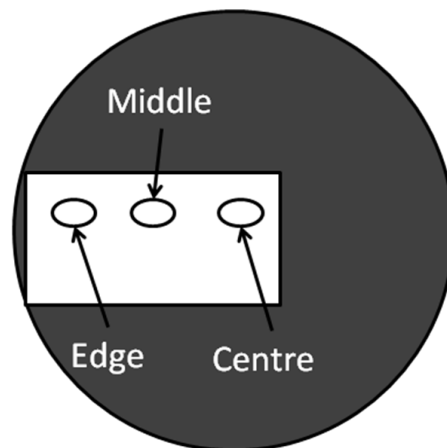


Figure 4-7 Sampling Locations for Vickers Hardness Tests

4.11 Validation: Electropotential Scans

The material used was the experimental steel (low carbon ferritic/pearlitic) and was Kold-mounted for use in a potential scan. The mounted sample was ground to 400 grit before

measurement. The solution used was the same as for all hydrogen charging, a 1.1 pH, 5% NaCl, deaerated. A Princeton PAR 263A potentiostat was used. The reference electrode was a saturated calomel electrode (SCE), the working electrode was the experimental steel sample, and the auxiliary electrode was a platinum sheet (see Figure 4-8 for apparatus configuration). A Luggins probe and a salt bridge were used. The area of the working electrode was 1.232 cm². The apparatus was assembled, and the solution purged with nitrogen gas for 30 minutes. The scan began when the observed potential between the working and reference electrodes were stable (20 minutes at 0.534 V SCE).

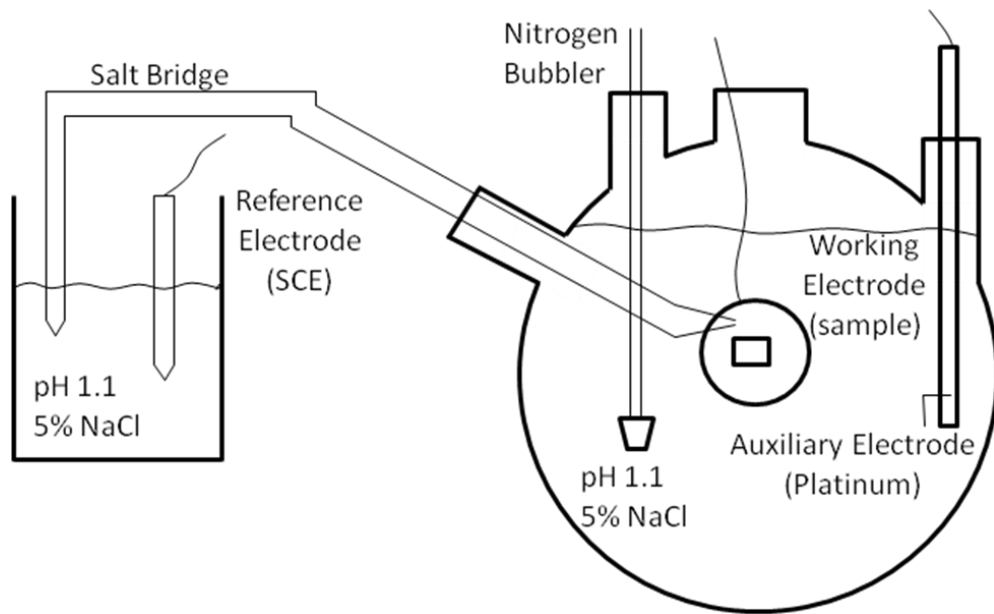


Figure 4-8 Experimental Set-up for Electropotential Scans

4.12 Effect of Charging Solution and Time on Apparent Surface Concentration

Purpose. The goal of this experiment was to determine the effect of changing the charging conditions (solution/surface chemistry) on the apparent hydrogen surface concentration.

Introduction. The amount of hydrogen entering a material depends on the aggressiveness of the charging condition. There are several ways to increase the intensity of charging including:

increasing the potential during electrochemical charging, increasing the acidity of the charging solution, or including poisoning substances (including sulfur to retard recombination of adhered hydrogen) [Seshadri et al, 1997]. Increasing the rate at which hydrogen enters the material should lead to an increase in the apparent surface concentration that can be estimated using the techniques previously described and the solution to Fick's Law. The apparent diffusion coefficient has been previously shown to vary depending on the charging conditions [Griffiths & Turnbull, 1995], so a change may be evident when the charging solution's intensity is varied. Hydrogen Sulfide (H₂S) presents a problem in the petrochemical industry as it is both a source of hydrogen and of sulfur, promoting hydrogen entry into pipeline steel. If oxygen is present in solution, the oxygen reduction reaction will compete with the hydrogen evolution reaction for the cathodic reaction, possibly reducing the amount of hydrogen available for entry in to the steel. The solution of Fick's Law in one dimension requires four parameters to implement: Surface Concentration, Bulk Concentration, Diffusion Coefficient, and Time. The main experiment kept time constant to examine the other three parameters but can also be varied.

Outcomes. What was to be determined: the change in the charging and diffusion characteristics of the system, as measured by the apparent surface concentration and diffusion coefficient.

Materials. The material used for this study is the same 38 mm (1.5 inch) x 100 mm (4 inches) round bar with the same configuration and pre-treatment as the previous diffusion experiments.

Method. The procedure for this experiment was the same as for the main experiment. That is: Bake-out, coating the entire specimen except one end, grinding the exposed surface to 400 grit, exposure to charging solution, and finally sectioning and mercury eudiometry. The difference in these experiments was in the charging solution and the charging time. For trial one, the same solution was used for charging with two exceptions: The nitrogen deaeration gas was replaced

with H₂S and the charging time reduced to 24 hours. For trial two, the solution was not deaerated at all and the charging time was 24 hours. For trial three, the standard solution was used but the sample was left for nine days to charge (216 hours). After charging all samples were sectioned and hydrogen collected through eudiometry according to the standard procedure.

Chapter Five: Results of Round Bar Hydrogen Diffusion Experiments

This chapter presents the results of experimentation related to the uniaxial diffusion of hydrogen in a sample of low carbon steel prepared from a round bar, following the procedures outlined in Chapter Four. This chapter covers an examination of the material as-received, validation experiments for the general techniques used, results of the main experiment, and results found for changing the solution chemistry.

5.1 Microstructure

Photomicrographs of the material's microstructure can be seen in Figure 5-1. Photos A) and C) represent the radial section (or longitudinal direction) of the round bar stock and photos B) and D) represent the transverse direction with corresponding scales as indicated. Photos C) and D) were taken with plane polarized light to enhance contrast. The ferritic/pearlitic microstructure is clearly evident. Significant banding is apparent in the longitudinal direction. Grain size was estimated using ASTM Standard E112 and the Hilliard Single Circle intercept procedure. The grain size was found to be $G_{ASTM} = 9.0$ for an average grain diameter of $15.9 \mu\text{m}$. With micrographs of the microstructure, ImageJ image processing software was used to calculate the area fractions of the pearlite and ferrite grains. The image was manipulated based on brightness to isolate the brighter ferrite grains from the darker pearlite grains then an area-fraction calculation was performed on the modified image. The percentage pearlite was found to be 14.2% leading to an estimated carbon weight percentage of 0.126%. Overall the microstructure is as expected from a sample of low carbon hot rolled steel.

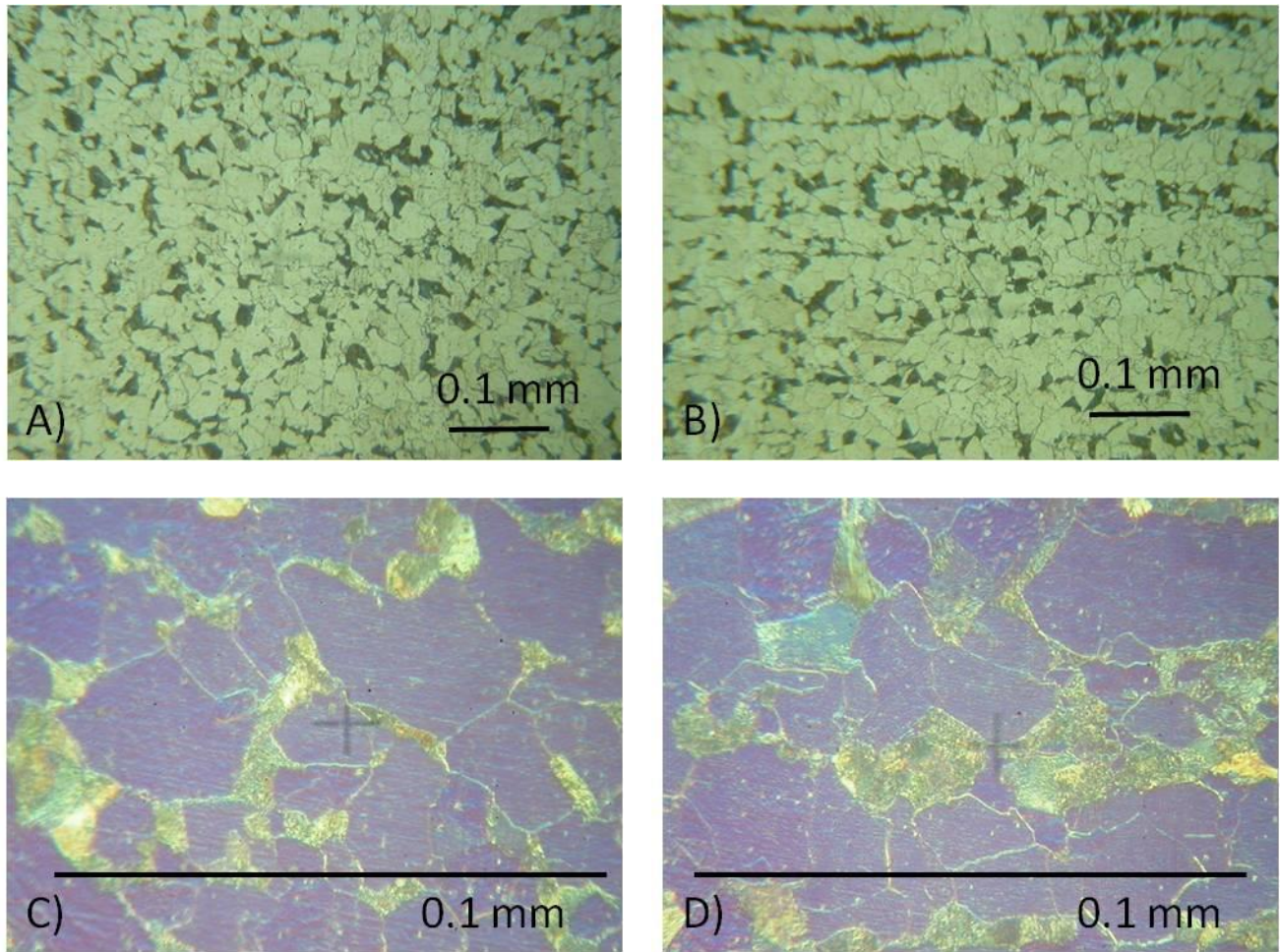


Figure 5-1 Photomicrographs of Experimental Steel in Radial (A, C) and Transverse (B, D) Directions

5.2 Determination of Appropriate Time to take Final Hydrogen Measurements

Round Bar Disc specimen: All these results show that with 72 hours in a mercury eudiometer at 110 °C the specimen have released at least 99% of the final, asymptotic hydrogen collected value. Things to note: All units started at room temperature and all units measured different final amounts (the total amount is not critical to this test). Units 1&3 were brought directly up to operating temperature of 110°C. Unit 4 was left at 20°C until after the 4 hours measurement was taken and then brought up to 110°C over the next 4 hours. Unit 2 was initially brought up to

approximately 90°C until after the 11 hours measurement then slowly brought up to 110°C over the next 11 hours.

Table 5-1 Time Required to Reach 90, 95, and 99% of Steady State Hydrogen Volume

	<i>Condition</i>	<i>Steady State Value (mL)</i>	<i>Time to Reach Percentage of Steady State Value (hours)</i>		
			90%	95%	99%
Unit 1	Direct Rise to 110°C	0.54	20	50	72
Unit 2	Slow Rise between 90-110°C	0.45	52	60	70
Unit 3	Direct Rise to 110°C	0.45	8	20	40
Unit 4	Cool Start then Ramp Up	0.10	7	8	10

Table 5-1 shows no matter what temperature regime was applied as the discharge condition, all samples reached at least 99% of the maximum hydrogen that could be liberated within 72 hours. In Figure 5-2 and Figure 5-3 the sample in Unit 2 shows an amount of hydrogen collected at 90°C that plateaus at 1.8 mL, then rises again and plateaus at 0.45 mL after the temperature is raised to 110°C due to hydrogen trapping effects, discussed in Section 6.3. This result is also seen in Figure 5-4 on the Unit 4 data, where the amount of hydrogen collected at 20°C quickly plateaus at 0.02 mL and then rises to another plateau at 0.10 mL after the temperature was raised to 110°C. Units 1 and 3 were brought directly to operating temperature at 110°C. This data was not corrected for standard temperature and pressure and is used only to qualitatively observe the effects of eudiometer temperature and time of taking readings.

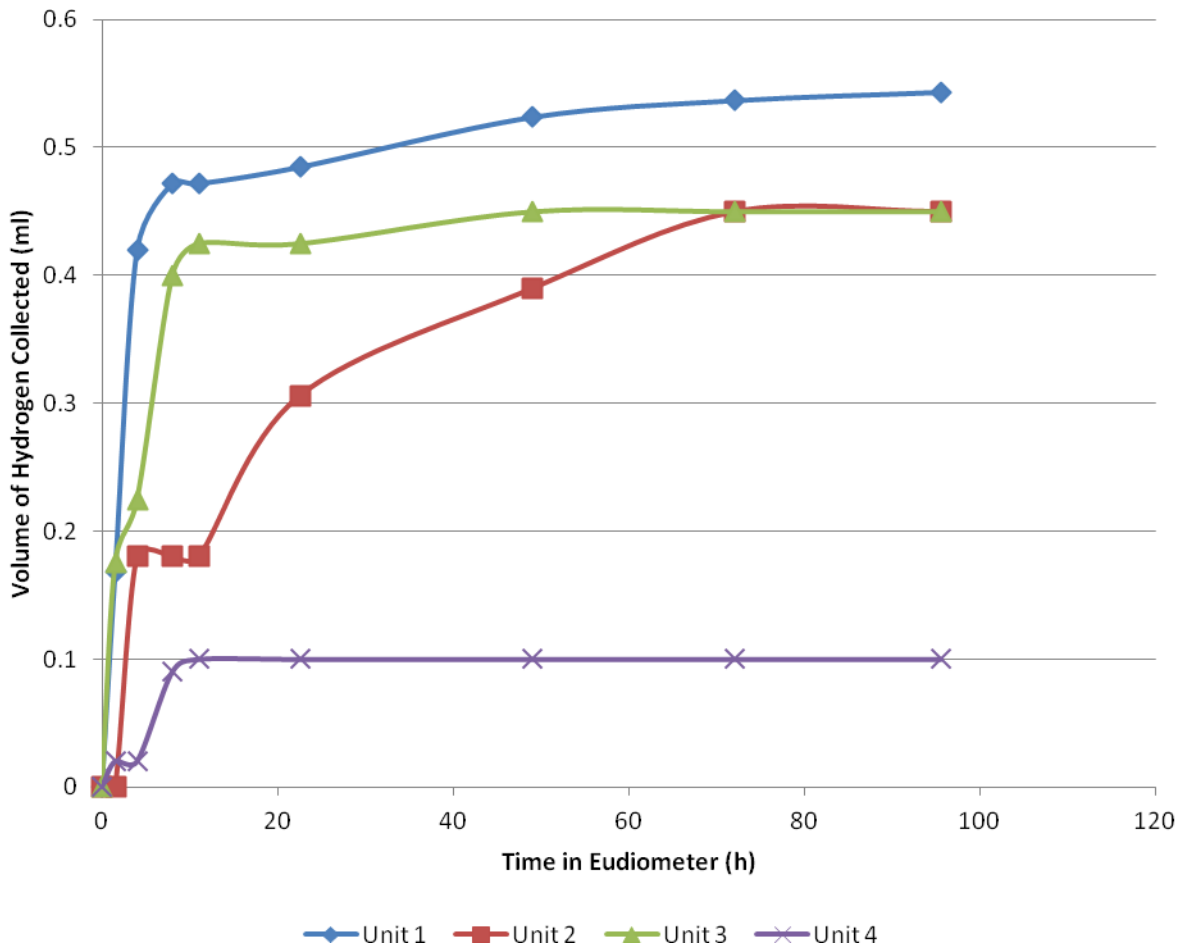


Figure 5-2 Hydrogen Release with Time in Eudiometer for Round Bar Disc Specimen

To determine the amount of hydrogen potentially released during the 60 minute period between removal of the sample from the charging solution to placement in the eudiometer, an interpolation from the time-release graph above can be used. For Unit 1 the interpolated value of hydrogen released at 1.0 hours is 1.1 ml, which would lead to a loss of 20% from the final total asymptotic value. This value seems quite large but only represents an upper bound. The actual amount would be much less, given that 1) the sample is not exposed to elevated temperatures until placed into the eudiometer and heating mantle turned on (diffusion is strongly related to temperature), and 2) it also takes four hours for the eudiometer to come to 110°C once started.

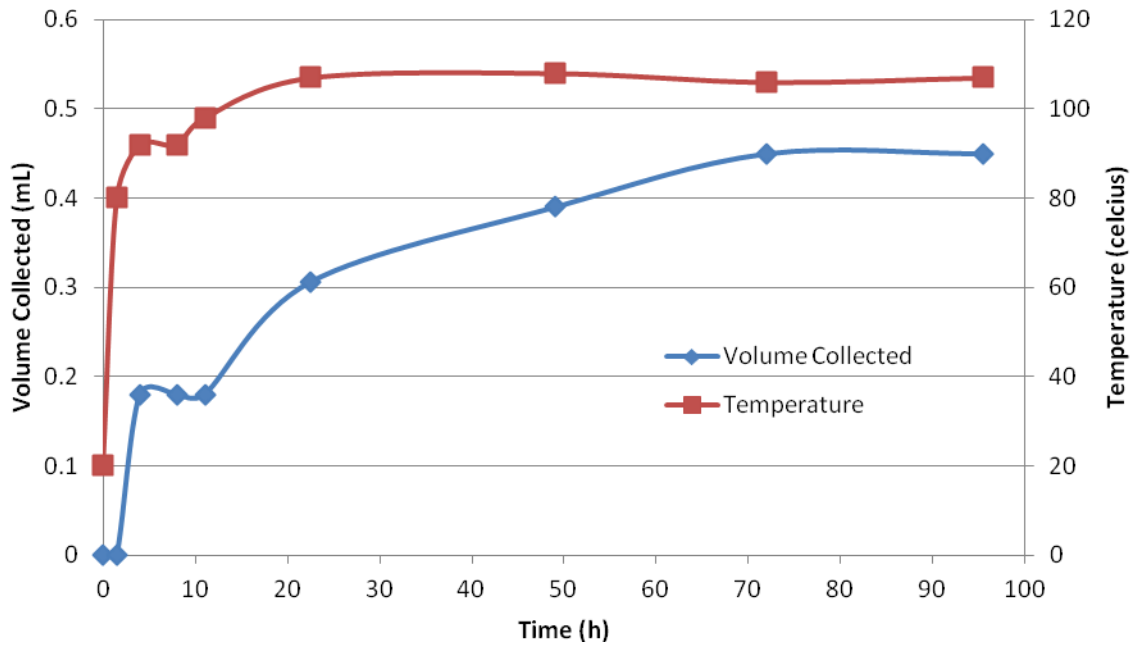


Figure 5-3 Hydrogen Collection and Mercury Temperature Profile for Unit 2

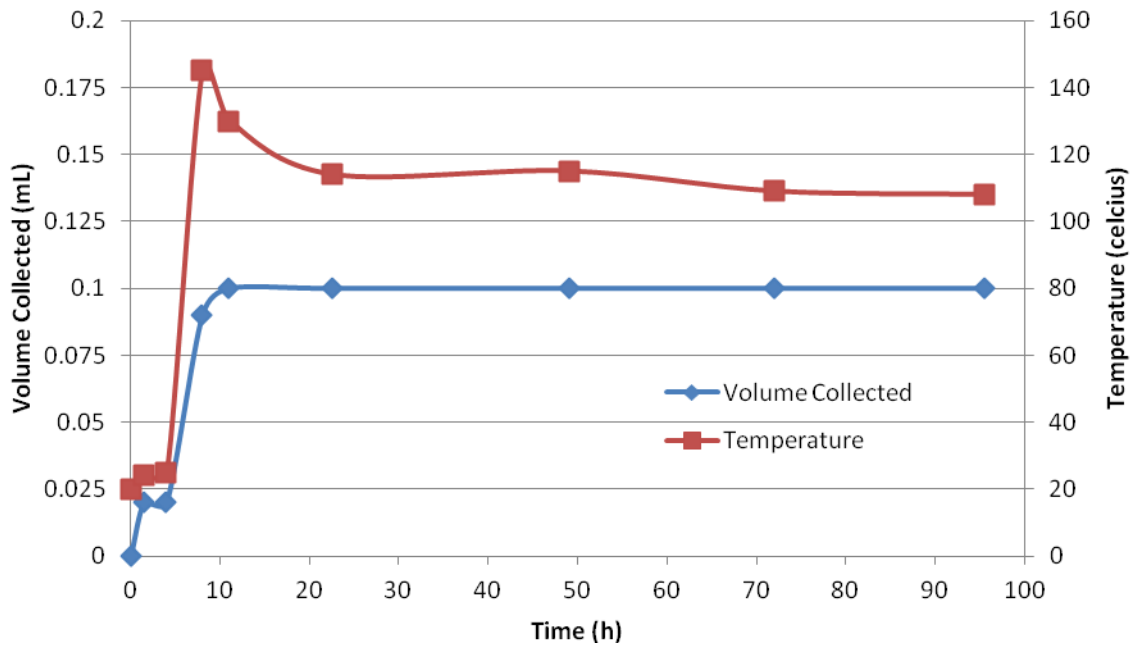


Figure 5-4 Hydrogen Collection and Mercury Temperature Profile for Unit 4

Tensile Test Specimen. The data presented in Figure 5-5 show that for all samples tested, the volume of hydrogen collected had reached its full amount within 20-30 hours, regardless of the total amount contained in the sample. Once the amount collected remained reached its maximum the reading remained stable throughout the testing period, up to at least 120 hours.

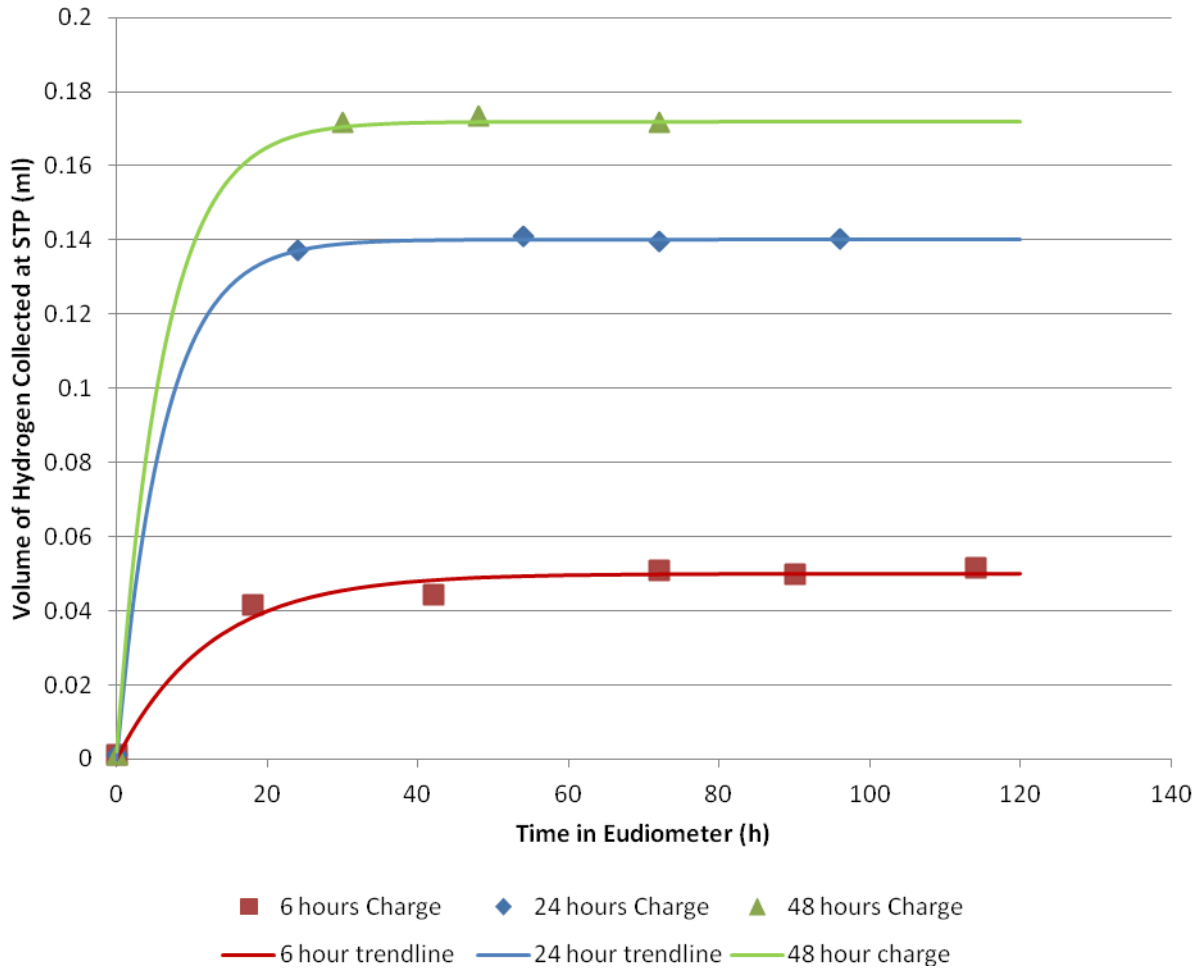


Figure 5-5 Hydrogen Evolution with Time for the Small Tensile Samples

5.3 Baseline Hydrogen Concentration Present after Bake-Out

The standard bake-out procedure of 110°C in the oven for 72 hours followed by mercury eudiometry to extract and collect any mobile hydrogen remaining in the sample produced a mean

hydrogen concentration on 0.087 ppm with a standard deviation of 0.049 ppm. These results are shown in Table 5-2 and plotted in Figure 5-6. These baseline values agree very well with the main experiment results (Section 5.7) which show a bulk concentration in an uncharged area of the steel specimen of 0.083 ppm with a standard deviation of 0.013 ppm. Eudiometry was also performed on three samples representing the as-received condition, showing an as-received hydrogen concentration of 0.099 ppm.

Table 5-2 Hydrogen Concentrations Measured After Bake-Out at 110 Celcius for 72 Hours

<i>Baseline Values</i>	<i>(ppm)</i>
Sample 1	0.109
Sample 2	0.122
Sample 3	0.032
Average	0.087
Standard Deviation	0.049

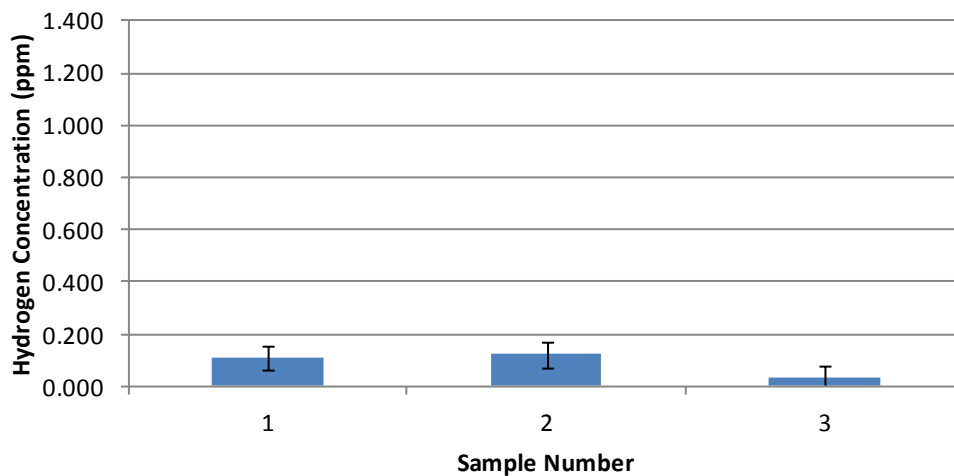


Figure 5-6 Hydrogen Concentrations after 72 h Bake-Out

5.4 Vicker's Hardness of Round Bar

Using the measurement locations specified in Figure 5-7 below, there are no significant differences in the hardness at different locations in the specimen material (see Table 5-3 and Figure 5-8). The statistical p-values (shown in Table 5-4) represent the results of testing the hypothesis that the data obtained at different locations represent different materials. All are well above the $p < 0.05$ threshold. In terms of the hardness, the material is considered uniform at all locations.

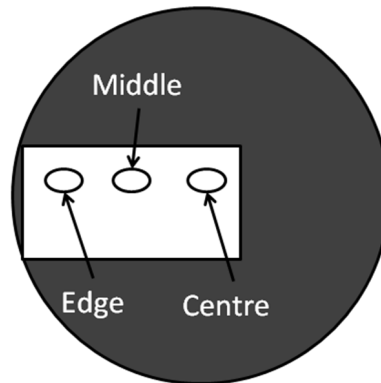


Figure 5-7 Sampling Locations on Round Bar for Vicker's Hardness Tests

Table 5-3 Results of Vicker's Hardness Tests for Round Bar

<i>Position</i>	<i>Edge</i>	<i>Middle</i>	<i>Centre</i>
Results	158	148	151
Vicker's Hardness Number (VHN)	158	148	148
	158	148	161
	164	154	148
	158	154	154
	145	158	158
		158	148
Mean Value	156.83	152.57	152.57
Standard Deviation	6.27	4.58	5.29

Table 5-4 Statistical p-Values Comparing the Different Sampling Locations

	<i>Edge/Middle</i>	<i>Edge/Centre</i>	<i>Middle/Centre</i>
p value	0.185	0.210	1.000

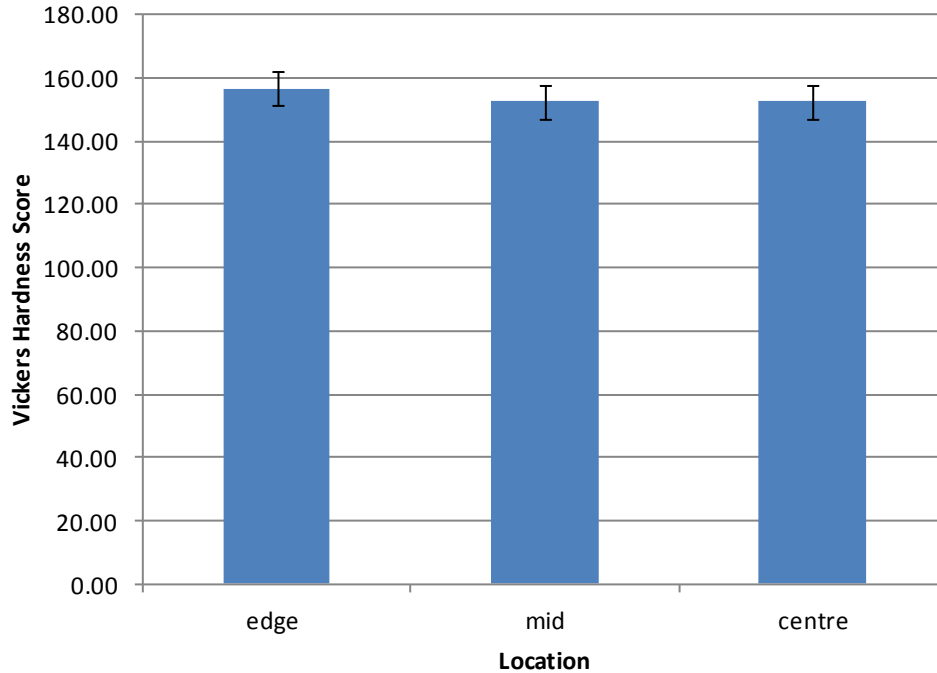


Figure 5-8 Results of Vicker's Hardness Testing at Different Sampling Locations

5.5 Electropotential Scans

The results of the potential scan of the experimental steel sample in 1.1 pH 5% NaCl deaerated with Nitrogen gas are presented below in Figure 5-9 and Figure 5-10. Notice E_{corr} at approximately -0.52 V SCE, and Tafel slopes of $\beta_a = 0.097$ mV/decade and $\beta_c = 0.117$ mV/decade near E_{corr} with a region above -0.41 V SCE that indicates a transition from Fe^{2+} to Fe^{3+} as the stable anodic corrosion product. This curve is as expected from a strongly acidic, deaerated solution. The corrosion current density at E_{corr} is calculated [Jones, 1996 pg 148] from the Tafel slopes and polarization resistance ($R_p = 555.6$ Vcm²/A) and is found to be $i_{corr} = 41.5$ μ A/cm².

$$i_{corr} = \frac{\beta_a \beta_c}{2.3(\beta_a + \beta_c)R_p}$$

$$R_p = \left(\frac{\partial E}{\partial i} \right)_{E_{corr}}$$

Where β_a and β_c are the Tafel slopes just above and below E_{corr} , respectively (Figure 5-9), and R_p is the polarization resistance calculated from the slope of the linear polarization resistance plot (Figure 5-10).

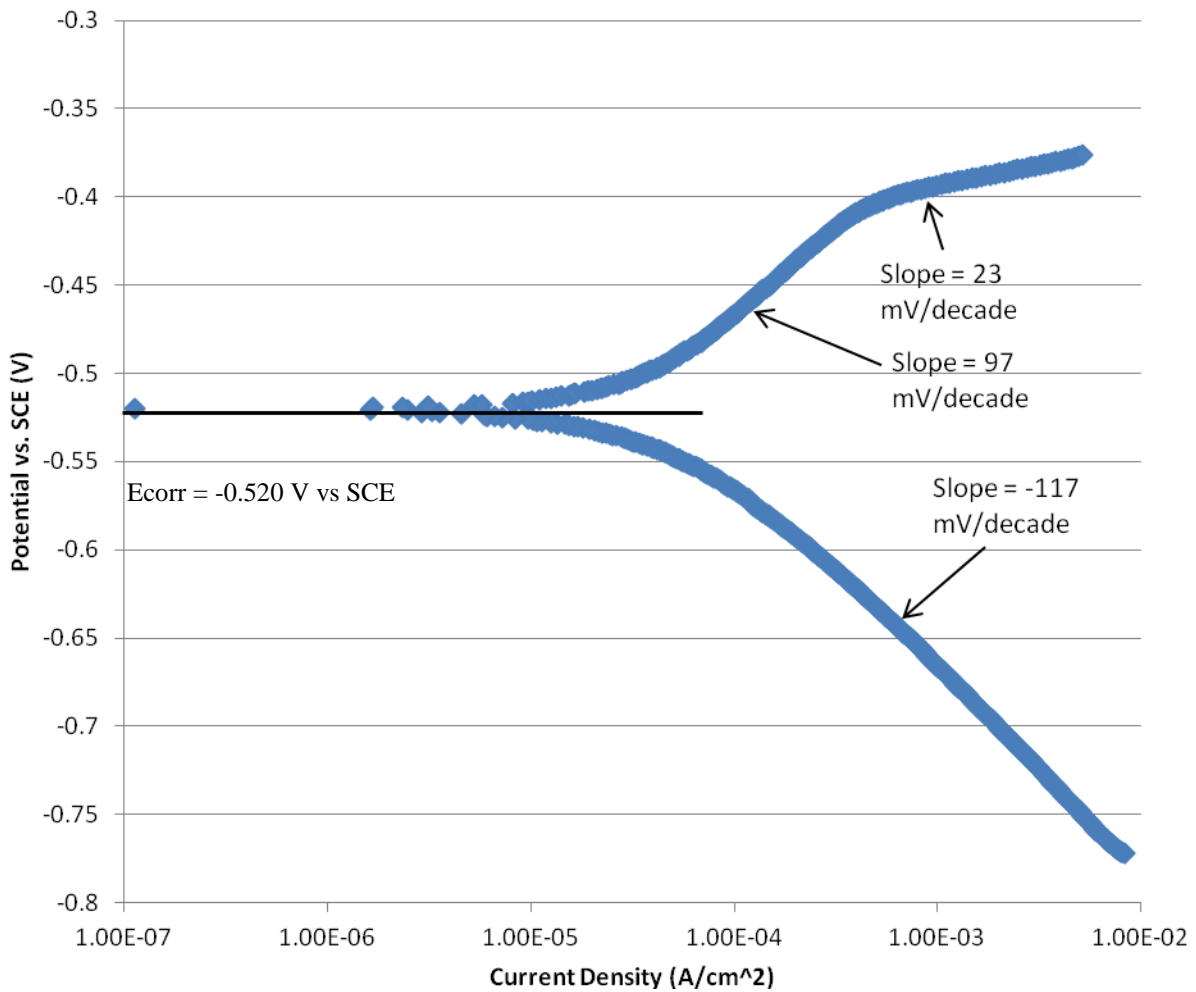


Figure 5-9 Potentiodynamic Scan of Experimental Material in Deaerated Acid Solution

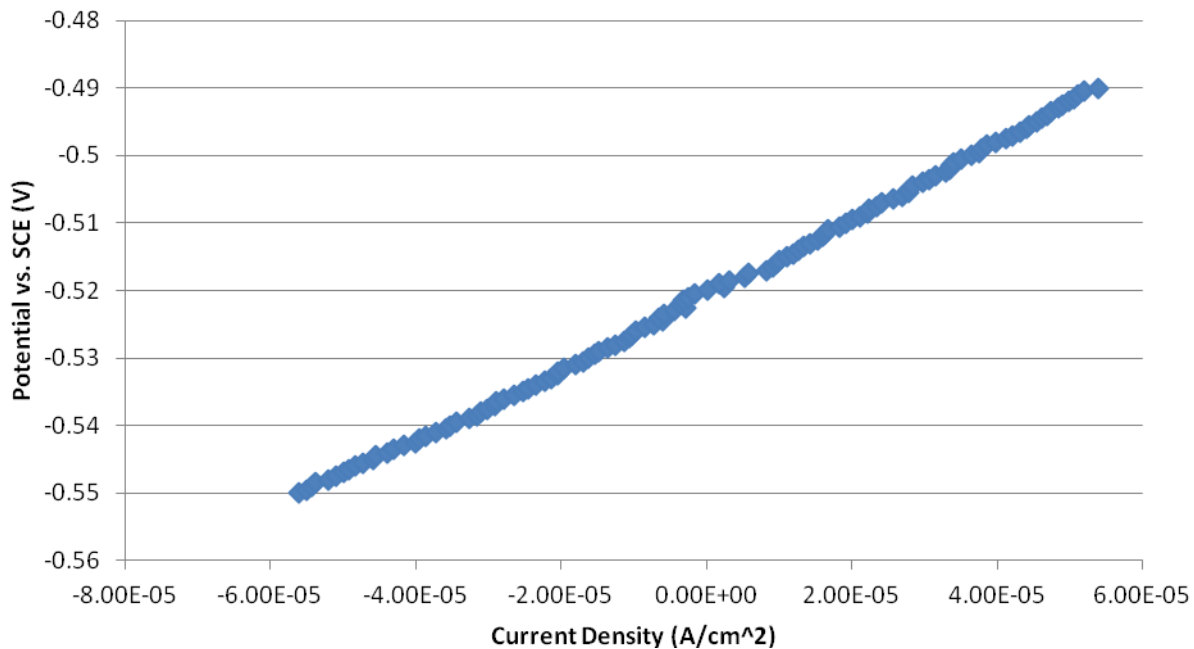


Figure 5-10 Linear Polarization Region of Potentiodynamic Scan within ± 30 mV of E_{corr}

5.6 Scanning Electron Microscope – X-Ray Energy Dispersion Spectroscopy

This technique was unable to determine any of the constituents of the adherent film on the liquid mercury and glassware aside from mercury

5.7 Main Experiment: Round Bar Test of Uniaxial Hydrogen Concentration Gradient

Each data point on the concentration versus position figures represents the calculated hydrogen concentration of each disc slice plotted against the location of the centroid of that slice with respect to the charging surface. Experimental data was plotted on the same graph as the solution to Fick's Second Diffusion Law. The three parameters that define the final shape of the solution were manipulated to determine the best-fit solution. The three parameters that define the shape of the curve are Diffusion Coefficient (D), Surface Concentration at the charging face (C_s), and Bulk Concentration (C_b).

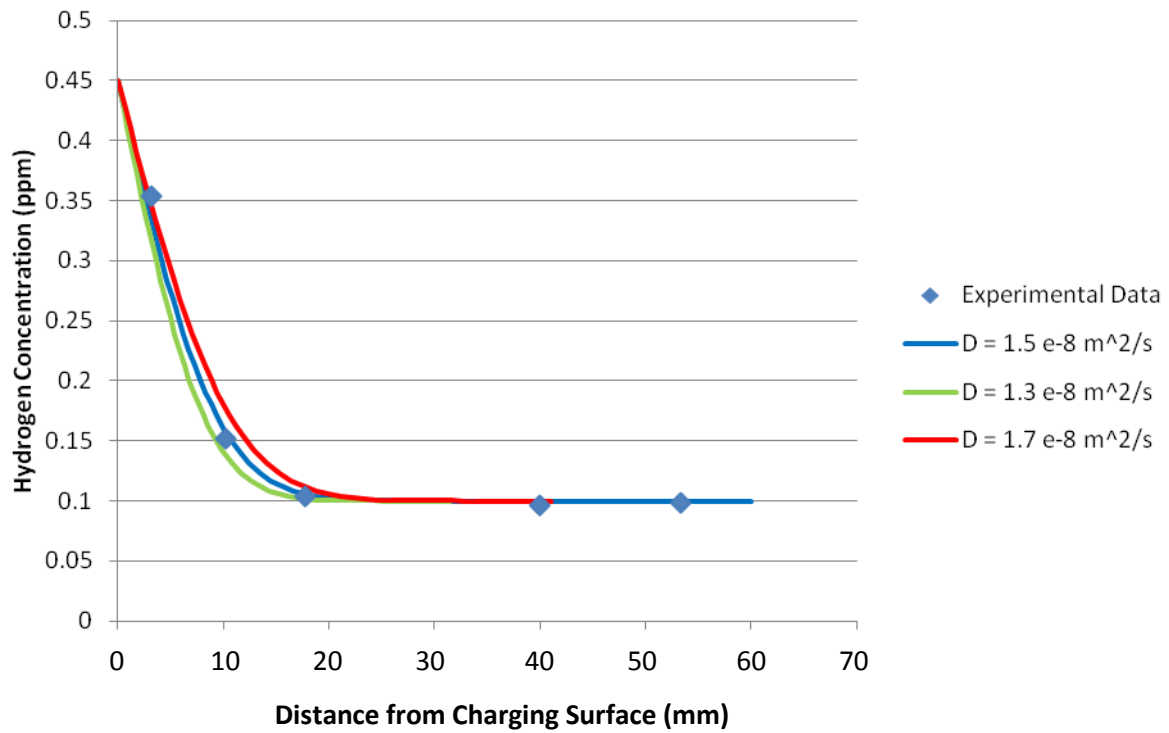


Figure 5-12 Effects of Small Variation in Diffusion Coefficient to Best Fit Procedure

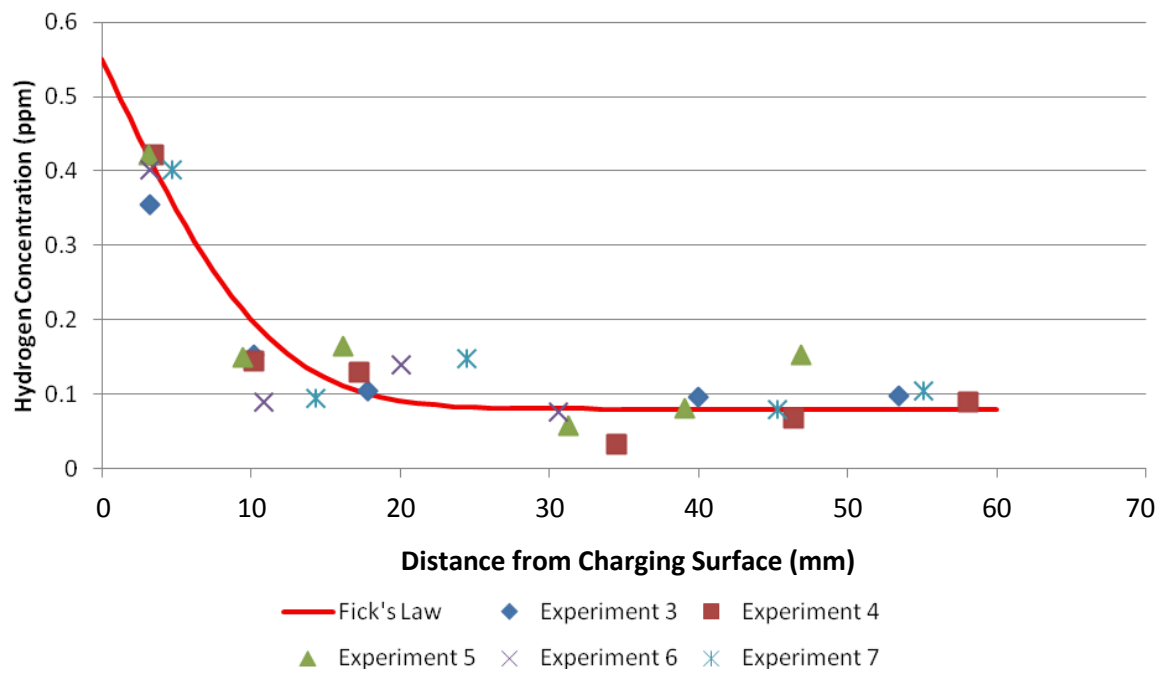


Figure 5-13 Comparison Plot of all Experimental Data

Table 5-5 Results for all Round Bar Hydrogen Diffusion Experiments

	<i>Diffusion Coefficient</i> (m ² /s)	<i>Surface Concentration</i> (ppm)	<i>Bulk Concentration</i> (ppm)
Experiment 3	1.5x10 ⁻⁸	0.45	0.10
Experiment 4	1.8x10 ⁻⁸	0.55	0.08
Experiment 5	1.8x10 ⁻⁸	0.55	0.08
Experiment 6	1.4x10 ⁻⁸	0.55	0.07
Average Value	1.63x10 ⁻⁸	0.525	0.083
Standard Deviation	0.21x10 ⁻⁸	0.050	0.013

Charging Surface Effect. The shape of the curve, and the value of the apparent diffusion coefficient, is highly dependent on the hydrogen concentration determined for the first data point (closest to the charging face). Two considerations make this data point different than the others: At this location the concentration is approximately five times greater than the bulk concentration, and it is the only location in the sample that has a surface in contact with the hydrogen-charging solution. There was a possibility that a part of the higher concentration seen was due to some hydrogen that remains adhered to the surface or on a surface film. To examine this possibility the first data point (representing the concentration seen in the material nearest the charging surface) for each trial was plotted against the weight of that sample in Figure 5-14. The surface area in contact with solution was the same for all samples, but each slice was a different width, leading to different weights. If the concentration seen was due to hydrogen held on the surface rather than spread through the material, then there should be a trend to lower apparent concentration with greater disc weight. As can be seen in the figure, no reasonable trend line can describe the data and there was no discernible relationship. This analysis was performed *post*

hoc on a small set of previously collected data but indicates that there is no hydrogen surface retention effect.

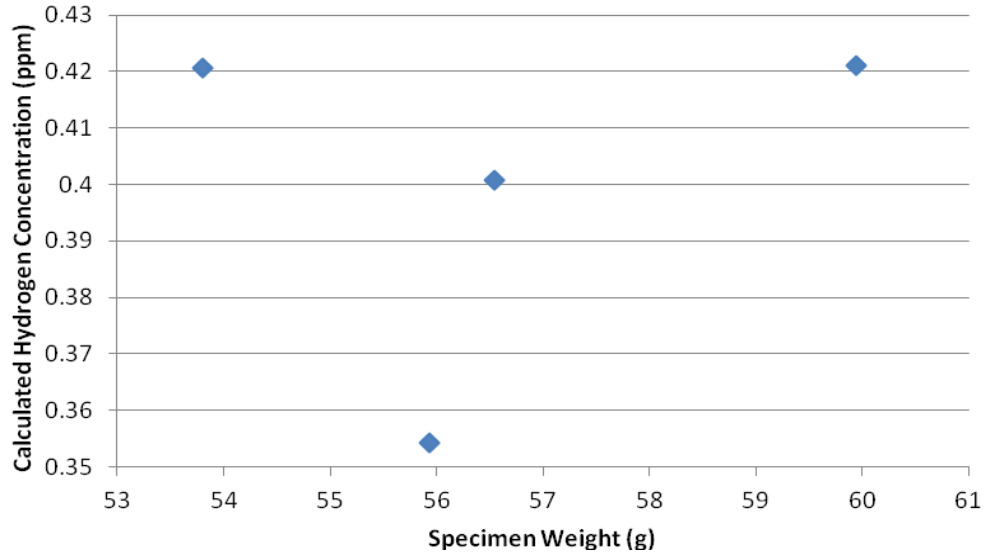


Figure 5-14 Testing the Effect of Hydrogen Trapped on the Charging Surface

5.8 The Effect of Charging Solution on Apparent Surface Concentration

The data presented in Figure 5-15 shows the concentration at certain locations in the round bar and overlays the best-fit solution of Fick's Diffusion Law for a charging solution deaerated with H₂S rather than nitrogen and charged for only 24 hours. This represents the most aggressive charging solution used in this work, leading to an apparent surface concentration of 9 ppm, a bulk concentration of 0.17 ppm, and a diffusion coefficient of $4.0 \times 10^{-8} \text{ m}^2/\text{s}$.

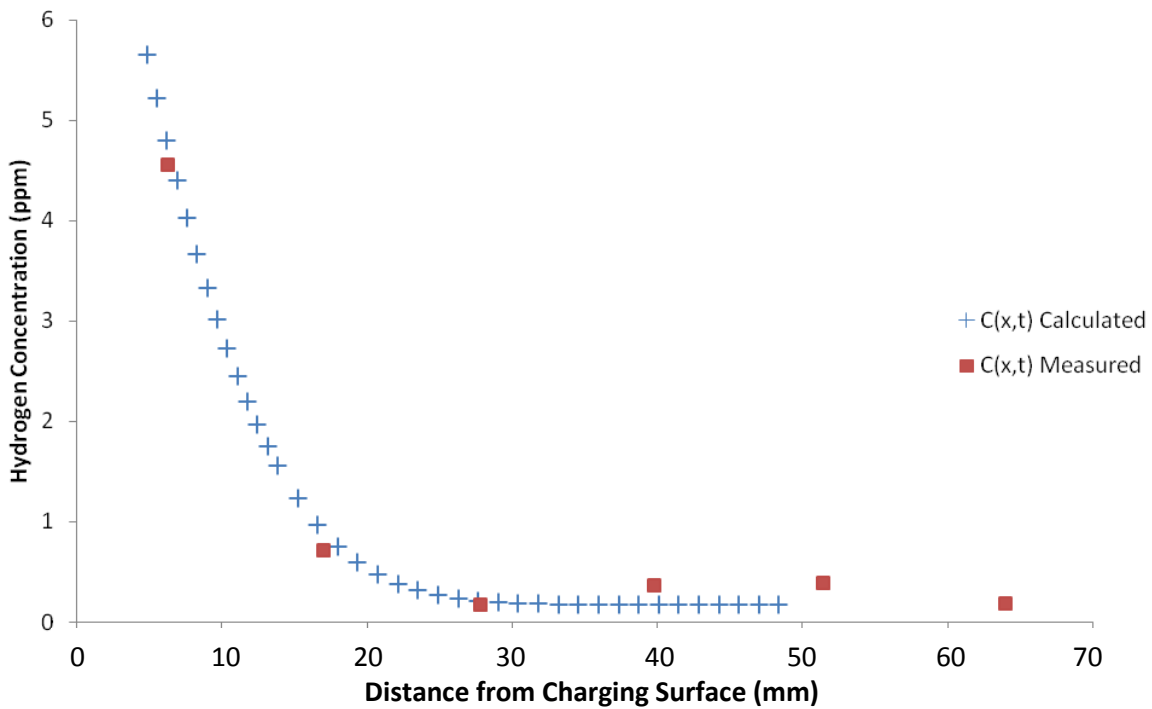


Figure 5-15 Hydrogen Diffusion Concentration Profile from Hydrogen Sulfide (H₂S)

Deaerated Solution

Similar to above, the data in Figure 5-16 represent the standard charging solution, only without nitrogen or H₂S deaeration, and therefore contains dissolved oxygen and was only charged for 24 hours. This charging condition leads to an apparent surface concentration of 1.4 ppm, a bulk concentration of 0.24 ppm, and a diffusion coefficient of $6.0 \times 10^{-8} \text{ m}^2/\text{s}$. Figure 5-17 represents the standard charging solution, with nitrogen deaeration, only charged for 9 days (216 hours) instead of the standard 48 hours. This data is harder to generate a best-fit solution, but the charging condition leads to an apparent surface concentration of 0.525 ppm, a bulk concentration of 0.11 ppm, and a diffusion coefficient of $6.0 \times 10^{-9} \text{ m}^2/\text{s}$.

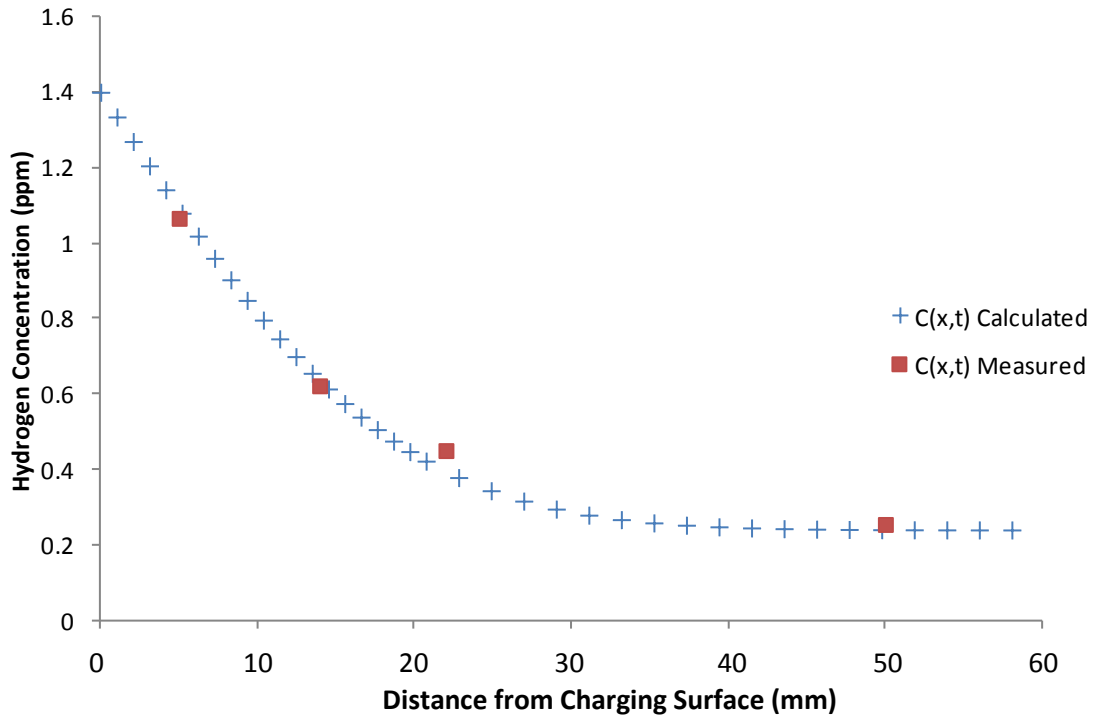


Figure 5-16 Hydrogen Diffusion Concentration Profile using Non-Deaerated Solution

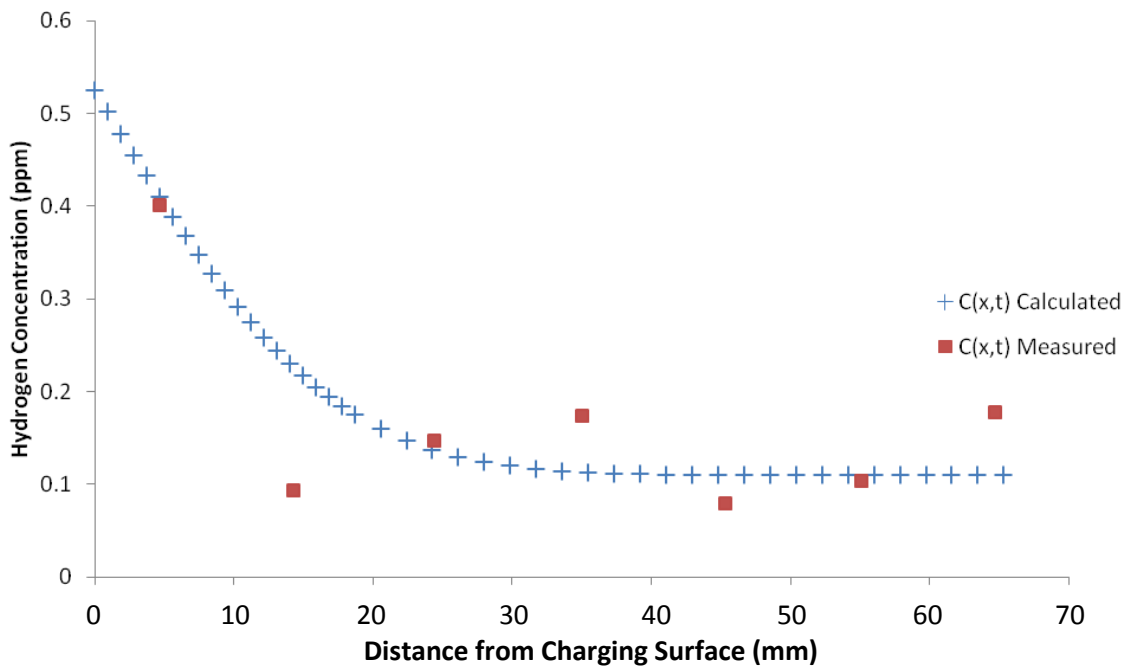


Figure 5-17 Hydrogen Diffusion Concentration Profile for Long-Term Charging (9 Days) in Standard Nitrogen Deaerated Solution

Chapter Six: **Discussion of Round Bar Hydrogen Diffusion Experiments**

The following chapter describes the most important results to emerge from the study of hydrogen diffusion in a sample of low-carbon steel. In common practice for over 50 years, Fick's Law has been used for microscopic and macroscopic measurement and calculation of hydrogen concentrations, most notably the hydrogen permeation electrochemical techniques and for modeling and calculation of hydrogen concentration near cracks as part of anodic dissolution and hydrogen embrittlement phenomena [Foster et al, 1965]. However, Fick's Law has never been validated for hydrogen concentration in metals through direct experiment until this work and also the work of Sainter et al [2011] which was published after this data was obtained but before publication of the thesis (see details below). The assumption of the validity of Fick's Law underlies all work in hydrogen diffusion in pipelines. The method presented in this thesis collects and directly measures the amount of hydrogen leaving a material. Whenever possible, a direct measure should be the gold standard rather than indirect measures. In other words, it is preferable to measure an actual quantity instead of measuring something that can only represent, or is related to, that quantity.

For the main experiment, a sample of round bar had hydrogen introduced from only one end. After charging with hydrogen the specimen was cut into discs and the concentration of hydrogen in each disc was measured. These concentrations were compared to a uniaxial solution to Fick's Diffusion Law to determine the characteristics of hydrogen diffusion in that material.

The layout of this chapter is roughly divided into three sections:

- i. Main Experiment: Hydrogen Diffusion in Round Bar and Fick's Law
- ii. Effect of Charging Solution and Time on Apparent Surface Hydrogen Concentration
- iii. Supplemental Observations

6.1 Main Experiment: New Method to Measure Diffusion Coefficient and Estimate Surface Concentration

The microstructure analysis showed that the experimental material was a typical low-carbon (0.13% carbon) ferritic/pearlitic steel with a uniform grain structure. The Vicker's hardness tests also confirmed that the material was uniform in terms of radial depth. The material shows no anisotropy in the radial or transverse directions.

The novel technique presented here uses passive hydrogen charging with longitudinal sectioning and mercury eudiometry. Experiments show that the concentration profile followed a 'Fickian' curve that could be used, along with a best fit analysis, to allow determination of the following parameters for this steel:

- i. Hydrogen Diffusion Coefficient, found to be $D = 1.63 \times 10^{-8} \text{ m}^2/\text{s}$ with a standard deviation of 0.21×10^{-8} (or 12.8% of the observed mean).
- ii. Hydrogen Surface Concentration, found to be $C_s = 0.525 \text{ ppm (mass)}$ with a standard deviation of 0.050 (or 9.5% of the observed mean).
- iii. Hydrogen Bulk Concentration, found to be $C_b = 0.083 \text{ ppm (mass)}$ with a standard deviation of 0.013 (or 15.7% of the observed mean).

These results point to more than just a set of properties for a particular material but to the validation of a direct hydrogen measurement technique with a solution to Fick's Diffusion Laws to reliably get these properties for many different materials. Hydrogen permeation and oxidation at egress methods, though easier and quicker, use indirect measurement and analysis with a model containing many assumptions to apply. In addition, these are hydrogen flux based measurements, and flux is not as important to the effect on material properties as is the concentration of hydrogen in the material at a given location at a given time.

This is the first instance known by the author to attempt to validate the use of Fick's Laws as they apply to hydrogen in steel. Sainter et al [2011] has published a method which shows a similar hydrogen concentration profile, though it differs in that they used an austenitic stainless steel, gaseous hydrogen charging, and Secondary Ion Mass Spectroscopy (SIMS) to detect and spatially resolve hydrogen concentrations. The work presented in this thesis was carried out prior to publication of the Sainter paper.

Applications. This technique is useful as supporting information in determining a material's suitability for hydrogen service, which will become increasingly important if society moves toward hydrogen as a method for energy transportation and desires to repurpose existing pipelines for use in hydrogen service. In industrial hydrogen piping the well-known Nelson Curves [Jones, 1996 pg 342] are used to relate the gaseous hydrogen pressure to the concentration of hydrogen in steel. Gaseous hydrogen is used as a feedstock for petroleum refining and ammonia production. The Nelson Curves are not suitable when considering the aqueous methods of hydrogen entry. Another area where the methods presented here can find application is in thermal hydrogen processing. For some titanium alloys, addition of dissolved hydrogen during thermo-mechanical processing can allow manipulation of the phase diagram to control microstructure [Eliezer et al, 2000]. In addition, the small amounts of added hydrogen can improve superplastic forming techniques, allowing titanium alloys to be worked at lower temperatures or with increased strain rates. Use of the techniques developed for this thesis could be used to predict the hydrogen concentrations at depth in a material and help to optimize component production conditions. The techniques developed here are also useful for materials science research as a tool for probing the behaviour of hydrogen dissolved in metals, as will be shown in the following chapter.

Limitations. It is important to recognize that the reported surface concentration represents that within the material closest to the interface with the environment, but not necessarily the concentration on the surface in contact with the environment. This study does not address the electrochemical reactions occurring on the surface of the metal or give an indication of adsorbed hydrogen's surface coverage.

6.2 The Effect of Charging Solution on Apparent Surface Concentration

The amount of hydrogen that can enter a material is obviously strongly dependant on the reactions that occur on the surface of the metal in contact with its environment. While this work was not done to probe the surface chemistry of the system (topics like surface coverage with adsorbed hydrogen, or manipulation of the electrical double layer) or how that surface changed over the experimental time scale, some conclusions can be drawn about the nature of the metal/solution interface and how it affects the amount and behaviour of hydrogen in a material. For all the testing conditions in this experiment, the base solution was the same used for the main experiment (5% NaCl and 1.1 pH). The modifications to the main experiment protocol were limited to deaeration gas (N_2 , H_2S , or none) and charging time (24, 48, or 216 hours). Hydrogen sulfide (H_2S) is a well-known promoter of hydrogen entry into a material. Not only is it a source of hydrogen but also a source of sulfur, which is a surface poison, increasing the corrosion rate and retarding the recombination of adsorbed hydrogen [Kelber & Seshadri, 2001, Jones, 1996 pg 368, Seshadri et al, 1997]. It is not surprising that the charging solution containing H_2S has the highest surface concentration of hydrogen for all conditions examined (9.0 ppm, see Table 6-1). Normally oxygen is removed from the system for these types of experiments. The most important reasons for this are: External corrosion on pipelines often occurs underground, where there is a depletion or absence of oxygen, and the oxygen reduction reaction competes with the

hydrogen evolution reaction as the cathodic reaction [Bockris & Reddy, 2000 pg 1671]. To ensure sufficient hydrogen is produced the oxygen reduction reaction is stopped by removing oxygen as a reactant. Never-the-less when oxygen is allowed into the system it resulted in a higher surface concentration of hydrogen (1.4 ppm compared to 0.53 ppm for deaerated system), possibly due to the aggressive environment promoting both reactions.

Table 6-1 Effects of Solution Composition and Time on Apparent Surface Concentration

<i>Condition</i>	<i>Most Aggressive</i>	<i>Oxygen Present</i>	<i>Longer Time</i>	<i>Main Experiment</i>
Solution Deaeration	H ₂ S	None	N ₂	N ₂
Charging Time	24 h	24 h	216 h	48 h
Diffusion Coefficient	4x10 ⁻⁸ m ² /s	6x10 ⁻⁸ m ² /s	6x10 ⁻⁹ m ² /s	1.63x10 ⁻⁸ m ² /s
Surface Concentration	9.0 ppm	1.4 ppm	0.525 ppm	0.525 ppm
Bulk Concentration	0.17 ppm	0.24 ppm	0.11 ppm	0.083 ppm

The more aggressive charging environment also raised the effective diffusion coefficient, in agreement with the findings of Griffiths & Turnbull [1995]. They attributed the difference to potentially the number of occupied hydrogen trap sites and the aggressivity of the solution in promoting hydrogen entry. This seems counter-intuitive, in that the diffusion conditions inside the metal lattice would be affected at all by external factors, and remains unexplained though attempts have been made to modify the McNabb-Foster diffusion model to incorporate surface effects [Makhlouf & Sisson, 1991]. A possible mechanism is that surface degradation leads to much higher surface area and therefore surface coverage, hydrogen ingress, and the effects of differential transport modes. The more aggressive the charging solution, the rougher the surface for a similar charging time. There are many different types of reversible hydrogen traps, which

during diffusion act to slow hydrogen's progress through the material. The lowest energy traps get filled first, and then as local concentration increases those traps get overwhelmed and hydrogen starts using other transport methods, which could lead to a different diffusion coefficient. After a trap gets filled each subsequent hydrogen atom's residence time is reduced as some hydrogen begins to 'flow over' the traps.

The trial with increased time (216 h versus 48 h normally) showed a relatively consistent surface concentration and lower diffusion coefficient, though in this case curve-fitting was more difficult. This stable surface concentration result supported the use of this charging environment for different charging times, as used in designing the experiments of the following chapter.

Aside from the benefit of using these results for experimental design, the results are important because H₂S-containing systems are very chemically active and industrially important, oxygenated systems are important to pipeline segments of shallow depth, and the timescales for stress corrosion cracking nucleation are measured in years or decades.

6.3 Supplemental Observations

Red lacquer Barrier. The red lacquer used to mask off portions of the experimental specimen proved an effective barrier to hydrogen entry into the material, as it was expected to do. The low bulk hydrogen concentrations seen farther away from the charging surface (Section 5.7) had a similar magnitude to the concentrations seen in baseline, baked-out uncharged specimen (Section 5.3).

Trapping Energies. The time to take final measurement experiments were designed to determine the optimum time for recording liberated hydrogen and were not designed to provide any information regarding the amount of hydrogen stored in the traps of different activation energies. They did, however, qualitatively demonstrate some of the features associated with

those phenomena. As an example, when collecting hydrogen from a charged sample (Figure 5-3) the eudiometer reached a steady state amount of hydrogen liberated at 90°C. Then, once the temperature was brought up to 110°C the amount of hydrogen collected grew asymptotically to a higher level. This indicates that there was some energy threshold between those temperatures that activated those traps, turning that hydrogen from ‘trapped’ into ‘mobile’ form. As mentioned in the Section 2.8.7 of the literature review, there are several thermally activated traps that could be responsible for this observation, including dislocations, inclusions, grain boundaries, and phase transitions. These traps are considered reversible as they are thought to strongly hold hydrogen at lower temperatures and weakly hold it at higher temperatures.

Potential Scans agree with Pourbaix Diagram. The potentiodynamic scans (Figure 5-9) showed no uncharacteristic behaviour, as expected from a simple material in a strongly acidic environment. There is no evidence of passivation (film-forming) behaviour during the scanning period. The Pourbaix diagram for iron in water (Figure 2-6) shows that for a pH = 1.1 the stable state of iron is Fe²⁺ and with high enough potential, shifts to Fe³⁺. This is reflected in the potential scan by the change in slope at approximately -0.4V vs. SCE.

No effect of Hydrogen Held on the Surface. To rule out the possibility that the higher hydrogen concentration readings near the charging surface were due to hydrogen adsorbed on the surface (or onto a surface film) the data were reorganized to detect any trend suggesting a surface effect (Figure 5-14). No apparent inflation of the results were found, suggesting all hydrogen liberated and collected from the disc samples was held within the bulk material and no significant amount was detected residing on the surface after removal from the charging solution.

Effect of Long Term Charging Leading to Blistering. Due to an unexpected absence from the lab, trial seven had charging conditions present for 9 days instead of 2. Once the specimen was

removed from the charging solution there were substantial blisters on the charging surface. Though this observation was not made from careful planning and experimental procedure, it did illustrate that the experimental solution and material could produce a high enough hydrogen concentration to cause damage to an unstressed material. This observation showed that at some time prior to 216 hours (9 days) there is an upper limit to the charging time that this material and solution combination could be used. This is important because it led to the determination of an upper bound on the operational parameters for future experimental design and the testing carried out in the following chapters.

Chapter Seven: **Experimental Methods for Performing Tensile Tests with Samples of Varying Hydrogen Concentration and Strain Rate**

This chapter examines the series of experiments conducted looking for the effects of varying the strain rate of tensile testing while simultaneously varying the concentration of hydrogen in the steel samples. All specimens used for calibration, validation, and testing were prepared out of a single batch of low carbon steel to minimize variability due to material differences, but from a different material than used for the diffusion experiments in the previous chapter. This work represents a new approach to looking at the effect of hydrogen on pipeline steel, partly inspired by the field of dynamic strain aging. For this work hydrogen is treated as a mobile solute in a metallic solid solution. Rather than the standard strain aging technique of varying the temperature during mechanical testing to speed-up or slow down solute diffusion through the range of dislocation velocity, in this case the strain rate (as a representation of dislocation velocity) is varied to examine hydrogen diffusion effects. Strain rate and hydrogen concentration are both known to affect the mechanical properties of steel. This experimental design combines effects of both parameters so their individual contributions to the material's overall response can be determined and to find which effect dominates the material's observed behaviour.

The order of topics in this chapter follows the general form: main experiment, calibration of hydrogen concentration in the tensile samples, standard procedures, and a series of experiments to validate the measurements and techniques.

7.1 Main Experiment: Tensile Tests of Low Carbon Steel with Varying Strain Rate and Hydrogen Concentration

The strain rate used for tensile testing is known to influence the mechanical properties of the metal [Saimoto & Diak, 2001]. Generally, an increase in strain rate is accompanied by an

increase in the flow stresses, observed through an increase in yield and tensile strength. A region of negative strain-rate sensitivity is also a phenomenon associated with solid solution systems. An increasing amount of hydrogen in steel is associated with a decrease in ductility. This series of experiments looks at the effect of varying both the strain rate and hydrogen concentration on several outcomes measured from tensile testing. The flow stresses (yield and ultimate) are compared across experimental conditions, as well an important feature of the flow curve, the strain hardening exponent. Ductility was not only examined through the fracture strain, but also broken down into the relative contributions of uniform plastic strain and necking strain.

Sample Preparation: Machining and Polishing Tensile Specimen. All tensile tests were performed on a common specimen type. The size and configuration of the specimen is detailed below in Figure 7-1. Machining operations were carried out on a HAAS HL-2 computer numerically controlled (CNC) milling machine. The starting material was purchased as 9.5 mm (3/8 inch) round bar. After machining, the samples were individually mounted on a Delta 17-209 drill press and progressively hand polished through 120, 240, 320, and 400 grit using dry paper. The polishing operation served two purposes: To remove the cold-worked surface remaining after the machining operation and to provide a uniform surface for the future solution-based hydrogen charging methods.

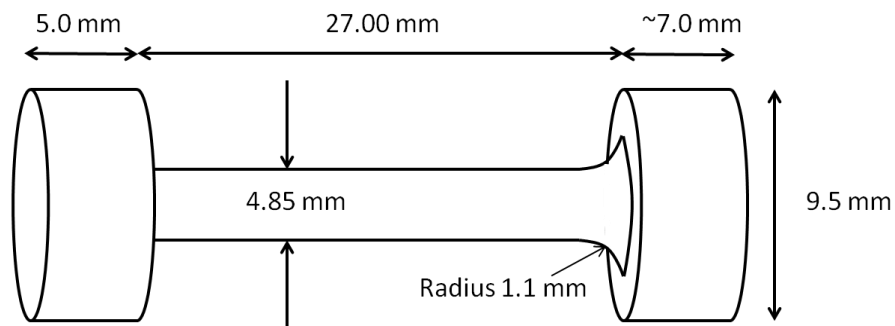


Figure 7-1 Tensile Specimen Machined from 9.5 mm (3/8 inch) Round Bar

Hydrogen Charging. The small tensile samples above were subjected to a hydrogen charging procedure similar to that of the round bar hydrogen concentration profile experiments. The steel samples were placed in a deaerated acidic solution (1.1pH, 5% NaCl, deaerated with nitrogen gas) and allowed to undergo passive corrosion. For a detailed description of the testing solution see Table 4-1. Some hydrogen, as an adsorbed intermediate species in the corrosion reactions, is absorbed into the material and becomes dissolved mobile hydrogen in the metal. The time in solution was proportional to the amount of hydrogen in the sample and therefore was used to control the hydrogen concentration. Samples were charged for 0, 3, 6, 12, 24, 36, 48, and 96 hours leading to internal hydrogen concentrations defined by the calibrated relationship developed in Section 7.3.

Once the specimen is removed from the charging solution, hydrogen immediately begins to egress from the material. For this reason, and because a number of samples are tested on a given day, care must be taken to ensure all samples are tested immediately after being removed from solution. To accomplish this, a small 50 ml Nalgene bottle with a tight fitting lid was filled with some of the deaerated acidic solution and used to transport the tensile specimens to the load frame. Only one specimen was removed from the small bottle for testing at a time. The small tensile specimen was wiped dry with a paper towel before being placed in the load frame for the tensile test.

Varying Strain Rate and Tensile Testing. The strain rate was controlled by manipulating the Tinius-Olsen H25K universal testing machine's crosshead speed. The actual strain rate was calculated later and was based on the cross-head speed and specimen gauge length. The cross-head speeds used for this experiment were 100, 50, 10, 2.5, 1, 0.25, and 0.1 mm/min. The samples were loaded onto the universal testing machine and tested to failure according to the

procedure in Section 7.4. Load and deformation data were recorded and the tensile test data was processed according to the procedure in Section 7.5. At least one sample was tested for each combination of strain rate and hydrogen concentration. Table 7-1 below shows all tested combinations of strain rate and hydrogen concentration, and which samples (with identification codes from A1, A3, A5 to T3) were tested at those conditions. A total of 56 tensile tests (one per unique condition) were required to cover the ranges of both input variables. Photographs were taken of the failure surface from both sides and the necking profile, to provide visual evidence to support the other observations.

Table 7-1 Sample Identifiers for Each Combination of Testing Parameters

	Crosshead Speed (mm/min)							
		100	50	10	2.5	1	0.25	0.1
Hydrogen Charging Time (h)	0	A5	B5	A1	T1	A3	T3	B1
	3	J1	I3	H5	I5	I1	H3	J3
	6	C1	Q5	C3	Q3	C5	Q1	D1
	12	L3	O5	M1	L1	M5	L5	M3
	24	E3	P5	E1	P3	D3	P1	D5
	36	K3	N5	J5	O1	K1	N3	O3
	48	G1	S5	G3	S3	H1	S1	G5
	96	F5	R5	F3	R3	F1	R1	E5

Validation Experiment. Significant surface change was visible after the samples' time in the acidic solution. A test of the effects of the surface condition was conducted and is outlined in Section 7.6.

7.2 Specimen Acquisition

The material for this experiment was low carbon steel. This is a different material than was used for the diffusion experimentation presented previously. The material was received as 9.5 mm (3/8 inch) round bar. The steel had a carbon percentage of approximately 0.12% and is hypoeutectic, consisting of ferrite and pearlite (see results Section 8.1). The microstructure was confirmed in the axial as well as transverse directions. The entirety of calibration and tensile testing was done on a single batch of steel to avoid variability in results due to material differences. To view sample microstructure and calculate carbon percentage, samples were mounted, polished, and etched according to the standard procedures presented in Section 4.3.

7.3 Calibration of Time in Solution to Hydrogen Concentration

Purpose. The goal of this experiment was to provide a calibrated relationship between charging time and hydrogen concentration in steel tensile test samples. This relationship is useful to relate the amount of hydrogen in a sample to certain mechanical properties as measured by the tensile test.

Introduction. Hydrogen charging was accomplished through the use of a corrosion reaction occurring on the surface of the steel sample in contact with acidic solution. Hydrogen is an intermediate adsorbed species in the corrosion reaction. Some hydrogen recombines and is evolved, and some is absorbed into the metal's crystal lattice. The amount of Hydrogen in the three possible conditions at the metal surface (adsorption, absorption, recombination) depends on a large number of interdependent factors: solute species and concentrations, temperature, steel microstructure and chemistry, surface condition, size and geometry of specimen (concentration

cells, stirring, etc.), and the presence and thickness of any corrosion film. Pourbaix diagrams are useful in determining the corrosion reactions taking place given the experimental conditions.

Due to the large number of interdependent factors a calculated model of hydrogen concentration and time in solution is not feasible. Therefore an empirical analysis will be used to calibrate the amount of time in solution to the amount of hydrogen that is absorbed into the metal.

Outcomes. What was to be determined: the relationship between time spent in solution to the concentration of hydrogen in a steel tensile sample. This calibration curve was used so that a number of charging conditions could be used and directly converted to hydrogen concentration. These values of concentration were then used to compare experimental results to models of hydrogen's effects on mechanical properties.

Material. Low carbon ferritic/pearlitic steel was machined to a small tensile specimen shape as shown in Figure 7-1. The surface of the specimen was ground progressively to 400-grit to provide a standardized starting condition. The solution used was 5% NaCl, 1.1 pH, stable throughout the experiment, and deaerated using bubbling nitrogen. The mercury eudiometers were used according to the welding standard, with several modifications as detailed in Section 4.4.

Method. Before any experimental work began, the samples were placed in an oven at 110°C for 72 hours to bake out any mobile hydrogen already present in the steel. Each sample was weighed and dimensions measured. After baking out to a uniform and very low hydrogen concentration the samples were placed horizontally in the deaerated acidic solution (Table 4-1) to undergo a passive corrosion reaction. Nine samples were charged for 0, 3.25, 6, 12.25, 13.25, 24, 48, 74.5, and 94 hours to thoroughly cover the continuous data space and provide information for as many charging conditions as possible. After charging, each sample was

removed from solution, the loosely bonded surface corrosion products removed with a paper towel (corrosion films have different hydrogen solubility than the underlying metal), and immediately placed into a separate individual eudiometer, with a modified sample carrier (see Figure 7-2). Each eudiometer was brought up to 110°C and the amount of hydrogen collected in the trap recorded. The final hydrogen amount was recorded after 72 hours in the eudiometer. For detailed information on the eudiometer procedure see section 4.4.

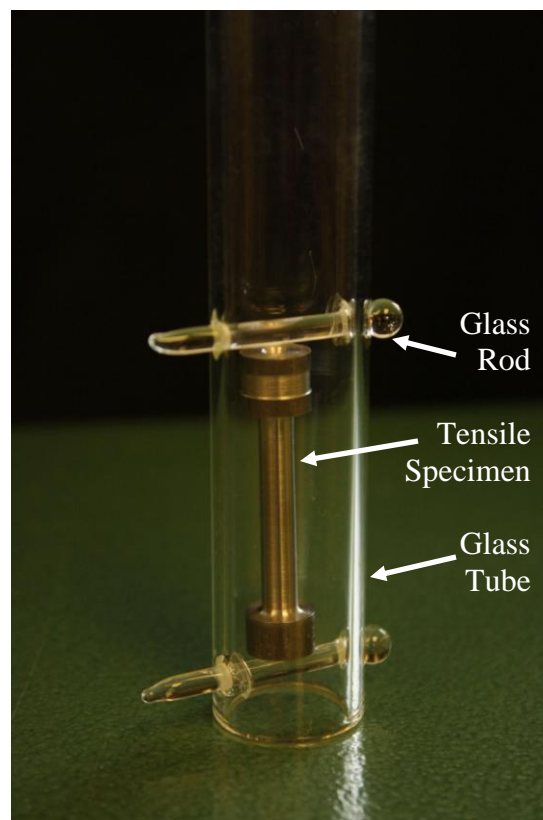


Figure 7-2 Glass Eudiometer Holder for Small Tensile Specimen

7.4 Standard Operating Procedure: The Tensile Test

Purpose. This procedure standardizes the method by which the Tinius-Olsen Universal Testing Machine was used to generate data from the tensile testing of small tensile specimen.

Introduction. The tensile test is a well established method to examine the mechanical properties of a sample. To minimize experimental bias and error, one procedure was used for all testing. Following a set procedure improves the accuracy and repeatability of experimental results, and increases workflow by optimizing material-handling and data-handling processes.

Outcomes. The outcome of the tensile testing procedure was a data file containing pairs of load (lb) and deformation (in) measurements.

Material. Tensile specimens from the different experimental protocols are brought to the testing room. The specimen configuration for these tests was a round bar small tensile specimen. The specimen had a reduced diameter section of approximately 4.85 millimeters diameter and 27.00 mm length (see the specimen configuration in Figure 7-1). The material was low carbon steel with a ferritic/pearlitic microstructure. For details on the specimen configuration see Section 7.1 and for specimen condition see the appropriate experimental protocols. For these experiments, a Tinius-Olsen 25 kN T-series bench-top Universal Testing Machine was used. Specifications for the tensile testing machine can be seen in Table 7-2. The testing machine was connected to a desktop PC running proprietary Tinius-Olsen TestNavigator software allowing the user to control the operation of the machine using the computer.

Table 7-2 Specifications for Tinius Olsen H25K Universal Testing Machine

<i>Model</i>	<i>H25K</i>
Capacity	25 kN
Testing Speed Range	0.001 to 1000 mm/min
Testing Speed Accuracy	± 0.005% of set speed
Position Measurement Accuracy	Greater of ± 0.01% or 0.001 mm
Load Cell	Z-type
Load Measurement Accuracy	± 0.5% of indicated load

Method. The different experimental protocols define the treatment of specimen before they are ready to be subjected to the tensile test. The following procedure is intended to begin when each tensile specimen is removed from its previous experimental condition.

The two sample holders were assembled at the top and bottom of the specimen and the retaining collars were put in place. Using the control panel on the testing machine the crosshead was moved up until the load cell was clear and the specimen and holders can be put in place. The lower holder was placed first, and was pinned into place. Next the crosshead was lowered until the upper pin could be inserted, locking the specimen into the machine. The crosshead was moved up to take up the slack in the machine until a load was placed on the specimen, then back it off until the load just returned to zero. The machine was manually set to read zero displacement and zero load. Then the specimen and machine were ready for testing and the computer was programmed with the test parameters.

Tensile tests were carried out at a constant rate of displacement, recording load (lb) and position (in). Through the testing program interface, the appropriate values of crosshead speed and measurement frequency were set. See Table 7-3 below for information relating testing speed,

approximate strain rate, and measurement frequency. Testing speed affected the size of the output data file, so a measurement frequency was chosen that allows enough data to be captured, but was not an overwhelmingly large file (several hundred to approximately two thousand measurements was usually sufficient). The specimen information was entered so that it was part of the output file. Specimen information included: Specimen ID, operator name, testing speed, hydrogen charging time, and specimen diameter. Once all specimen information was entered and the test parameters were set, START was selected and the computer began the test and started recording data.

Once the test was complete, data files were reviewed and accepted if the test record and values were reasonable. The broken tensile specimen was disassembled and removed from the machine with the parts placed into the labelled specimen holder for photographing later. The testing machine was then ready to begin the next test. After all testing was completed, a back-up copy of all test data was made. The resulting data was analyzed according to the procedure laid out in Section 7.5.

Table 7-3 Experimental Settings for the Tensile Testing Machine

<i>Testing Speed</i> (mm/min)	<i>Approximate Strain Rate</i> (s ⁻¹)	<i>Sampling Frequency</i> (s ⁻¹)	<i>Approximate Data Set</i> (number of observations)
0.1	6.17x10 ⁻⁵	1	1700
0.25	1.54x10 ⁻⁴	0.5	1500
1.0	6.17x10 ⁻⁴	0.3	800
2.5	1.54x10 ⁻³	0.1	1800
10	6.17x10 ⁻³	0.01 (maximum)	450
50	3.09x10 ⁻²	0.01 (maximum)	90
100	6.17x10 ⁻²	0.01 (maximum)	50

7.5 Standard Procedure: Data Collection and Tensile Test Data Processing

Purpose. The goal of this procedure was to take the raw data from the tensile testing machine and perform a thorough tensile test analysis in both engineering and true stress and strain. The output of these operations was used to examine the effects of the experimental parameters on the mechanical properties of the steel.

Introduction. The desktop PC connected to the testing machine recorded values for load and deformation throughout the tensile test. The raw data was converted to engineering stress and strain then plotted. The effects of the machine (machine stiffness and looseness in fittings) needed to be removed from the data set so that key mechanical property values could be determined. The most important engineering stress and strain properties from this section were ultimate stress, yield stress, fracture strength, and elongation at fracture. Next, the engineering stress and strain values needed to be converted to true stress and strain. The theory and formulas for this conversion are only applicable up to the value of the ultimate stress and are detailed below. The true plastic stress was then calculated between the end of the yield stress region up to the ultimate stress. The Flow Curve was generated by a logarithmic plot of true stress versus true plastic strain. A best-fit analysis of the resulting flow curve to the flow equation produced the strain hardening exponent. The final operations on the data set were to locate and calculate the true plastic strain, the true final plastic strain, and the necking strain.

Outcomes. The output of these operations was: The engineering yield stress, ultimate stress, fracture stress, and elongation at fracture, the strain hardening exponent, the true plastic strain, and the true necking strain.

Method. Before testing the specimen were subjected to the experimental conditions specified by the experimental procedures. Prior to any experimental testing, all specimens were labelled and

were measured for diameter at three locations and length of the reduced section. A table format for recording this information, as well as the testing conditions is found below in Table 7-4.

Table 7-4 Sample Raw Data Table Collected Prior to Tensile Testing

<i>Sample</i>	<i>Diameter 1</i> (mm)	<i>Diameter 2</i> (mm)	<i>Diameter 3</i> (mm)	<i>Length</i> (mm)	<i>Test Speed</i> (mm/min)	<i>[H] time</i> (h)
C1	4.83	4.80	4.78	27.03	100	6
C3	4.85	4.79	4.78	26.94	10	6
C5	4.80	4.77	4.75	27.00	1	6
D1	4.82	4.78	4.78	27.00	0.1	6
D3	4.80	4.78	4.77	26.98	1	24
D5	4.87	4.84	4.81	26.97	0.1	24

After testing, a data file was saved containing two columns of paired data representing the load (pounds) and deformation (inches) at that time point. The raw data was then imported into the first two columns of an Excel spreadsheet with the following column headings and top matter:

Table 7-5 Spreadsheet Format for Processing Tensile Test Data

Sample ID	G3		Date	02-Mar-12		Troy Eggum	PhD Candidate, UofC		
[H]	1.7045	ppm	Diameter	4.84	mm	Df		mm	
Crosshead	10	mm/min	Length	27.01	mm	Ao	18.398	mm^2	
Strain Rate	6.17E-03	1/s	Modulus	200	Gpa	Af	0.000	mm^2	
			Machine	Zero	Machine				True
			Measured	Strain	Stiffness	Corrected	True	True	Plastic
Load	Deformation	Stress	Strain	Correction	Correction	Strain	Stress	Strain	Strain
(lbs)	(in)	(Mpa)	(m/m)	(m/m)	(mm/mm)	(mm/mm)	(Mpa)	(m/m)	(m/m)

The shaded cells in the top matter were filled with data specific to the specimen and the experimental conditions that specimen experienced. The strain rate was calculated by:

$$\text{Strain Rate (s}^{-1}\text{)} = \frac{\text{Crosshead Speed (}\frac{\text{mm}}{\text{min}}\text{)} \times \frac{1 \text{ min}}{60 \text{ s}}}{\text{Specimen Length (mm)}}$$

With the load and deformation values in place, the first operation was to convert those values into engineering stress, and machine measured strain. Engineering stress was calculated by first converting pounds to Newtons, and then dividing by the original area of the reduced section. Machine measured strain was calculated by converting the deformation from inches to millimeters, and then dividing by the original length of the reduced section.

$$\text{Engineering Stress (MPa)} = \frac{\text{Load (lb)} \times 4.448 \left(\frac{\text{N}}{\text{lb}}\right)}{\pi \left(\frac{\text{Diameter (mm)}}{2}\right)^2}$$

$$\text{Machine Measured Strain (}\frac{\text{mm}}{\text{mm}}\text{)} = \frac{\text{Deformation (in)} \times 25.4 \left(\frac{\text{mm}}{\text{in}}\right)}{\text{Original Length (mm)}}$$

The slope of the linear portion of the stress-strain curve should intersect the origin at zero stress and zero strain. The initial machine measured strain did not do this because of the crosshead movement required for the apparatus to tighten and because of some looseness in the fittings and clamps. The entire machine measured curve was simply shifted to the left by subtracting an amount such that the intercept implied by the linear portion rests at zero stress and zero strain, called the Zero Strain Correction (see Figure 7-3 for the shift in the curve).

The testing machine was not perfectly stiff so a portion of the slope seen in the linear portion was due to flex of the testing machine itself. The correction for this involved using the Young's Modulus of the steel specimen. Most steels have a Young's Modulus that falls within a very narrow range between 200 – 208 GPa. This type of steel has a modulus of 200 GPa, so the

correction involved using a linear transformation to make the slope of the linear portion equal to 200 GPa. The correction factor is called the Machine Stiffness Correction and was calculated for each tensile trial and was a proportional function to the current stress level. This value was subtracted from the Zero Strain Correction to get the Corrected Strain, which was finally a measure of the Engineering Strain.

True stress and true strain were calculated from engineering stress and strain using the following formulas [Ling, 1996]:

$$\text{True Stress } \hat{\sigma} = \sigma(\varepsilon + 1)$$

$$\text{True Strain } \hat{\varepsilon} = \log(\varepsilon + 1)$$

Where σ is engineering stress and ε is engineering strain. Finally, the true plastic strain was calculated by subtracting the elastic strain from the true strain value using the following method:

$$\text{True Plastic Strain } \hat{\varepsilon}_p = \hat{\varepsilon} - \frac{\sigma}{200 \text{ GPa}}$$

Care must be taken when calculating true stress and true strain as the formulas listed above are only valid from zero up to the ultimate stress. Plastic strains only occur after yielding so the method to calculate true plastic strain is only valid between the end of yielding (or any yield point elongation) up to the ultimate stress. The true plastic strain was then plotted versus true stress on a logarithmic plot and a trend line of the form $\hat{\sigma} = K\hat{\varepsilon}^n$ fitted, where K is a constant and n is the strain hardening exponent [Callister, 2003 pg 132] (see Figure 7-4 for an example of this plot).

The yield and ultimate stress values were read directly from the table of values, looking for local maxima. Sometimes upper and lower yield points were observed. The lower yield is usually

reported by convention because the upper yield has much more variability associated with it. Engineering strain at fracture was read directly from the table. The uniform plastic strain and final plastic strain were calculated from the engineering strains at the ultimate stress and final fracture, respectively, by subtracting the elastic strain according the following formulae:

$$\text{Uniform Strain } \varepsilon_{up} = \varepsilon_u - \frac{\sigma_u}{200 \text{ GPa}}$$

$$\text{Final Plastic Strain } \varepsilon_{fp} = \varepsilon_f - \frac{\sigma_f}{200 \text{ GPa}}$$

Where σ_u and ε_u are the ultimate stress and uniform strain and σ_f and ε_f are the final stress and strain. Finally, the necking strain was calculated:

$$\text{Necking Strain } \varepsilon_n = \varepsilon_{fp} - \varepsilon_{up}$$

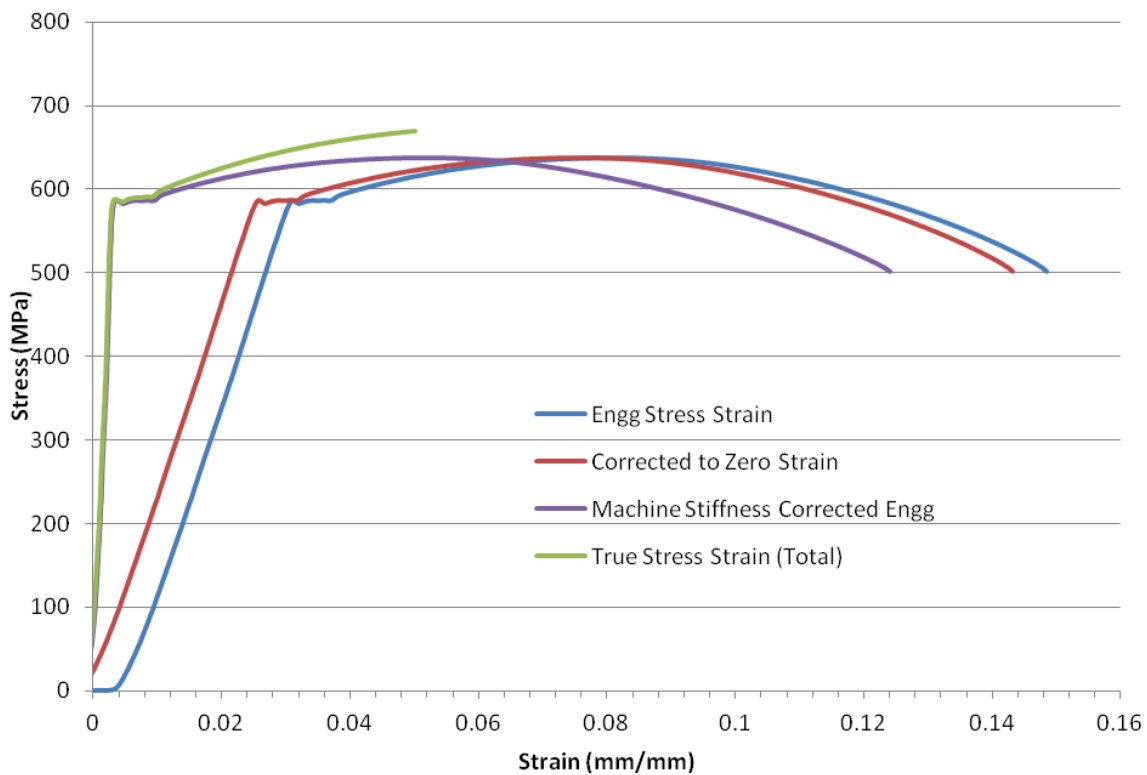


Figure 7-3 Typical Plot of Tensile Data and Effect of Data Transformations

Logarithmic plot of true stress versus true strain, where slope is strain hardening exponent:

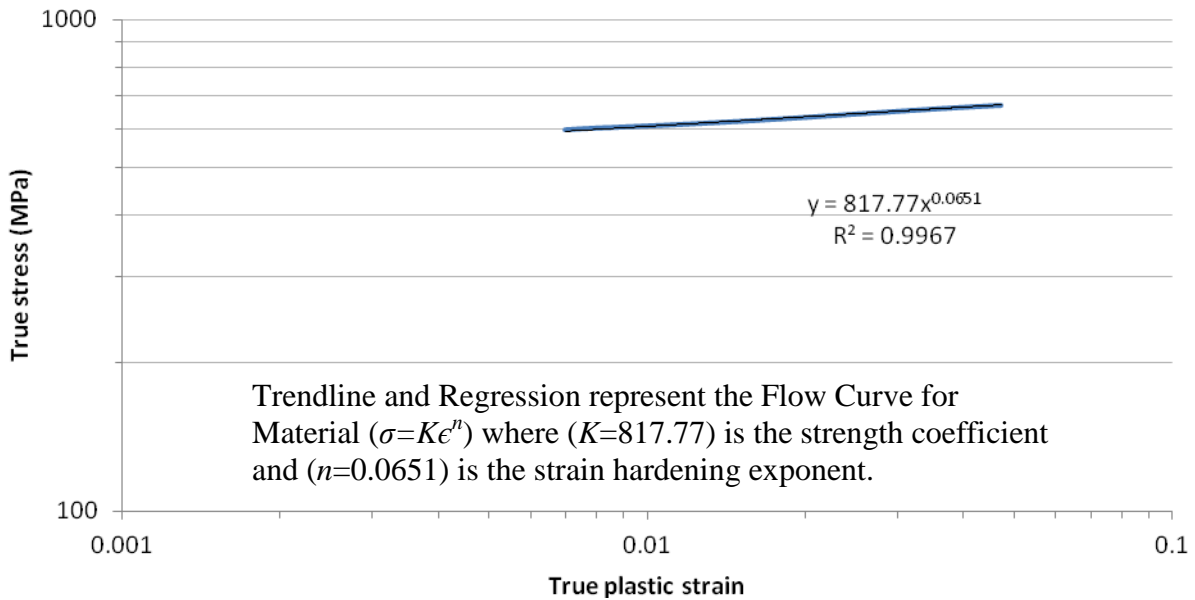


Figure 7-4 Typical Plot of True Stress and True Plastic Strain for Tensile Test Results

7.6 Effect of Surface Condition on Tensile Tests

Purpose. The goal of this experiment was to observe and quantify the effect of the solution charging regime on the outcome measures of the tensile tests.

Introduction. Hydrogen charging was accomplished through the use of a corrosion reaction occurring on the surface of the steel sample in contact with acidic solution. The anodic reaction on the surface of the steel will tend to ‘eat away’ some of the steel, altering the surface. Pits observed on the surface of specimen were due to this process. The results of tensile tests are known to be sensitive to the surface condition of the sample.

As in previous experiments, the amount of time in solution reflects the amount of hydrogen that absorbs into the metal as illustrated by the calibration experiments. For this experiment, the

amount of time in solution should reflect the amount of surface degradation and may have an effect on the results of the tensile tests carried out in earlier experiments.

Outcomes. What was to be determined: which of our outcome measures are sensitive to surface condition and to what extent? Will the observations of the other experiments need to be corrected to account for this?

Material. The same material, sample configuration, and solution were used for this experiment as for other work from this chapter.

Method. Before any experimental work began, the samples were placed in an oven at 110°C for 72 hours to bake out any mobile hydrogen already present in the steel. The samples were placed horizontally in the deaerated acidic solution to undergo a passive corrosion reaction. The surface condition of the sample should be directly related to the amount of time in solution. Eight samples were charged for 0, 3, 6, 12, 24, 36, 48, and 96 hours to represent the different experimental conditions staged thus far. After charging, the samples were removed from solution and the loosely bonded surface corrosion products removed with a paper towel (to match the procedure from other experiments). Next, to bake out any hydrogen in the steel and return it to a zero concentration condition, all samples were placed for 72 hours in an oven at 110°C. All specimen were photographed to allow for visual comparison of the samples. Lastly, the specimens were subjected to a tensile test following the procedure described in Section 7.4. All tensile tests were carried out at a strain rate of $1.54 \times 10^{-3} \text{ s}^{-1}$.

Measures/Observations/Analysis. As per previously developed techniques, the ‘time in solution’ data (independent variable) was plotted against yield stress, ultimate stress, strain at fracture, strain hardening exponent, uniform strain, and necking strain. A best-fit analysis was used with a linear model or standard function. R^2 values were used to determine if a relationship

existed and its strength. The data were reported as time vs. outcomes. Photographic records from each sample (post-charging surface, failure surface, and necking profile) were used to illustrate the major phenomena occurring and provide supporting visual evidence to accompany the observations from the other data.

7.7 Repeatability of Tensile Tests

Purpose. The goal of this experiment was to find the baseline (zero hydrogen charging) values for all outcome measures and to get an estimate of the technique's measurement variances.

Introduction. With such a large data space (56 unique combinations of interest for strain rate and hydrogen concentration, as identified in Section 7.1) it was not practical or desirable to repeat each measurement enough times to calculate individual measurement variances. In fact, when allocating test conditions to a finite number of prepared specimens, preference was given to thoroughly exploring the data space to determine the underlying continuous functions. For that reason this repeatability experiment was designed to give an estimate of the variances associated with each outcome measure for the experimental technique used.

Outcomes. What was to be determined: the baseline values of the outcome measures for a zero hydrogen charging condition and estimates of the variance of the overall technique.

Method. The same material, sample configuration, and bake-out procedure were used for this experiment as for other work from this chapter. Four samples were used. The samples did not undergo any solution hydrogen charging, tensile tests and data processing were carried out in the standard manner.

7.8 Effects of Momentum on Tests with High Crosshead Speeds

Purpose. To determine the effect, if any, of dynamic flex or rebound in the testing machine seen during tensile tests at the highest strain rates.

Introduction. Depending on the mass and stiffness of the tensile testing machine there may be some artifact in the data resulting from machine flex or rebound. The methods of analysis for this work rely on a quasi-static method of load application and material response (i.e. energy methods were not considered). Any system energy lost to dynamic processes in the machine could alter the desired outcome measures.

Outcomes. What was to be determined: is there any evidence of non-linear response from the system during tests with high crosshead speed? A plot of displacement versus time will show any effects.

Method. The same material, sample configuration, and bake-out procedure were used for this experiment as for other work from this chapter. Three samples were tested at crosshead speeds of 2.5, 100, and 250 mm/min corresponding to strain rates of 1.54×10^{-3} , 6.17×10^{-2} , and $1.54 \times 10^{-1} \text{ s}^{-1}$, respectively. The samples did not undergo any solution hydrogen charging. Pairs of data points were recorded for current displacement and time.

7.9 Effect of Hydrogen Egress during Tensile Tests

Purpose

To determine the effect, if any, of hydrogen leaving the tensile specimen during typical tensile test times by pausing the tensile test for a predetermined time, and to quantify that effect on the experimentally determined mechanical properties.

Introduction

Hydrogen immediately begins to leave the material when it is removed from the charging solution. The samples tested at a strain rate of $6.17 \times 10^{-5} \text{ s}^{-1}$ take about 40 minutes to complete, with the time depending mostly on the sample's total elongation. Depending on the amount of hydrogen released, there will be an effect on the observed outcomes whose values are dependent

on hydrogen concentration. If we consider that mobile hydrogen can diffuse to areas of higher dislocation density, there may also be an effect on other system properties such as re-pinning of dislocations, leading to reestablishment of upper and lower yield points and Lüders regions. If these effects are present they should be more apparent the more time a sample rests.

Outcomes

What was to be determined: is there a change in the ultimate stress, fracture strength, or necking strain that is related to a decrease in the hydrogen concentration in the tensile specimen and does that change depend on the amount of time hydrogen is allowed to egress from the sample?

Method

The same material, sample configuration, and bake-out procedure were used for this experiment as for other work from this chapter. Six samples were placed into the standard charging solution to charge with hydrogen for 48 hours to almost reach the asymptotic concentration. The standard tensile test procedure was followed with one exception: Each sample was taken past the yield strength, then the test was paused and the load on the sample reduced. Then the samples were left to rest in the machine for 0, 10, 20, 30, or 40 minutes before being reloaded through the ultimate strength and to failure. All tests were conducted at a strain rate of $1.54 \times 10^{-3} \text{ s}^{-1}$. The yield strength, ultimate strength, fracture stress, and necking strain were recorded and plotted together on a stress-strain diagram so the effects of increasing rest/egress time could be determined. The individual stress-strain curves were examined for evidence of the reestablishment of upper and lower yield points and Lüders region.

Chapter Eight: **Experimental Results of Tensile Tests with Varying Strain Rate and Hydrogen Concentration**

This chapter contains all the results of the experiments concerning the effects of varying strain rate and dissolved hydrogen concentration on the sample steel's behaviour during a tensile test.

The material is divided into seven sections:

Section 8.1 - Examination of the microstructure of the experimental material used.

Section 8.2 - Calibration of hydrogen concentration in the material to the amount of time spent in the hydrogen charging solution.

Section 8.3 - Tests of the repeatability of the experimental procedure and an indication of the detection limits.

Section 8.4 - Tests on the effect of the samples' surface condition, which degrades increasingly with more time spent in the charging solution.

Section 8.5 - Tests on the effect of hydrogen leaving the sample during testing.

Section 8.6 - Tests on the effect of momentum in the testing machine for high strain rate tests

Section 8.7 - Results of the Main Experiment for all outcome measures.

The sections below present the experimental results obtained from experiment and presentation of observations. Presentation of findings requiring substantial analysis or manipulation of data for clear presentation is also found in the discussion (Chapter Nine:) for this material.

8.1 Microstructure of Steel Specimen Material

Photomicrographs of the material's microstructure can be seen in Figure 8-1. Photos A) and C) represent the radial or longitudinal direction of the round bar stock and photos B) and D) represent a transverse section with corresponding scales as indicated. Photos C) and D) were taken with plane polarized light to enhance contrast. The ferritic/pearlitic microstructure is

clearly evident. Significant banding is apparent in the longitudinal direction. Grain size was estimated using ASTM Standard E112 and the Hilliard Single Circle intercept procedure. The grain size was found to be $G_{ASTM} = 10.5$ for an average grain diameter of $9.4 \mu\text{m}$. Using micrographs of the microstructure, ImageJ image processing software was used to calculate the area fractions of the pearlite and ferrite grains. The image was manipulated based on brightness to isolate the brighter ferrite grains from the darker pearlite grains then an area-fraction calculation was performed on the modified image. The carbon percentage of the material can be calculated using the iron-carbon diagram, knowledge of the eutectoid carbon concentration, and the lever rule. The percentage pearlite was found to be 12.7% leading to an estimated carbon weight percentage of 0.116%. Overall the microstructure is as expected from a sample of low carbon hypoeutectic steel. The values for yield and tensile strength observed in the repeatability tests (Section 8.3) are higher than expected for a material of this carbon content, but could be accounted for by the smaller than expected grain size.

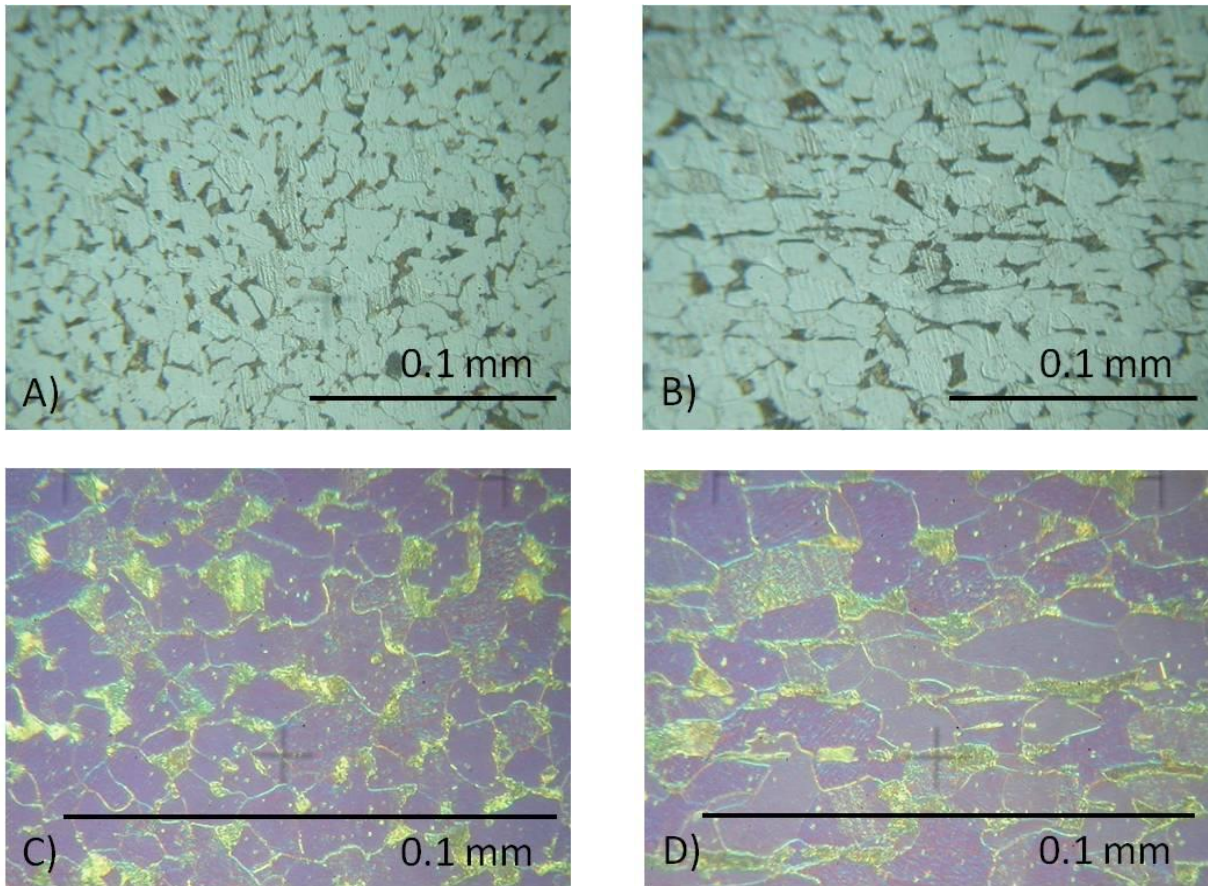


Figure 8-1 Microstructure of the Low Carbon Steel used for Tensile Tests shown in Radial (or Longitudinal) (A, C) and Transverse (B, D) Sections

8.2 Calibration of Time in Solution to Hydrogen Concentration

Using mercury eudiometry and the analysis techniques described in Section 4.4 with the associated weight, atmospheric pressure, and temperature measures, a calibration was developed to calculate the concentration of hydrogen in each specimen that corresponds to the amount of time spent in the charging solution. The results for each of the nine calibration points are listed in Table 8-1 and plotted in Figure 8-2.

To establish the range of hydrogen concentrations studied, a number of criteria were considered. From previous experiments with the same charging solution, hydrogen charging for 9 days (216

hours) was found to produce hydrogen blistering on the surface, a condition detrimental to the material and very difficult to control experimentally. Therefore a range of hydrogen charging times was selected ranging from zero to 96 hours (4 days). To cover that range, and anticipating that some of the greatest rates of change in material properties would be seen for low concentrations, charging would start at 3 hours and double through the remainder for charging times of 3, 6, 12, 24, 48, and 96 hours. Any extra calibration data points were added to fill in detail in a range where the behaviour changed or to repeat points that are suspected to be outliers. To best determine and define the underlying continuous relationship (as opposed to assembling it piece-wise) calibration points were chosen to cover the data space with as many unique data points as possible, rather than repeating particular measurements.

Table 8-1 Hydrogen Charging Time and Associated Hydrogen Concentrations

<i>Charging Time (h)</i>	<i>Hydrogen Concentration (ppm)</i>
0.0	0
3.25	0.263
6.0	0.509
12.25	0.732
13.25	1.393
24.0	1.396
48.0	1.716
74.5	1.813
94.0	1.790

These hydrogen concentrations were plotted versus time in solution and a calibration curve constructed. The observed curve (Figure 8-2) appeared to be an asymptotic growth shape and was similar to a previously published calibration (Figure 8-3), though the charging and discharge

methods were different. A best-fit analysis was used to describe the curve, with an asymptotic growth model of the form:

$$[H] = [H]_{\infty} (1 - e^{-Kt})$$

Where $[H]$ is hydrogen concentration in parts-per-million, $[H]_{\infty}$ is the asymptotic concentration, K is the growth constant, and t is time in hours. The values found for the constants are $[H]_{\infty} = 1.84$ ppm and $K = 0.055$. The calibration curve can be seen below in Figure 8-2.

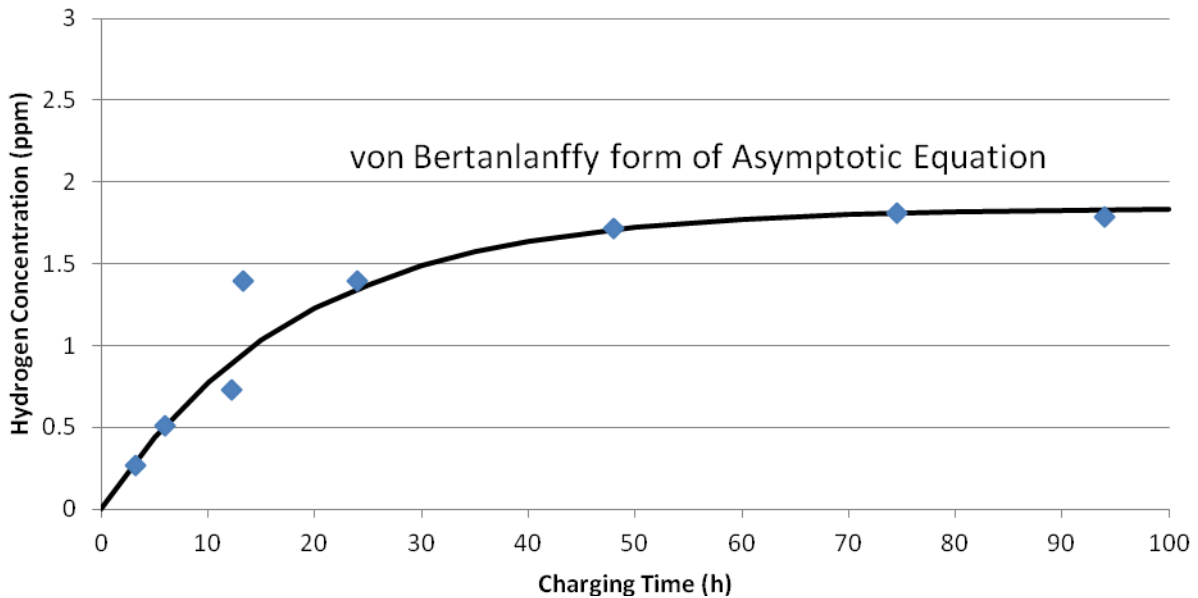


Figure 8-2 Calibration Curve for Hydrogen Concentration vs. Time in Solution

There are several features apparent from the curve. From 0 to approximately 50 hours the concentration grows asymptotically toward 1.84 ppm. After approximately 50 hours the concentration does not increase appreciably through the testing range. This asymptotic growth pattern has been previously observed in hydrogen systems as noted by Escobar et al [2009], though they used different materials, a potential charging method, and thermal hydrogen desorption analysis (see Figure 8-3). It is important that the charging conditions and material

condition be kept as constant as possible throughout the different experiments, especially given the different time spent in the charging solution, as the effective diffusion coefficient is known to vary by an order of magnitude depending on the aggressiveness of the charging conditions [Griffiths & Turnbull, 1995]. Any contribution of an oxide film will be minimal as the effective diffusion coefficient of an intact film has been shown to be ten orders of magnitude greater than the steel substrate [Olden et al, 2008].

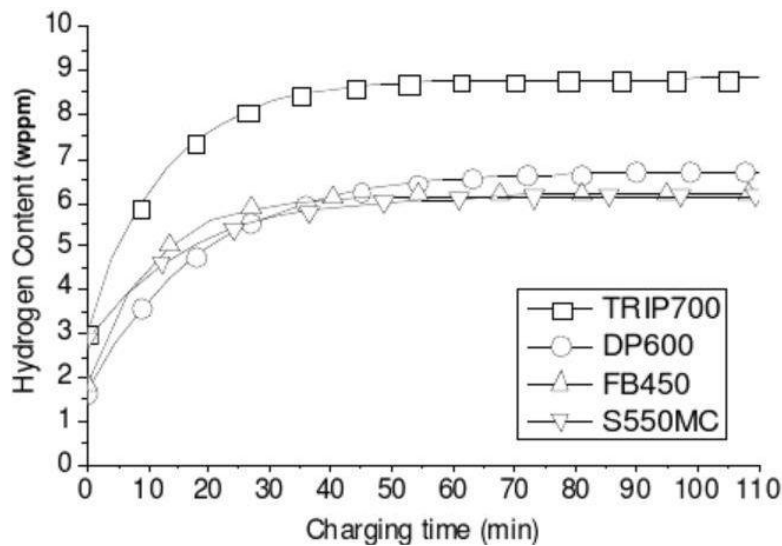


Figure 8-3 Hydrogen Concentration versus Charging Time Calibration from Escobar, 2009

8.3 Repeatability of Tensile Tests and Basic Material Properties

Four tensile tests were performed on specimen with exactly the same treatment and were compared for all outcome measures. Treatment included: surface finish grind to 400 grit, mobile hydrogen bake-out at 110°C for 72 hours, zero hours charging time, all samples tested at a strain rate of $1.54 \times 10^{-3} \text{ s}^{-1}$, and all samples tested on the same day. Table 8-2 shows the mean value obtained for each of the output measures used in the main experiment, with the standard deviation for that set of measures and a comparison of the magnitude of the standard deviation to the mean. These results are also graphically presented in Figure 8-4, Figure 8-5, Figure 8-6, and

Figure 8-7. The results for coefficient of variation show a relatively tight distribution of measurements for all measured outcomes, especially when considering the flow stresses (yield and ultimate). The Total Plastic Strain seen in Figure 8-7 results from adding the uniform and necking strains together, therefore its standard deviation is a weighted combination of its constituents.

Table 8-2 Means and Standard Deviations for the Repeatability Tests of all Outputs

	<i>Mean</i>	<i>Standard Deviation</i>	<i>Standard Deviation as % of Mean</i>
Yield Strength (MPa)	560.09	3.56	0.63 %
Ultimate Strength (MPa)	622.51	2.51	0.40 %
Fracture Strain (%)	14.55	0.46	3.19 %
Strain Hardening Exponent	0.0658	0.0024	3.63 %
Uniform Plastic Strain (mm/mm)	0.0460	0.0022	4.86 %
Final Plastic Strain (mm/mm)	0.1434	0.0046	3.23 %
Necking Strain (mm/mm)	0.0974	0.0034	3.50 %

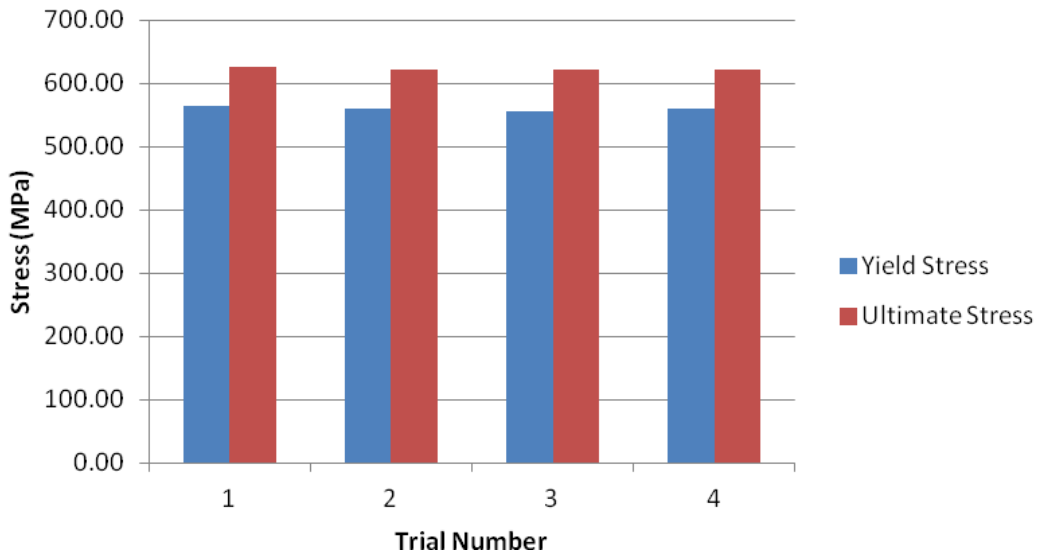


Figure 8-4 Repeatability of Yield and Ultimate Stress Measurement at 0 ppm Hydrogen

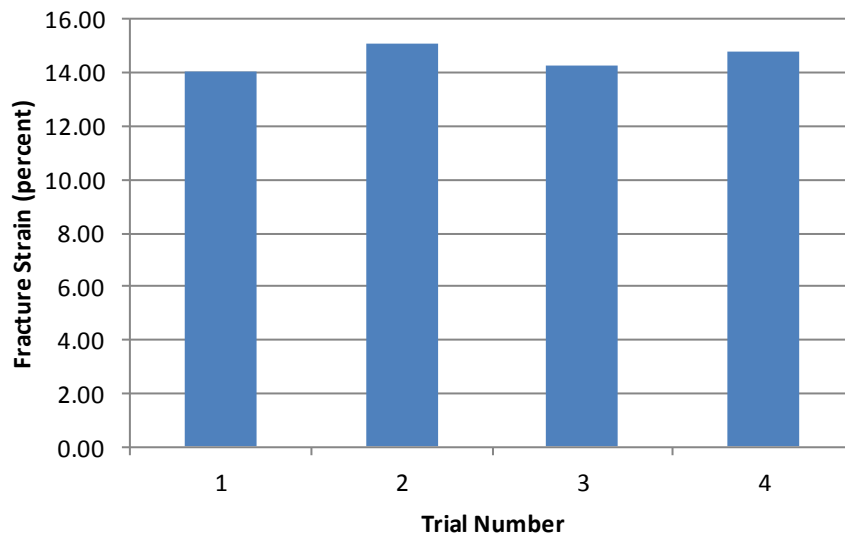


Figure 8-5 Repeatability of Fracture Strain Measurement at 0 ppm Hydrogen

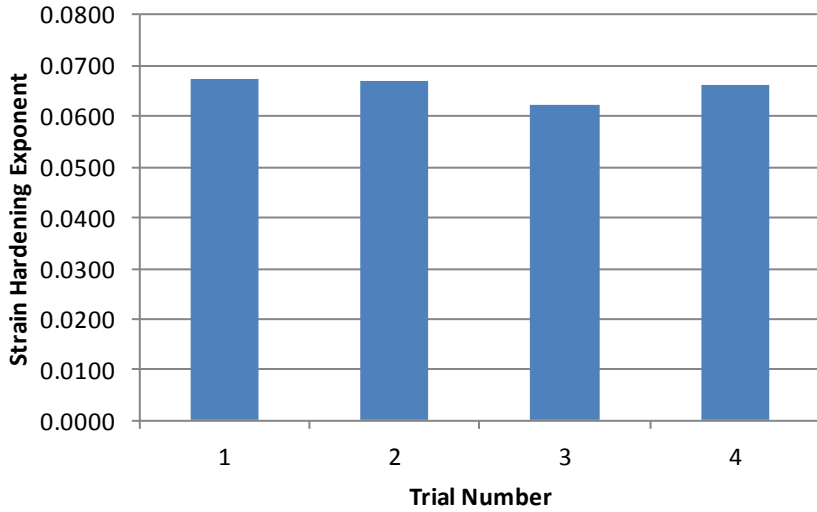


Figure 8-6 Repeatability of Strain Hardening Exponent Measurement at 0 ppm Hydrogen

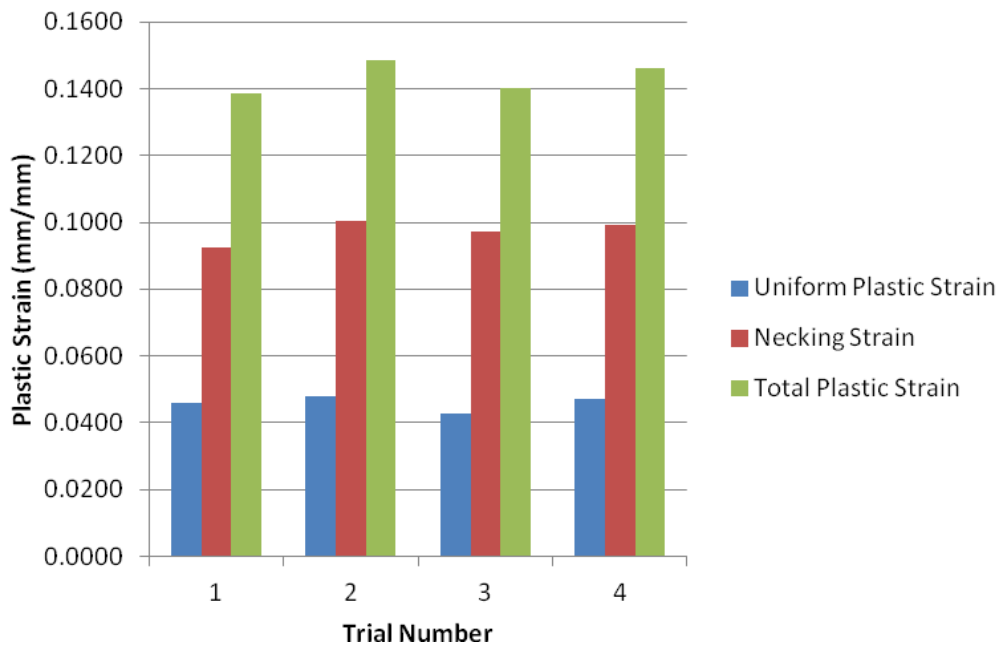


Figure 8-7 Repeatability of Plastic Strain Measurements at 0 ppm Hydrogen

8.4 Effect of Surface Condition on Tensile Tests

To quantify the effect of surface corrosion alone (without hydrogen present), eight samples were tested after undergoing varying amounts of surface degradation caused by time in the charging solution. There was significant surface damage apparent that increased with increasing time in solution. The samples in Figure 8-8 are placed in order of time/damage starting on the left with 96 hours exposure and zero exposure on the right. After charging for 96, 48, 36, 24, 12, 6, 3, or zero hours the charged samples were removed from the solution. Then the standard hydrogen bake-out procedure was used to remove any mobile dissolved hydrogen. Tensile testing was carried out to determine the effect of the change in surface condition for all of the tensile test output variables.

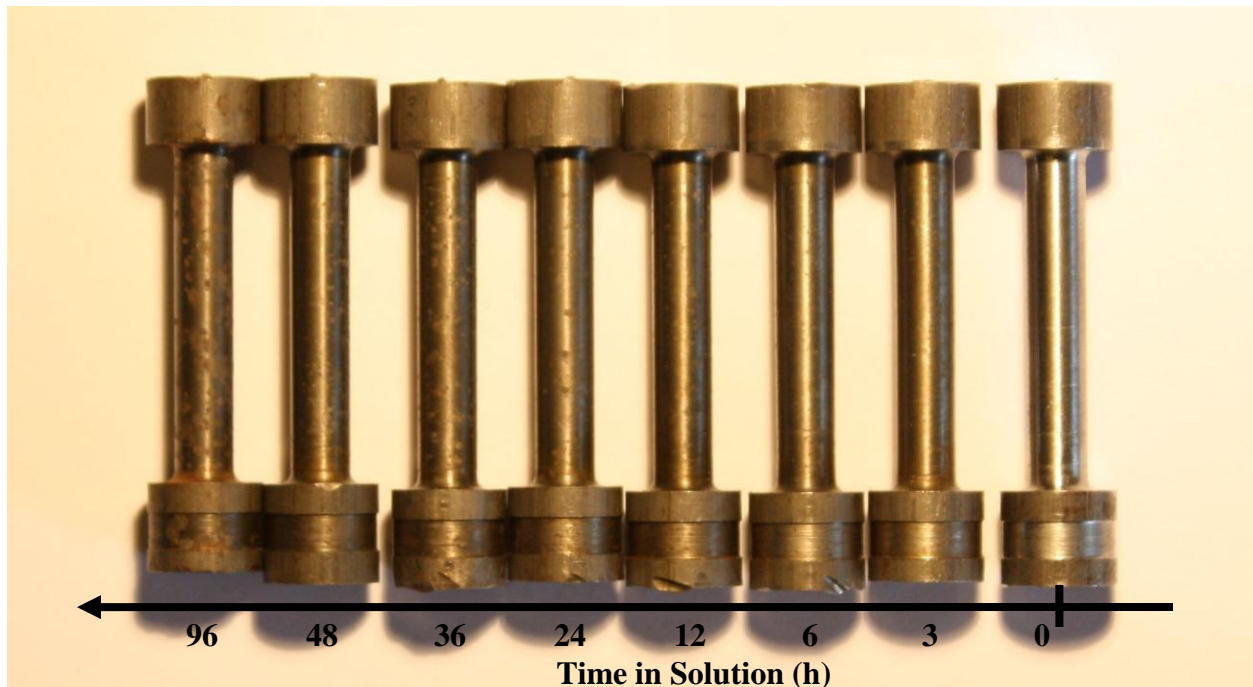


Figure 8-8 Photograph of Tensile Samples showing Extent of Surface Corrosion

As seen in Figure 8-9, Figure 8-10, and Figure 8-11 there is no measureable effect from the surface condition on any of the output measures. All plots are flat and show no change between

samples that spent little or no time in solution to those that spent almost 100 hours in the charging solution. Table 8-3 presents the mean, standard deviation, and coefficient of variation of all eight trials for all output measures. In terms of the output measures resulting from the tensile test, removing the hydrogen using the bake-out procedure appears to return the material to original condition. At a $p < 0.001$ probability all output measures are the same for the repeatability and surface condition experiments.

Table 8-3 Means and Standard Deviations for the Surface Condition Tests of all Outputs

	<i>Mean</i>	<i>Standard Deviation</i>	<i>Standard Deviation as % of Mean</i>
Yield Strength (MPa)	561.32	2.57	0.46 %
Ultimate Strength (MPa)	622.46	3.38	0.54 %
Fracture Strain (%)	14.55	1.00	6.89 %
Strain Hardening Exponent	0.0652	0.0014	2.14 %
Uniform Plastic Strain (mm/mm)	0.0463	0.0036	7.73 %
Final Plastic Strain (mm/mm)	0.1434	0.0101	7.02 %
Necking Strain (mm/mm)	0.0971	0.0071	7.30 %

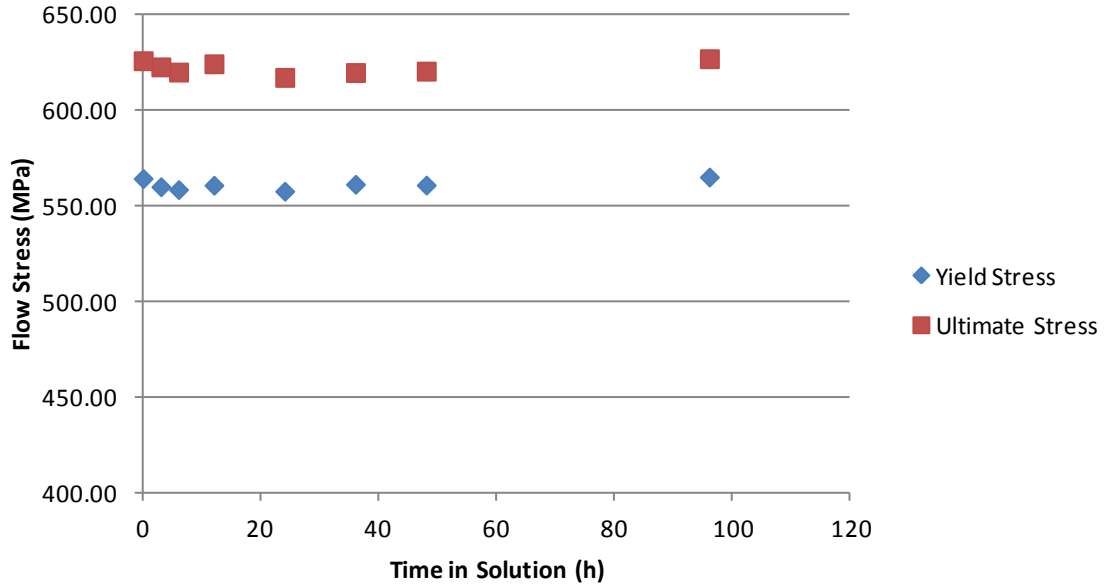


Figure 8-9 Effect of Surface Corrosion on Yield and Ultimate Strengths

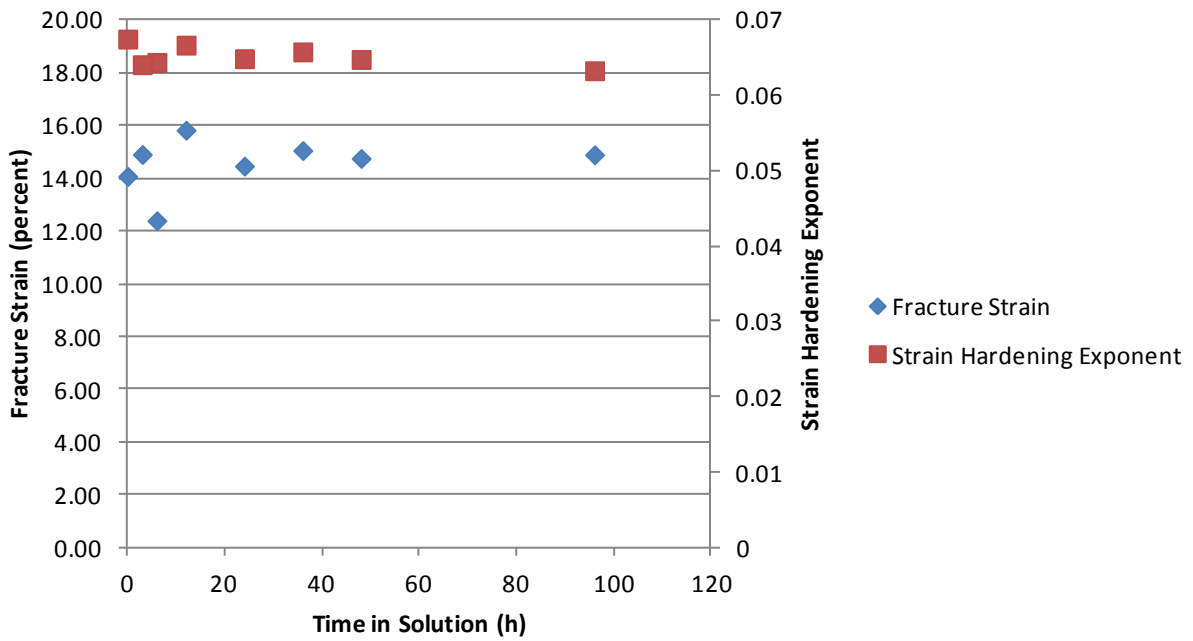


Figure 8-10 Effect of Surface Corrosion on Fracture Strain and Strain Hardening

Exponent

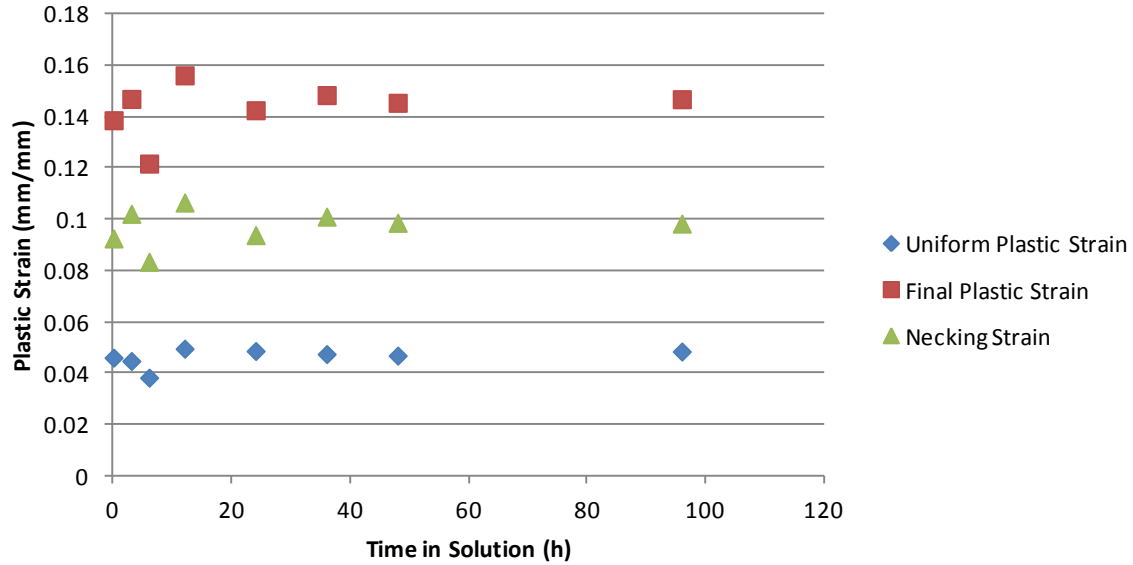


Figure 8-11 Effect of Surface Corrosion on Plastic Strains (Uniform, Necking, and Total)

8.5 Effect of Hydrogen Egress during Tensile Tests

This intent of this testing was to examine the effect of hydrogen leaving the sample during the tensile test procedure, which in the main experiment lasted from a few seconds to 40 minutes, depending on strain rate. Six samples were tested using a uniform hydrogen charging time of 48 hours, leading to an approximate hydrogen concentration of 1.7 ppm. Each sample was loaded past the yield point at a strain rate of $1.54 \times 10^{-3} \text{ s}^{-1}$, then unloaded and allowed to rest for a predetermined time, and finally reloaded to failure. Two samples were tested with a rest time of zero minutes, and one sample each for rest times of 10, 20, 30, and 40 minutes. Increasing the rest time allows for more hydrogen to exit the sample. A sample plot of the stress-strain data produced can be seen in Figure 8-12. Upon reloading, there is no re-establishment of upper and lower yield points although the material does re-enter progressive yielding at a stress higher than it left. Following this higher yield, there is a flattened Lüders region that eventually rejoins the original flow stress path. The features of this plot are reproduced on the plots for all conditions.

Each of the plots of stress and strain are not shown, but the elevation of this subsequent reloading yield point above the overall path does not appear to have a magnitude dependant effect of increasing rest time (therefore decreasing hydrogen concentration).

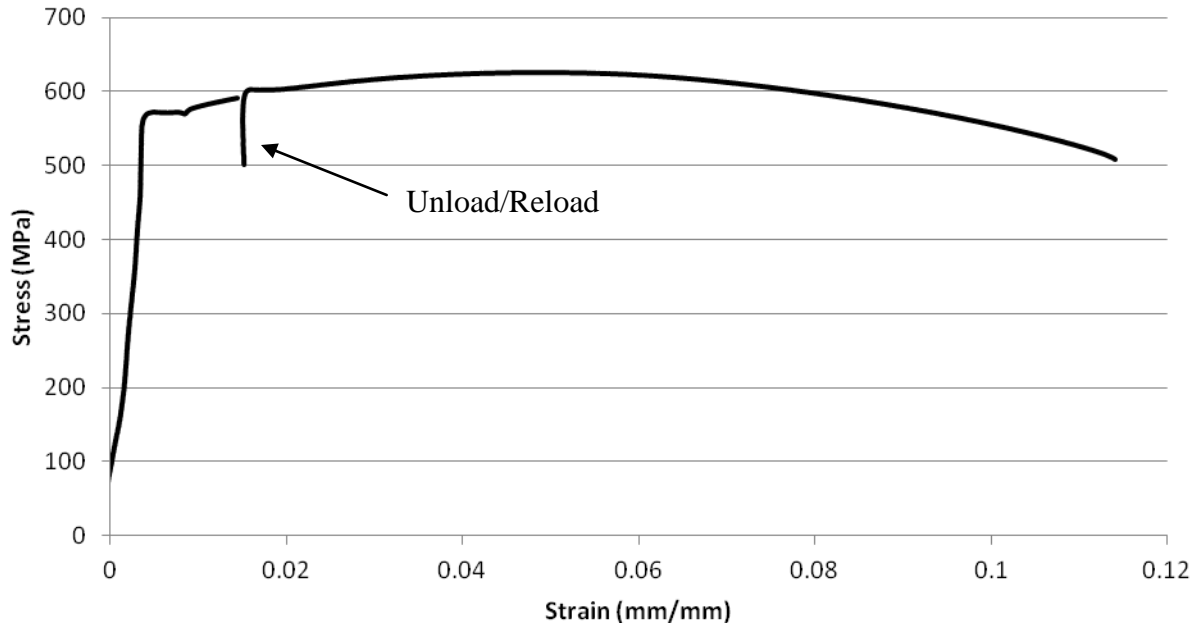


Figure 8-12 Stress-Strain Curve showing Unload Cycle (20 minutes rest for this sample)

The portion of the test up to yield was the same for each sample, and as seen in Figure 8-13 the yield strength for all tests was relatively consistent. The ultimate and fracture stresses are also plotted, with the fracture stress showing increased variation. To remove some of the natural variability between samples, the ultimate and fracture stresses were plotted (Figure 8-14), this time normalized by dividing by the sample's yield strength. From this figure the normalized ultimate strength is seen to be very consistent, but the fracture stress still retains its variability. Also plotted on a secondary axis in Figure 8-13 is the necking strain, which follows an inverse of the fracture stress pattern. No clear relationship is present with increasing rest (hydrogen egress)

time, although necking strain has a much higher coefficient of variance and therefore much more variability is expected. These findings show no effect from the amount of time it takes to perform the tensile test at any of the tested strain rates.

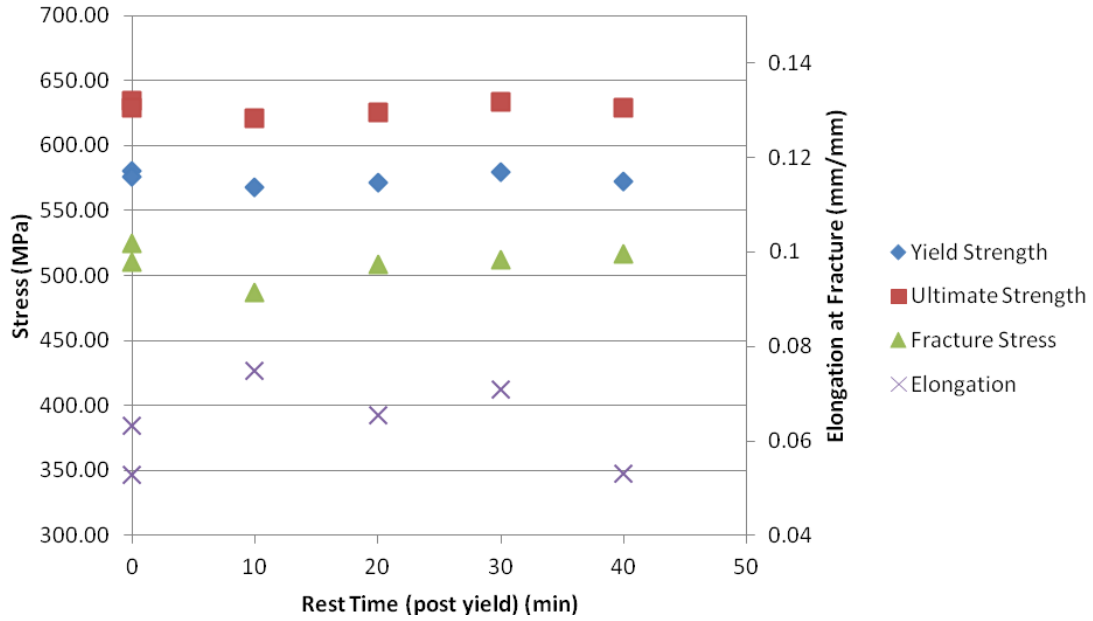


Figure 8-13 Flow Stresses and Elongation versus Rest (Hydrogen Egress) Time

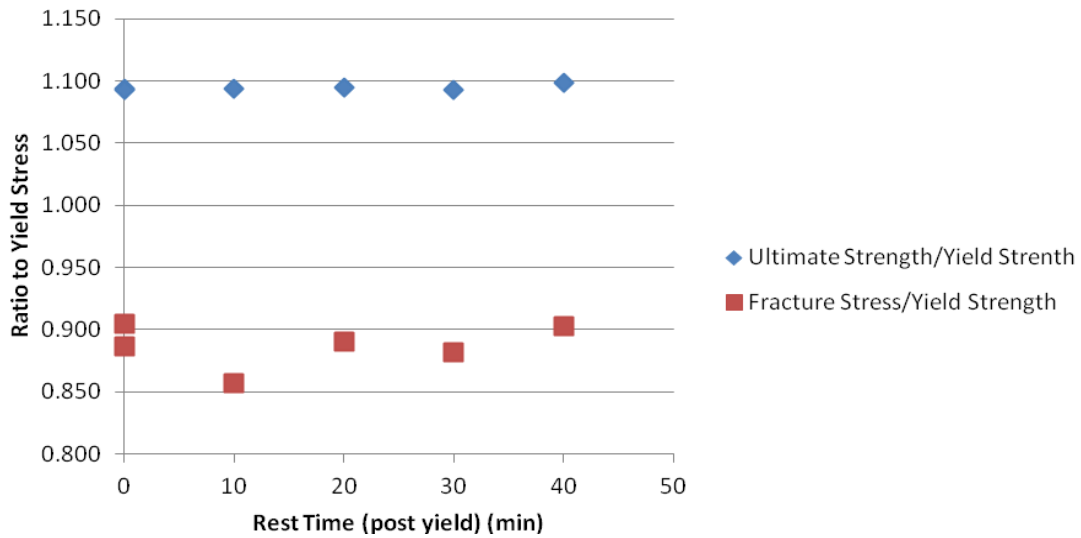


Figure 8-14 Plot of Normalized Ultimate and Fracture Stresses versus Rest Time

8.6 Effect of Momentum on Tests with Highest Crosshead Speeds

To rule out the possibility of elastic rebound or momentum effects during the tensile tests at the highest crosshead speeds, three tensile tests were carried out while recording time and displacement. Because the tensile tests were displacement controlled, and displacement was recorded at regular time intervals any elastic rebound or momentum effects would be recorded as a deviation from a straight line in a displacement versus time plot. The two curves plotted in Figure 8-15 represent the highest strain rate tested for this work (100 mm/min or $6.17 \times 10^{-2} \text{ s}^{-1}$) and another strain rate above that (250 mm/min or $1.54 \times 10^{-1} \text{ s}^{-1}$). Also tested was a much slower strain rate (2.5 mm/min or $1.54 \times 10^{-3} \text{ s}^{-1}$) (not shown). As can be seen, there is no deviation from a straight line displacement versus time response for either speed. Further, when the slopes of each line are compared they correspond exactly to the values expected by comparing to the crosshead speeds (249.88 mm/min, 99.90 mm/min, and 2.504 mm/min).

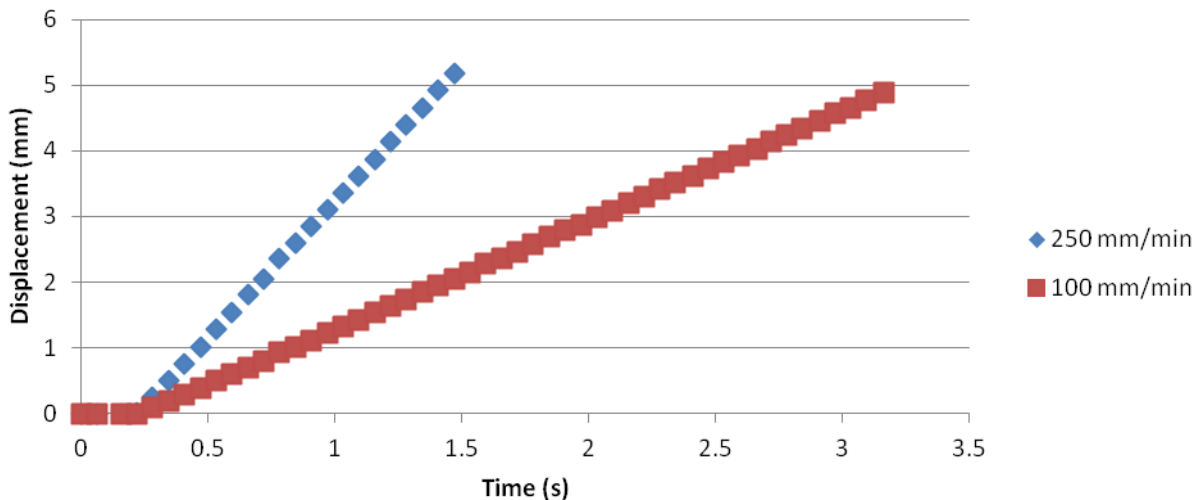


Figure 8-15 Displacement versus Time Plot to Check for Momentum Effects during Tensile Tests at High Crosshead Speeds

8.7 Main Experiment: Tensile Tests of Low Carbon Steel with Varying Strain Rate and Hydrogen Concentration

The remainder of this chapter concerns the results from the tensile test experiments. The two main variables that were controlled, namely hydrogen concentration in the tensile sample and strain rate for the tensile test, will be analyzed for their effect on each of the outcome measures. A general linear model was applied for a statistical analysis of all variables, yielding results both in terms of statistically significant relationships (p-values) and for correlation measures. It is sometimes difficult to visualize three-dimensional data (plotting strain rate and hydrogen concentration versus each outcome). Therefore all outcome measures are plotted two ways: First against strain rate, grouped by hydrogen concentration, and secondly plotted against hydrogen concentration, grouped by strain rate. This allows for visual identification of relationships between the variables whether they are dominated by strain rate, hydrogen concentration, or both.

Then some simplified table/contour plots are presented to show any trends between strain rate and hydrogen concentration and some features of the stress/strain curve. These three tables are based on 1) presence of yield point elongation, 2) presence of upper and lower yields, and 3) whether the yield point elongation had a serrated (jagged) appearance. The last section presents photographic evidence of the failed tensile specimen by looking at the final failed surface.

8.7.1 Statistical Analysis of Outcome Measures

All recorded data were organized into a table containing the values of the input variables (strain rate ($\dot{\epsilon}$) and hydrogen concentration ($[H]$)) and all of the output variables from each observation (yield strength (σ_y), ultimate strength (σ_u), elongation at fracture (ϵ_f), strain hardening exponent (n), uniform plastic strain (ϵ_{up}), necking strain (ϵ_n), and fracture stress (σ_f)).

Main Effects. Table 8-4 presents the statistical p-values for an analysis based on an assumed linear relationship between the values of the input variable and a particular outcome measure. Statistically significant relationships are shaded for identification. Care must be taken when analyzing the results based on a linear relationship, because some effects may not be linear. Never-the-less, this is a useful tool to begin to analyze a large amount of data. Strain rate has a statistically significant effect on all of the measured output measures except elongation at fracture and necking strain. Hydrogen concentration in the material is shown to only have a significant effect on yield strength, fracture strain, and necking strain. Analysis of the data set looking for interactions between the input variables (increased sensitivity to one variable given the presence of the other) found no significant effects, though at $p = 0.099$ for strain hardening exponent and uniform strain there may be a marginal interaction. R^2 is a measure of the effect size, or how much of the observed behaviour of the output measure is due to the effects of the input variable. The only output measures that are shown to be affected by both of the input variables are yield strength and fracture stress.

Table 8-4 Statistical p-Values for all Main Effects, Interactions, and Effect Size for all Outcome Measurements from the Tensile Test

	Outcome Measures						
	σ_y	σ_u	ϵ_f	n	ϵ_{up}	ϵ_n	σ_f
$\dot{\epsilon}$	<0.001	<0.001	0.162	<0.001	<0.001	0.203	<0.001
$[H]$	0.009	0.438	<0.001	0.911	0.874	<0.001	<0.001
$\dot{\epsilon}_x [H]$	0.286	0.573	0.153	0.099	0.099	0.185	0.997
R^2	0.589	0.470	0.478	0.534	0.445	0.621	0.800

Correlation analyses. The Pearson correlation coefficients were calculated for each of the input variables against each of the output variables and are plotted in Table 8-6 and Table 8-7. The correlation analysis is based on an assumed linear underlying relationship and indicates the relative strength of the relation. It provides no information regarding the functional relationship that may exist. Table 8-5 below defines what represents a strong or weak correlation and supports their categorization by relating to levels of significance (not the same significance values of Table 8-4 above). The shading conventions introduced for the correlation strength here are used to indicate the strength of correlations in Table 8-6 and Table 8-7.

Table 8-5 Pearson Correlation Category Definitions for Main Experiment

Correlation Strength	\pm Value	p value
None	< 0.25	1.0 – 0.5
Small	0.25 – 0.55	0.5 – 0.2
Medium	0.55 – 0.75	0.15 – 0.05
Strong	> 0.75	< 0.05

The values below in Table 8-6 answer the question: Is there a correlation between strain rate and our outcomes at various hydrogen concentrations?

Table 8-6 Correlation Coefficients between Strain Rate and Various Outcome Measures

[H] (ppm)	σ_y	σ_u	ϵ_f	n	ϵ_{up}	ϵ_n	σ_f
0.000	0.881	0.786	-0.277	0.732	0.594	-0.814	0.985
0.280	0.444	0.629	0.088	0.726	0.534	-0.410	0.725
0.517	0.786	0.883	0.297	0.664	0.621	-0.030	0.614
0.890	0.707	0.628	0.790	0.881	0.860	0.629	0.683
1.349	0.917	0.817	0.237	0.777	0.707	0.175	0.393
1.586	0.703	0.553	0.256	0.855	0.794	-0.164	0.821
1.709	0.899	0.700	0.294	0.820	0.575	-0.020	0.803
1.831	0.505	0.358	0.238	0.716	0.879	-0.325	0.835
Average	0.730	0.669	0.240	0.771	0.696	-0.120	0.732

The values below in Table 8-7 answer the question: Is there a correlation between hydrogen concentration and our outcomes at various strain rates?

Table 8-7 Correlation Coefficients between Hydrogen Concentration and Various Outcome Measures

Strain Rate (s^{-1})	σ_y	σ_u	ϵ_f	n	ϵ_{up}	ϵ_n	σ_f
6.17×10^{-5}	0.456	0.023	-0.727	0.100	0.232	-0.810	0.874
1.54×10^{-4}	0.243	-0.090	-0.761	0.141	0.473	-0.945	0.850
6.17×10^{-4}	0.694	0.627	-0.735	-0.220	-0.195	-0.765	0.842
1.54×10^{-3}	-0.417	-0.463	-0.766	0.449	-0.211	-0.843	0.912
6.17×10^{-3}	0.416	0.247	-0.737	-0.341	-0.455	-0.755	0.844
3.09×10^{-2}	0.680	0.003	-0.804	-0.800	-0.568	-0.839	0.970
6.17×10^{-2}	0.147	-0.359	-0.666	0.369	0.127	-0.825	0.955
Average	0.317	-0.002	-0.742	-0.043	-0.085	-0.826	0.892

These correlation tables support the observations seen in the main effects of Table 8-4 (statistical significance). Namely that yield strength, ultimate strength, fracture strain, strain hardening exponent, and uniform plastic strain are all affected by strain rate and that fracture strain and necking strain are affected by hydrogen concentration. As mentioned previously, statistical significance, correlations, and effect size do not indicate the functional relationship between the inputs and observations. They only indicate that some underlying function probably exists. To determine what those relationships are, we must examine the graphs of the variables themselves.

8.7.2 Flow Stresses (Yield Stress and Ultimate Stress)

Figure 8-16 and Figure 8-17 plot yield strength and ultimate strength versus strain rate. The positive trend of increasing yield strength at increasing values of strain rate is readily apparent, as would be expected from this well-known phenomenon [Hertzberg, 1996 pg 49]. The difference between the maximum (608 MPa) and minimum (548 MPa) observed yield strength values is over fifteen times the standard deviation of the measurements conducted for the repeatability study (Section 8.3). Similarly, difference between the maximum (655 MPa) and minimum (605 MPa) observed values of the ultimate strength is almost twenty times the standard deviation seen in the repeatability study. There is considerable overlap between the individual curves that would represent the various hydrogen concentrations. These curves were separated in Figure 8-20 and Figure 8-21 to show their individual shapes. The yield strength trend line follows a power law of the form $\sigma_y = 602 \dot{\epsilon}^{0.0079}$ and the ultimate strength $\sigma_u = 653 \dot{\epsilon}^{0.00596}$

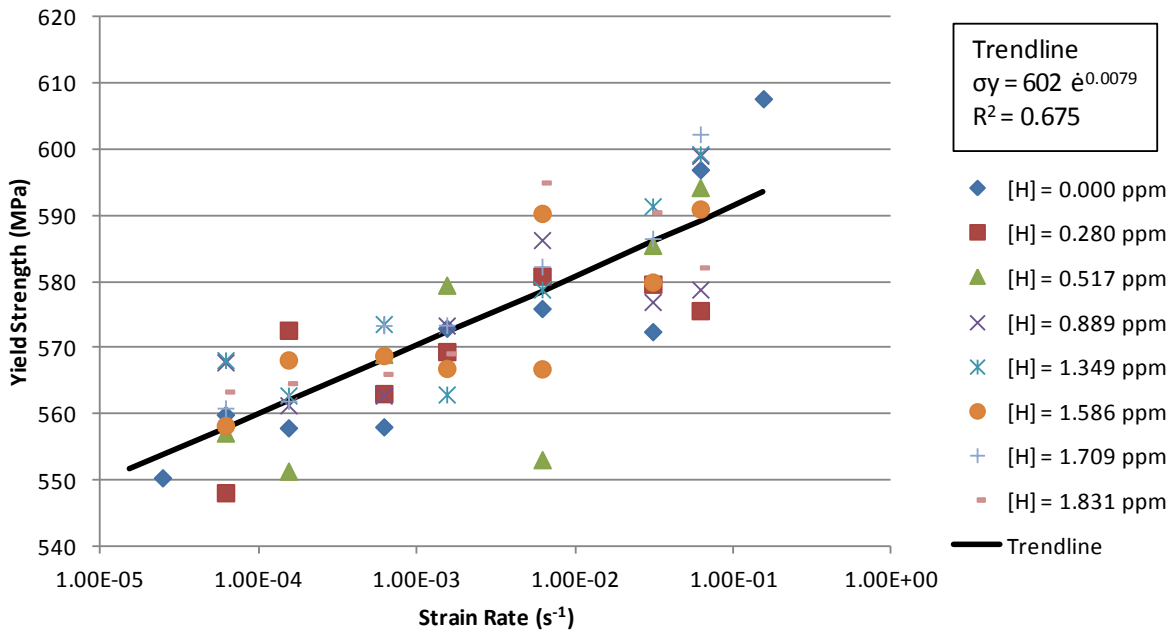


Figure 8-16 Strain Rate vs. Yield Strength for all Hydrogen Concentration Conditions

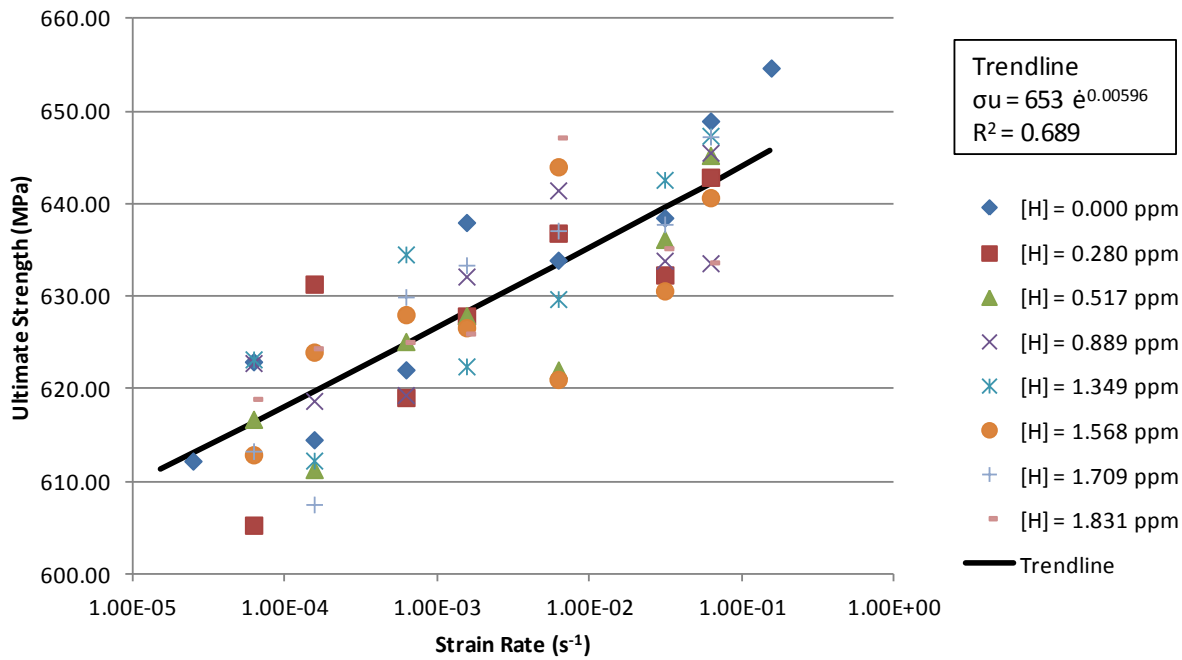


Figure 8-17 Strain Rate vs. Ultimate Strength for all Hydrogen Concentration Conditions

Figure 8-18 and Figure 8-19 show exploded plots of yield strength and ultimate strength versus hydrogen concentration. The statistical results shown in Table 8-4 indicated a significant relationship between hydrogen concentration and yield strength but no significant relationship with ultimate strength. As can be seen from the curves in Figure 8-18 the effect of hydrogen, though statistically significant, is minimal in terms of the change in yield and is often ignored in materials engineering practice.

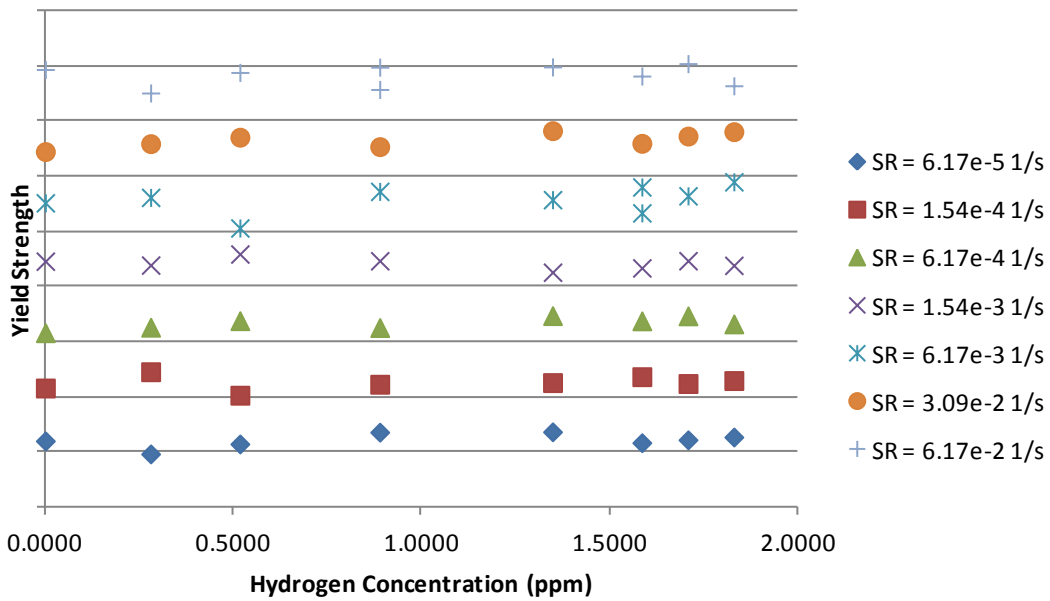


Figure 8-18 Exploded Plot of Hydrogen Concentration vs. Yield Strength (curves generated for each strain rate are artificially separated for clarity)

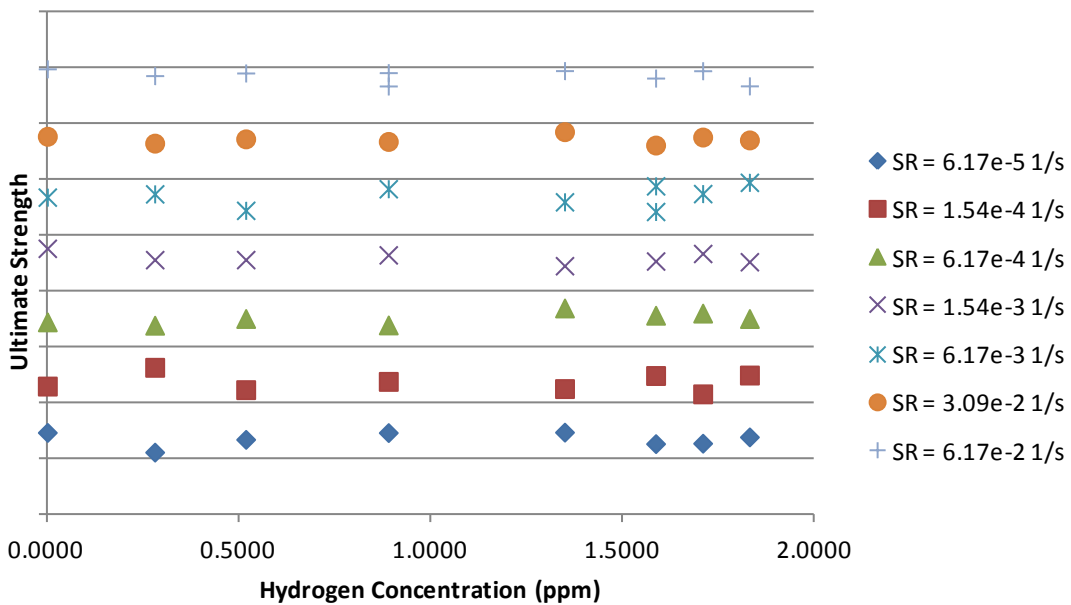


Figure 8-19 Exploded Plot of Hydrogen Concentration vs. Ultimate Strength (curves generated for each strain rate are artificially separated for clarity)

When looking at the exploded yield strength versus strain rate curves (Figure 8-20) several other features become apparent other than the overall increase. First, looking at the curve for $[H] = 1.8306$ ppm, the highest concentration used in this study, we see a slow rate of increase until after the strain rate reaches $1.54 \times 10^{-3} \text{ s}^{-1}$. It peaks around $6.17 \times 10^{-3} \text{ s}^{-1}$ and declines after. For the curves produced by $[H] = 1.3485$ ppm, $[H] = 1.5860$ ppm, and $[H] = 1.7087$ ppm there is a generally smooth and consistent increase throughout the strain rate range. The curves for the lower hydrogen concentrations have more complex shapes and do not always follow a monotonic increase. These observations are repeated for the ultimate strength versus strain rate curves (Figure 8-21).

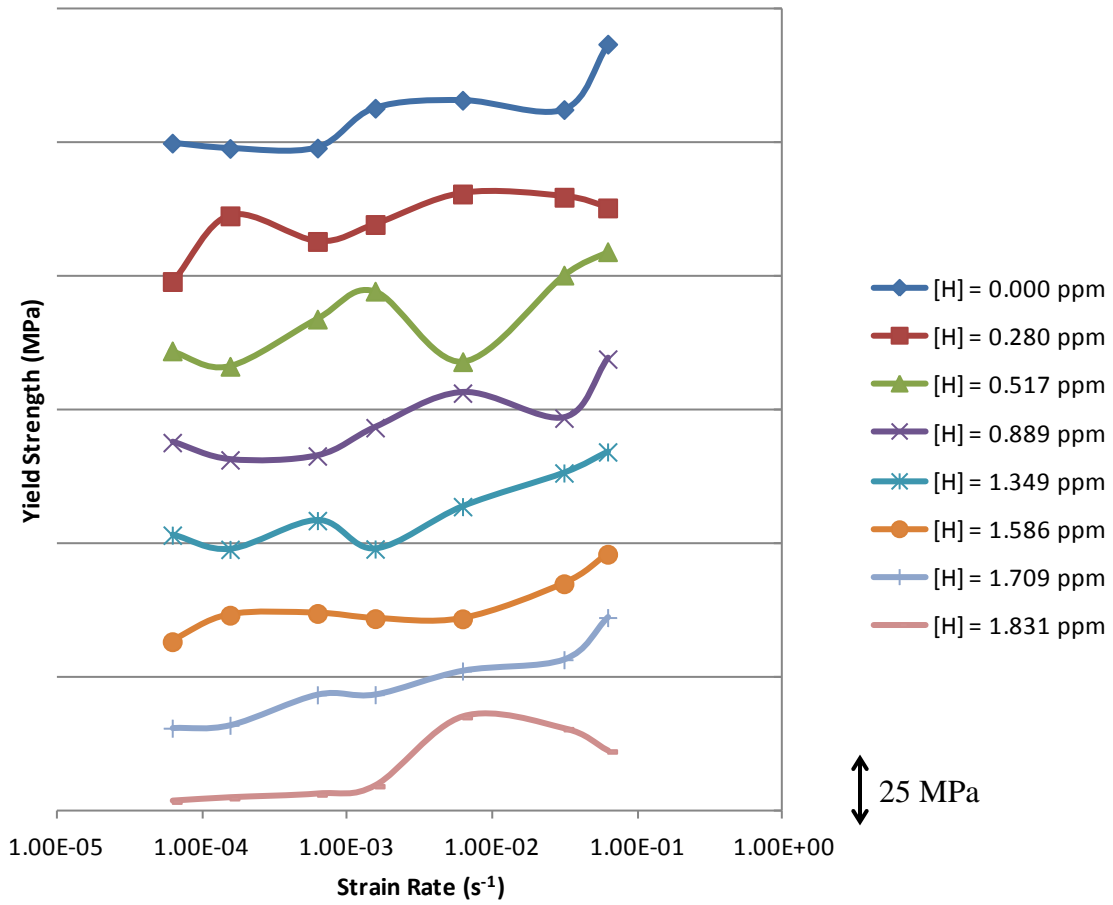


Figure 8-20 Exploded Plot of Strain Rate vs. Yield Strength (curves generated for each hydrogen concentration are artificially separated for clarity)

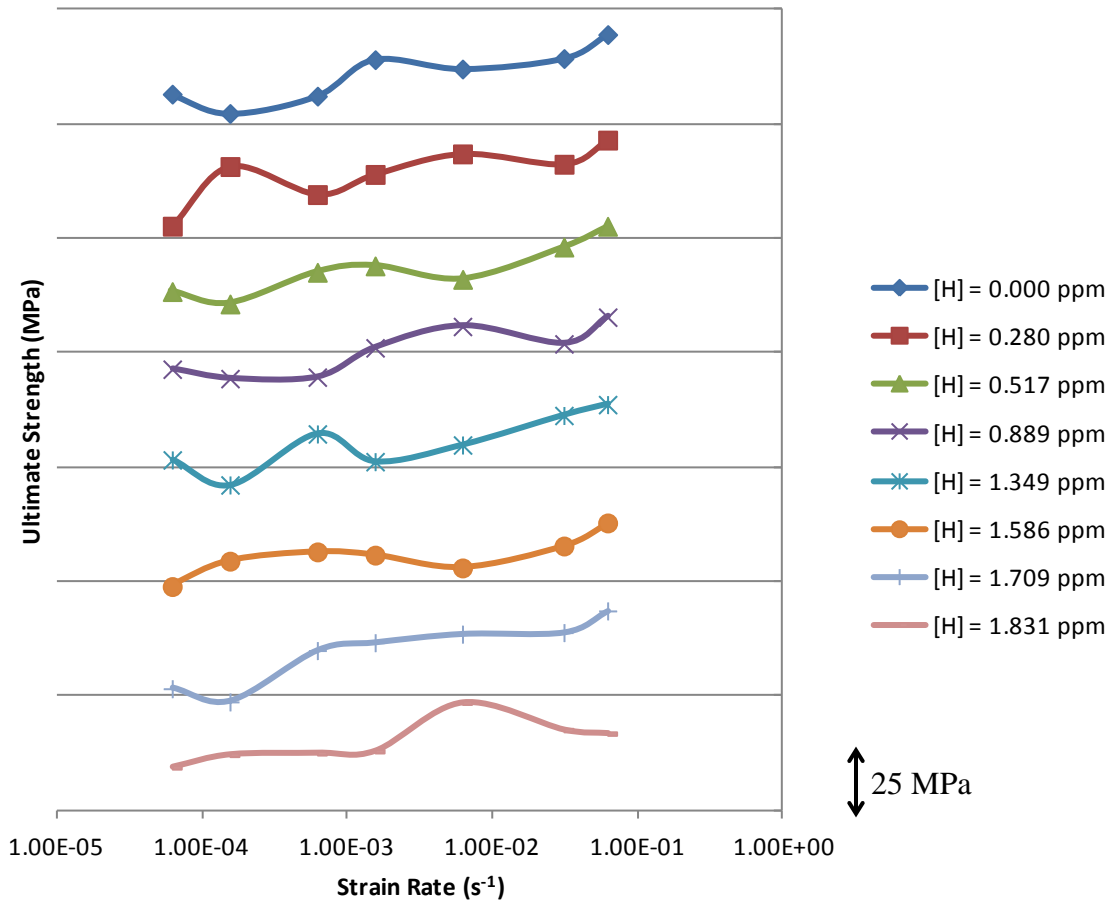


Figure 8-21 Exploded Plot of Strain Rate vs. Ultimate Strength (curves generated for each hydrogen concentration are artificially separated for clarity)

8.7.3 Fracture Stress

Figure 8-22 and Figure 8-23 plot the fracture stress versus strain rate and hydrogen concentration. A trend of increasing fracture stress with increasing strain rate is apparent, and follows a power law trend line of $\sigma_f = 516 e^{0.0113}$ with a best-fit $R^2 = 0.131$. A stronger trend of increasing fracture stress with increasing hydrogen concentration is also apparent that follows a linear relationship of $\sigma_f = 43.707[H] + 439.2$ with a best fit $R^2 = 0.609$. As indicated in the statistical table above (Table 8-4), both strain rate and hydrogen concentration have a

relationship to fracture stress at a $p < 0.001$ level. The interaction term of $p = 0.997$ indicates that there is no sensitivity of one factor to the other and the overall result seen is purely additive.

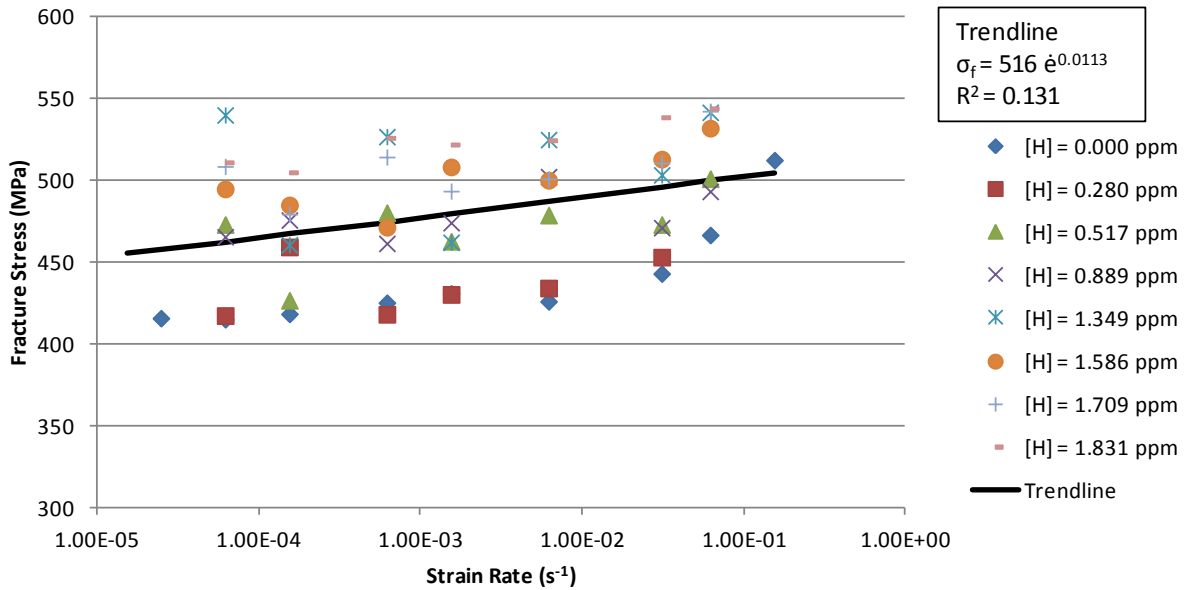


Figure 8-22 Fracture Stress versus Strain Rate for all Hydrogen Concentrations

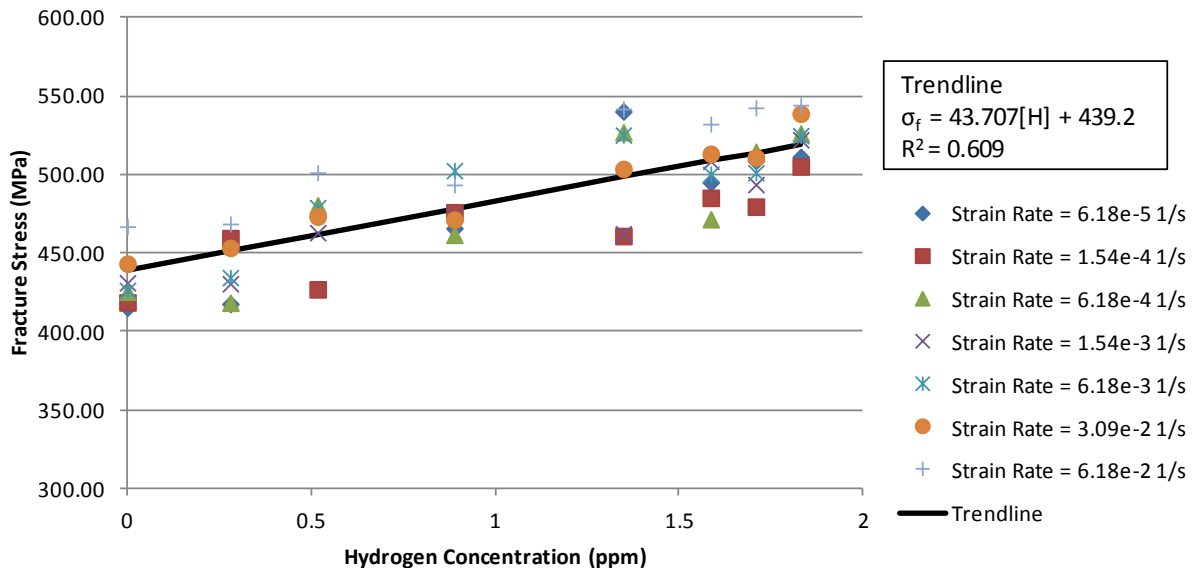


Figure 8-23 Fracture Stress versus Hydrogen Concentration for all Strain Rates

8.7.4 Fracture Strain

Figure 8-24 plots the strain rate versus fracture strain. The table of statistical significance (Table 8-4) indicated a marginally significant relationship, and a slight trend toward increasing fracture strain with increasing strain rate is apparent in the figure. Much stronger is the trend toward decreasing fracture strain with an increase in hydrogen concentration as seen in Figure 8-25. This is an expected result as the effects of hydrogen embrittlement are well known. The difference between the maximum (16.3% elongation) and minimum (8.5% elongation) observed values of fracture strain is almost seventeen times the standard deviation of the repeatability measurement from Section 8.3. The strain rate versus fracture strain trend line follows a power law of the form $\epsilon_f = 13.82 \dot{\epsilon}^{0.0207}$ and the hydrogen concentration versus fracture strain follows a third order polynomial of the form $\epsilon_f = -1.946[H]^3 + 5.709[H]^2 - 5.967[H] + 14.42$.

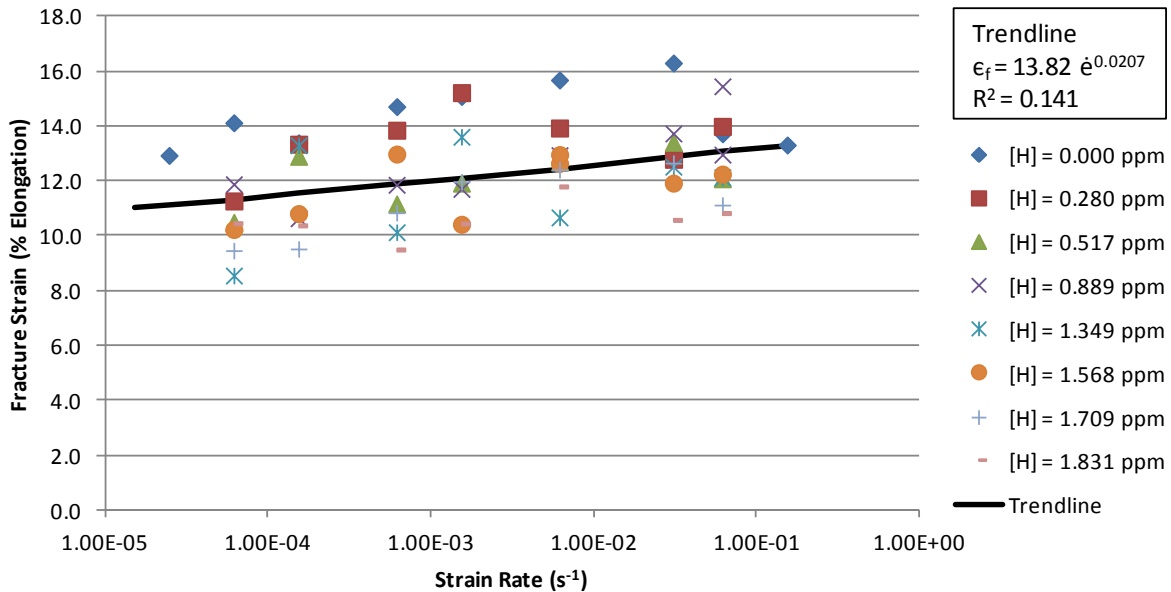


Figure 8-24 Strain Rate vs. Fracture Strain for all Hydrogen Concentration Conditions

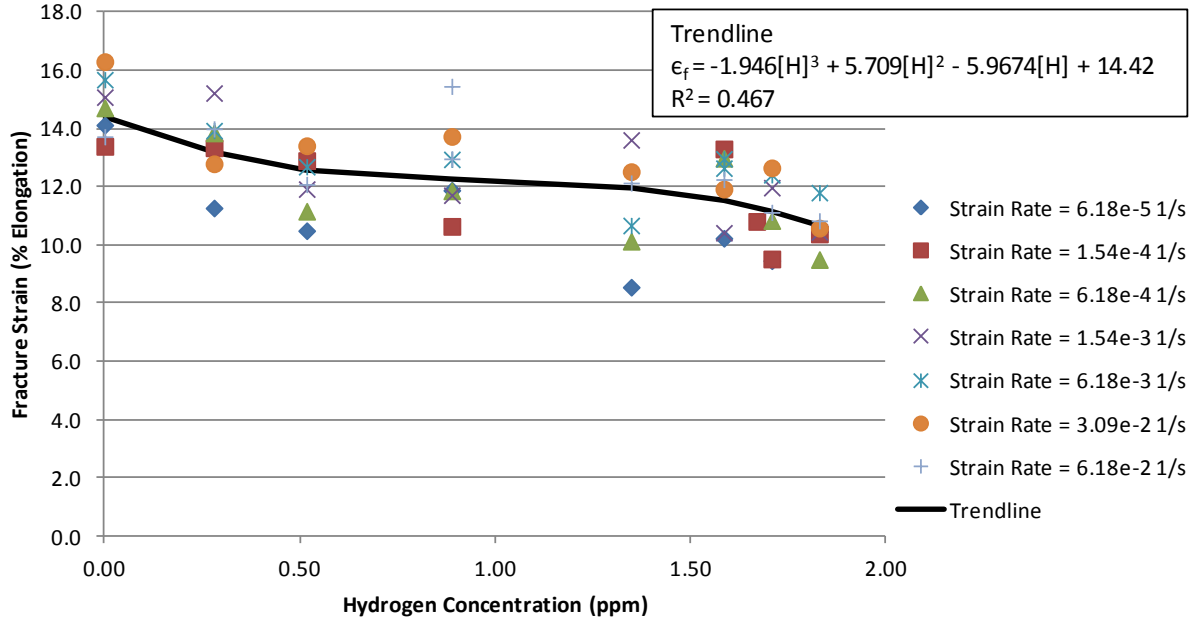


Figure 8-25 Hydrogen Concentration vs. Fracture Strain for all Strain Rate Conditions

8.7.5 Strain Hardening Exponent

Figure 8-26 shows the plot of strain rate versus strain hardening exponent. There is a trend towards increasing strain hardening exponent with increasing strain rate. The difference between the maximum (0.0776) and minimum (0.0461) values of strain hardening exponent is thirteen times the standard deviation of the repeatability measurement from Section 8.3. The strain rate versus strain hardening exponent trend line follows a power law of the form $n = 0.0752 e^{0.0331}$.

Figure 8-27 shows the plot of hydrogen concentration versus strain hardening exponent. There is no observed relation between these variables.

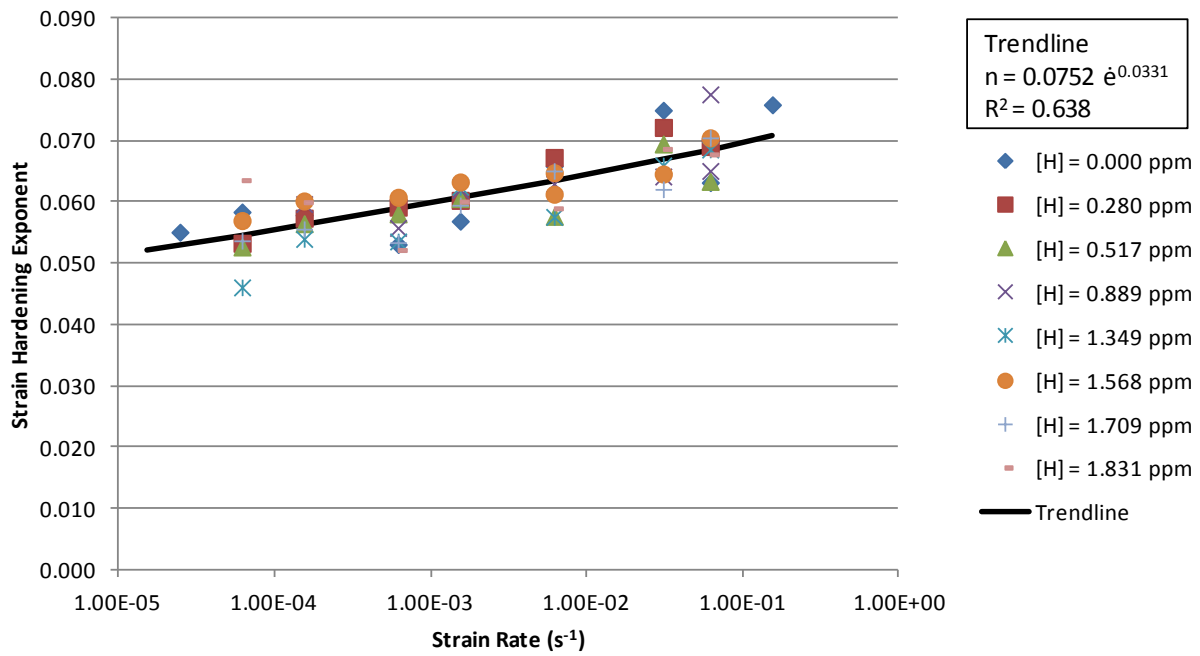


Figure 8-26 Strain Rate vs. Strain Hardening Exponent for all Hydrogen Concentrations

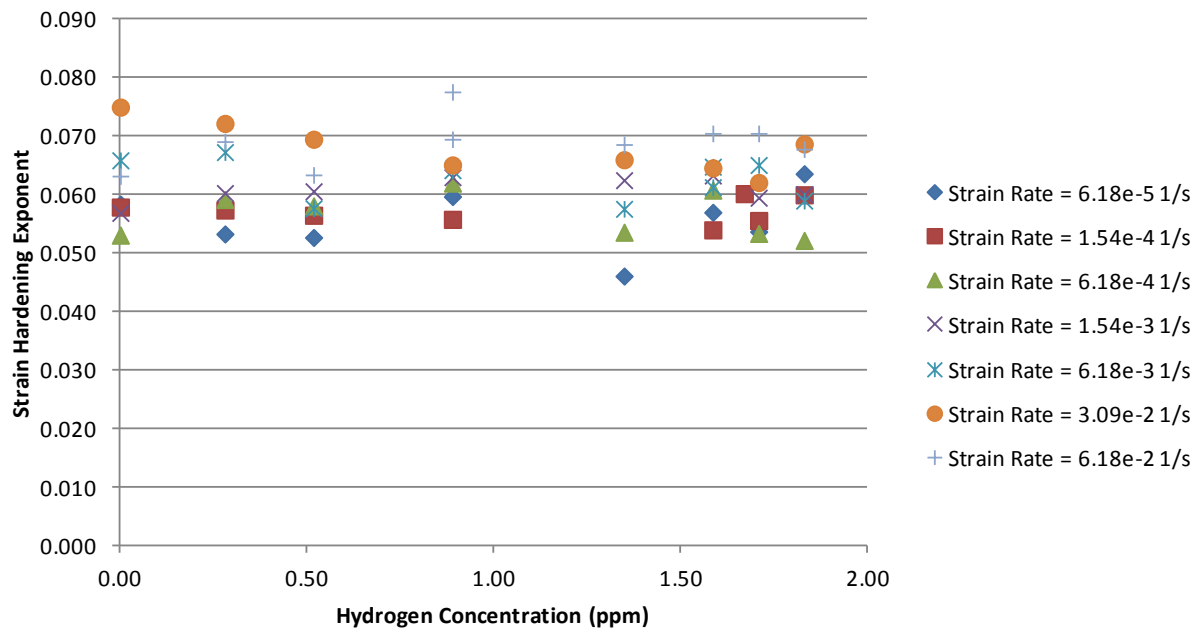
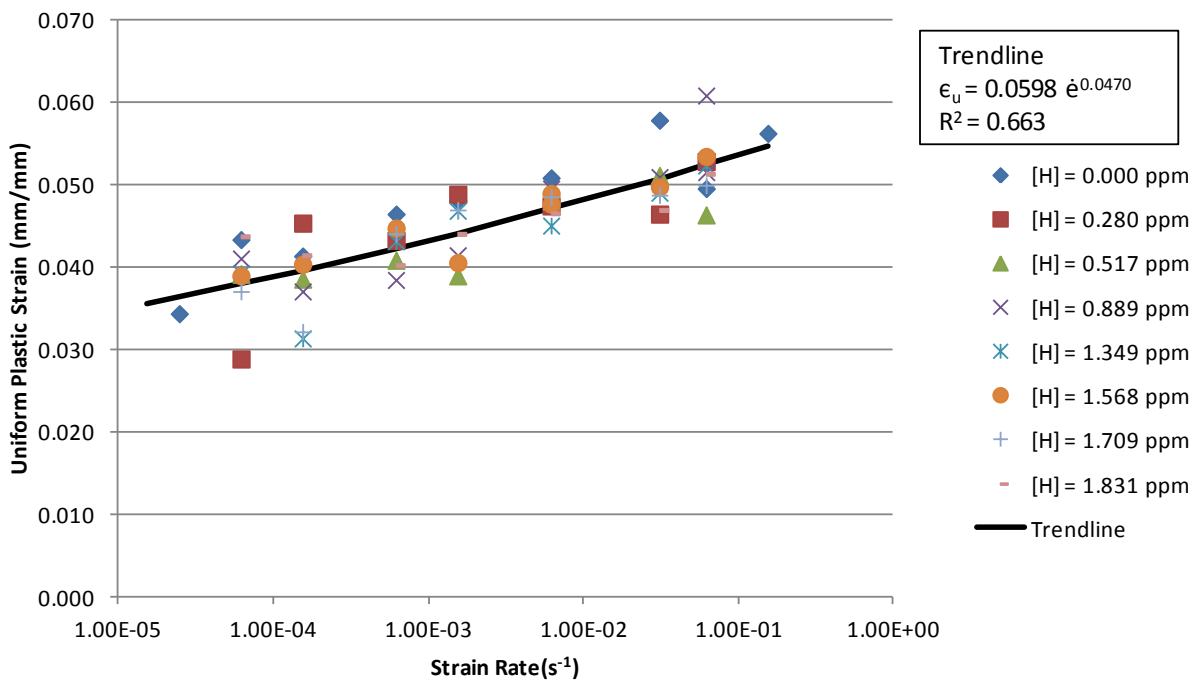


Figure 8-27 Hydrogen Concentration vs. Strain Hardening Exponent for all Strain Rates

8.7.6 Plastic Strains (Uniform Strain and Necking Strain)

Figure 8-28 shows the plot of strain rate versus uniform plastic strain. There is a trend towards increasing uniform plastic strain with increasing strain rate. The difference between the maximum (0.0609) and minimum (0.0289) values of uniform plastic strain is almost fifteen times the standard deviation of the repeatability measurement from Section 8.3. The strain rate versus fracture strain trend line follows a power law of the form $\epsilon_u = 0.0598 \dot{\epsilon}^{0.0470}$. Figure 8-29 shows the plot of hydrogen concentration versus uniform plastic strain. There is no observed relation between these variables.



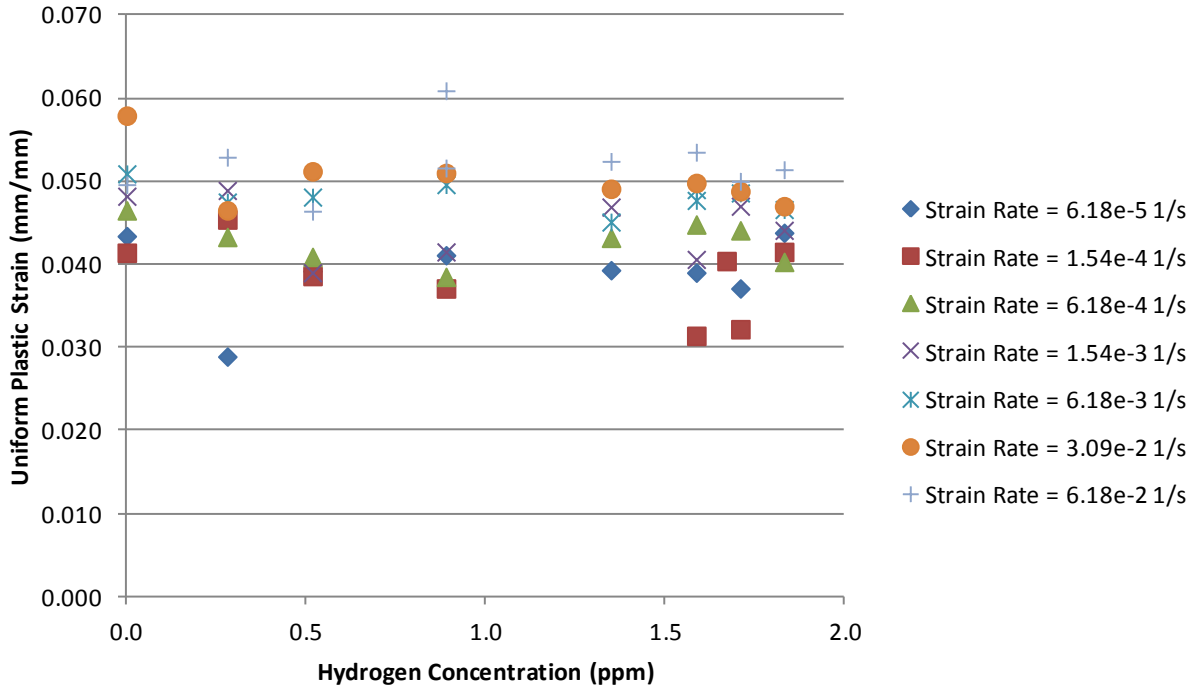


Figure 8-29 Hydrogen Concentration vs. Uniform Plastic Strain for all Strain Rates

Figure 8-30 shows the plot of strain rate versus necking strain. There is no observed relation between these variables. Figure 8-31 shows the plot of hydrogen concentration versus necking strain. There is a trend towards decreasing necking strain with increasing strain rate. The difference between the maximum (0.1038) and minimum (0.0435) values of uniform plastic strain is almost eighteen times the standard deviation of the repeatability measurement from Section 8.3. The hydrogen concentration versus necking strain trend line follows a third order polynomial of the form $\epsilon_n = (-1.13[H]^3 + 3.45[H]^2 - 4.39[H] + 9.44) \times 10^{-2}$.

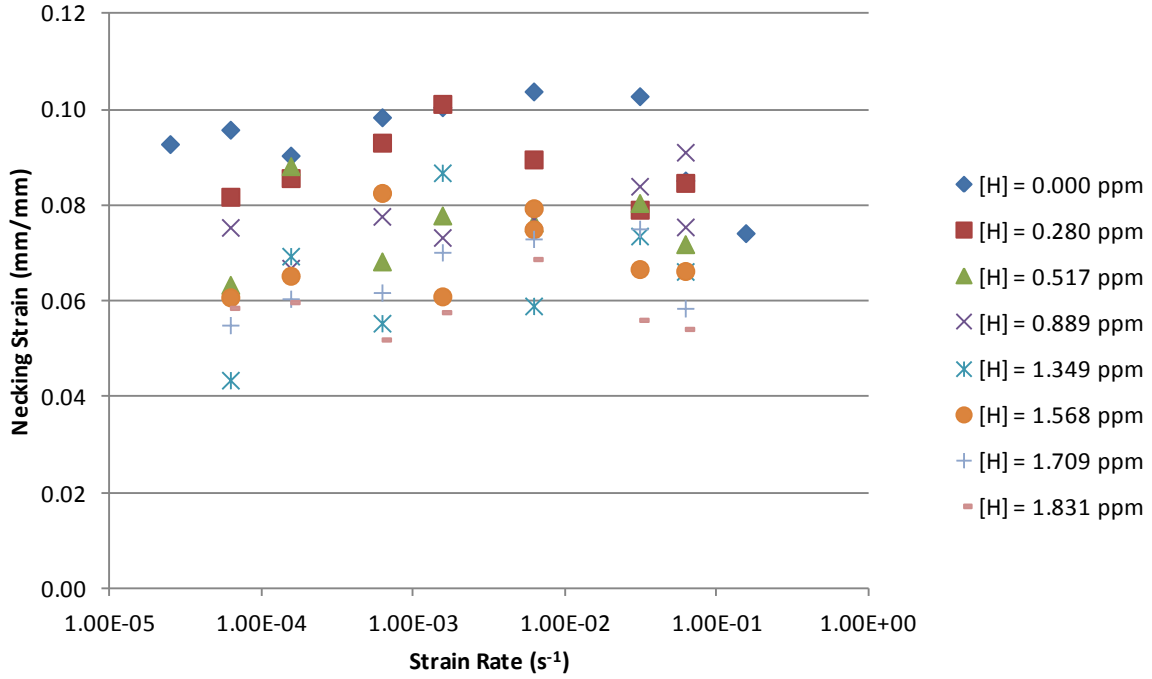


Figure 8-30 Strain Rate vs. Necking Strain for all Hydrogen Concentrations

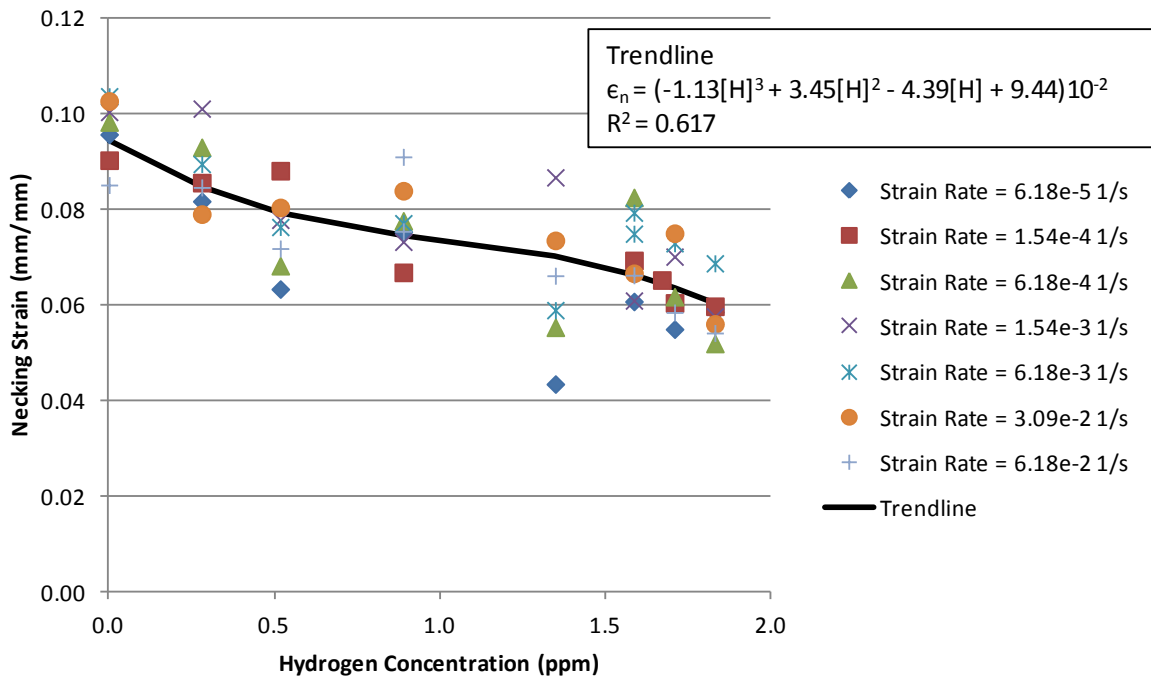


Figure 8-31 Hydrogen Concentration vs. Necking Strain for all Strain Rates

8.8 Presence of Yield Point Elongation, Upper and Lower Yields, and Serrated Yielding

Table 8-8 is a simplified contour plot using the input variables of strain rate and hydrogen concentration with each cell containing information of whether there was apparent yield point elongation (Y = yes, N = no). Table 8-9 is set up in a similar manner but each cell contains information regarding the presence or absence of an upper and lower yield point. The lack of upper and lower yields noted in the table for strain rates of $3.09 \times 10^{-2} \text{ s}^{-1}$ and $6.17 \times 10^{-2} \text{ s}^{-1}$ indicate a lack of information rather than a definitive absence. The strain rates simply overwhelmed the sampling frequency of the testing machine and as such the apparatus was unable to detect and record such fine features if they were present. There does not appear to be any relationship between the variables illustrated in these tables.

Table 8-8 Table/Contour Plot Indicating the Presence of Yield Point Elongation

Presence of Yield Point Elongation							
Hydrogen Concentration (ppm)	Strain Rate (s^{-1})						
	6.17e-5	1.54e-4	6.17e-4	1.54e-3	6.17e-3	3.09e-2	6.17e-2
0.000	Y	N	N	N	Y	Y	Y
0.280	N	Y	N	Y	Y	Y	Y
0.517	Y	N	Y	Y	N	Y	N
0.889	Y	Y	Y	N	Y	N	Y
1.349	N	N	Y	N	Y	Y	Y
1.568	Y	N	Y	N	Y	N	N
1.709	Y	N	N	Y	Y	Y	Y
1.831	Y	Y	N	N	Y	Y	Y

Table 8-9 Table/Contour Plot Indicating Presence of Upper and Lower Yield Points

Presence of Upper and Lower Yield Points							
Hydrogen Concentration (ppm)	Strain Rate (s⁻¹)						
	6.17e-5	1.54e-4	6.17e-4	1.54e-3	6.17e-3	3.09e-2	6.17e-2
0.000	Y	N	N	Y	N	N	N
0.280	Y	Y	Y	Y	Y	N	N
0.517	Y	Y	N	N	Y	N	N
0.889	N	Y	Y	Y	Y	N	N
1.349	Y	N	Y	Y	N	N	N
1.568	N	N	Y	Y	Y	N	N
1.709	N	N	N	Y	Y	N	N
1.831	Y	Y	Y	Y	N	N	N

Table 8-10 is also a simplified contour plot using the input variables of strain rate and hydrogen concentration with each cell containing information of whether there was apparent serrated yielding. Qualitatively speaking, there may be a trend that flows diagonally down, right to left, where the combination of strain rate and hydrogen concentration produced no serrated yielding, but there were no dissimilarities seen on any other plots of outcome measures that correlate with these findings. Similar to Table 8-9 the findings of no serrated yielding for the two highest strain rate conditions probably indicate a lack of resolution due to limitations in the sampling frequency of the testing machine.

Table 8-10 Table/Contour Plot Indicating the Presence of 'Serrated' Yielding

Presence of 'Serrated' Yielding							
Hydrogen Concentration (ppm)	Strain Rate (s ⁻¹)						
	6.17e-5	1.54e-4	6.17e-4	1.54e-3	6.17e-3	3.09e-2	6.17e-2
0.000	Y	Y	Y	N	Y	N	N
0.280	Y	Y	N	Y	Y	N	N
0.517	Y	N	Y	Y	N	N	N
0.889	Y	Y	Y	Y	Y	N	N
1.349	N	Y	Y	Y	N	N	N
1.568	Y	Y	Y	N	Y	N	N
1.709	Y	N	Y	Y	Y	N	N
1.831	Y	Y	N	Y	N	N	N

8.9 Failure Surface Imaging

Figure 8-32 contains two representative images captured of one side of the final failure surfaces of the tensile samples after testing. Image A) was tested at 0.00 ppm hydrogen and a strain rate of $3.09 \times 10^{-2} \text{ s}^{-1}$, and B) was tested at 1.4620 ppm and $6.17 \times 10^{-5} \text{ s}^{-1}$, representing the conditions showing the most and least ductility, respectively. Readily apparent is the larger final area of the necked section for the low ductility sample. Both samples show ductile fracture with microvoid coalescence and a significant shear lip.

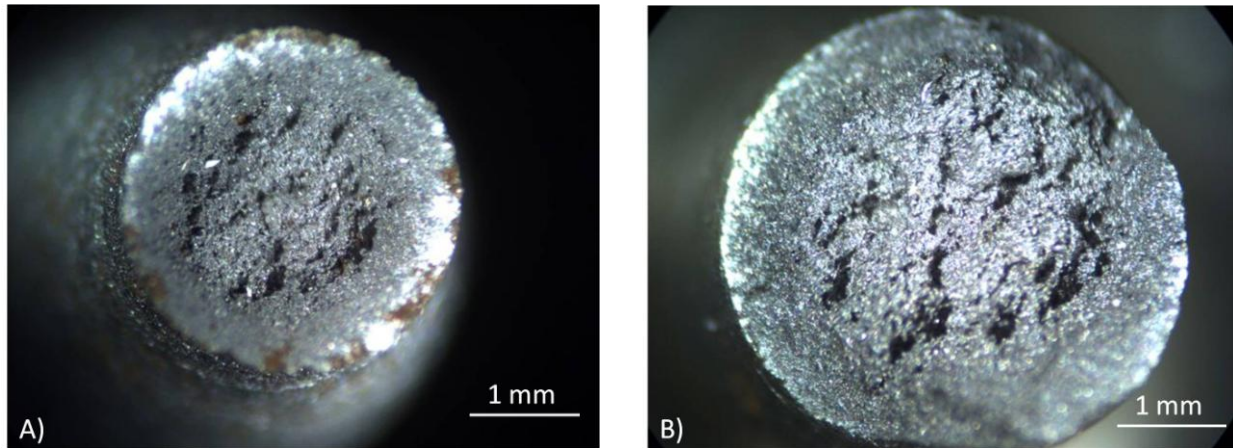


Figure 8-32 Failure Surfaces for Samples Showing the Most (A) and Least (B) Ductility

Figure 8-33 is a composite figure showing the failure surface for all samples tested. All images are taken at the same magnification, so trends seen in feature size are real. There is no trend apparent moving from left to right (increasing strain rate). There is a trend to larger final area moving from top to bottom (increasing hydrogen concentration). There appears to be a trend to greater sized gross deformation features as hydrogen concentration increases.

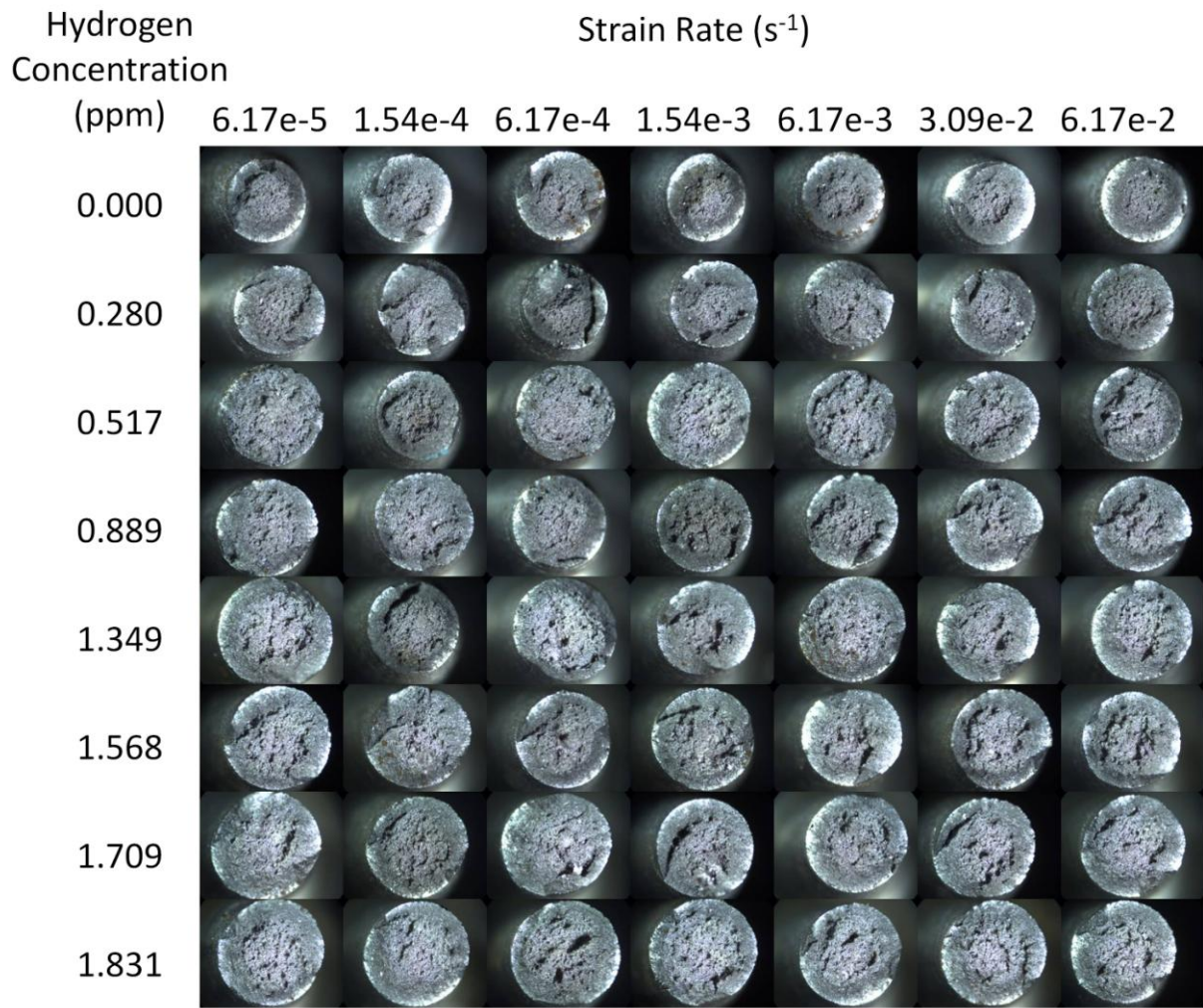


Figure 8-33 Photo-Table of Failure Surfaces for Each Testing Condition

Chapter Nine: **Discussion of Tensile Tests with Varying Strain Rate and Hydrogen Concentration**

The following chapter describes and analyzes the most important results obtained from the experiments dealing with the manipulation of two input parameters, hydrogen concentration and strain rate, and the resulting changes to a number of outcome measures from the tensile test. The outcomes measure a number of important characteristics of the steel's behaviour including yield strength, ultimate strength, fracture stress, elongation at fracture, strain hardening exponent, uniform plastic strain, necking strain, and features of the stress/strain curve around the yield point. The goal of this work is to probe the effects of mobile dissolved hydrogen in a field of moving dislocations. Previous research on another system of mobile solutes, carbon and nitrogen in the dynamic strain aging effect, produced a great deal of knowledge regarding the nature of dislocation movement and the effect of impurities in interfering with that movement. In dynamic strain aging research temperature is varied in order to get the diffusion rate of the solute to match dislocation velocities. In the work presented here temperature is held constant and the strain rate is varied in an attempt to match the diffusion rate. Another major factor in this work and an entirely new approach is to use a two factor design, studying the mechanical properties of the experimental steel while varying both the hydrogen concentration and the strain rate. Several new observations are noted below that would not have been possible to detect without having two input parameters and this type of experimental design.

An important factor in this series of experiments that leads to the increased sensitivity necessary to detect small effects is the use of a single batch of material, and that all specimens were machined at the same time on the same machine, and all were carefully prepared to the same surface finish.

9.1 Microstructure

The microstructural examination revealed that the test material is a typical and inexpensive low carbon steel with a ferritic/pearlitic grain structure. This material is similar to some older pipeline grades, with higher yield and ultimate strengths likely due to the small grain size (average diameter 9.4 μm). The ASTM E112 grain size determination method conservatively estimated the carbon content to be 0.116% by weight. Overall, the experimental material does provide a useful analogy to older pipeline steel and insight into the behaviour of dissolved hydrogen in all steels.

9.2 Hydrogen Concentration Profile in the Tensile Test Sample

Using the knowledge gained from the round bar diffusion work, an estimate can be made of the concentration profile inside the tensile samples at the time of testing. The solution to Fick's Law, established previously (Section 2.8.6), can be used to calculate the concentration of hydrogen at specified depths in the sample material. For the purposes of this exercise all calculations assume ambient laboratory room temperature ($T = 20^\circ\text{C}$) and the diffusion rate is taken to be $D = 1.63 \times 10^{-8} \text{ m}^2/\text{s}$. For the purpose of demonstration of the concentration profile within each sample, all surface concentrations were taken to be $C_s = 1.00 \text{ ppm}$, bulk concentrations were set to some arbitrary non-zero value ($C_b = 0.083 \text{ ppm}$), and all concentrations at depth are referenced to the surface. Figure 9-1 gives a clear indication of the depth at which appreciable amounts of hydrogen have accumulated. There is never a completely flat concentration profile and some samples show areas where no hydrogen has diffused to yet. Using a timed method of hydrogen charging these concentration profile effects cannot be avoided, as once the sample is removed from the charging condition hydrogen will begin to exit the material. It is still true in all cases that for a greater average measured hydrogen

concentration the greater the concentration will be at all depths. Knowing the average hydrogen concentration (total amount of hydrogen divided by volume), bulk concentration, and diffusion coefficient a diagram of this type could also be used to estimate the surface concentration.

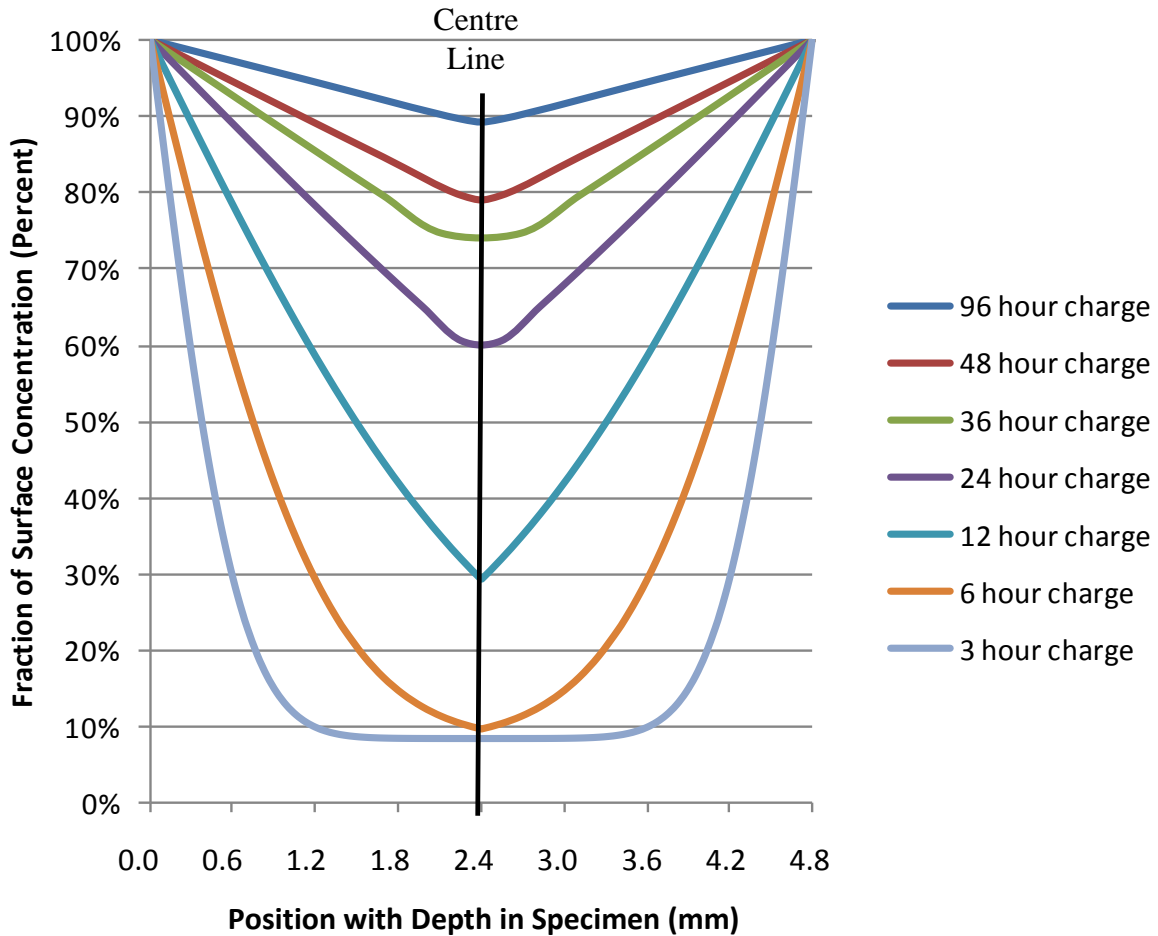


Figure 9-1 Plot of Hydrogen Normalized to Surface Concentration within Tensile Specimen

Note that the effect of the concentration profiles seen above on the average measured concentration of an experimental sample agree in principle with the results of the calibration, in that an asymptotic concentration is approached. The difference between surface and bulk concentrations, which is the driving force (the gradient) for continued diffusion into the material, gets less as time increases. This may also be important for the mechanical behaviours presented

later, given that the differences in average hydrogen concentration for the 36, 48, and 96 hours samples are very slight (as seen in the calibration), but the differences in hydrogen concentration at centreline (or degree of hydrogen penetration) are more pronounced.

The calculations presented above apply to the reduced section of the tensile specimen. They also apply to the larger-diameter ends, as they also have a characteristic dimension of approximately 5 mm, though in their case the 5 mm depth is from the end faces (see Figure 9-2). Stated another way, no significant volume of the tensile specimen is further than 2.5 – 3 mm away from a charging face and thus would have similar concentration profiles as the reduced section. This supports the use of the average hydrogen concentration (from eudiometry) to define the hydrogen concentrations seen in the reduced section.

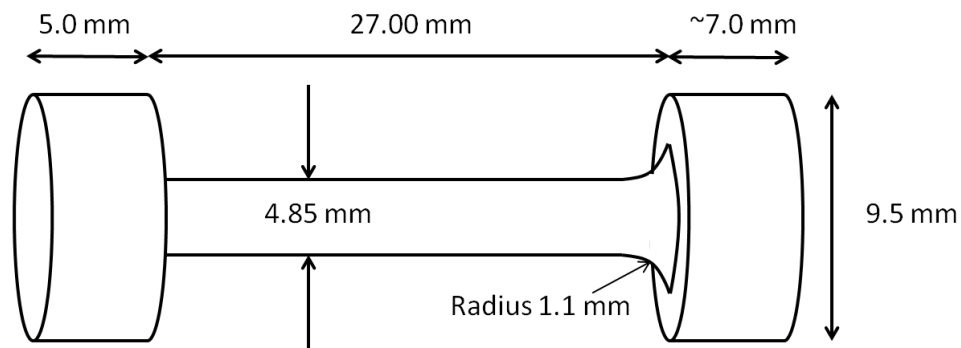


Figure 9-2 Tensile Specimen Configuration

Sainter et al [2011], in very recent hydrogen diffusion work in stainless steel, experimentally found a similar concentration profile with depth using secondary ion mass spectroscopy. They excised a disc of material from a charged sample and found the measured concentration agreed with the predicted profile shown in Figure 9-3.

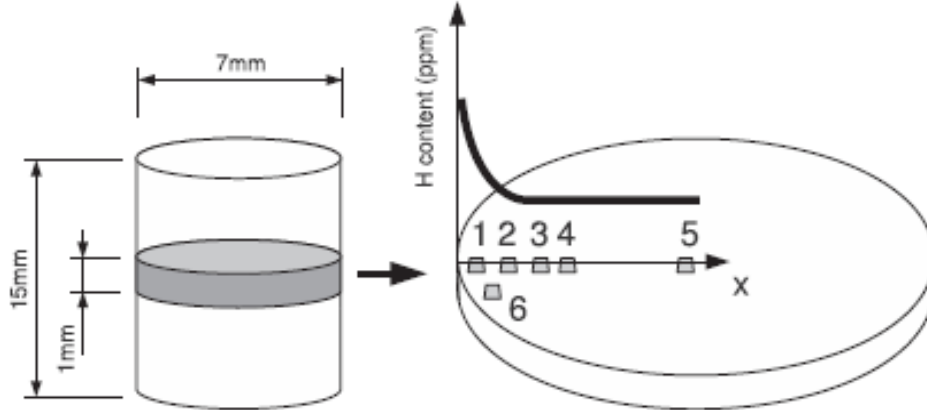


Figure 9-3 Radial Hydrogen Concentration in a Round Bar Sample from Sainter, 2011

9.3 Validation: Repeatability and Effect of Surface Degradation

Repeated tests on uncharged samples indicated that all measured parameters could be determined with a standard deviation of between 13-20 times less than the range of values measured in the main experiment. This indicates that our method, assuming the measurements are drawn from a normally distributed sampling, can detect differences much smaller than that covering the range of our collected data and that all detected differences are real.

Considerable surface degradation in the form of general corrosion as well as corrosion pits were seen the more time the samples spent in the charging solution. All samples, no matter the time spent in solution, returned to their original state (in terms of all our measured properties) after undergoing the hydrogen bake-out procedure. The effect of surface degradation does not impact the relationships between the variables reported in the main experiment. A question raised by these results is: How can this effect be reconciled with other results in the literature that show permanent degradation of the internal structure of the material through the action of hydrogen causing cracks due to H_2 formation in voids and embrittlement cracks due to internal stresses (even without external load)? The simplest answer is that the defects in the experimental

material were not sufficient to allow significant damage in the experimental time scale.

Industrially this concept is used when a vessel is suspected of accumulating hydrogen.

Periodically the temperature of the vessel is raised to ‘bake-out’ any accumulated hydrogen.

9.4 Main Experiment: Results Replicating Previous Knowledge

The experimental methods designed for this research have successfully replicated some well-known relationships. In materials science, increasing the strain rate is known to generally increase the flow stresses (yield and ultimate) and the strain hardening exponent [Hertzberg, 1996 pg 49], though to what extent is defined by the specific material. Manipulating the strain rate during these experiments has produced the same effects. Similarly, there is a great deal of literature and industrial sponsored research that shows hydrogen’s embrittling effect on steel, commonly noted through measurement of decreased elongation at fracture or increased percent reduction in area, again dependant on the specific material, and which is also evident in these experimental results. This is an indication that the careful techniques developed for the experimental work here can replicate and support conventional wisdom, and conversely in that the agreement with the canon of previous research supports the validity of this new approach, and that there is sufficient sensitivity in the outcome measures to detect functional relationships.

9.5 Main Experiment: New Observations

This experimental work represents a new approach to the study of hydrogen in steel. In the literature, the effect of hydrogen has been tested at impact ($\sim 10^3 \text{s}^{-1}$ or greater), standard quasi-static ($\sim 10^{-3} \text{s}^{-1}$), and very low strain rates ($\sim 10^{-7} \text{s}^{-1}$ or slower), but not using a comprehensive approach to apply a range of hydrogen concentrations and cover a broad range of strain rates in a controlled manner. Also, having the ability to vary both strain rate and hydrogen in the *same experiment* allows for determination of the effect of both parameters in a rigorous manner.

Hydrogen Egress during Tensile Tests. A minimum strain rate of $6.17 \times 10^{-5} \text{ s}^{-1}$ was chosen for these tests because of the ability of hydrogen to diffuse out of the material when it is removed from the charging solution. A tensile test at that strain rate takes about 40 minutes to complete. Any longer than that (even at room temperature) would risk having too much hydrogen come out of the sample and change the material's properties. Interpolating the hydrogen release with time during eudiometry data (Section 4.8) we can estimate how much hydrogen could come out of a sample after 40 minutes (approximately 14% lost). This was confirmed by a single eudiometry test where a sample was charged for 96 hours, then allowed to sit for 40 minutes on the bench before placing in the eudiometer (18% lost compared to control). The concentration profile calculation analysis above (Section 9.2) could potentially be used to find egress rates, although the boundary conditions required for the solution are no longer constant and the resistance of the metal-solution interface would need to be factored into the diffusion coefficient.

The experiments involving hydrogen charging, loading past the yield point, then resting for some time before reloading to failure (Section 8.5) showed no effect on ultimate stress, fracture stress, or necking strain from rest times (representing the amount of hydrogen allowed to escape from the sample). However there are some interesting effects seen while reloading. There was no re-establishment of upper and lower yield points, showing no effect of hydrogen in re-pinning dislocations to carbon solute atoms, though there was little chance to detect an effect like this given the low temperatures and low mobility of carbon solutes. There was elevation of the subsequent yield point upon reloading the sample after resting indicating the general hardening effect of hydrogen as a mobile solute, though determining an empirical relationship based on this is difficult given the small size of the effect. Given the low temperatures and lack of carbon or nitrogen diffusion, the re-establishment of a Lüders deformation region is a strong indication that

hydrogen is behaving as a mobile solute, diffusing to areas of higher local strain. Replication of Lüders effects seen in other dynamic strain aging systems opens many possibilities for applying the knowledge gained from dynamic strain aging research to the study of hydrogen and dislocations.

Flow Stresses (Yield and Ultimate). The yield strength and ultimate strength demonstrate a relationship with strain rate according to a power law, as indicated in the results chapter. What is more difficult is to see the underlying relationships between the flow stresses and strain rate because of the number of overlapping curves and the scatter and variability in each curve.

Yield Strength. To reduce the scatter and variability there are four sets of data plotted in Figure 9-6 representing: **1)** the uncharged condition, **2)** the increasing slope portion of the calibration curve (all data 0.280 to 0.899 ppm), **3)** the flattened portion of the calibration curve (all data 1.349 to 1.709 ppm), and **4)** the highest hydrogen concentration (1.831 ppm). These divisions naturally arise from the calibration data (see Figure 9-4 for groupings) and also are morphologically indicated when observing the curve-shapes indicated and discussed in the results chapter (reproduced as Figure 9-5).

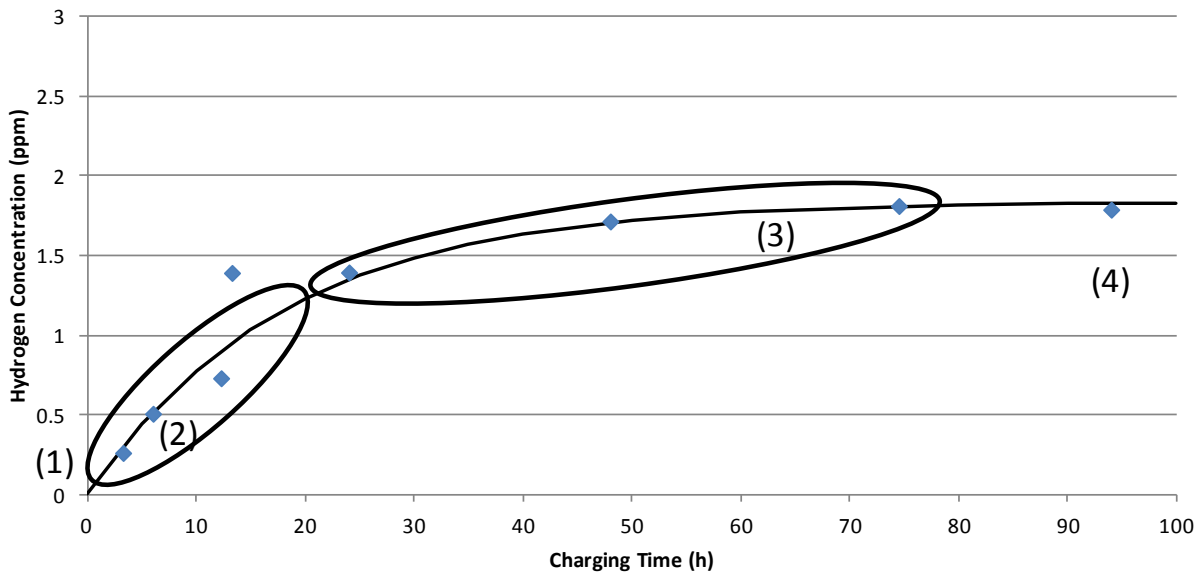


Figure 9-4 Calibration Data showing Groups Applied for Discussion and Analysis

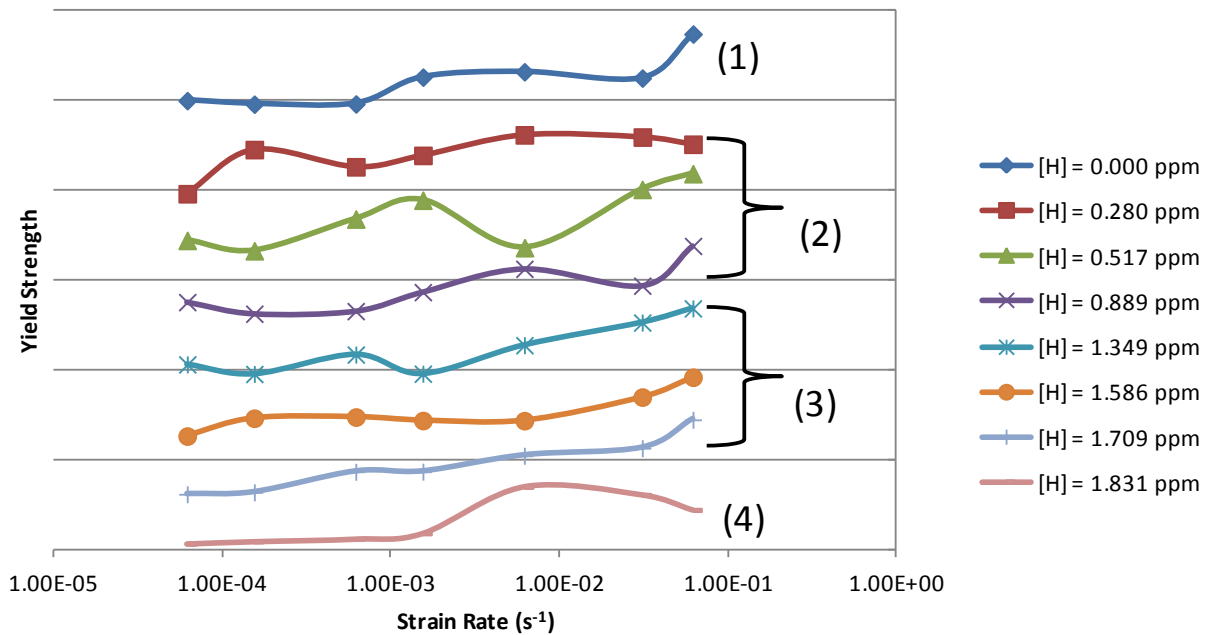


Figure 9-5 Exploded Plot of Strain Rate versus Yield Strength Showing Analysis Groups

From Figure 9-6 below it is readily observed that once this grouping operation is performed there is considerable overlap with the grouped data presented in this way and that the increase is not

simply monotonic, but indicates a linear relationship from $6.17 \times 10^{-5} \text{s}^{-1}$ to around $1.54 \times 10^{-3} \text{s}^{-1}$, which is a strong function of strain rate and weak function of hydrogen concentration, and then an increase in the strength of the strain rate function after $3.09 \times 10^{-2} \text{s}^{-1}$. The curve for 1.831 ppm hydrogen does not follow this pattern. The data envelope presented in Figure 9-7 further illustrates this and the individual curves are separated and drawn in Figure 9-8 for visualization.

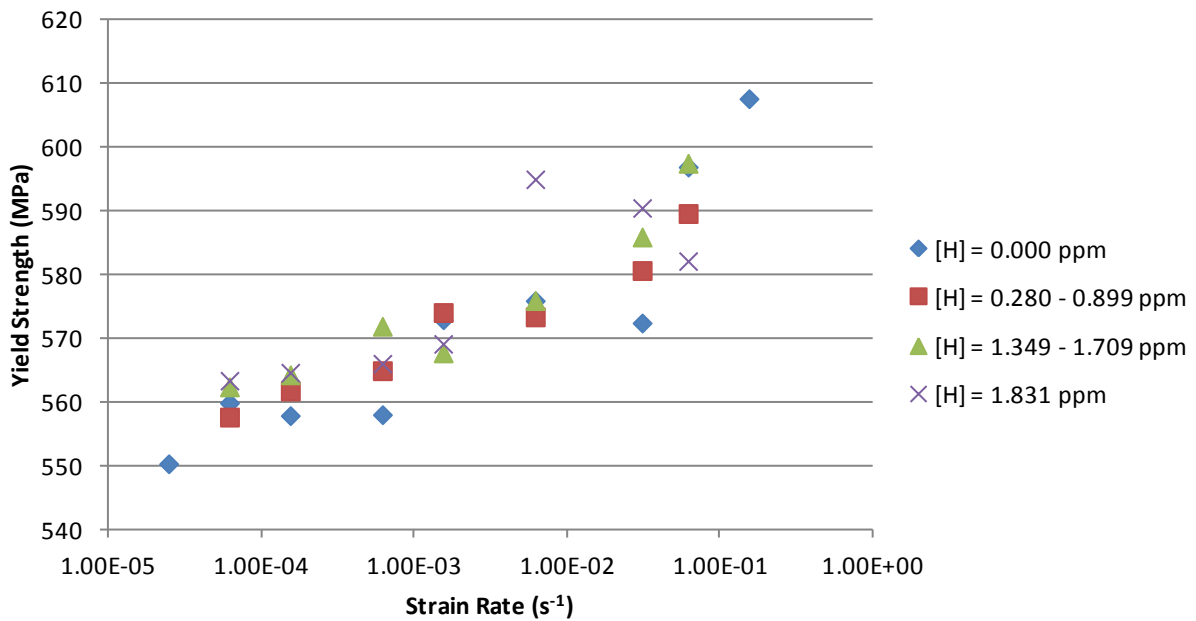


Figure 9-6 Yield Strength vs. Strain Rate with Data Pooled into Ranges to Reduce Scatter

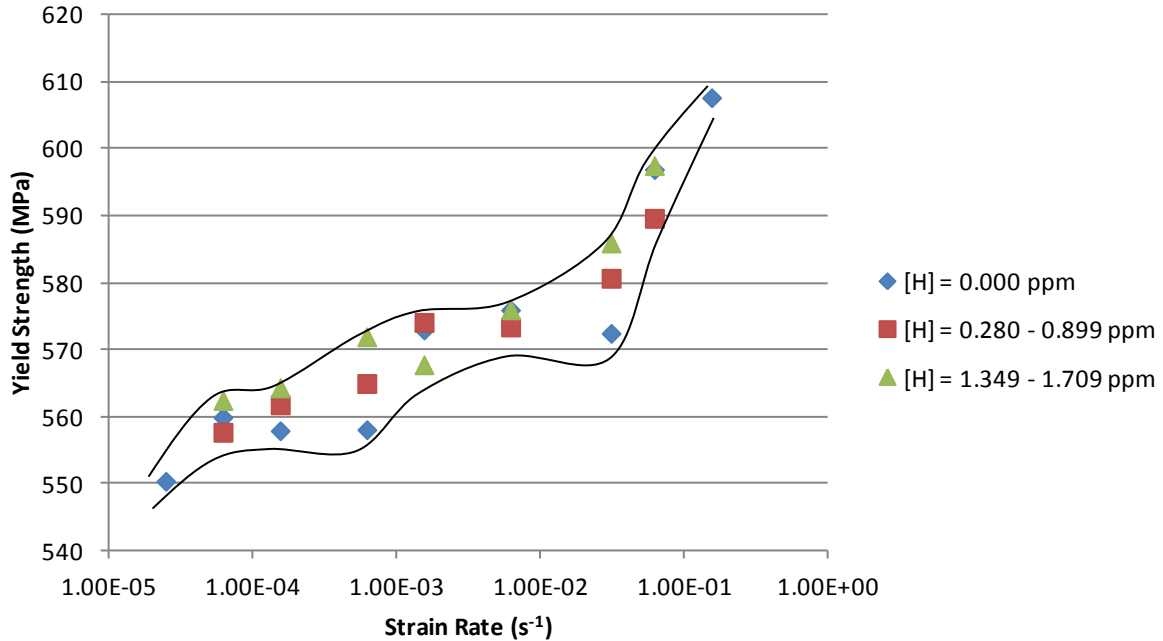


Figure 9-7 Yield Strength vs. Strain Rate Showing Envelope for Pooled Data

A few features are apparent from Figure 9-8: All curves show a prominent bulge at some point in the data range, and for the top three curves this prominence occurs at a lower strain rate with increasing hydrogen concentration, and the prominence for 1.831 ppm hydrogen does not follow that pattern. Keep in mind that each of the two middle curves in Figure 9-8 is formed from the combined effect of the group 2) and group 3) curves (21 separate measurements each), so the prominence is not simply a result of a random elevated measurement. The question to be considered of this entirely new observation is: What could be the cause of additional, small increase in yield strength (above the normal trend) over a small range of strain rates, with a hydrogen-related decrease in the location of that range?

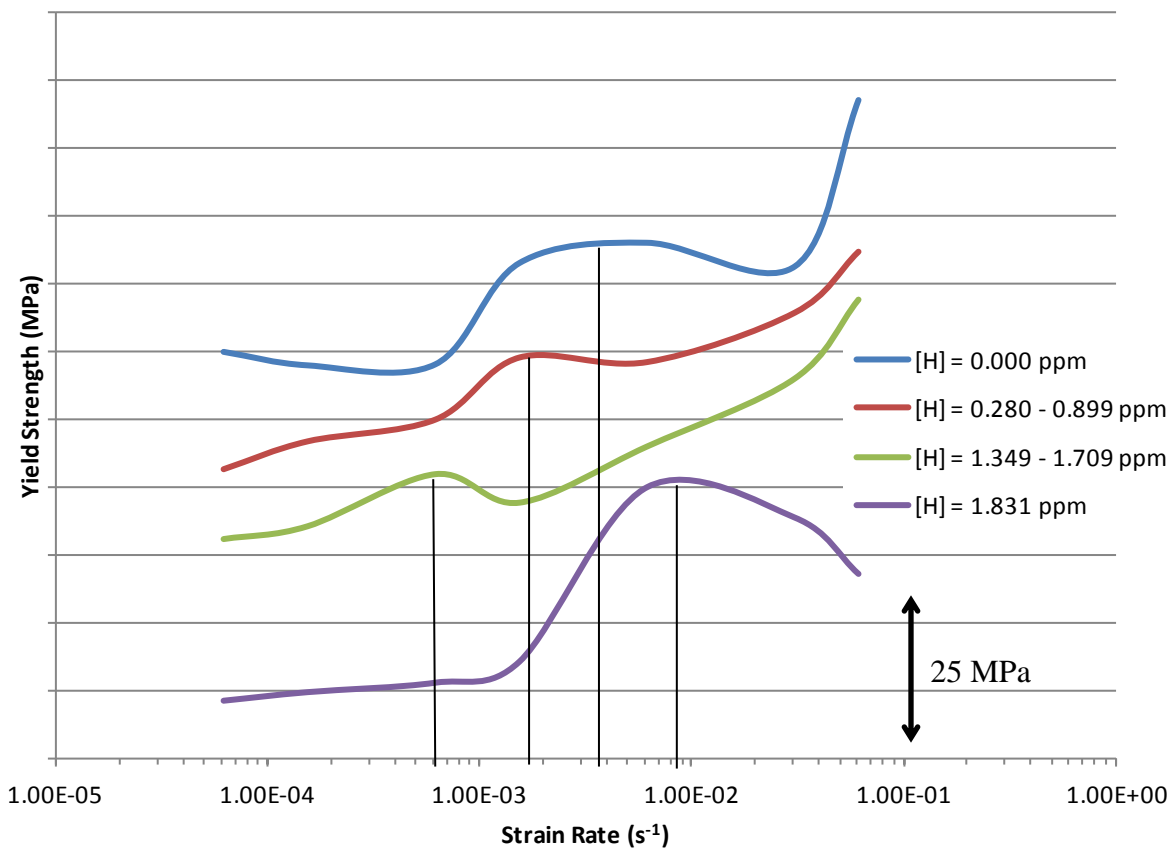


Figure 9-8 Curves showing form of Yield Strength vs. Strain Rate Pooled Data

Of the mechanisms currently considered for hydrogen's effects on mechanical behaviour (Hydrogen Enhanced Localized Plasticity, Hydrogen Induced Decohesion, hydrogen dragging of dislocations, and hydrogen impeding cross slip) only hydrogen drag on dislocations and impedance of cross slip predict a higher energy for plastic flow, as is indicated by the prominence in each figure. Oriani [1980] found that hydrogen increased the stress associated with Lüders bands in pearlitic steel during tensile tests and attributed it to dislocation drag or impeding cross slip. In terms of dislocations, two main phenomena occur at yield: The strain field finally provides enough energy for large scale dislocation movement to occur, and new dislocations are generated. In our case lower strain rates, along with increasing saturation of

available sites with hydrogen defines the range where one of these mechanisms has the most effect. What is apparent is that the observed temporary elevation in yield strength is due to some combination of increasing hydrogen concentration with decreasing dislocation velocity and/or decreasing dislocation generation rate, possible due to a greater number of proximal hydrogen atoms available to interfere with nearby dislocations.

Ultimate Strength. A similar plot (Figure 9-9) of the ultimate strength versus strain rate for the pooled data shows the overall increasing trend and an apparent decrease in the range of $6.17 \times 10^{-3} \text{ s}^{-1}$ to $3.09 \times 10^{-2} \text{ s}^{-1}$. When the ultimate strength curves are separated and plotted a similar trend emerges, though without a prominence indicated for the curve representing hydrogen concentrations between 0.280 to 0.899 ppm.

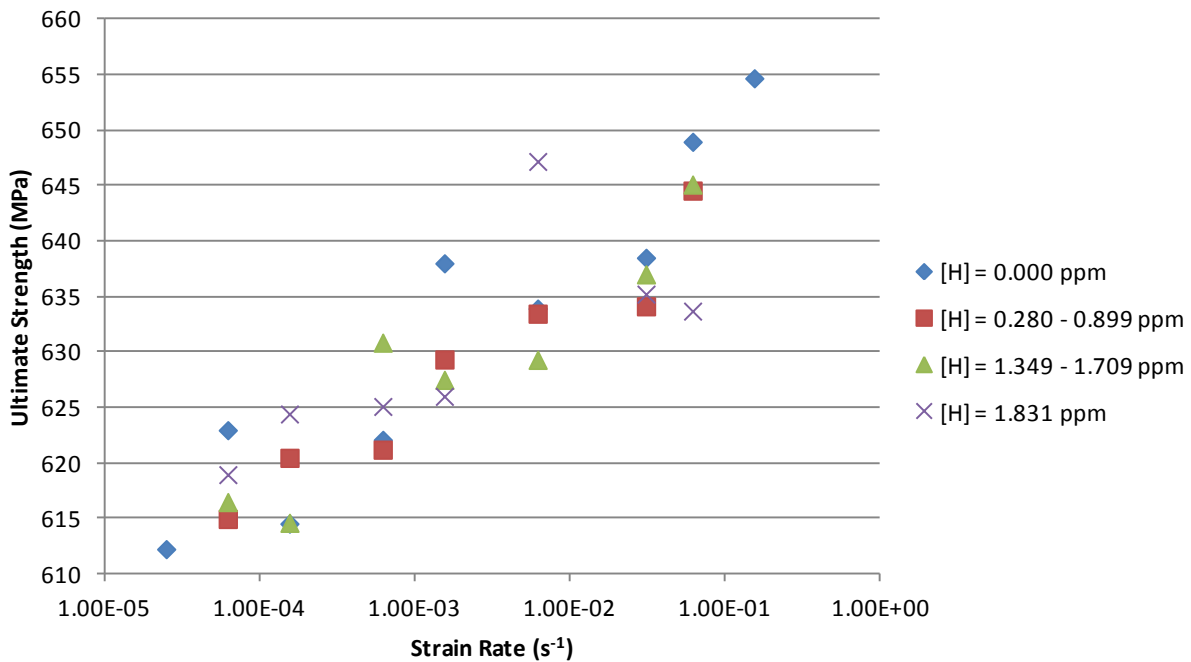


Figure 9-9 Ultimate Strength vs. Strain Rate, Pooled into Ranges to Reduce Scatter

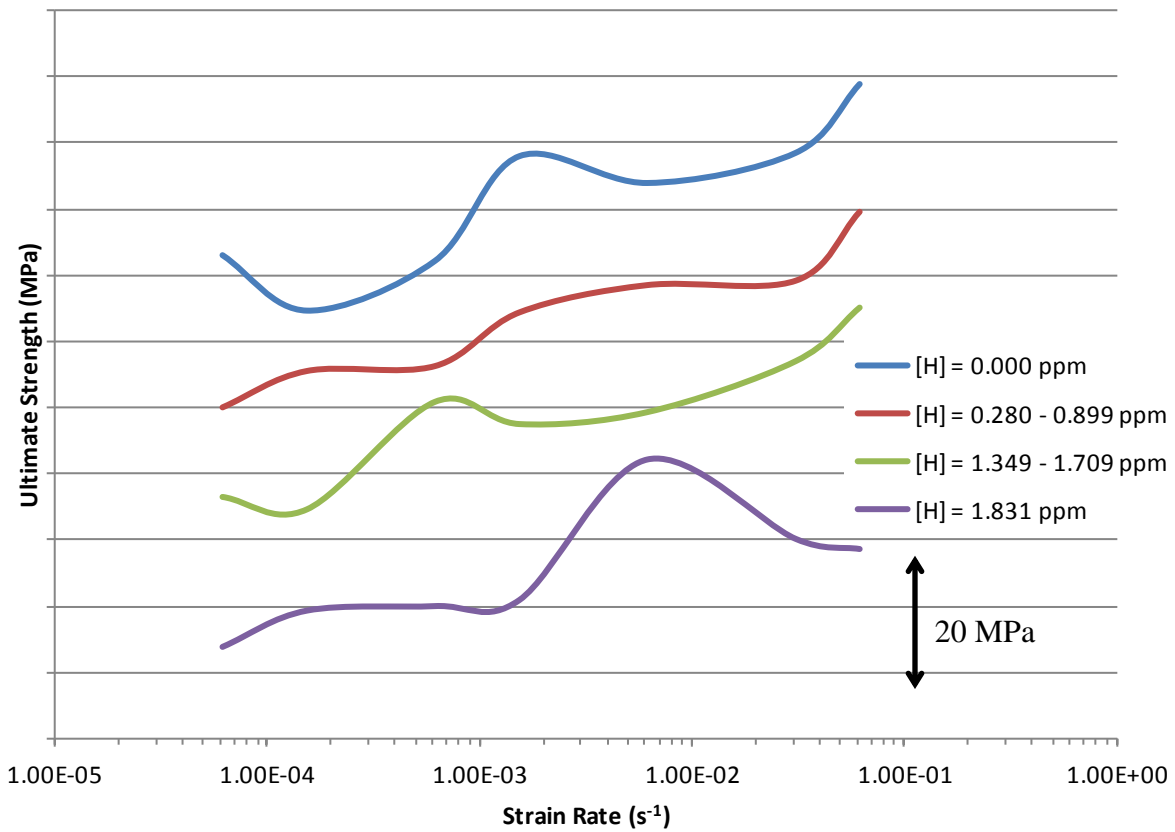


Figure 9-10 Curves showing form of Ultimate Strength vs. Strain Rate Pooled Data

Point of Final Fracture. The point of final fracture refers to the final level of stress and strain experienced by the material before breaking (σ_f, ϵ_f). In order to simplify presentation of the final fracture points, a single value was used to represent each hydrogen concentration. The values (σ_f, ϵ_f) were calculated as an average for all strain rates tested at each hydrogen concentration. These pooled final fracture values are plotted in Figure 9-11 along with an overlaid typical stress-strain curve (in this case the trial for 0.000 ppm hydrogen and strain rate of $6.17 \times 10^{-5} \text{ s}^{-1}$). The curve is overlaid for visualization purposes only and clearly shows that the point of fracture simply follows the curve shape, such that increasing hydrogen concentration lowers the elongation at fracture (lowers ductility) and raises fracture stress by a corresponding amount that

is defined by the stress-strain curve. A similar relationship does not exist when plotting the effect of strain rate by pooling the hydrogen concentrations.

It is the reduction of ductility that leads to higher fracture strains, due to running backwards up the curve. As seen in the following sections dealing with the components of plastic strain, hydrogen's effect on overall ductility loss is due to its effect within the necking region. In these tensile tests, the overall effect of hydrogen is mostly limited to the portion of the test after a tensile instability has been established, and that it must be due to the change from a state of uniform deformation to the state of triaxiality within the tensile instability that gives rise to the effects of hydrogen.

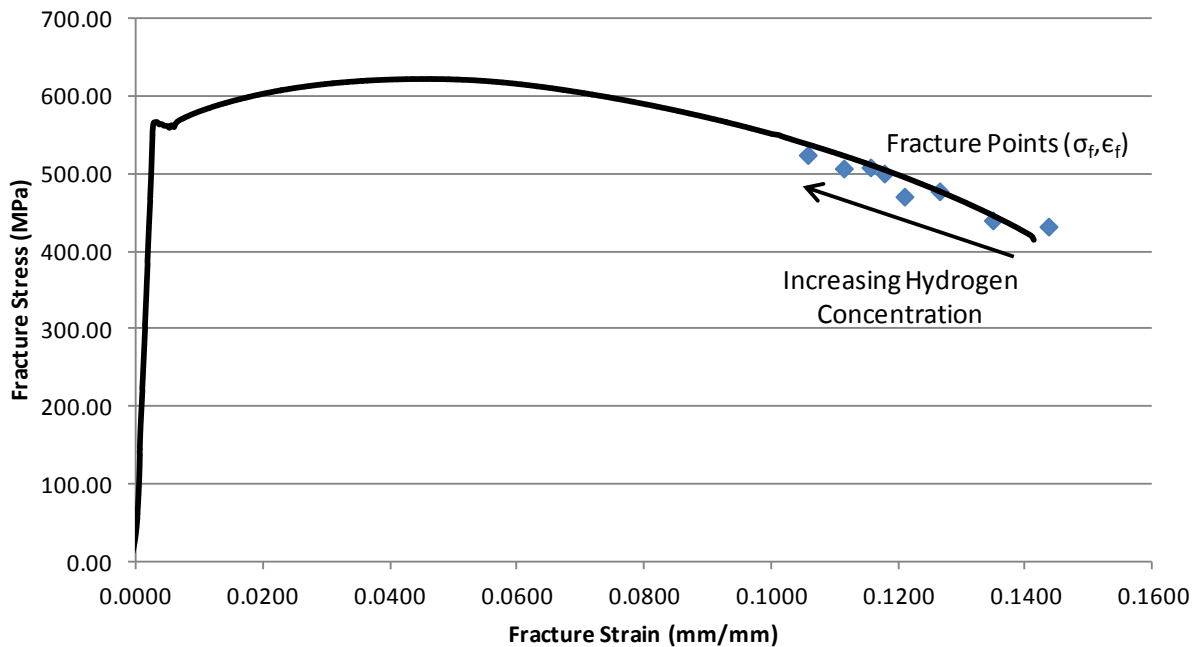


Figure 9-11 Plotting Fracture Points (σ_f , ϵ_f) for different Hydrogen Concentrations with an Overlaid Typical Stress-Strain Curve

Necking Strain. The correlation and statistical significance results reported previously noted no relationship between strain rate and necking strain. If the same technique of pooling data that

was described above is applied to this data (for the same reasons as above), a clear trend is noted of a curved, concave down relationship where necking strain is elevated for intermediate values of the strain rates used in this study (Figure 9-12). This type of effect would not be detected using the assumption of an underlying linear relationship as was necessary for that statistical analysis. This observation is not likely to be a result of hydrogen as the curve shapes are consistent but has impact on the overall trends seen below when decomposing the total strain into contributions from the uniform and necking regions. The decrease seen at the highest strain rates is not a result of a testing machine artifact in the form of rebound or momentum, as was demonstrated by the displacement-time experiments of Section 8.6.

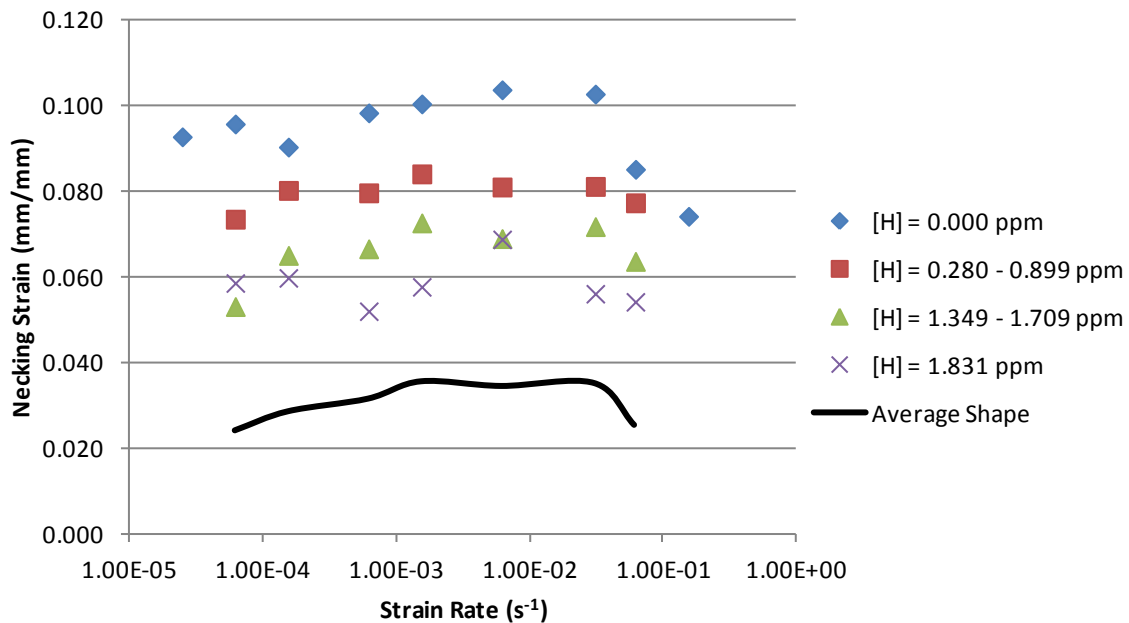


Figure 9-12 Pooled Necking Strain vs. Strain Rate

Components of Total Plastic Strain. Experimental measurements were taken of the uniform plastic strain and the necking (also plastic) strain. Since the total plastic strain is just a combination of the two, and for the most part defines the elongation at fracture, it is useful to

look closely at the contribution each makes to the total. The previous statistical analysis indicated that elongation at fracture and necking strain are strongly related to hydrogen concentration, while uniform strain is unrelated. This effect can clearly be seen in Figure 9-13 where the overall decreasing trend is entirely attributable to the effect of hydrogen. For this plot measurements at all strain rates were averaged for a particular hydrogen concentration before plotting. This leads to some very interesting observations: That hydrogen has no effect on the deformation seen during uniform loading, and that it is only when a point of tensile instability is encountered, and the largely uniaxial strain field gives way to a triaxial condition during necking, that the effect of hydrogen on overall elongation is encountered.

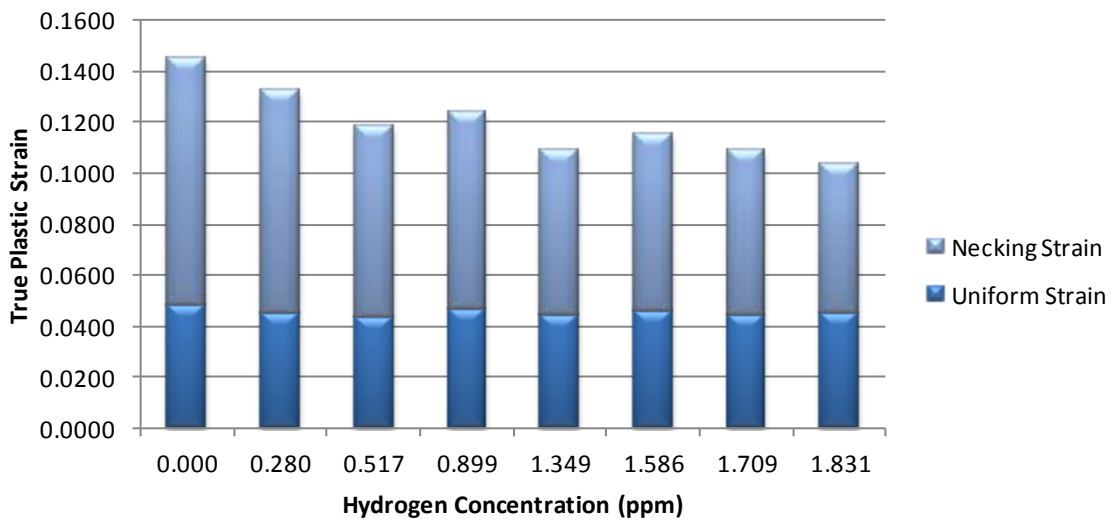


Figure 9-13 Contributions of Uniform and Necking Strains to the Total Plastic Strain, sorted by Hydrogen Concentration

Similarly, we can plot the contributions to total plastic strain in a way that isolates the effects of varying strain rate (Figure 9-14). There is a clear trend demonstrating increasing uniform strain with increasing strain rate. It is also clear that necking strain is a much larger contributor to the

total strain and that even though the relationship noted above (Figure 9-12) between necking strain and strain rate was not detected by the statistical analysis, it has a great effect on defining the overall trend seen with increasing strain rate (Figure 9-14). Together Figure 9-13 and Figure 9-14 show that when considering the two contributors to total plastic strain there are two distinct phenomena occurring: The uniform strain response is dominated by a sensitivity to strain rate while the necking strain is dominated by a sensitivity to hydrogen concentration, and that there is no effect (or very little) when you consider the opposite. The overall observed total strain (and elongation at fracture) is simply the result of the additive effects of its components (uniform plastic, necking, and elastic if considering elongation at fracture).

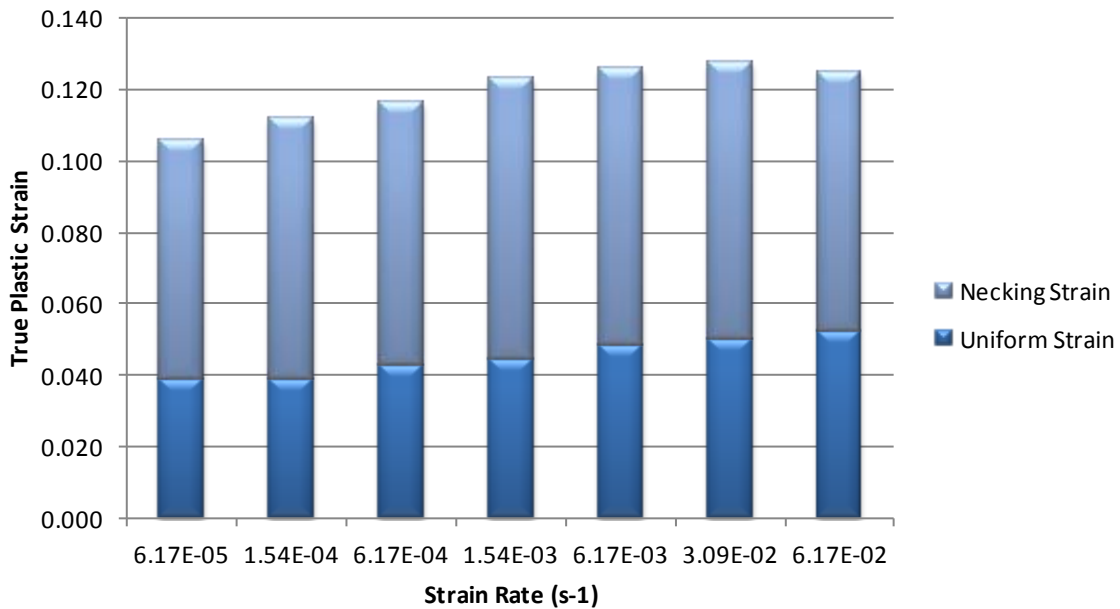


Figure 9-14 Contributions of Uniform and Necking Strains to the Total Plastic Strain, sorted by Strain Rate

These findings are important in what information the standard tensile test is able to provide, especially in the study of hydrogen. The results of tensile tests on the effect of hydrogen should

not be used to generalize about a material's performance pre-yield or post yield up to the ultimate strength. In a uniaxial stress state the tensile test gives no indication of a material's response to hydrogen. Once in a triaxial stress state (past the ultimate strength up to final fracture) the tensile test will give an indication of the material's susceptibility to hydrogen's effects. As discussed below in Section 9.7, this could be due to the transition between plane stress and plane strain or the effect of an increase in dislocation velocity. The increase in dislocation velocity is intriguing when considering the study of hydrogen as a mobile solute. It is well known that hydrogen has no effect on the results of impact testing of carbon steel. Therefore at impact speeds there is no effect of hydrogen as a mobile solute, yet in the difference between uniaxial and triaxial deformation speeds there is an effect on elongation and fracture stress. This difference could be seen in the strain energy absorption, also known as the Modulus of Toughness.

Solid Solution Strengthening Effect. Hydrogen in solid solution can be thought of as an alloying element, residing in an interstitial hole much like carbon or nitrogen. Most alloying elements follow the solid solution strengthening relation, $\Delta\sigma \sim Gc^{1/2}b\epsilon^{3/2}$, where c is the solute concentration, ϵ is the lattice dilation parameter, b is the Burger's Vector, and G is the shear modulus [Hertzberg, 1996 pg 131]. The plotting of the flow stresses (averaging measurements for all strain rates at a particular hydrogen concentration) in Figure 9-15 shows no relationship of this form. From this data increasing hydrogen concentration seems to slightly raise all yield strengths and slightly lower all ultimate strengths from the zero hydrogen condition.

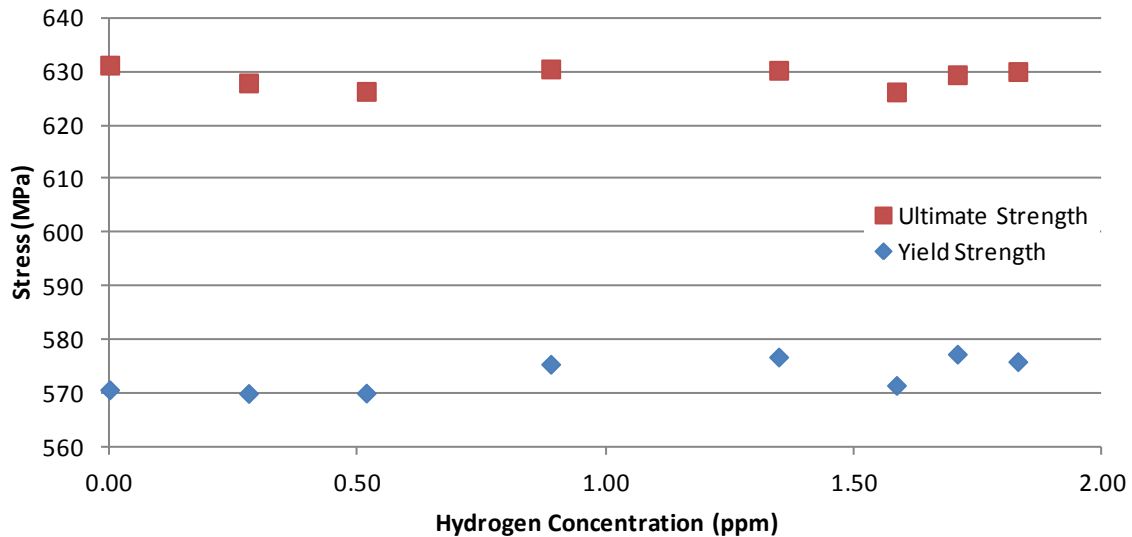


Figure 9-15 Plot of Pooled Flow Stresses vs. Hydrogen Concentration to Visualize Solution Strengthening Effects

9.6 Main Experiment: Yield Point Elongation, Upper and Lower Yields, Lüder Region

It was hoped that observation of gross features of the yield region would produce some visible evidence of mobile solute in solid solution effects. The presence and appearance of the Lüder strain region and upper and lower yields are generally affected by dislocation pinning and strain burst phenomena but aside from the presence of a Lüder region, which is a feature common to many low carbon steels, there is no evidence to be reported.

9.7 Overall Effect of Strain Rate and Hydrogen Concentration on the Tensile Test

The study of hydrogen's effects on tensile deformation and failure behaviour is extremely complicated due to the number of competing processes working to soften or harden the material. Even after decades of study there is scant evidence and much conjecture regarding the contributions, or even existence, of the competing phenomena. A material's behaviour is strongly influenced by microstructure so generalization to all materials, or even to all steels, is

not straightforward. Figure 9-16 summarizes most of the effects from the preceding discussion. This figure should help to inform what results can be obtained from tensile tests with varying strain rate and hydrogen concentration and with interpretation of the data. However, the generalizations made here only apply to the range of strain rates and hydrogen concentrations studied, and to our experimental material.

Summary of Effects. The effects can be roughly divided by the ultimate strength, in other words the end of uniform deformation and the onset of the tensile instability (see Figure 9-16). To the left of the ultimate strength the effects of strain rate dominate behaviour and hydrogen plays very little role. Increasing strain rate increases yield strength, ultimate strength, and the uniform plastic strain. To the right of the ultimate strength the effects of hydrogen concentration dominate the steel's behaviour. Increasing hydrogen concentration decreases the necking strain, leading to an overall decrease in the elongation at fracture. A decrease in elongation with hydrogen is a well known phenomenon, but the decrease is completely due to changes during necking, which is a new observation. Fracture strain is sensitive to both strain rate and hydrogen concentration, but the effects are completely independent of each other. The effect of strain rate is to shift the entire curve upward, resulting in all flow stresses increasing. The effect of hydrogen on final fracture is to decrease necking strain, and move back along the stress-strain curve by an amount defined by the decrease in strain. There is also a very slight increase in the yield strength with increasing hydrogen concentration, indicating a small amount of solution hardening, though this effect disappears by the time the ultimate strength is reached.

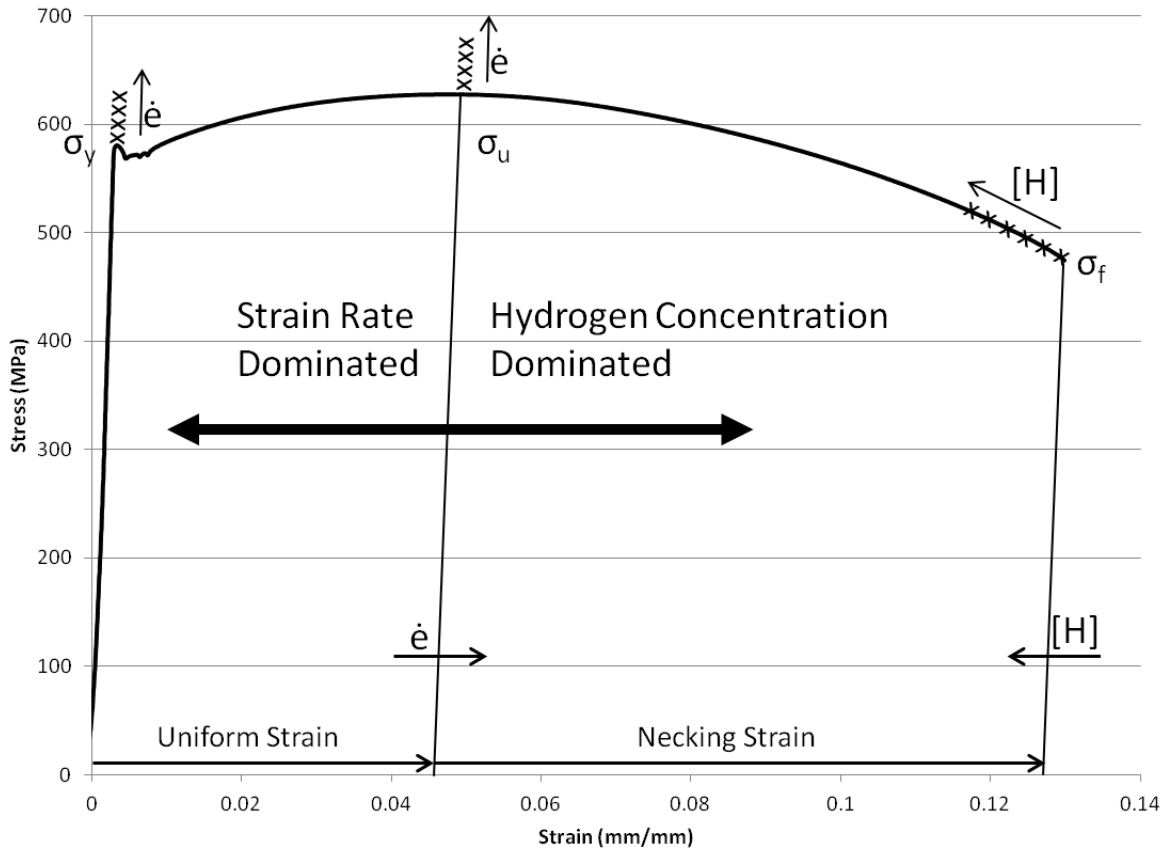


Figure 9-16 Overall Effects of Increasing Strain Rate ($\dot{\epsilon}$) and Hydrogen concentration ($[H]$) on the Tensile Response of a Low Carbon Steel

There are two distinct regimes acting during each tensile test, and only in the post-tensile-instability region does hydrogen have an effect. The only things that change about the sample between these regimes are a change from uniaxial to triaxial conditions and the formation of microvoids leading to failure. Previous research has identified an increase in the number of microvoids formed in hydrogen-containing samples (and a decrease in their size) and attributed both the decreased elongation and increase in plasticity to this [Oriani & Josephic, 1980,

Sofronis & Robertson, 2006]. It has been proposed that the decrease in elongation may be due to hydrogen recombination in the microvoids and exerting a great internal pressure, but this recombination is not likely without the longer duration of the slow strain rate tensile tests (below the strain rate of the current work). More likely is the increase in surface area from microvoid generation acting as a source and sink for dislocations. How this increase in plasticity leads to an overall decrease in elongation is not clear. That leaves the uniaxial-triaxial change to consider. Sample configurations that take advantage of triaxial conditions have been shown to be more sensitive to environmental hydrogen effects, making them useful for rank-order determinations [Stoltz, 1981, Thompson, 1985, Wang et al, 2005]. The greatest hydrogen-dependent loss of ductility during tensile tests was found for plane strain samples, notched tensile, and finally standard axisymmetric tensile samples. There is an increase in the local deformation rate during necking. All deformation is localized to the necking region, and it deforms in all directions. Therefore the dislocation velocity is increased, although to an unknown extent. A solution to determine if dislocation velocity is responsible for hydrogen effects might be to just increase the strain rate for tensile tests. That is not easy as the apparatus used for this study was already at its highest resolution. Also, very high strain rates are achieved in impact testing but those tests measure energy absorption and no effect of hydrogen is seen in practice. If testing the effects of hydrogen is desired it is much more practical to use sample configurations that exploit triaxiality in loading such as the notched tensile specimen, compact specimen, or axisymmetric notched tensile specimen.

When considering the future applicability of the results of this work, applications should be considered where considerable strain is present and deformation rates are high, such as in rolling or forming operations, or cracked components with high stress concentrations. This work does

not address the long term effects of hydrogen accumulation or stress corrosion cracking nucleation. There is also possible application of these findings to the small scale diffusion behaviour of hydrogen in steel and crack stress field interactions.

Chapter Ten: **Field SCC Examination**

The following chapter presents an observational study involving a field specimen of pipe that failed due to the effects of stress corrosion cracking (SCC). A SCC crack colony was examined with emphasis on the relationships between observed pits and the SCC crack field. Specimen history is presented before a novel technique is developed to examine the morphology of the SCC colony. The pipe sample was viewed from the outside-in, then layers of pipe material were stripped away to yield the structure of the crack field progressing into the material's depth. The role of hydrogen in the development of SCC is examined along with hydrogen concentration measurements at different locations and depths within the material.

10.1 **Overview**

A field-failed pipeline with SCC was examined to demonstrate crack field structure. SCC is known to be a result of the synergistic effects of stress, corrosion, and a susceptible material. Hydrogen is also likely a key factor in SCC initiation, growth, and fracture. The following work describes a new sectioning technique which will provide novel observations of near-neutral pH SCC, including the change of SCC colony appearance with increasing depth into the material. Hydrogen concentrations were measured of the as-received material within the SCC colony, as-received outside the colony, a bake-out value for comparison, and a new technique to estimate the difference in concentrations between the inner and outer surfaces.

10.2 **Specimen Acquisition and Field History**

A field-failed SCC pipe specimen was kindly provided by Det Norske Veritas (DNV), an international risk management company. The sample has extensive SCC resulting from external corrosion, and failed in the fall of 2005 during a hydrotest at 86% of specified minimum yield stress (SMYS). The SCC feature was reported to be 111 mm (4.375 inches) long and 52.5%

thickness on the bottom of the pipe, located at 5:30 from top dead centre looking downstream. The final failure mechanism of this pipe was a coalesced crack of 52.5% depth. The remaining ligament failed in a brittle manner. Under normal conditions this material behaves in a more ductile manner. In engineering practise the change from ductile to brittle failure often indicates the presence of hydrogen. The 324 mm (12.75 inch) diameter pipe had specified wall thickness of 5.8 mm (0.228 inch) minimum, was made of X56 steel, and was installed in the late 1970s. In service the pipeline carried high vapor pressure ethane, ethylene, propane, and butane. The pipe was buried and had a protective coating on its exterior. Samples of the failed pipe were cut away with a torch and stored at room temperature until analyzed. A cut-away section of the pipe showing extensive SCC colony formation on the pipe's exterior surface can be seen in Figure 10-1.



Figure 10-1 Pipe Specimen Showing Radial Curvature and Surface Cracks

10.3 Microstructure Revealed through Polishing and Nital Etching

Several metallurgical samples were prepared to view the specimen from two directions, representing the long axis of the pipe (Axial Direction) and looking towards the centre of the pipe from outside (Radial Direction). Figure 10-2 is a schematic showing these directions in relation to the pipe sample shown above.

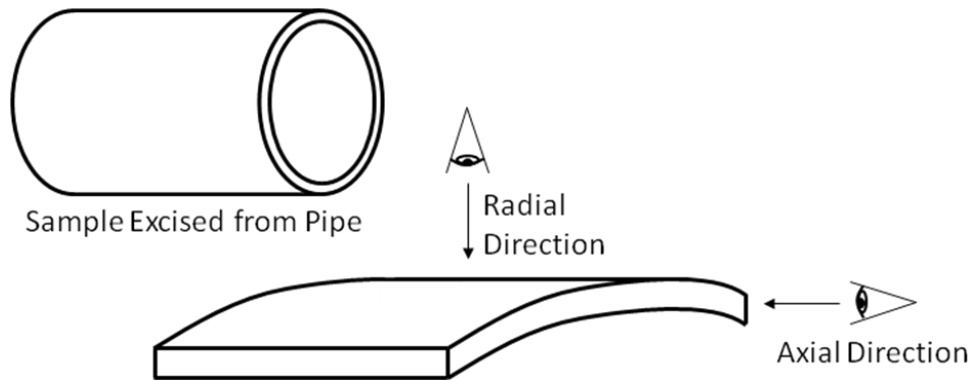


Figure 10-2 Schematic of Pipe Section showing Axial and Radial Directions used to View Specimen Microstructure and SCC Features

To prepare metallurgical specimen to examine the microstructure, samples were subjected to the procedures presented in Section 4.3. Roughly this consisted of mounting the pipe sample in Bakelite, grinding from 240 through 600 grit, polishing from 15 μm to 0.05 μm , and then etching in a 2% Nital solution to reveal microstructure. The specimen showed a ferritic/pearlitic microstructure as expected from a sample of X56 pipeline steel (see Figure 10-3).

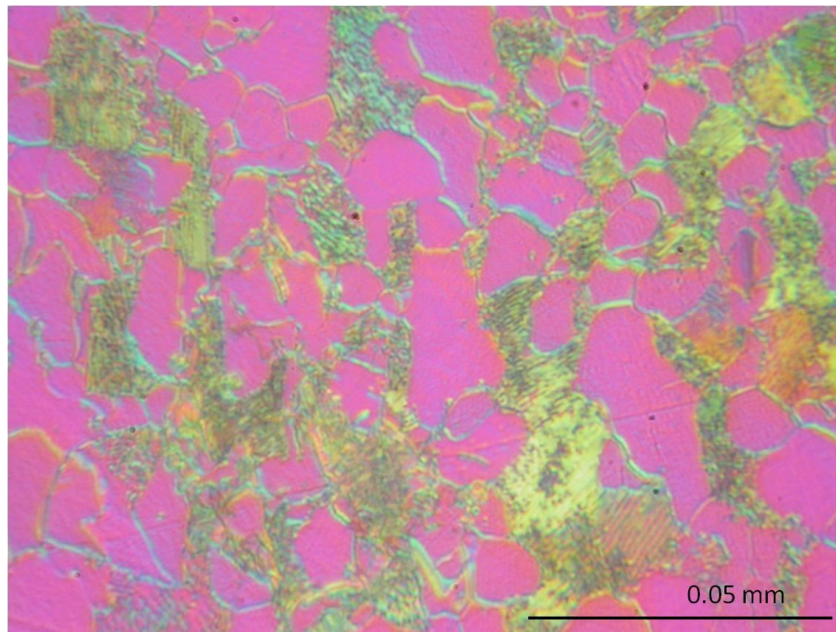


Figure 10-3 Ferritic/Pearlitic Microstructure of Pipe Sample

10.4 Method for Electroless Nickel Plating

Some samples were nickel plated to aid in edge feature retention and to observe the adhered corrosion products found in the pits and cracks. Standard electroplating might have negatively affected the surface features, so an electroless nickel plating method was used instead. The plating solution was prepared according to the formula listed in Table 10-1 below. A 10 mm x 40 mm pipe specimen and the solution were placed in the fume hood in a 600 ml beaker on a hotplate with temperature maintained at 88°C. The plating reaction was very vigorous with gas evolution so no stirring was necessary. Distilled water was added occasionally to make up for evaporation. After 1.5 hours the heat was removed and the nickel plated sample was removed from the cooled solution after another 30 minutes. Metallurgical samples were prepared from this plated sample using the same procedure used throughout the thesis.

Table 10-1 Composition of Electroless Nickel Plating Solution

<i>Electroless Nickel Plating Solution</i>	<i>200 ml</i>
Sodium Acetate	2.6 g
Nickel Sulfate Hydrate	3.1 g
Sodium Hypophosphite	2.8 g
Distilled Water	200 ml

10.5 Methods for Depth-wise Sectioning

Samples were cut out of the pipe and mounted for metallurgical analysis. The samples were mounted in two orientations, a section mounted looking in the axial direction of the pipe, and a section mounted looking in a radial direction (outside-in). For details of these orientations see Figure 10-2. The radially-mounted sections allowed visualization of the surface of the pipe, and also subsurface features as the sample was ground to a new depth. The sample was ground,

polished, etched, and imaged before repeating the process, progressing depth-wise into the material (see Figure 10-4 for procedure flow chart). In this way a three-dimensional perspective of the crack's topography was obtained.

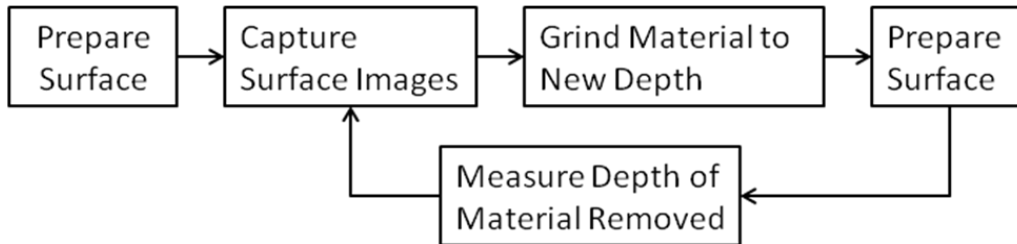


Figure 10-4 Flowchart for Generating Successive Images

10.6 Registering Images and Following Features

Preparing surfaces for microstructural examination is a routine procedure in materials science.

What was needed was to develop a workable procedure capable of measuring the amount of material removed between capturing images, then registering successive images so that particular pit or crack structures could be followed. To estimate the amount of material removed through the grinding and polishing operation, the focussing mechanism on the microscope itself was used. A sensitive dial gauge (0.01 mm resolution), a common machine shop tool, was used to calibrate the rotation of the focus controls to the movement of the lens with respect to the table (For setup see Figure 10-5). The calibration result for moving the lens upward was [Difference in Fine-Focus Adjustment Dial Readings] * 7.24×10^{-4} = Focal Plane Travel (mm).



Figure 10-5 Experimental Setup for Calibrating Lens Movement to the Adjustment Gauge

It is important to know, when imaging samples after material removal, how much material was removed. Grinding and polishing is a manual operation, so specific protocols for removing a specified amount of material are not useful. Instead a method was developed to determine how much material was removed by registering large features and using calibrated microscope table movement. To measure the depth of material removed after grinding and polishing a new surface, the narrow plane of focus of the instrument was used. First the visible image was focused on the flat, ground surface. Then the plane of focus was moved to some recognizable feature at a different depth from the surface, like the bottom of a corrosion pit. The movement of the focus adjustment knobs and the calibration of depth were used to determine the depth of that feature from the flat-ground surface. After a regrinding operation, the depth from the surface to the bottom of the same feature was again determined. The difference between the depths

represents the amount of material removed from the sample during the grinding and polishing operation and has been in the range of 40-140 μ m.

To register images, careful maps were drawn to provide recognizable features that would be present on successive images. One such map can be seen in Figure 10-6 below. The results of following these features are presented in Figure 10-9 below.

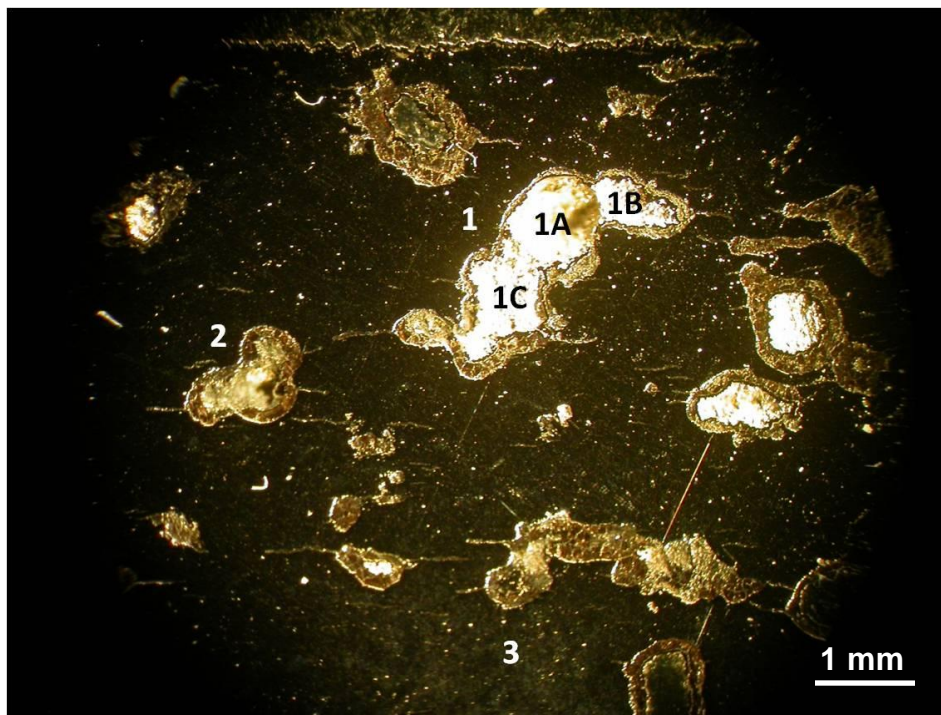


Figure 10-6 Map of Surface Pit and Crack Features

10.7 Results and Discussion for SCC Sample Depth-Wise Sectioning

Axial Sectioning Observations. The microstructure of the pipe has been shown to be mainly ferritic/pearlitic in structure, as would be expected from X56 composition (see Figure 10-8 and Figure 10-3). Close examination of crack profiles reveal two competing processes, crack growth into the material and aggressive anodic dissolution, as seen from the widened crack walls and semicircular surface shape (Figure 10-7). Also seen in this figure is an example of the normally,

but not exclusively, uniform crack depth of approximately 0.5mm. Because the crack is so wide, determination of transgranular or intergranular progression are not possible as seen by the relative grain size shown in Figure 10-8.

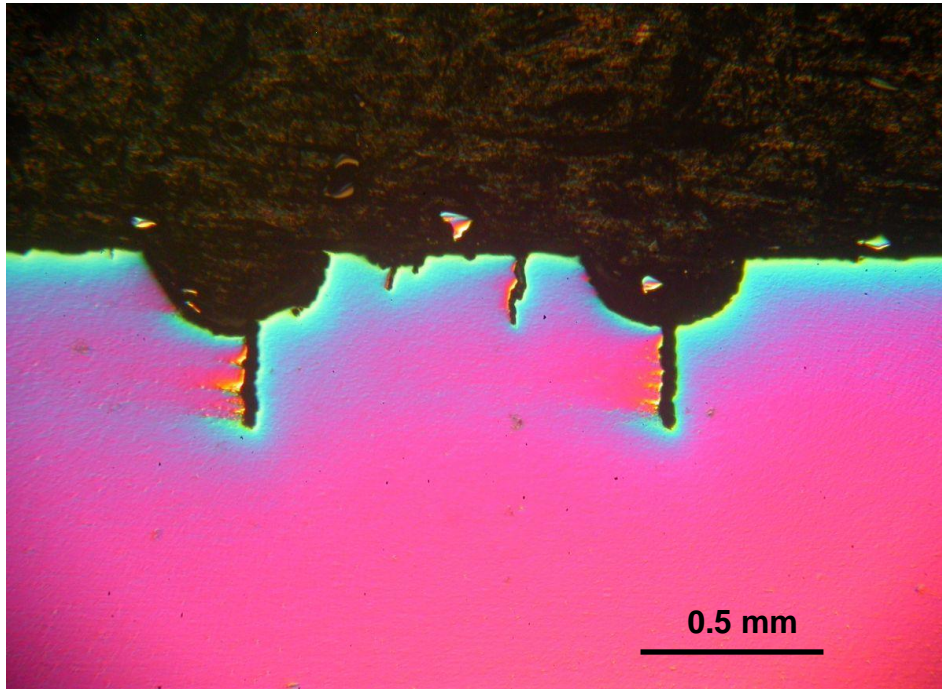


Figure 10-7 Axially Sectioned SCC Specimen Showing Cracking and Anodic Dissolution

Also visible in Figure 10-7 are cracks, growing from the outer surface, that are not associated with a pit. Yet in this figure, and all others taken from the axial perspective, every observed corrosion pit has a crack emanating from it. In general, for the SCC colony on this specimen, you can have cracks without pits, but not pits without cracks. The relatively uniform maximum crack depth of about 0.5 mm arises from: decreasing stress intensity from outer to inner pipe surfaces coupled with increasing crack length leading to build-up of corrosion products, and a reduction in the dissolution reaction rate due to Le Chatelier's Principle (a build up in reaction products shifts the equilibrium in favour of the reactants). What is not clear is the growth-state

of the smaller cracks. It is likely that they are not growing due to being shielded from the local hoop stress field by the two longer cracks at the bottom of pits to either side.

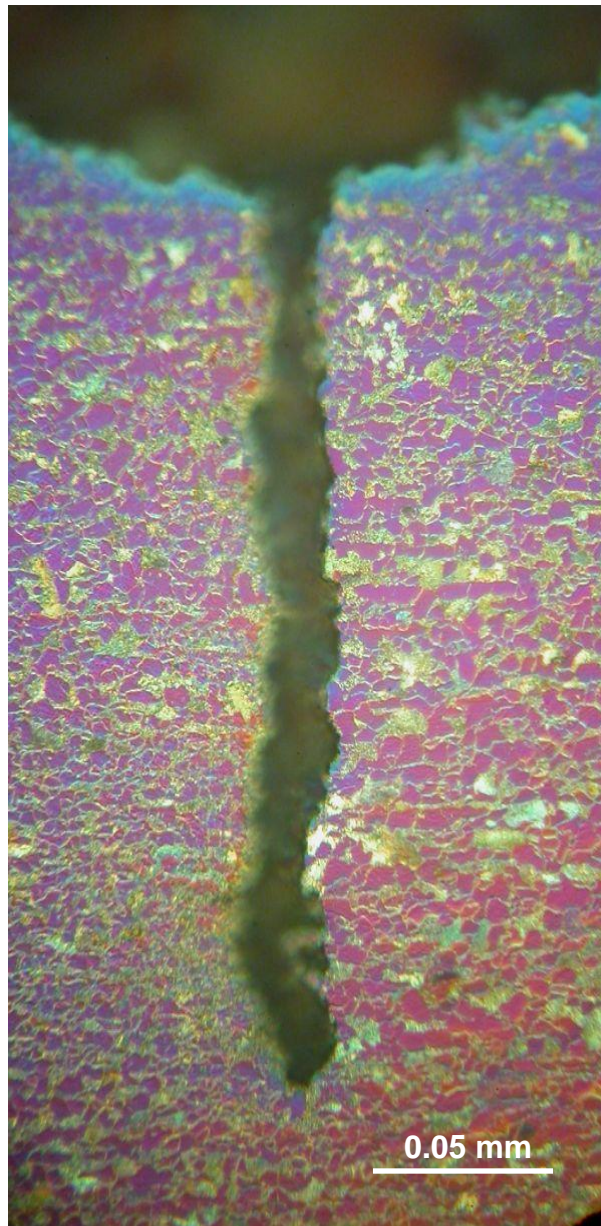


Figure 10-8 Etched Sample Showing Grain Size and Crack Size

Radial Sectioning Observations. The side-by-side images in Figure 10-9 illustrate two images of the same specimen, with the image on the right resulting from a removal of 120 μm depth. Certain pit and large crack features appear randomly oriented at first but reveal an underlying field of cracks oriented along the pipe axis. Figure 10-10 shows an enlarged image of one of the features from Figure 10-9 and illustrates that large pits can contain multiple cracks. Figure 10-11 shows crack interference in that as the cracks grow longer and closer together they tend to depart from a direction purely perpendicular to the hoop stress and curl towards each other. This indicates a growth mechanism with an increasing shear component and the ability of growing cracks to eventually coalesce into a single, larger crack feature.

Another general observation noted is the apparent trend of pit depth with distance from final failure crack. From a maximum feature depth of 300 μm near the final fracture, 200 μm at 3 cm from final fracture, and 132 μm at 6 cm from final fracture.

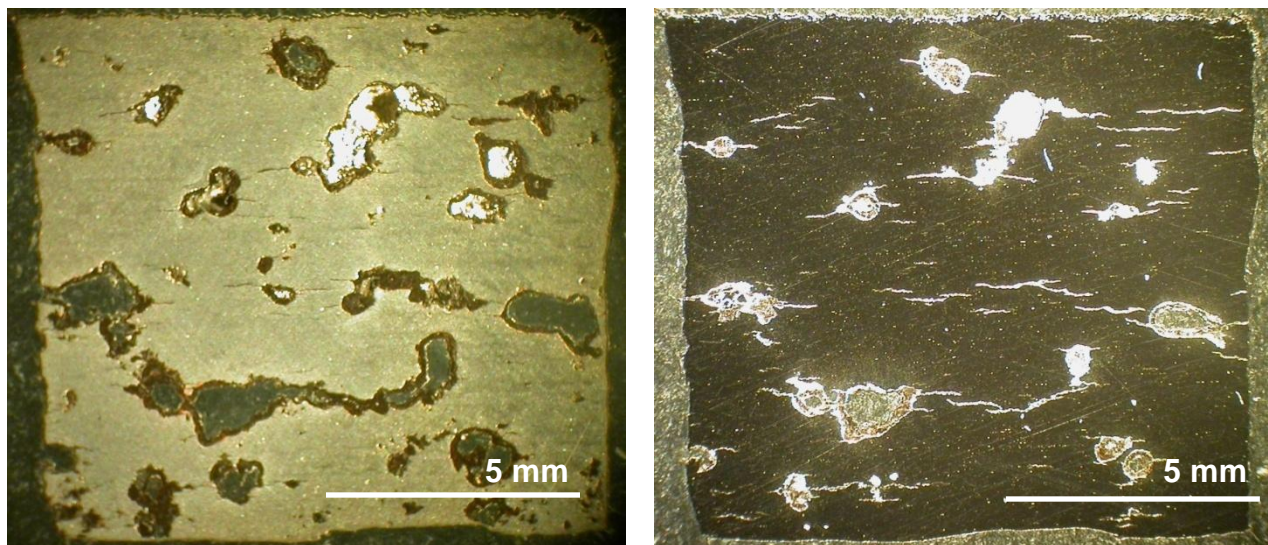


Figure 10-9 SCC Colony Radial Section Showing Crack Alignment after Removal of 120 Micrometers of Material

Also noticeable in Figure 10-9 is that although the crack field is oriented along the pipe axis (perpendicular to the hoop stress), the pits have no obvious growth direction, except when a number of pit/crack combinations join together. This leads to two important observations: 1) crack formation and growth is sensitive to the state of stress in the pipe, and 2) pit formation and growth is insensitive to the state of pipe stress.

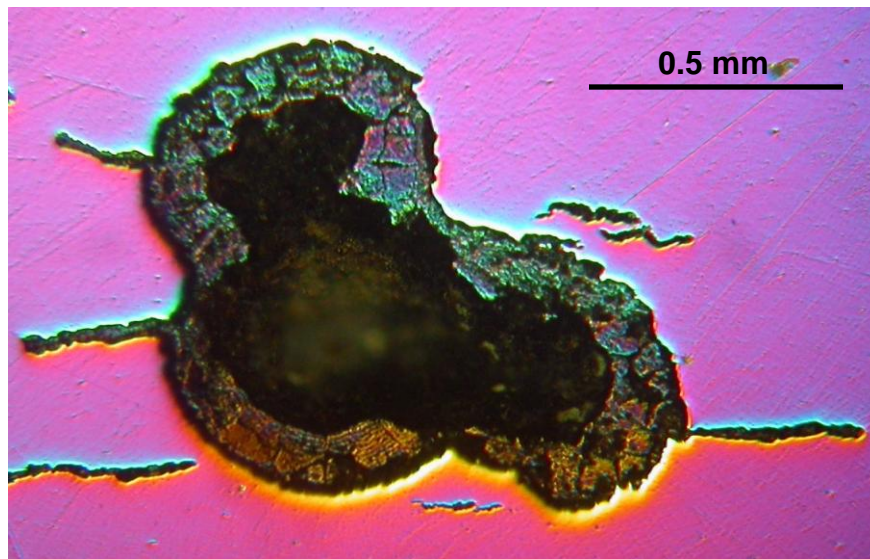


Figure 10-10 Multiple Cracks Associated with One Pit and Thickness of Corrosion Products

In Figure 10-10 above there are multiple cracks visible emanating from one pit, and also cracks not spawned directly from the pit, although with close proximity. Figure 10-11 shows that growing cracks interact with each other (also shown multiple places in Figure 10-9) and can eventually join to form one crack with a much longer effective length. This feature of multiple crack coalescence leads to very long cracks and eventually one very long running fracture and total pipe failure.

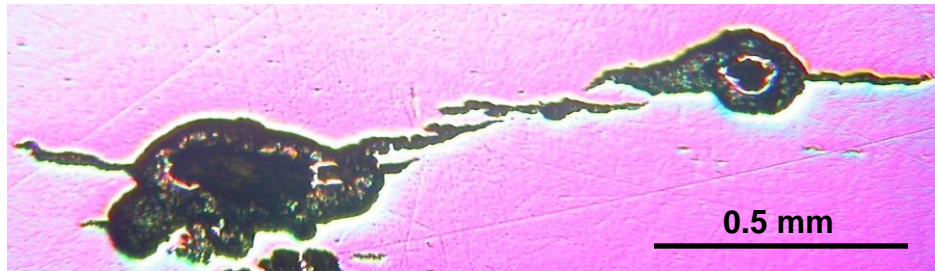


Figure 10-11 Crack Interference and Coalescence

Figure 10-12 reinforces the above observations regarding small crack generation adjacent to the pit and includes more detail about the thickness of the corrosion products in the pit. This sample was nickel-plated using an electroless plating method (useful for edge retention) showing a rough surface with non-uniform depth of corrosion products. Particularly noticeable is the breakdown of the thickness of the film in the lower right of the image at the point where the larger crack emanates from the pit.

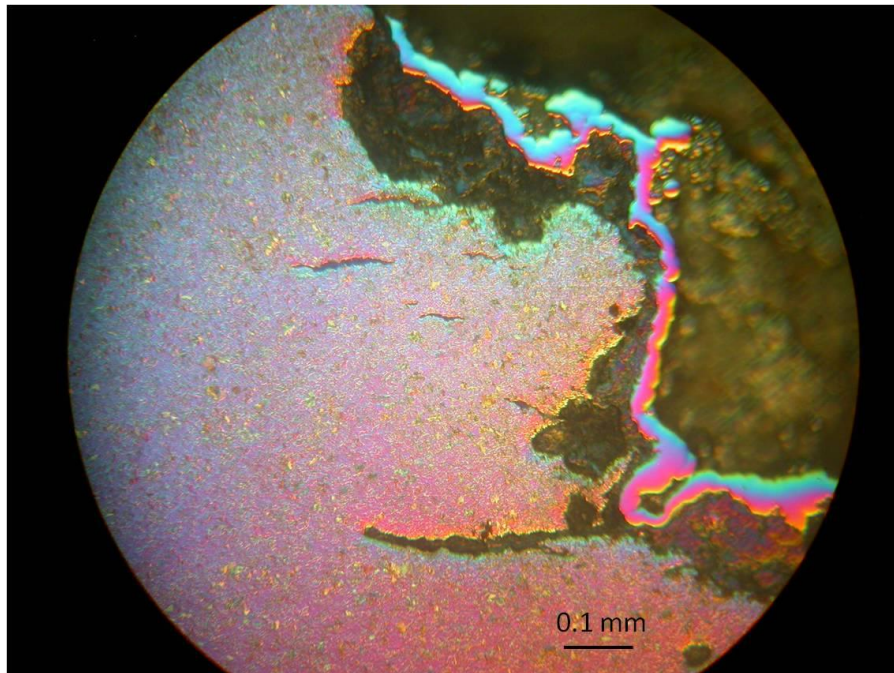


Figure 10-12 Nickel Plated (for edge retention, the nickel appears unetched) and Nital Etched Sample showing Small Secondary Cracks and Thickness of Corrosion Products

Short Timescale Pit Generation. The goal of the following procedure was to demonstrate how easy it is to generate pits using only the properties of localized corrosion (corrosion cells) and in the absence of an applied stress field. Using one of the mounted metallurgical samples with a freshly prepared surface at 0.05 μm polish (mirror surface), a fine mist of distilled water was applied, left on for 30 seconds, then dried with compressed air and imaged. The result of this process is illustrated in Figure 10-13. The experiment was able to generate multiple pits, centred possibly on inclusions or just a local centre of enhanced corrosive attack. This is a demonstration of the power of localized corrosion cells. Even a very small volume of quiescent, and in this case pure, water was able to actively and quickly corrode the metal, setting up a micro-galvanic couple using only minor inconsistencies in the metal's structure or simply a concentration gradient within the droplet. This offers an analogy to the localized corrosion environment under failed coating that is a feature of SCC failures.

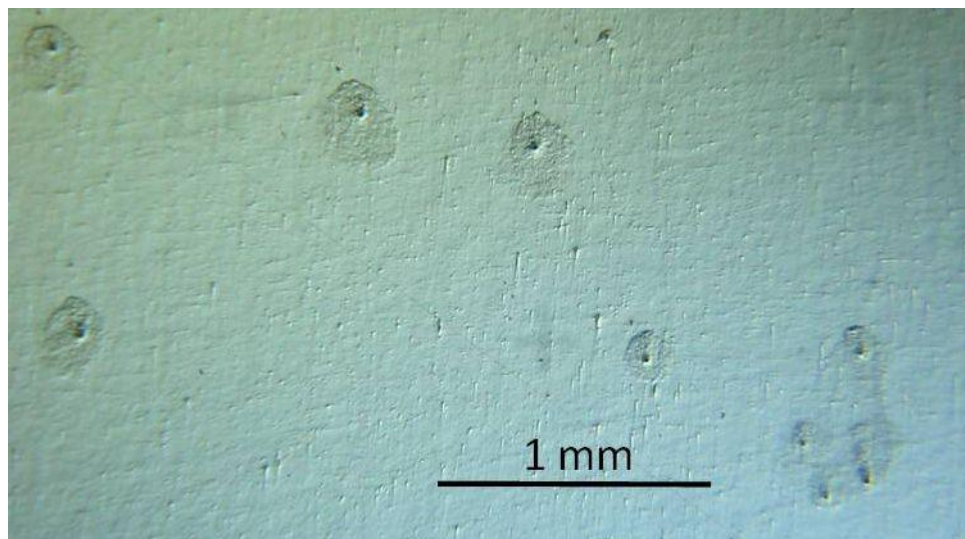


Figure 10-13 Image showing Rapid Localized Corrosion (Pit Generation)

10.8 Residual Hydrogen in the Pipe Sample

To determine any trends in residual hydrogen eighteen samples were excised from the pipe in various locations and their hydrogen concentrations determined. Six samples (approximately 10 mm x 25 mm) were prepared from material in the SCC colony region of the pipe for analysis of the dissolved mobile hydrogen concentration. Three were used to determine the as-received hydrogen concentration, and three were subjected to the bake-out procedure. Six pipe samples were prepared from a region away from the SCC colony for comparison. Three samples were tested as-received and three were baked-out. Six samples were also prepared, from steel within the SCC colony, to determine if hydrogen was preferentially located near the outer or inner surface of the pipe. These samples were cut with 45° bevels in such a way that the triangular cross-section of the piece would be weighted with either more material from the external diameter or internal diameter (see Figure 10-14). The bake-out and eudiometry procedures are detailed in Section 4.4 (of the diffusion methods chapter).

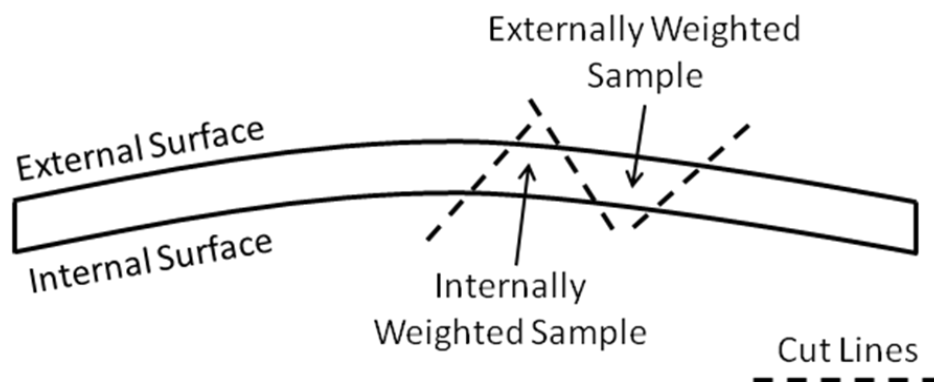


Figure 10-14 Sample Configuration for Externally and Internally Weighted Samples Cut from a Pipe Sample

The results are shown below in Table 10-2 and indicate that the sampling and eudiometry technique was able to detect a significant difference in hydrogen concentration between the steel

within the SCC colony and material outside the colony ($p = 0.015$) and between the material within the colony and the internally weighted samples ($p = 0.029$). There is no difference detected when baking out material within the SCC colony but there is a significant difference between the as-received and baked-out material from outside the SCC colony ($p = 0.050$). Although there is a difference between the measured means of the external and internally weighted samples these measurements lead to a result that is not quite statistically significant ($p = 0.086$). Together these results indicate that there is higher hydrogen concentration in the steel at the site of the SCC colony and that there is a preference for hydrogen to reside near the external surface of the pipe. It is also clear that the steel within the SCC colony does not release its hydrogen when baked at 110°C as does steel outside the colony.

Table 10-2 Residual Hydrogen Concentrations in the Pipe Sample

<i>Location or Condition</i>	<i>Mean Hydrogen Concentration (ppm)</i>	<i>Standard Deviation (ppm)</i>
As-received within SCC Colony	3.22	0.21
Baked-out within SCC Colony	3.38	0.53
As-received away from SCC Colony	1.73	0.59
As-received away from SCC Colony and Baked-out	0.75	0.17
External Surface Weighted	3.19	0.55
Internal Surface Weighted	2.25	0.46

The pipeline steel has been able to hold on to significant amounts of hydrogen several years after the initial failure. The SCC colony still had a residual concentration higher than steel away from the colony and the hydrogen was preferentially located near the exterior surface of the pipe.

Also significant is that the material within the colony did not release any hydrogen after baking

while the material away from the colony did. This indicates that the highly strained material near the cracks, with an increased concentration of dislocation tangles, holds hydrogen in much higher energy traps than uncracked steel. This observation could have great impact on the pressure vessel fabrication industry as vessels are commonly baked to remove hydrogen before entering service and also in operations as some vessels are baked routinely to remove accumulated hydrogen once in-service.

10.9 Overall Discussion

This field-failed pipe suffered from SCC that had developed under disbonded coating. As part of the normal SCC progression for this type of failure, the failed coating allowed water and soil salts to collect next to the pipe steel, and simultaneously shield that section of pipe from the beneficial effects of cathodic protection. This resulted in the isolated section of pipe, along with thermal conditions and mechanical loading, developing SCC colonies and eventually failing during hydrotest.

When an electrolyte is separated from the general environment, the local chemistry can become very aggressive [Jones, 1996 pg 199], whether it is in the form of pitting, crevice corrosion, crack corrosion, or the small concentration cells generated by the droplets of water as seen in the pit generation experiment above. Generation of the corrosion pits seen in the failed specimen could happen quite quickly as soon as water is allowed to get next to the steel. As seen in the photomicrographs, the corrosion pits are not oriented and therefore are not influenced by the applied stress field. The stress corrosion cracks are in all cases aligned with the pipe axis, perpendicular to the hoop stress, and are not necessarily associated with a corrosion pit. Pits do not need a crack to develop, and cracks do not necessarily need pits to develop. A summary of the characteristics of the two major features seen is presented in Table 10-3.

Table 10-3 Characteristics of the Two Main Features of this Field-Failed SCC Specimen

<i>Corrosion Pits</i>	<i>SCC Cracks</i>
Pure Dissolution Process	Dissolution Plus Stress Field
Like Crevice Corrosion, Corrosion Cells	Crack Growth
Localized Corrosion Attack	Anodic Dissolution
Hydrogen Producing	Hydrogen Producing

What these observations indicate is that corrosion pits will develop under disbonded coating first and that, in time, cracks start to develop in response to the applied stress field. There are many systems where localized corrosion takes place leading to a pinhole failure [Jones, 1996 pg 199] yet in this system it was a coalescing crack in an SCC colony that lead to failure. Knowing that hydrogen is produced in corrosion reactions and can adsorb on and enter the steel, affecting material properties, it is very likely that the long incubation times seen in near-neutral pH SCC development is due to hydrogen's effects.

Hydrogen is produced in corrosion reactions under disbonded coating. Some of this hydrogen enters the steel and diffuses to, and collects in, defects in the material. In time (usually years of service), significant hydrogen can collect at defects and cause internal damage, leading to an increase in defect size and formation of microcracks (seen around large pits). These cracks undergo anodic dissolution and crack growth, producing more hydrogen (as evidenced by the high residual hydrogen concentration seen above) and sensitizing other nearby areas of the material. In summary, the early localized corrosion under disbonded coating forms pits and generates hydrogen, leading to increased sensitivity in the steel to the applied load, defect formation and crack growth, and further hydrogen production in a vicious cycle.

Of the phases of SCC progression (Figure 10-15) the first two phases, incubation and initiation of the crack field, are the least understood. SCC failures seen in oil and gas pipelines have incubation periods that range from years to decades, making them difficult to model and test in an experimental situation. This information developed in this thesis can help to inform the models of SCC progression, especially in the nucleation/incubation and initiation phases.

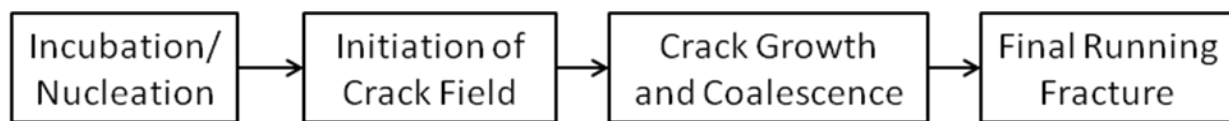


Figure 10-15 Phases of the Progression of SCC

An understanding of the progression from pits to cracks to final fracture and the role of hydrogen is as follows:

- i. Breakdown of pipe coating and infiltration of electrolyte causing corrosion, pit formation and growth.
- ii. Surface and pit corrosion generates hydrogen, some of which diffuses into the steel.
- iii. After some amount of time the material became susceptible to the hoop stress and cracks developed, both emerging from pits and on the pipe's surface and likely due to hydrogen accumulation.
- iv. Corrosion continues, with continued generation of hydrogen, and cracks grow and link together.
- v. Eventually the crack field has enough linked cracks that the effective crack length is long enough to lead to a running fracture and pipe failure.

The pitting and cracking events are separated (cracks emerge from the bottom of pits and from the free surface) and the steel is obviously designed to not normally be susceptible to crack progression at the applied stress. Therefore there must be a factor that sensitizes the steel to the applied stress, which in this case must be hydrogen's accumulation in the material.

Accumulating hydrogen and the hoop stress can then work synergistically to create sensitivity in the steel and lead to the progression of SCC.

Chapter Eleven: **Conclusions and Future Work**

This work examined hydrogen dissolved in low carbon steel. The first section detailed hydrogen diffusion and the concentration profile in a material undergoing passive corrosion. The diffusion rates and concentration profile knowledge were used in the next section, which studied the effect of diffused hydrogen on the mechanical properties of a similar low carbon steel. Finally, knowledge gained from these experiments was used, along with some new analysis techniques, to help interpret the failure mode of a SCC field-failed pipeline.

11.1 Hydrogen Diffusion in Low Carbon Steel.

Fick's Law of diffusion has been used to study hydrogen transport phenomena for steel systems but never validated through direct measurement. Predictions of a material's performance in hydrogen environments are based on methods that rely on an assumption of hydrogen transport following Fick's Law, even though that most basic assumption has not been tested directly. The methods and experiments presented in this part of the thesis used a round bar, hydrogen charging through passive corrosion, and a novel sectioning technique to test a uniaxial model of hydrogen diffusion through low carbon steel. The following is a summary of the conclusions from this work:

Major Conclusions.

1. The apparent hydrogen diffusion coefficient, surface concentration, and bulk concentration can be determined using passive solution charging sectioning, and mercury eudiometry (direct hydrogen measurement).
2. The apparent surface concentration of hydrogen increases with increased aggressiveness of charging solution, indicating increased corrosion rates.

3. The apparent diffusion coefficient increases with increased aggressiveness of charging solution.

Secondary Conclusions.

4. The main experimental conditions (1.1 pH, 5% NaCl, N₂ deaeration) showed stable surface concentration over a range of charging times and therefore was useful as an experimental ‘constant’ (non-varying parameter) for further experimentation.
5. Any hydrogen adsorbed on the metal surface is easily removed and will not affect the results of Fick’s Law analysis.

Further Questions and Future Work. One question that remains is why the diffusion rate is sensitive to the charging conditions. Once the hydrogen enters the steel, there is no contact with the surface anymore so how can the two be related? What does this mean for a pipe with failed coating underground, where the surface is changing, the electrolyte is changing, and presumably the diffusion coefficient is changing? Another area of study that could lead to interesting results is to link the hydrogen concentration profile and apparent surface concentration to the corrosion rate and exchange current. Knowledge of these values may shed light on the reactions and hydrogen surface coverage on the electrolyte-metal interface. As in many examinations of the behaviour of materials, this work could be applied to a variety of other metals, microstructures, and alloys.

11.2 Hydrogen Effect on Material Properties of Low Carbon Steel.

Historically much work has been done to study the effects of hydrogen on the properties of steel. In the current work hydrogen is treated as a mobile solute and tested in varying concentrations with varying strain rate in the same experiment. Some of the observations below could not have

been seen without simultaneously varying both parameters. The following is a summary of the conclusions of this work:

Major Conclusions.

1. The necking strain was affected by the hydrogen concentration and unaffected by the strain rate while the uniform strain was affected by the strain rate and unaffected by the hydrogen concentration, making the stress-strain curve separable into two general regions: pre-ultimate where the material behaviour was dominated by strain rate, and post-ultimate where the material behaviour was dominated by sensitivity to hydrogen concentration.
2. Increasing hydrogen concentration moved the point of final fracture backwards up the typical stress-strain curve.
3. Elevation of the yield and ultimate strength with increasing strain rate. A trend is apparent, especially with the pooled data, in that there were two regimes. Below a strain rate of $6.17 \times 10^{-2} \text{ s}^{-1}$ there was a lower sensitivity to strain rate and above that value was an increased sensitivity.
4. There was a small localized increase in flow stresses over a range of strain rates (above the trend noted above). The location of this increase appeared dependant on hydrogen concentration.
5. Reestablishment of Lüders regions show hydrogen quickly diffused to areas of high local strain through elevation of the subsequent yield stress and flattened stress-strain curve until rejoining the previous path.

Secondary Conclusions.

6. The experimental procedure produced very good repeatability and sensitivity to changes in material properties, especially the flow stresses.
7. Surface degradation associated with time in solution did not affect the measured properties in the range of experimental conditions studied, either for the surface damage (pits, general corrosion) or for internal hydrogen damage.
8. In this system, hydrogen slightly raised the yield strength (hardening) and slightly lowered the ultimate (softening), yet neither effect conforms to the typical solid solution strengthening relationship that applies to other interstitial solutes.
9. Increasing strain rate increased yield strength, ultimate strength, fracture stress, uniform plastic strain, and strain hardening exponent.
10. Increasing hydrogen concentration decreased necking strain and elongation at fracture, and increases fracture stress.

The tensile response shows the effect of hydrogen is limited to the necking region, so tests that emphasize triaxiality will work better to determine hydrogen's effects. Tests of this type are used for hydrogen material classification [Stoltz, 1981] and this research demonstrates why they are appropriate. An interesting observation is that with increasing hydrogen concentration there is a loss in ductility without much of a change in either yield or ultimate strength. Quite often in material science, changing a material (alloying, processing) results in a realignment of the strength-ductility balance. Changes made to improve strength often come at the cost of ductility, and improvements to ductility often come at the cost of strength. Two notable exceptions to this are grain refinement (generally strength increase without sacrificing ductility) and the effect of hydrogen (loss of ductility without changes to strength).

Further Questions and Future Work. When evaluating materials for hydrogen service, this work indicates that certain strain rates are better to determine the hydrogen effect. A material screening or ranking test should be designed to maximize the detectable difference between candidate materials, so choosing an appropriate strain rate will increase the separation between the materials' hydrogen response. This research did not determine whether the hydrogen effects were seen because of the state of triaxiality or due to increased strain rate. Ways to test this might include extending the strain rates studied, especially the faster strain rates, or working with theoretical models of dislocation velocity tied to applied deformation rates. Small, but detectable, differences were seen with hydrogen increasing the yield strength (hardening) and decreasing the ultimate strength (softening). These techniques might be useful in determining the differential effects of strengthening and softening mechanisms of hydrogen, a research area that has very little experimental support. As in many examinations of the behaviour of materials, this work could be applied to a variety of other metals, microstructures, and alloys.

11.3 Examination of SCC Field-Failed Pipe.

Exemplars of failed pipelines are useful tools to examine the root cause of industrially significant failure modes. While the coating type from this pipe is no longer used for corrosion protection on new pipelines, there is a large amount of similar pipe still in use today. In-line inspection (ILI) tools, external corrosion direct assessment (ECDA), and hydrotesting are the primary means of detecting SCC before a failure occurs, but knowledge of the mechanisms of SCC are useful in predicting a material's performance. In today's economy pipelines are bought, sold, and repurposed so any information that leads to safer operation is of benefit to all. The following is a summary of the conclusions of this failed pipe analysis:

Major Conclusions.

1. The cracking and pitting processes were separable. Pits showed no directionality associated with the applied pipe stress field, but the cracks were all oriented perpendicular to the hoop stress. Though all pits generate cracks, there are cracks that did not emerge from pits.
2. Hydrogen was located in greater concentrations at the site of the SCC colony than in pipe away from the colony.
3. Within the SCC colony, hydrogen was found in greater concentrations near the external surface of the pipe than near the internal surface.
4. Hydrogen was held much more tenaciously in the cracked section of pipe than in areas away from the SCC colony.
5. Pitting and general corrosion generated hydrogen, which sensitized the steel to the applied stress, leading to crack formation and growth perpendicular to the applied hoop stress.

Secondary Conclusions.

6. A method was developed to examine the morphology of a SCC colony as it progresses into the depth of the material and relate that to a crack depth visualization procedure.
7. This failure showed wide cracks indicating aggressive and continued anodic dissolution.
8. It was relatively easy to create conditions of local corrosion chemistry that generated pits
9. The indicated SCC progression was:
 - i. Electrolyte collected on the metal surface under damaged coating.
 - ii. General corrosion and pits developed, generating hydrogen.
 - iii. Hydrogen sensitized the material to the stress field, cracks initiated and grew.

- iv. Multiple cracks grew and interacted with each other, eventually coalescing into an effectively larger crack feature.
- v. The large crack feature and hydrogen weakened the material's resistance to a running crack failure and the pipe burst during hydrotest.

11.4 Concluding Remarks

Hydrogen in carbon steel has negative impact on material performance and is indicated in many modes of material failure in service, whether it is through SCC, hydrogen embrittlement, hydrogen cracking, or other phenomena. Yet the mechanisms of those effects are poorly understood despite decades of research. In addition to the above observations this work has provided: validation of the use of Fick's diffusion laws, a tool to examine the surface concentration of diffusible hydrogen that can be related to environmental conditions, a sensitive tool for determining changes in the flow stresses due to hydrogen, validation for the use of tensile tests using a triaxial state of deformation, and observations on the incubation and nucleation phases of SCC colony formation.

References

- Almeida, L. H., Le May, I., & Emygdio, P. R. O. (1998). Mechanistic Modeling of Dynamic Strain Aging in Austenitic Stainless Steels. *Materials Characterization*, 41, 137-150.
- ANSI. (R2006). ANSI AWS A4.3 1993, Standard Methods for Determination of the Diffusible Hydrogen Content of Martensitic, Bainitic, and Ferritic Steel Weld Metal Produced by Arc Welding. Washington, DC: American National Standards Institute.
- Astaf'ev, V. I., Narushev, V. M., & Tetyueva, T. V. (1999). A Method for Testing Pipe Steels under the Conditions of Sulfide Stress Cracking. *Materials Science*, 35(4), 587-591.
- ASTM. (2009). ASTM E8/E8M, Standard Test Methods for Tension Testing of Metallic Materials. West Conshohocken, PA: ASTM International.
- ASTM. (2009). ASTM E399, Standard Test Method for Linear-Elastic Plane-Strain Fracture Toughness K_{IC} of Metallic Materials. West Conshohocken, PA: ASTM International.
- ASTM. (2010). ASTM Standard E112, Standard Test Methods for Determining Average Grain Size. West Conshohocken, PA: ASTM International.
- ASTM. (2011). ASTM E384, Standard Test Method for Knoop and Vickers Hardness of Materials. West Conshohocken, PA: ASTM International.
- Balik, J., & Lukac, P. (1989). Influence of Solute Mobility on Dislocation Motion I. Basic Model. *Czechoslovak Journal of Physics*, B39, 447-457.
- Balik, J., & Lukac, P. (1989). Influence of Solute Mobility on Dislocation Motion II. Application of the Basic Model. *Czechoslovak Journal of Physics*, B39, 1138-1146.
- Baranowski, B., Majchrzak, S., & Flanagan, T. B. (1971). The Volume Increase of FCC Metals and Alloys due to Interstitial Hydrogen over a Wide Range of Hydrogen Contents. *Journal of Physics F: Metal Physics*, 1, 258-261.
- Bayoumi, M. R. (1993). The Mechanics and Mechanisms of Fracture in Stress Corrosion Cracking of Aluminium Alloys. *Engineering Fracture Mechanics*, 54(6), 879-889.
- Belogazov, S. M. (2003). Peculiarity of Hydrogen Distribution in Steel by Cathodic Charging. *Journal of Alloys and Compounds*, 356-357, 240-243.
- Birnbaum, H. K., Fukushima, H., & Baker, J. (1982). Application of High Resolution Secondary Ion Mass Spectrometer Techniques (Ion Probe) to Studies of Hydrogen in Metals. *Metallurgical Society of AIME*, 149-154.
- Birnbaum, H. K., & Sofronis, P. (1994). Hydrogen-Enhanced Localized Plasticity - A Mechanism for Hydrogen-Related Fracture. *Materials Science & Engineering A*, A176, 191-202.

- Bockris, J. O. M., & Reddy, A. K. N. (2000). Modern Electrochemistry 2B: Electrode Processes in Chemistry, Engineering, Biology, and Environmental Science. In (2 ed., pp. 1669-1673). New York: Kluwer Academic, Plenum Publishers.
- Brown, J. T., & Baldwin, W. M. (1953). The Effects of Stress Concentration and Triaxiality of the Plastic Flow of Metals. Cleveland, Ohio: Case Institute of Technology and Office of Naval Research, US Navy.
- Bruemmer, S. M., & Was, G. S. (1994). Microstructural and Microchemical Mechanisms Controlling Intergranular Stress Corrosion Cracking in Light Water Reactor Systems. *Journal of Nuclear Materials*, 216, 348-363.
- Bulger, J. T., Lu, B. T., & Luo, J. L. (2006). Microstructural Effect on Near-Neutral pH Stress Corrosion Cracking Resistance of Pipeline Steels. *Journal of Materials Science*, 41, 5001-5005.
- Burwell, D., Brongers, M. P. H., & Beavers, J. A. (2004). Review of Test Methods for Evaluating Hydrogen Embrittlement Susceptibility of Materials. Paper presented at the Flaw Evaluation, Service Experience, and Materials for Hydrogen Service, San Diego, CA.
- Callister, W. D. (2003). *Materials Science and Engineering an Introduction* (6 ed.). New York: John Wiley & Sons, Inc.
- CEPA. (2007). *Stress Corrosion Cracking Recommended Practices*. Calgary, Alberta: Canadian Energy Pipeline Association.
- Cheng, Y. F. (2007). Fundamentals of Hydrogen Evolution Reaction and its Implications on Near-Neutral pH Stress Corrosion Cracking of Pipelines. *Electrochimica Acta*, 52, 2661-2667.
- Cheng, Y. F. (2007). Thermodynamically Modeling the Interactions of Hydrogen, Stress and Anodic Dissolution at Crack-Tip During Near-Neutral pH SCC in Pipelines. *Journal of Materials Science*, 42, 2701-2705.
- Cheng, Y. F., & Niu, L. (2007). Application of Electrochemical Techniques in Investigation of the Role of Hydrogen in Near-Neutral pH Stress Corrosion Cracking of Pipelines. *Journal of Materials Science*, 42, 3425-3434.
- Chew, B. (1971). A Void Model for Hydrogen Diffusion in Steel. *Metal Science Journal*, 5, 195-200.
- Cotterill, P. (1961). The Hydrogen Embrittlement of Metals. *Progress in Materials Science*, 9, 205-301.
- Davis, R. T., & Butler, T. J. (1958). The Reduction of Passive Films by Hydrogen Diffusion through Steel. *Journal of the Electrochemical Society*, 105(10), 563-568.
- Dean, F. W. H., & Fray, D. J. (2000). Ultrasensitive Technique for Detection of Hydrogen Emanating from Steel and other Solid Surfaces. *Materials Science and Technology*, 16, 41-46.

- Despic, A. R., Raicheff, R. G., & Bockris, J. O. M. (1968). Mechanism of the Acceleration of the Electrode Dissolution of Metals during Yielding under Stress. *Journal of Chemical Physics*, 49(2), 926-938.
- Draheim, K. J., & Schlipf, J. (1996). Simulation of Dynamic Strain Aging and the Portevin-Le Chatelier Effect. *Computational Materials Science*, 5, 67-74.
- Duprez, L., Verbeken, K., & Verhaege, M. (2009). Effect of Hydrogen on the Mechanical Properties of Multiphase High Strength Steels. *Proceedings of the 2008 International Hydrogen Conference*, 62-69.
- Duval, A., & Robinson, M. (2009). Measurement and Prediction of Hydrogen Embrittlement in High Strength Carbon Steel. *Corrosion Engineering, Science and Technology*, 44(5), 340-346.
- Eliezer, D., Eliaz, N., Senkov, O. N., & Froes, F. H. (2000). Positive Effects of Hydrogen in Metals. *Materials Science & Engineering A*, A280, 220-224.
- Escobar, D. M. P., Verbeken, K., Duprez, L., & Verhaege, M. (2009). Experimental Evaluation of the Hydrogen Distribution in Steel by Thermal Decomposition Spectroscopy. *Proceedings of the 2008 International Hydrogen Conference*, 477-484.
- EUB. (2007). *Pipeline Performance in Alberta, 1990-2005*. Calgary, AB: Alberta Energy and Utilities Board.
- Fernandes, P. J. L., & Jones, D. R. H. (1997). Mechanisms of Liquid Metals Induced Embrittlement. *International Materials Reviews*, 42(6), 251-261.
- Foct, F., Bouvier, O. D., & Magnin, T. (2000). Stress Corrosion Cracking Mechanisms of Alloy 600 Polycrystals and Single Crystals in Primary Water - Influence of Hydrogen. *Metallurgical and Materials Transactions*, 31A, 2025-2036.
- Foster, P. K., McNabb, A., & Payne, C. M. (1965). On the Rate of Loss of Hydrogen from Cylinders of Iron and Steel. *Transactions of the Metallurgical Society of AIME*, 233, 1022-1031.
- Fukai, Y. (1984). Site Preference of Interstitial Hydrogen in Metals. *Journal of the Less-Common Metals*, 101, 1-16.
- Gamboa, E., & Atrens, A. (2003). Stress Corrosion Cracking Fracture Mechanisms in Rock Bolts. *Journal of Materials Science*, 38, 3813-3829.
- Garber, R., Bernstein, I. M., & Thompson, A. W. (1976). Effect of Hydrogen on Ductile Fracture of Spheroidized Steel. *Scripta Metallurgica*, 10, 341-345.
- Grabke, H. J., & Riecke, E. (2000). Absorption and Diffusion of Hydrogen in Steels. *Materiali in Tehnologije*, 34(6), 331-342.

- Griffiths, A. J., & Turnbull, A. (1995). On the Effective Diffusivity of Hydrogen in Low Alloy Steels. *Corrosion Science*, 37(11), 1879-1881.
- Gy, R. (2003). Stress Corrosion of Silicate Glass: A Review. *Journal of Non-Crystalline Solids*, 316, 1-11.
- Hardie, D., Charles, E. A., & Lopez, A. H. (2006). Hydrogen Embrittlement of High Strength Pipeline Steels. *Corrosion Science*, 48, 4378-4385.
- Hart, E. W. (1967). Theory of the Tensile Test. *Acta Metallurgica*, 15, 351-355.
- Head, G. E., Nix, W. D., & Barrett, C. R. (1970). Effect of Substitutional Solute on the Motion of Dislocations at High Temperatures. *Scripta Metallurgica*, 4, 907-912.
- Hertzberg, R. W. (1996). *Deformation and Fracture Mechanics of Engineering Materials* (4th ed.). Hoboken, NJ: John Wiley and Sons, Inc.
- Hirth, J. P. (1980). Effects of Hydrogen on the Properties of Iron and Steel. *Metallurgical and Materials Transactions*, 11A, 861-890.
- Hong, S. G., & Lee, S. B. (2005). Mechanism of Dynamic Strain Aging and Characterization of its effect on the Low-Cycle Fatigue Behaviour in type 316L Stainless Steel. *Journal of Nuclear Materials*, 340, 307-314.
- Hutchings, R. B., Ferriss, D. H., & Turnbull, A. (1993). Ratio of Specimen Thickness to Charging Area for Reliable Hydrogen Permeation Measurement. *British Corrosion Journal*, 28(4), 309-312.
- Iacoviello, F., Galland, J., & Habashi, M. (1998). A Thermal Outgassing Method (T.O.M.) to Measure the Hydrogen Diffusion Coefficients in Austenitic, Austeno-Ferritic and Ferritic-Perlitic Steels. *Corrosion Science*, 40(8), 1281-1293.
- Ichitani, K., & Kanno, M. (2003). Visualization of Hydrogen Diffusion in Steels by High Sensitivity Hydrogen Microprint Technique. *Science and Technology of Advanced Materials*, 4, 545-551.
- Ina, K., & Koizumi, H. (2004). Penetration of Liquid Metals into Solid Metals and Liquid Metal Embrittlement. *Materials Science and Engineering*, A387-389, 390-394.
- Itagaki, M. (2002). Electrochemical Analyses of Anodic Dissolution Mechanism of Metal. *Corrosion Engineering*, 51, 259-269.
- Itagaki, M., Hori, F., & Watanabe, K. (2000). UV/Vis Spectrophotometry/Channel Flow Electrode to Determine Anodic Dissolution of Metal. *Analytical Sciences*, 16, 371-375.
- Iyer, R. N., & Pickering, H. W. (1990). Mechanism and Kinetics of Electrochemical Hydrogen Entry and Degradation of Metallic Systems. *Annual Review of Materials Science*, 20, 299-338.

- Jiang, G., & Li, Y. (2011). A Model for Calculating Hydrogen Solubility in Liquid Transition Metals. *Metallurgical and Materials Transactions*, 42A, 1038-1043.
- Jones, D. A. (1996). *Principles and Prevention of Corrosion* (2 ed.). Upper Saddle River, New Jersey: Prentice-Hall, Inc.
- Kanayama, H., Ndong-Mefane, S., Ogino, M., & Miresmaeili, R. (2009). Reconsideration on the Hydrogen Diffusion Model Using the McNabb-Foster Formulation. *Memoirs of the Faculty of Engineering, Kyushu University*, 69(4), 149-161.
- Kelber, J., & Seshadri, G. (2001). Adsorbate-Catalyzed Anodic Dissolution and Oxidation at Surfaces in Aqueous Solutions. *Surface and Interface Analysis*, 31, 431-441.
- King, H. W. (1971). Quantitative Size-Factors for Interstitial Solid Solutions. *Journal of Materials Science*, 6, 1157-1167.
- Koch, G. H., Brongers, M. P. H., Thompson, N. G., Virmani, Y. P., & Payer, J. H. (2002). *Corrosion Costs and Preventative Strategies in the United States*. Houston, TX: National Association of Corrosion Engineers (NACE).
- Krom, A. H. M., Maier, H. J., Koers, R. W. J., & Bakker, A. (1999). The Effect of Strain Rate on Hydrogen Distribution in Round Tensile Specimens. *Materials Science & Engineering A*, A271, 22-30.
- Kysar, J. W. (2003). Energy Dissipation Mechanisms in Ductile Fracture. *Journal of the Mechanics and Physics of Solids*, 51, 795-824.
- Lepinoux, J., & Magnin, T. (1993). Stress Corrosion Microcleavage in a Ductile FCC Alloy. *Materials Science and Engineering*, A164, 266-269.
- Li, R., & Ferreira, M. G. S. (1996). The Thermodynamic Conditions for Hydrogen Generation Inside a Stress Corrosion Crack. *Corrosion Science*, 38(2), 317-327.
- Ling, Y. (1996). Uniaxial True Stress-Strain after Necking. *AMP Journal of Technology*, 5, 37-48.
- Magnin, T., Chambreuil, A., & Chateau, J. P. (1996). Stress Corrosion Cracking Mechanisms in Ductile FCC Materials. *International Journal of Fracture*, 79, 147-163.
- Magnin, T., Renaudot, N., & Foct, F. (2000). The use of UHP Ni and Ni Base Single Crystals of Study the Stress Corrosion Cracking Mechanisms of Alloy 600 in PWR Environment. *Materials Transactions, JIM*, 41(1), 210-218.
- Makhlouf, M. M., & Sisson, R. D. (1991). Modeling Surface Effects on Hydrogen Permeation in Metals. *Metallurgical Transactions*, 22A, 1001-1006.

- Mao, S. (2001). The Mechanism of Hydrogen-Facilitated Anodic-Dissolution-Type Stress Corrosion Cracking: Theories and Experiments. *Philosophical Magazine A*, 81(7), 1813-1831.
- Mao, S. X., & Li, M. (1998). Mechanics and Thermodynamics on the Stress and Hydrogen Interaction in Crack Tip Stress Corrosion: Experiment and Theory. *Journal of the Mechanics and Physics of Solids*, 46(6), 1125-1137.
- McCormick, P. G. (1972). A Model for the Portevin-Le Chatelier Effect in Substitutional Alloys. *Acta Metallurgica*, 20, 351-354.
- Melitis, E. I., & Hochman, R. F. (1986). A Review of the Crystallography of Stress Corrosion Cracking. *Corrosion Science*, 26(1), 63-90.
- Melitis, E. I., & Huang, W. (1991). A Study of the Three-Dimensional Region at Crack Tips by the Method of Caustics. *Engineering Fracture Mechanics*, 39(5), 875-885.
- Nishimura, R. (1992). Stress Corrosion Cracking of Type 430 Ferritic Stainless Steel in Chloride and Sulfate Solutions. *Corrosion*, 48(11), 882-890.
- Olden, V., Thaulow, C., & Johnsen, R. (2008). Modelling of Hydrogen Diffusion and Hydrogen Induced Cracking in Supermartensitic and Duplex Stainless Steels. *Materials and Design*, 29, 1934-1948.
- Oriani, R. A., & Josephic, P. H. (1980). Effects of Hydrogen on the Plastic Properties of Medium-Carbon Steels. *Metallurgical Transactions*, 11A, 1809-1820.
- Park, G. T., Koh, S. U., Jung, H. G., & Kim, K. Y. (2008). Effect of Microstructure on the Hydrogen Trapping Efficiency and Hydrogen Induced Cracking of Linepipe Steel. *Corrosion Science*, 50, 1865-1871.
- Parkins, R. N. (1987). Factors Influencing Stress Corrosion Crack Growth Kinetics. *Corrosion*, 43(3), 130-139.
- Parkins, R. N., & Singh, P. M. (1990). Stress Corrosion Crack Coalescence. *Corrosion*, 46(6), 485-499.
- PFeil, L. B. (1926). The Effect of Occluded Hydrogen on the Tensile Strength of Iron. *Proceedings of the Royal Society*, A112(A780), 182-195.
- Piggott, M. R., & Siarkowski, A. C. (1972). Hydrogen Diffusion through Oxide Films on Steel. *Journal of the Iron and Steel Institute*, 210(12), 901-905.
- Ray, G. P., A, J. R., & Thomas, J. G. N. (1994). Some Aspects of Crack Initiation in Mild Steel under Corrosion Fatigue Conditions. *Journal of Materials Science*, 29, 47-53.
- Richardson, O. W. (1904). The Solubility and Diffusion in Solution of Dissociated Gases. *Philosophical Magazine Series 6*, 7(39), 266-274.

Rios, R., Magnin, T., Noel, D., & Bouvier, O. D. (1995). Critical Analysis of Alloy 600 Stress Corrosion Cracking Mechanisms in Primary Water. *Metallurgical and Materials Transactions*, 26A, 925-939.

Saimoto, S., & Diak, B. J. (2001). Strain Rate Sensitivity of Ultra-Low Carbon Steels. *Materials Science & Engineering A*, A319-321, 294-298.

Sainter, N., Awane, T., Olive, J. M., Matsuoka, S., & Murakami, Y. (2011). Analyses of Hydrogen Distribution around Fatigue Crack of Type 304 Stainless Steel using Secondary Ion Mass Spectrometry. *International Journal of Hydrogen Energy*, 36, 8630-8640.

Sanchez, J., Fulla, J., Andrade, C., & de Andres, P. L. (2008). Hydrogen in α -Iron: Stress and Diffusion. *Physical Review B*, 78, 7p.

Saunders, I. (2005). Interstitial Sites in Cubic Crystals, *Phys313 Lecture Notes* (pp. 14). Lancaster, UK.

Scott, P. (1994). A Review of Irradiation Assisted Stress Corrosion Cracking. *Journal of Nuclear Materials*, 211, 101-122.

Senadheera, T. D. A. A., & Shaw, W. J. D. (2009). Improvements in the Mercury Displacement Method for Measuring Diffusible Hydrogen Contents in Steels. *Journal of Testing and Evaluation*, 37(3), 8pg.

Seshadri, G., Lin, T. C., & Kelber, J. (1997). The Promotion of the Anodic Dissolution of Polycrystalline Iron Surfaces by Adsorbed Sulfur: A UHV-Electrochemical Study. *Corrosion Science*, 39(5), 987-1000.

Shaw, W. J. D. (1986). Stress Corrosion Cracking Behaviour of IN-9021 Aluminum Alloy. *Metallography*, 19, 227-233.

Shaw, W. J. D., Bison, A., & LeBlanc, T. (1998). Paper 392: Parameters Affecting Electrochemical Hydrogen Permeation Measurements. *Transactions of Corrosion 98*, San Diego.

Shaw, W. J. D., & Matie, D. G. (1998). Limits and Correlations of Vacuum Induced Hydrogen Flux in Corrosive Environments. Calgary, Alberta: University of Calgary, Department of Mechanical Engineering.

Siddiqui, R. A., & Abdullah, H. A. (2005). Hydrogen Embrittlement in 0.31% Carbon Steel Used for Petrochemical Applications. *Journal of Materials Processing Technology*, 170, 430-435.

Sieradzki, K., & Newman, R. C. (1987). Stress-Corrosion Cracking. *Journal of Physics and Chemistry of Solids*, 48(11), 1101-1113.

- Smith II, R. D., Landis, G. P., Maroef, I., Olson, D. L., & Wildeman, T. R. (2001). The Determination of Hydrogen Distribution in High-Strength Steel Weldments Part 1: Laser Ablation Methods. *Welding Journal*, 80(5), 115s-121s.
- Smith II, R. D., Landis, G. P., Maroef, I., Olson, D. L., & Wildeman, T. R. (2001). The Determination of Hydrogen Distribution in High-Strength Steel Weldments Part 2: Opto-Electronic Diffusible Hydrogen Sensor. *Welding Journal*, 80(5), 122-125.
- Sofronis, P., & Robertson, I. M. (2006). Viable Mechanisms of Hydrogen Embrittlement - A Review. Paper presented at the Hydrogen in Matter: Second International Symposium on Hydrogen in Matter.
- Srinivas, M., Malakondaiah, G., Murty, K. L., & Rao, P. R. (1991). Fracture Toughness in the Dynamic Strain Ageing Regime. *Scripta Metallurgica et Materialia*, 25, 2585-2588.
- Stoltz, R. E. (1981). Plane Strain Tensile Testing for Measuring Environment Sensitive Fracture. *Metallurgical Transactions*, 12A, 543-545.
- Sudarshan, T. S., Louthan, M. R., & McNitt, R. P. (1978). Hydrogen Induced Suppression of Yield Point in A-106 Steel. *Scripta Metallurgica*, 12, 799-803.
- Suess, S. J. (2007). Stress Corrosion Cracking of Various Alloys - Part 1. *Materials Performance*, 46(8), 74-79.
- Thompson, A. W. (1985). Hydrogen-Assisted Fracture at Notches. *Materials Science and Technology*, 1, 711-718.
- Thompson, A. W., & Bernstein, I. M. (1978). The Role of Plastic Fracture Processes in Hydrogen Embrittlement. *Fracture*, 2, 249-254.
- Tirbonod, B. (2004). A Model for an Anodic Dissolution Cell in Connection to its Dimensions for Stress Corrosion Cracking. *Corrosion Science*, 46, 2715-2741.
- Toribio, J. (1993). Role of Hydrostatic Stress in Hydrogen Diffusion in Pearlitic Steel. *Journal of Materials Science*, 28, 2289-2298.
- Turnbull, A. (2001). Modeling of the Chemistry and Electrochemistry in Cracks - A Review. *Corrosion*, 57(2), 175-189.
- Turnbull, A., Carroll, M. W., & Ferriss, D. H. (1989). Analysis of Hydrogen Diffusion and Trapping in a 13% Chromium Martensitic Stainless Steel. *Acta Metallurgica*, 37(7), 2039-2046.
- Turnbull, A., Ferriss, D. H., & Anzai, H. (1996). Modelling of the Hydrogen Distribution at a Crack Tip. *Materials Science and Engineering*, A206, 1-13.
- Turnbull, A., & Hutchings, R. B. (1994). Analysis of Hydrogen Atom Transport in a Two-Phase Alloy. *Materials Science and Engineering*, A177, 161-171.

Turnbull, A., Hutchings, R. B., & Ferriss, D. H. (1997). Modelling of Thermal Desorption of Hydrogen from Metals. *Materials Science and Engineering*, A238, 317-328.

Turnbull, A., Zhou, S., & Hinds, G. (2004). Stress Corrosion Cracking of Steam Turbine Disc Steel-Measurement of the Crack-Tip Potential. *Corrosion Science*, 46, 193-211.

Wang, M., Akiyama, E., & Tsuzaki, K. (2005). Crosshead Speed Dependence of the Notch Tensile Strength of a High Strength Steel in the Presence of Hydrogen. *Scripta Materialia*, 53, 713-718.

Wang, M., Akiyama, E., & Tsuzaki, K. (2007). Effect of Hydrogen on the Fracture Behaviour of High Strength Steel During Slow Strain Rate Test. *Corrosion Science*, 49, 4081-4097.

Wang, Y., Srolovitz, D. J., Rickman, J. M., & Lesar, R. (2000). Dislocation Motion in the Presence of Diffusing Solutes: A Computer Simulation Study. *Acta Materialia*, 48, 2163-2175.

Wang, Z. F., Briant, C. L., Kumar, K. S., Wei, X. J., Li, J., & Ke, W. (1998). Effect of Anodic Dissolution and Hydrogen Absorption of Plastic Zone at Fatigue Crack Tip in Structural Steel. *Materials Transactions, JIM*, 39(3), 365-369.

Winter, M. (1993). WebElements Periodic Table of the Elements. Retrieved September 25, 2009, from <http://www.webelements.com/>

Winzer, N., Atrens, A., Song, G., Ghali, E., Dietzel, W., Kainer, K. U., et al. (2005). A Critical Review of the Stress Corrosion Cracking (SCC) of Magnesium Alloys. *Advanced Engineering Materials*, 7(8), 659-693.

Yan, M., & Weng, Y. (2006). Study on Hydrogen Absorption of Pipeline Steel under Cathodic Charging. *Corrosion Science*, 48, 432-444.

Zachoczynski, T. (1985). Entry of Hydrogen into Iron Alloys from the Liquid Phase. In R. A. Oriani, J. P. Hirth & M. Smialowski (Eds.), *Hydrogen Degradation of Ferrous Alloys* (pp. 215-247). Park Ridge, USA: Noyes Publications.

Zhao, J. Z., De, A. K., & Cooman, B. C. D. (2000). Kinetics of Cottrell Atmosphere Formation during Strain Aging of Ultra-Low Carbon Steels. *Materials Letters*, 44, 374-378.

Zheng, W., & Hardie, D. (1991). The Effect of Hydrogen on the Fracture of a Commercial Duplex Stainless Steel. *Corrosion Science*, 32(1), 23-36.

Zhou, X. Y., Congelton, J., & Bahraloom, A. (1998). Mechanisms of Stress Corrosion Cracking for Iron-Based Alloys in High-Temperature Water. *Corrosion*, 54(11), 898-909.

Zhou, X. Y., Congelton, J., & Han, Y. M. (2000). Mechanisms of Stress Corrosion Cracking for Iron Base Alloys in Hot Ca(NO₃)₂ Solution. *British Corrosion Journal*, 35(3), 217-223.